



QUANTITATIVE SUSCEPTIBILITY MAPPING IN NEURODEGENERATION

EDITED BY: Minming Zhang, Hongjiang Wei, Fuhua Yan, Mark Haacke and
Yi Wang

PUBLISHED IN: Frontiers in Neuroscience



frontiers

Frontiers eBook Copyright Statement

The copyright in the text of individual articles in this eBook is the property of their respective authors or their respective institutions or funders. The copyright in graphics and images within each article may be subject to copyright of other parties. In both cases this is subject to a license granted to Frontiers.

The compilation of articles constituting this eBook is the property of Frontiers.

Each article within this eBook, and the eBook itself, are published under the most recent version of the Creative Commons CC-BY licence.

The version current at the date of publication of this eBook is CC-BY 4.0. If the CC-BY licence is updated, the licence granted by Frontiers is automatically updated to the new version.

When exercising any right under the CC-BY licence, Frontiers must be attributed as the original publisher of the article or eBook, as applicable.

Authors have the responsibility of ensuring that any graphics or other materials which are the property of others may be included in the CC-BY licence, but this should be checked before relying on the CC-BY licence to reproduce those materials. Any copyright notices relating to those materials must be complied with.

Copyright and source acknowledgement notices may not be removed and must be displayed in any copy, derivative work or partial copy which includes the elements in question.

All copyright, and all rights therein, are protected by national and international copyright laws. The above represents a summary only. For further information please read Frontiers' Conditions for Website Use and Copyright Statement, and the applicable CC-BY licence.

ISSN 1664-8714

ISBN 978-2-88971-379-0

DOI 10.3389/978-2-88971-379-0

About Frontiers

Frontiers is more than just an open-access publisher of scholarly articles: it is a pioneering approach to the world of academia, radically improving the way scholarly research is managed. The grand vision of Frontiers is a world where all people have an equal opportunity to seek, share and generate knowledge. Frontiers provides immediate and permanent online open access to all its publications, but this alone is not enough to realize our grand goals.

Frontiers Journal Series

The Frontiers Journal Series is a multi-tier and interdisciplinary set of open-access, online journals, promising a paradigm shift from the current review, selection and dissemination processes in academic publishing. All Frontiers journals are driven by researchers for researchers; therefore, they constitute a service to the scholarly community. At the same time, the Frontiers Journal Series operates on a revolutionary invention, the tiered publishing system, initially addressing specific communities of scholars, and gradually climbing up to broader public understanding, thus serving the interests of the lay society, too.

Dedication to Quality

Each Frontiers article is a landmark of the highest quality, thanks to genuinely collaborative interactions between authors and review editors, who include some of the world's best academicians. Research must be certified by peers before entering a stream of knowledge that may eventually reach the public - and shape society; therefore, Frontiers only applies the most rigorous and unbiased reviews. Frontiers revolutionizes research publishing by freely delivering the most outstanding research, evaluated with no bias from both the academic and social point of view. By applying the most advanced information technologies, Frontiers is catapulting scholarly publishing into a new generation.

What are Frontiers Research Topics?

Frontiers Research Topics are very popular trademarks of the Frontiers Journals Series: they are collections of at least ten articles, all centered on a particular subject. With their unique mix of varied contributions from Original Research to Review Articles, Frontiers Research Topics unify the most influential researchers, the latest key findings and historical advances in a hot research area! Find out more on how to host your own Frontiers Research Topic or contribute to one as an author by contacting the Frontiers Editorial Office: frontiersin.org/about/contact

QUANTITATIVE SUSCEPTIBILITY MAPPING IN NEURODEGENERATION

Topic Editors:

Minming Zhang, Zhejiang University, China

Hongjiang Wei, Shanghai Jiao Tong University, China

Fuhua Yan, Shanghai Jiao Tong University, China

Mark Haacke, Wayne State University, United States

Yi Wang, Cornell University, United States

Citation: Zhang, M., Wei, H., Yan, F., Haacke, M., Wang, Y., eds. (2021). Quantitative Susceptibility Mapping in Neurodegeneration. Lausanne: Frontiers Media SA.
doi: 10.3389/978-2-88971-379-0

Table of Contents

- 04 Editorial: Quantitative Susceptibility Mapping in Neurodegeneration**
Fuhua Yan, Naying He and E. Mark Haacke
- 06 Susceptibility and Volume Measures of the Mammillary Bodies Between Mild Cognitively Impaired Patients and Healthy Controls**
Zhijia Jin, Sean K. Sethi, Binyin Li, Rongbiao Tang, Yufei Li, Charlie Chia-Tsong Hsu, Naying He, E. Mark Haacke and Fuhua Yan
- 15 Paramagnetic Metal Accumulation in the Deep Gray Matter Nuclei is Associated With Neurodegeneration in Wilson's Disease**
Xiang-Zhen Yuan, Gai-Ying Li, Jia-Lin Chen, Jian-Qi Li and Xiao-Ping Wang
- 26 Multi-Echo Quantitative Susceptibility Mapping for Strategically Acquired Gradient Echo (STAGE) Imaging**
Sara Gharabaghi, Saifeng Liu, Ying Wang, Yongsheng Chen, Sagar Buch, Mojtaba Jokar, Thomas Wischgoll, Nasser H. Kashou, Chunyan Zhang, Bo Wu, Jingliang Cheng and E. Mark Haacke
- 40 Iron Content in Deep Gray Matter as a Function of Age Using Quantitative Susceptibility Mapping: A Multicenter Study**
Yan Li, Sean K. Sethi, Chunyan Zhang, Yanwei Miao, Kiran Kumar Yerramsetty, Vinay Kumar Palutla, Sara Gharabaghi, Chengyan Wang, Naying He, Jingliang Cheng, Fuhua Yan and Ewart Mark Haacke
- 53 Increased Brain Iron Detection by Voxel-Based Quantitative Susceptibility Mapping in Type 2 Diabetes Mellitus Patients With an Executive Function Decline**
Jing Li, Qihao Zhang, Nan Zhang and Lingfei Guo
- 64 Correlation Between Cerebral Venous Oxygen Level and Cognitive Status in Patients With Alzheimer's Disease Using Quantitative Susceptibility Mapping**
YangYingQiu Liu, JunYi Dong, QingWei Song, Nan Zhang, WeiWei Wang, BingBing Gao, ShiYun Tian, ChunBo Dong, ZhanHua Liang, LiZhi Xie and YanWei Miao
- 73 Alterations of Iron Level in the Bilateral Basal Ganglia Region in Patients With Middle Cerebral Artery Occlusion**
Lei Du, Zifang Zhao, Xiuxiu Liu, Yue Chen, Wenwen Gao, Yige Wang, Jian Liu, Bing Liu and Guolin Ma
- 83 Alterations and Associations Between Magnetic Susceptibility of the Basal Ganglia and Diffusion Properties in Alzheimer's Disease**
Xiuxiu Liu, Lei Du, Bing Zhang, Zifang Zhao, Wenwen Gao, Bing Liu, Jian Liu, Yue Chen, Yige Wang, Hongwei Yu and Guolin Ma
- 95 Systematic Review: Quantitative Susceptibility Mapping (QSM) of Brain Iron Profile in Neurodegenerative Diseases**
Parsa Ravanfar, Samantha M. Loi, Warda T. Syeda, Tamsyn E. Van Rheenen, Ashley I. Bush, Patricia Desmond, Vanessa L. Cropley, Darius J. R. Lane, Carlos M. Opazo, Bradford A. Moffat, Dennis Velakoulis and Christos Pantelis
- 126 Nigral Iron Deposition is Associated With Levodopa-Induced Dyskinesia in Parkinson's Disease**
Tianbin Song, Jiping Li, Shanshan Mei, Xiaofei Jia, Hongwei Yang, Yongquan Ye, Jianmin Yuan, Yuqing Zhang and Jie Lu



Editorial: Quantitative Susceptibility Mapping in Neurodegeneration

Fuhua Yan^{1*}, Naying He¹ and E. Mark Haacke^{1,2}

¹ Department of Radiology, Ruijin Hospital, Shanghai Jiao Tong University School of Medicine, Shanghai, China, ² Department of Biomedical Engineering and Radiology, Wayne State University, Detroit, MI, United States

Keywords: quantitative susceptibility mapping, neurodegenerative disease, brain iron, deep grey matter, paramagnetic and diamagnetic materials

Editorial on the Research Topic

Quantitative Susceptibility Mapping in Neurodegeneration

Magnetic resonance imaging offers a wide variety of contrast mechanisms to study soft tissue in the body. Some common methods include: T1 weighted (T1W) imaging, T2 weighted (T2W) imaging, spin density imaging, diffusion weighted imaging (DTI), flow imaging, and susceptibility weighted imaging (SWI). Using the complex data from the SWI scans, it is possible to produce magnetic source images using a novel reconstruction method that takes the phase data and reconstructs what is referred to as a quantitative susceptibility map (QSM). The phase images represent local frequency changes caused by local changes in the magnetic field which in turn are introduced because of the presence of a magnetic source. Some of the familiar paramagnetic materials include deoxygenated blood, hemosiderin and ferritin while some of the more familiar diamagnetic materials include calcium deposits (in the pineal gland, choroid plexus, basal ganglia, and in vessel wall), calcium in bone, and myelinated tissue. A number of diseases cause local changes in iron content including: Parkinson's disease (PD), Huntington's disease, Friedrich's Ataxia and keratopathies in the brain and hemochromatosis in the liver. The ability to measure iron has clear implications if iron is involved in the pathophysiology or correlates with disease state, but it must be remembered that iron also changes as a function of age (Li Y. et al.). Also, measuring oxygen saturation would be key in stroke and potentially in dementia and other neurodegenerative diseases as well. Although QSM has been studied for more than 15 years (Haacke et al., 2015), it has taken some time to find its way into clinical studies. The goal of this special issue was to point towards future clinical applications of QSM. In this issue, iron was studied in patients with: Parkinson's disease, Alzheimer's disease, mild cognitive impairment, diabetes mellitus, occlusion of the middle cerebral artery, and Wilson's disease.

A systematic overview of the role of iron in various neurodegenerative diseases is given by Ravanfar et al. They reviewed 80 records by searching MEDLINE, Embase, Scopus, and PsycInfo databases to determine which diseases had at least one structure that demonstrated increased iron content. They found that different parts of the deep grey matter were affected for different diseases (including Alzheimer's disease, Parkinson's disease, amyotrophic lateral sclerosis, Wilson's disease, Huntington's disease, Friedrich's ataxia, etc.). In some disorders, the increased magnetic susceptibility correlated with disease duration and severity of clinical features. They conclude that QSM is a promising tool to study changes in brain iron.

More specifically, Song et al. investigated iron deposition in PD patients associated with levodopa-induced dyskinesia (LID). They evaluated the ability of substantia nigra (SN) iron content to discriminate PD with and without LID. Interestingly, they found that the susceptibility of the SN for PD patients with LID was higher than that in PD patients without LID. Liu X. et al. evaluated data for both QSM and DTI in an Alzheimer disease cohort. They studied iron in the

OPEN ACCESS

Edited and reviewed by:

Wendy Noble,
King's College London,
United Kingdom

*Correspondence:

Fuhua Yan
yfh11655@rjh.com.cn

Specialty section:

This article was submitted to
Neurodegeneration,
a section of the journal
Frontiers in Neuroscience

Received: 13 June 2021

Accepted: 28 June 2021

Published: 22 July 2021

Citation:

Yan F, He N and Haacke EM (2021)
Editorial: Quantitative Susceptibility
Mapping in Neurodegeneration.
Front. Neurosci. 15:724550.
doi: 10.3389/fnins.2021.724550

basal ganglia and found that the susceptibility of the right caudate nucleus in patients with AD correlated with cognitive scores. Several other diffusion measures also correlated positively with the magnetic susceptibility of the right caudate nucleus in patients with Alzheimer's disease. Their findings revealed that the magnetic susceptibility of the caudate nucleus may be an MRI-based biomarker of the cognitive dysfunction of AD and abnormal excessive iron distribution in the basal ganglia had adverse effects on the diffusion properties of the white matter. Jin et al. studied iron in the mammillary body for a group of mild cognitively impaired (MCI) patients. They did not find significant correlations with the patient's cognitive status but they were able to establish a normative range of iron in the mammillary bodies. They did find that susceptibility was elevated in the right mammillary body in MCI patients compared to healthy controls and that there was a small but significant reduction in volume with age for the MCI group. Li J. et al. studied the brain iron changes in patients with diabetes mellitus. They evaluated brain iron accumulation in type 2 diabetes mellitus (T2DM) patients with executive function decline using a voxel-based quantitative susceptibility. They found patients with T2DM had higher iron than healthy controls in the basal ganglia and frontal lobe. There appeared to be some correlation with cognitive testing and iron in the thalamus. Du et al. studied patients with middle cerebral artery occlusion. They found changes of iron in the basal ganglia and evaluated the ability of iron content to predict the presence of middle cerebral artery occlusion. Yuan et al. studied paramagnetic metal accumulation in the deep grey matter in patients with Wilson's Disease. Not only did they find increases in susceptibility throughout the deep grey matter, but they also found a reduction in their volumes. Of clinical interest, the Unified Wilson's Disease Rating (UWDRS) neurological subscores were positively correlated with the susceptibility values of all examined deep grey matter structures. An area of great interest is measuring oxygen saturation, particularly for stroke patients. Liu Y. et al. evaluated many of the veins associated with specific structures and found that there was a significant negative correlation with a number of cognitive measures in patients with AD. This decreasing cerebral venous oxygen level suggests that there is a reduced flow but still high cerebral metabolic rate of oxygen utilisation.

On a more technical front, Gharabaghi et al. presented a new approach for multi-echo QSM using a method referred to as Strategically Acquired Gradient Echo (STAGE) Imaging using a

structural constrained approach. They evaluated both simulated data and human data and showed high accuracy relative to other methods. This approach helps take advantage of the benefits of both short echoes and long echoes without constraining one to the other. Finally, a key issue for more broad use of QSM is its reliability across sites and across manufacturers with different resolutions. Li Y. et al. studied a large population of over 600 healthy adults, ranging from 20 to 90 years old, across 3 sites, 3 manufacturers and two field strengths. Generally, they found that the iron growth as a function of age was well-replicated across all the variables although smaller structures tended to have the largest errors. They also found that volume was generally negatively correlated with age. As usual they found that most structures significantly increased their iron content with age and that this was even more evident when the local high iron content regions were assessed. This iron dependence with age is critical to catalogue when studying any neurodegenerative disease with suspected increases in iron content since the data needs to be age corrected.

In summary, there has been great progress in using QSM to study neurodegenerative diseases. Despite the different QSM methods that are available today, as long as the same approach is used for a given study and as long as the age-related iron effect is removed, this method offers a new means to study the pathophysiology of neurodegenerative diseases that complements and generally improves upon the use of T_2^* measures of iron content (Ghassaban et al., 2018; Yan et al., 2018). The papers presented in this special issue show the potential of QSM to enhance diagnosis of patients with neurodegenerative disease. As QSM becomes more broadly accepted, no doubt other clinical applications of measuring susceptibility will emerge.

AUTHOR CONTRIBUTIONS

FY, NH, and EH wrote the manuscript. All authors contributed to the article and approved the submitted version.

FUNDING

This work was supported, in part, by the National Natural Science Foundation of China (Grant No. 81801652 for NH and 81971576 for FY and NH), a grant from the Shanghai Sailing Program (18YF1414700) for NH, and the Innovative Research Team of High-level Local Universities in Shanghai.

REFERENCES

- Ghassaban, K., Liu, S., Jiang, C., and Haacke, E. M. (2018). Quantifying iron content in magnetic resonance imaging. *Neuroimage*. 187:77–92. doi: 10.1016/j.neuroimage.2018.04.047
- Haacke, E. M., Liu, S., Buch, S., Zheng, W., Wu, D., and Ye, Y. (2015). Quantitative susceptibility mapping: current status and future directions. *Magn. Reson. Imaging* 33, 1–25. doi: 10.1016/j.mri.2014.09.004
- Yan, F., He, N., Lin, H., and Li, R. (2018). Iron deposition quantification: applications in the brain and liver. *J. Magn. Reson. Imaging* 48, 301–317. doi: 10.1002/jmri.26161

Conflict of Interest: The authors declare that the research was conducted in the absence of any commercial or financial relationships that could be construed as a potential conflict of interest.

Copyright © 2021 Yan, He and Haacke. This is an open-access article distributed under the terms of the Creative Commons Attribution License (CC BY). The use, distribution or reproduction in other forums is permitted, provided the original author(s) and the copyright owner(s) are credited and that the original publication in this journal is cited, in accordance with accepted academic practice. No use, distribution or reproduction is permitted which does not comply with these terms.



Susceptibility and Volume Measures of the Mammillary Bodies Between Mild Cognitively Impaired Patients and Healthy Controls

Zhijia Jin^{1†}, Sean K. Sethi^{2,3†}, Binyin Li⁴, Rongbiao Tang¹, Yufei Li⁵, Charlie Chia-Tsong Hsu⁶, Naying He^{1*}, E. Mark Haacke^{1,2,3,7} and Fuhua Yan¹

¹ Department of Radiology, Ruijin Hospital, Shanghai Jiao Tong University School of Medicine, Shanghai, China, ² Magnetic Resonance Innovations, Inc., Bingham Farms, MI, United States, ³ Department of Radiology, Wayne State University, Detroit, MI, United States, ⁴ Department of Neurology, Ruijin Hospital, Shanghai Jiao Tong University School of Medicine, Shanghai, China, ⁵ Institute for Medical Imaging Technology, School of Biomedical Engineering, Shanghai Jiao Tong University, Shanghai, China, ⁶ Department of Medical Imaging, Gold Coast University Hospital, Southport, QLD, Australia, ⁷ Department of Biomedical Engineering, Wayne State University, Detroit, MI, United States

OPEN ACCESS

Edited by:

Hamid R. Sohrabi,
Murdoch University, Australia

Reviewed by:

Antonello Novelli,
University of Oviedo, Spain
Cristina Lanni,
University of Pavia, Italy

*Correspondence:

Naying He
hny12267@rjh.com.cn

[†] These authors have contributed
equally to this work

Specialty section:

This article was submitted to
Neurodegeneration,
a section of the journal
Frontiers in Neuroscience

Received: 15 June 2020

Accepted: 24 August 2020

Published: 15 September 2020

Citation:

Jin Z, Sethi SK, Li B, Tang R, Li Y,
Hsu CC-T, He N, Haacke EM and
Yan F (2020) Susceptibility
and Volume Measures of the
Mammillary Bodies Between Mild
Cognitively Impaired Patients
and Healthy Controls.
Front. Neurosci. 14:572595.
doi: 10.3389/fnins.2020.572595

Purpose: To investigate the baseline values and differences for susceptibility and volume of the mammillary bodies between mild cognitively impaired (MCI) patients and healthy controls (HCs), and further explore their differences in relation to gender, MCI subtypes and apolipoprotein E (APOE) genotypes.

Methods: T1-weighted and multi-echo gradient echo imaging sequences were acquired on a 3T MR scanner to evaluate the T1W based volume and susceptibility differences in the mammillary body for 47 MCI and 47 HCs. *T*-tests were performed to compare volume and susceptibility between groups, and right and left hemispheres. Correlation analysis was used to relate the volume and mean susceptibility as a function of age in MCI and HC groups separately, and to investigate the relationship of susceptibility with the neuro-psychological scales in the MCI group.

Results: Susceptibility was found to be elevated within the right mammillary body in MCI patients compared to HCs ($p < 0.05$). There were no differences for the mammillary body volumes between the MCI and HC groups, although there was a reduction in volume with age for the MCI group ($p = 0.007$). Women showed decreased mammillary body volume compared to men in the HC group ($p = 0.004$). No significant differences were found in relation to MCI subtypes and APOE genotypes. No significant correlations were observed between mammillary body susceptibility with neuro-psychological scales.

Conclusion: This work provides a quantitative baseline for both the volume and susceptibility of the mammillary body which can be used for future studies of cognitive impairment patients underlying the pathology of the Papez circuit.

Keywords: mammillary body, quantitative susceptibility mapping, mild cognitive impairment, brain iron, volume

INTRODUCTION

Alzheimer's disease (AD) is the most common form of dementia which leads to cognitive impairment and memory loss. Mild cognitive impairment (MCI) was initially conceptualized as a symptomatic prodementia phase of AD. The manifestation of MCI is the gradually progressive cognitive decline not yet meeting the criteria for dementia (Albert et al., 2011). Since MCI is a heterogeneous condition with different aetiologies, many studies today further classify MCI into amnesic MCI (aMCI) and non-amnesic MCI (naMCI) depending on whether memory is impaired or not (Petersen and Morris, 2005; Hughes et al., 2011). It is reported that aMCI patients have an annualized conversion rate of 12 to 28% and have 8.6-fold higher odds of developing AD (Petersen et al., 1999; Lehrner et al., 2005; Schmidtke and Hermeneit, 2008). While aMCI is highly associated with progression to AD, other subtypes of MCI patients might remain stable or even revert to normal cognition (Barnes et al., 2014; Roberts et al., 2014). Therefore, there is an increasing interest on investigating the non-invasive biomarkers underlying MCI which could potentially supplement clinical approaches for future studies.

Histopathologic hallmarks of AD include both intracellular pathological neurofibrils as well as extracellular accumulation of amyloid beta (A β) plaques (Selkoe, 2001; Hardy and Selkoe, 2002). Early AD has a predilection to involve the limbic system including the entorhinal cortex, hippocampus and the mammillary bodies before spreading to other brain regions (Braak et al., 1993; Xu et al., 2000; Baloyannis et al., 2016). The mammillary bodies are an essential component in Papez' circuit, which is a network of related structures that support memory and cognition (Papez, 1995). The mammillary bodies are directly linked with brain regions that are thought to be vital for episodic memory and spatial memory (the hippocampus, anterior thalamic nuclei and tegmental regions) (Neave et al., 1997; Hildebrandt et al., 2001; Metzler-Baddeley et al., 2012). The mammillary bodies receive a dense input from the hippocampus via the fornix. Interestingly, the right and left fornical fibers convey different functional information. The left fornix primarily conveys verbal memory while the right conveys visuospatial memory (Tucker et al., 1988; Hodges and Carpenter, 1991; McMackin et al., 1995; Saunders and Aggleton, 2007). This connection continues from the mammillary bodies to the anterior thalamic nuclei by way of the mammillothalamic tract (Cruce, 1975; Vann et al., 2007, 2011). Earlier hypotheses only considered the mammillary bodies as a hippocampal relay, which underestimates their independent role in memory. Actually, except for this circuit, it has been assumed that the reciprocal connections between the mammillary bodies and tegmental regions (Bassett and Taube, 2001) are independent of the hippocampus but are critical for sustaining the mammillary bodies' function in memory (Vann, 2009). Damage to the mammillary bodies and their connection fibers can lead to an inability to lay down new episodic memories (Tsivilis et al., 2008; Metzler-Baddeley et al., 2012). However, few imaging studies have focused on the functionality of the mammillary bodies in humans due to their location and small size.

In addition to A β plaques and neurofibrillary degeneration, elevated brain iron and CSF ferritin are increasingly reported as a hallmark of AD that could perhaps predict MCI conversion to AD (Ayton et al., 2015, 2017; Kim et al., 2017). The specific underlying mechanisms of iron accumulation in AD remain unclear. Nevertheless, the close link between iron and the pathogenesis of AD is supported by a variety of evidence. For example, it has been observed that iron accumulates in the same brain regions that exhibit A β accumulation, such as the hippocampus, frontal cortex and parietal cortex, and most amyloid plaques are found to contain iron (Good et al., 1992; Liu et al., 2011). Iron accumulation is also associated with neurofibrillary tangle (NFT) formation, and the binding of ferric iron and tau protein is found to precede the accumulation of hyperphosphorylated tau and the subsequent formation of NFTs (Smith et al., 1997; Yamamoto et al., 2002; Li et al., 2015). The redox-active iron combined with the A β and NFT aggregation in AD generate increasing oxidative stress. Under such circumstances, the visualization and reliable quantitative evaluation of excess iron accumulation suggests the potential therapeutic benefit of lowering brain iron in AD patients.

Several studies using T₂* mapping and susceptibility weighted imaging (SWI) found increased iron content in brain gray matter including the hippocampus, frontal and parietal regions in AD patients (Wang et al., 2013; van Rooden et al., 2014). However, conventional gradient echo (GRE) imaging approaches are affected by blooming artifacts and cannot be easily quantified. Phase images do not directly measure local tissue susceptibility due to the non-local relationship between phase and the underlying magnetic susceptibility distribution (Schweser et al., 2011; Li et al., 2012). Quantitative susceptibility mapping (QSM) has made it possible to directly map tissue magnetic susceptibility which has been shown to correlate well with iron content in brain tissue (Liu et al., 2009; Langkammer et al., 2012; Lim et al., 2013).

Therefore, the goal of this study was to generate susceptibility and volume baseline values as a function of age for the mammillary bodies to ascertain if there is an iron content increase and to investigate the susceptibility and volume differences of the mammillary bodies between healthy controls (HCs) and MCI patients. In addition, we also investigated the susceptibility and volume differences of the mammillary bodies between genders, aMCI, naMCI and MCI patients with and without apolipoprotein E (APOE) ϵ 4.

MATERIALS AND METHODS

Participants

This study was approved by the local ethics committee and all subjects signed a consent form. Forty-seven (47) MCI subjects (mean age: 63.8 ± 6.9 years, range: 51–78 years; 33 females) were recruited from the memory clinic of the Neurology Department in Ruijin Hospital. Forty-seven (47) age- and gender-matched HCs (mean age: 63.5 ± 6.6 years, range: 51–75 years, 33 females) were recruited from the local community by advertisement. All participants were of unrelated Chinese Han descent with >6 years of education (MCI: 12.3 ± 2.5 years,

HC: 11.2 ± 3.8 years). According to the diagnostic guidelines of the United States National Institute on Aging-Alzheimer's Association (NIA-AA) (Albert et al., 2011) for MCI due to AD, our diagnosis was based on a detailed medical history interview, neurologic examinations and cognition tests. All MCI patients were screened using the Mini Mental State Examination (MMSE, $24 \leq \text{MMSE} \leq 28$) (Katzman et al., 1988), the Hamilton Depression Rating Scale (HAMD score ≤ 10) (Hamilton, 1960) and the global score of Clinical Dementia Rating Scale (global score = 0.5) (Morris, 1997). Neuro-psychological assessment for the episodic memory and visuospatial memory using the Auditory Verbal Learning Test (AVLT)-Huashan version (Zhao et al., 2012) and the Rey-Osterrieth Complex Figure Test (CFT) (Shin et al., 2006) was performed by two neurologists with 3 years of experience each. Patients with MCI were further classified into two subtypes: aMCI, if the number of words answered correctly in the 20-min delayed recall of the AVLT (AVL-LR) was less than 4, or naMCI, if the AVL-LR number was greater than 4 (Zhao et al., 2012). The APOE genotype of 45 MCI patients was measured from peripheral blood samples, with 2 of the MCI patients missing the blood sample collection. None of the HCs had memory complaints or indications of cognitive deficits. The exclusion criteria for both the MCI and HC groups included the following: (a) structural abnormalities that could impair cognitive function, such as tumor, subdural hematoma, or contusion from a previous head trauma; (b) a history of stroke, addiction, neurologic or psychiatric disease, or treatment that would affect cognitive function; and (c) large-vessel disease and/or diseases with large volume white matter lesions (i.e., Fazekas grade III).

Image Acquisition

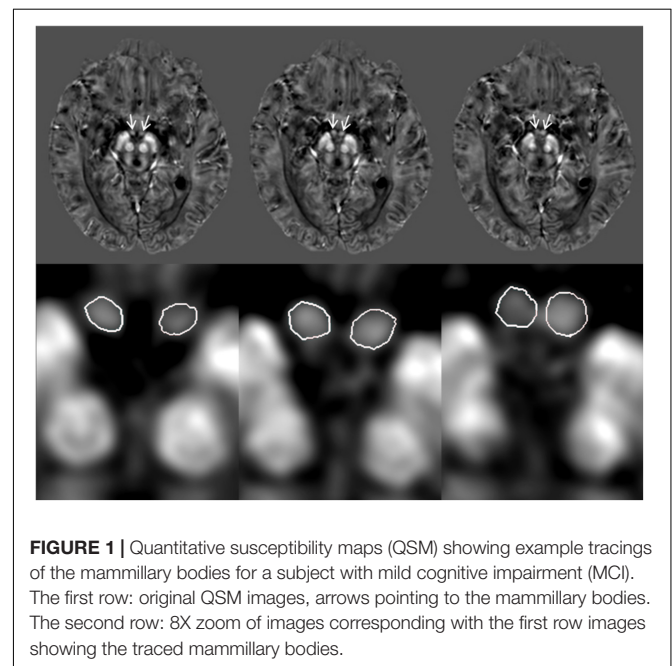
All subjects were imaged with gradient echo and T1-weighted (T1W) imaging sequences on a 3T Ingenia scanner (Philips Medical Systems, Best, The Netherlands) with a fifteen-channel phased array head coil. The three-dimensional (3D) multi-echo GRE data were acquired with the following imaging parameters: TR = 59.3 ms, number of echoes = 16, TE1 = 2.7 ms, TE spacing = 2.9 ms, bandwidth = 488 Hz/pixel, flip angle = 12° , field of view (FOV) = 22 cm, matrix size ($N_x \times N_y$) = 256×256 , resolution = $0.86 \times 0.86 \times 1.0 \text{ mm}^3$, acceleration factor = 2 (approximately 70% of k-space was sampled), slices = 136 and total acquisition time = 10 min 42 s. The sagittal 3D T1W images were acquired with a magnetization-prepared rapid acquisition gradient echo (MPRAGE) sequence with the following parameters: TR = 8.1 ms, TE = 3.7 ms, flip angle = 8° , FOV = $236 \text{ mm} \times 236 \text{ mm}$, and an acquisition voxel size = 1 mm^3 isotropic. Conventional MR images, including 2D T2-weighted fluid-attenuated inversion recovery (FLAIR) and 2D diffusion weighted imaging (DWI), were acquired in the transverse plane for screening of cerebrovascular diseases, white matter hyperintensity and space-occupying lesions in the brain. The whole brain was covered for all MR scans, including the multi-echo GRE sequence. All transverse oriented scans were collected along the anterior commissure–posterior commissure (AC-PC) line.

Image Reconstruction and Post-processing

A custom algorithm was used to generate QSM using data from all 16 echoes (Li et al., 2011). All QSM and T1W data were traced on an interpolated zoomed image (8X magnification) using SPIN Software (SpinTech, Inc., Bingham Farms, Michigan, United States). A semi-automated dynamic programming method was used to demarcate the right and left mammillary bodies (Jiang et al., 2007). An intra-class correlation coefficient (ICC) statistic for absolute agreement (Shrout and Fleiss, 1979) was calculated between two raters who traced the mammillary bodies on the QSM and T1W images for 30 randomized cases (15 HC and 15 MCI). An example of the boundary delineation on the QSM data is illustrated in **Figure 1**. The mammillary bodies were visible on 3–4 consecutive slices on the QSM and T1W images.

Statistical Analysis

An independent two-sample *t*-test was performed to compare age and education between the MCI and HC groups. A chi-square test was performed to assess the inter-group gender heterogeneity between these groups. Independent-sample *t*-tests were performed to compare volume and susceptibility in the mammillary body between patients with MCI and HCs, patients with aMCI and naMCI, APOE $\epsilon 4$ carriers and non-carriers, and female and male. To observe whether bilateral differences of volume and susceptibility exist within the mammillary bodies in MCI and HC subjects, paired-sample *t*-tests were performed. For the *t*-tests, a value of $p < 0.05$ was considered significant. Pearson correlation analyses were used with age as an independent variable using volume and mean susceptibility as dependent variables in MCI and HC groups. To investigate the correlation



of mean susceptibility in the mamillary bodies with the AVLT and CFT scores, a partial correlation analysis was performed with age as a covariate. A conservative statistical significance of p value < 0.01 was used in the multiple correlation analysis to control for the inflation of type I error. All statistical analyses were run on the data using SPSS (IBM Corp. Released 2013. IBM SPSS Statistics for Windows, Version 22.0. Armonk, NY: IBM Corp.).

RESULTS

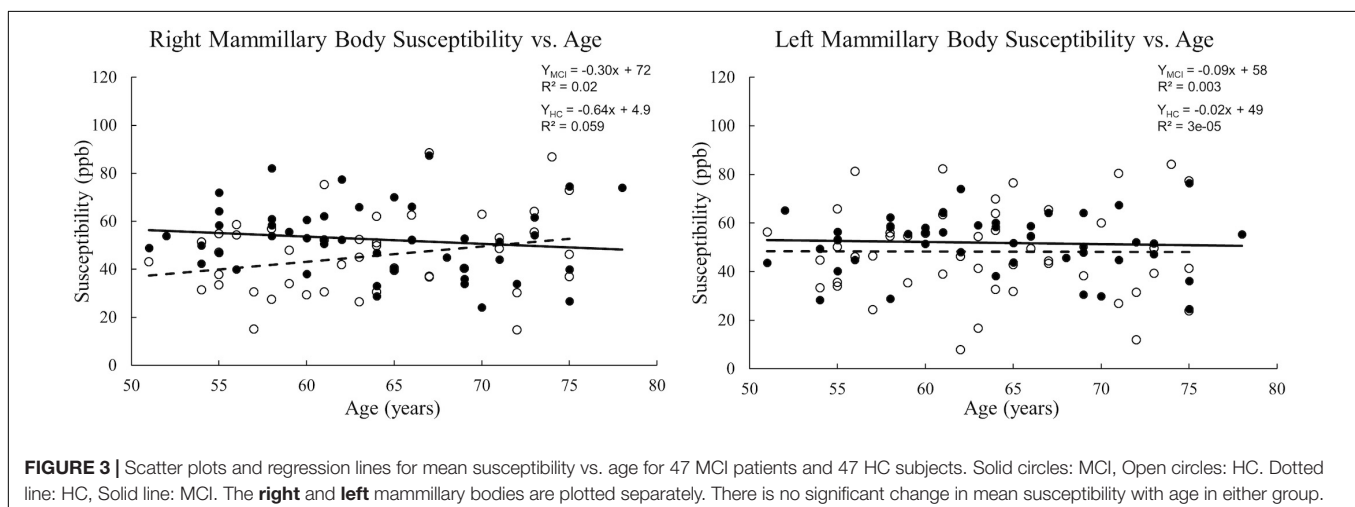
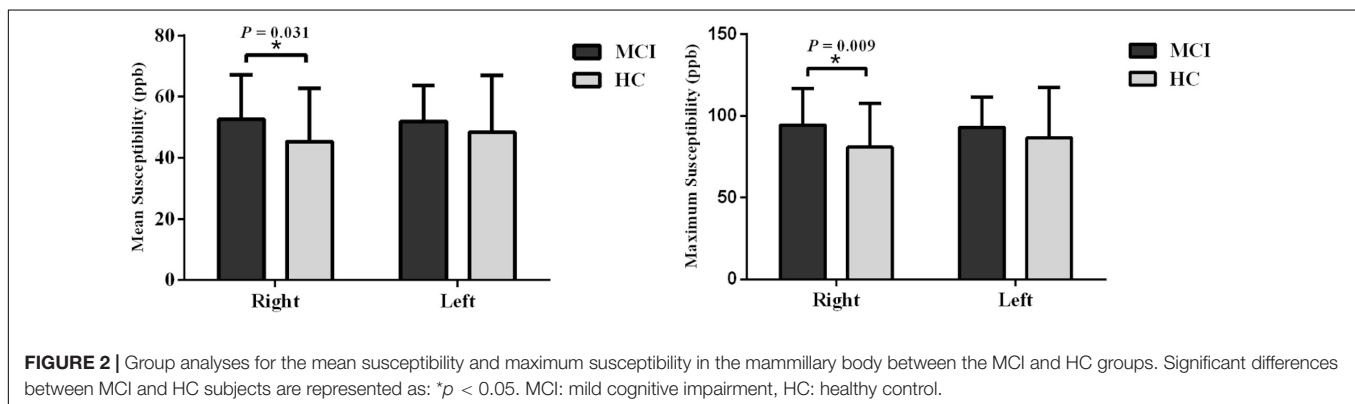
Demographic and Clinical Characteristics Analyses

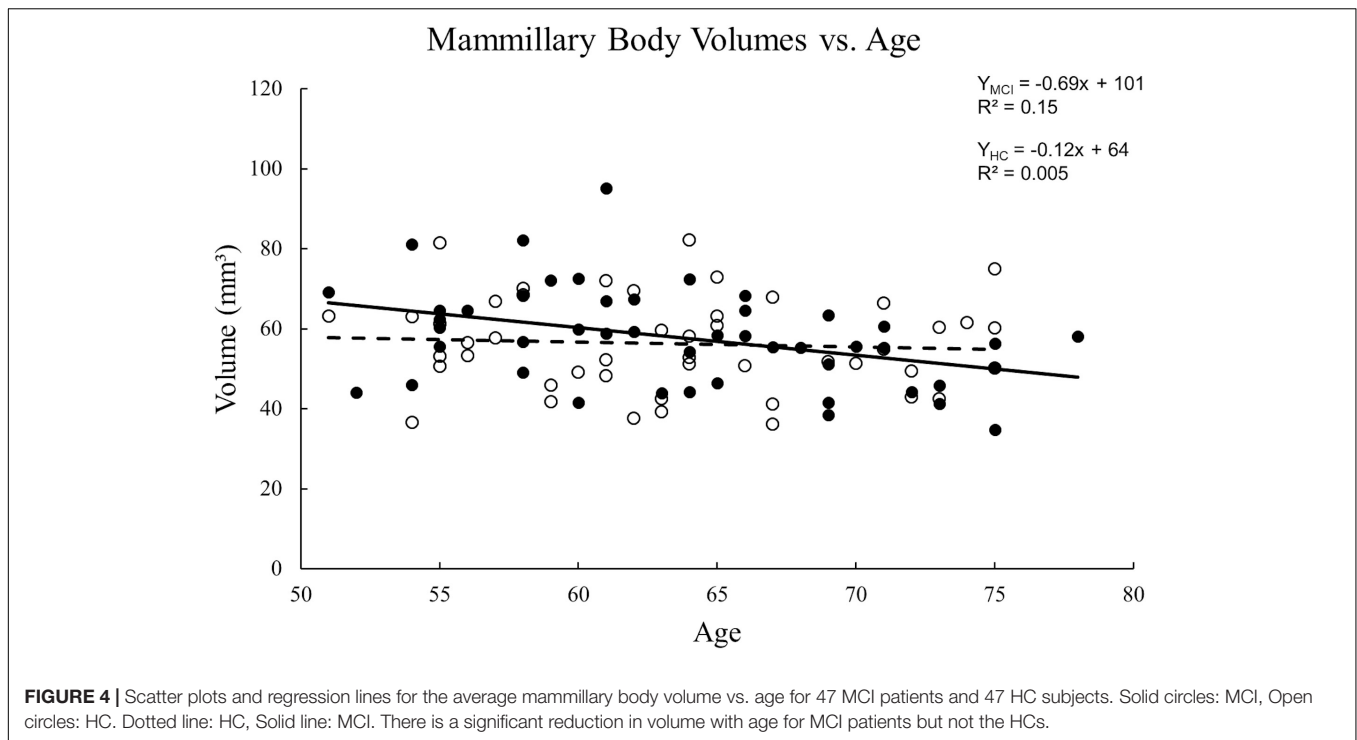
There was no significant difference of age, gender or education between the MCI and HC groups. The MMSE score for MCI patients was 27.5 ± 0.7 . For the episodic memory and visuospatial memory assessments, the AVLT scores were 15.6 ± 4.7 for immediate recall, 4.6 ± 2.3 for 5-min recall, 4.6 ± 2.4 for 20-min recall and 19.9 ± 2.7 for 20-min recognition. The CFT scores were 35.3 ± 1.6 for copy and 16.9 ± 7.7 for recall. According to the 20-min delayed recall of the AVLT, 22/47 MCI patients were classified into the aMCI group and 25/47 were put in the naMCI group. Further, 45 MCI patients with the APOE genotype were also broken up into a high-risk group

with APOE $\epsilon 4$ ($n = 15$) and a low-risk group without APOE $\epsilon 4$ ($n = 30$).

Susceptibility Analysis

When tracing the mamillary bodies on QSM using the semi-automated method, the ICCs for the right and the left sides were 0.91 and 0.92, respectively. A breakdown of the mean susceptibility, maximum susceptibility, and statistics for paired t -tests between right and left sides is shown in **Supplementary Table S1**. No differences were observed between sides for any of the groups (all p values > 0.05). As shown in **Figure 2**, mean susceptibility and maximum susceptibility increased in the right mamillary body in the MCI group as compared to HC group, but no significant susceptibility difference was found in the left mamillary body. There was no significant change of mean susceptibility as a function of age in the right or left mamillary bodies in either the MCI group, or the HC group as shown in **Figure 3**. No significant susceptibility differences in the mamillary body were found in relation to gender, MCI subtypes or APOE genotypes (**Supplementary Table S2**). No significant correlations ($p > 0.01$) were observed between mean susceptibility of the mamillary body and 5-min delayed AVLT score, 20-min delayed AVLT score, or the CFT recall score in the MCI group.





T1W Based Volume Analysis

The ICC between the two raters for tracing the mammillary body volumes on T1W was 0.85. No volume differences were observed between MCI and HC groups in either sides of the mammillary body ($p > 0.05$). Women showed significant decreased mammillary body volume when compared to men in the HC group, but not in the MCI group (Supplementary Table S2). No significant volume differences were found in the mammillary body between aMCI and naMCI, or APOE $\epsilon 4$ carriers and non-carriers (Supplementary Table S2). There was no volume significance between right and left sides of the mammillary body in MCI and HC groups ($p > 0.05$), thus we used the average volume of both sides for correlation analysis. A negative correlation between volume and age (Figure 4) was observed in the MCI group ($R^2 = 0.152$, $p = 0.007$), while in the HC group, no significant correlation was found ($p > 0.01$).

DISCUSSION

The mammillary bodies and their main projections play a substantial role in spatial memory and delayed memory recall. This is the motivation to investigate the baseline values and differences for susceptibility and volume of the mammillary bodies between MCI and HC subjects. To our knowledge, this is the first study using QSM to quantify iron deposition in the mammillary bodies in MCI. The results showed a susceptibility roughly equal to that of gray matter, around 50ppb, with an increased iron level in the

right mammillary body in MCI patients compared with HCs. The susceptibility values for the mammillary bodies presented herein could be used as a baseline for future studies of brain iron change in cognitively impaired patients including patients with AD, behavioral variant frontotemporal dementia (FTD) and amyotrophic lateral sclerosis (ALS) which affect the Papez circuit.

In vivo studies of the iron accumulation in the mammillary bodies are limited (De Reuck et al., 2014). A previous magnetic resonance imaging study at 7.0 T of iron deposition in post-mortem brains of patients with neurodegenerative and cerebrovascular diseases observed no iron accumulation in the mammillary bodies (De Reuck et al., 2014). However, in that study, the severity of the iron load was evaluated semi-quantitatively using a ranking approach based on the intensity and distribution of hypo-intensity signal on T2*-weighted imaging. Generally, T2* is not as sensitive to iron changes as QSM and is also a noisier measurement. Both post-mortem experiments (Langkammer et al., 2012; Sun et al., 2015) and *in vivo* (Schweser et al., 2011; Bilgic et al., 2012) experiments have demonstrated that magnetic susceptibility assessed by QSM is highly correlated with known iron concentrations of various structures in the brain. The iron levels measured here of roughly 50 ppb are similar to those seen between gray matter and white matter and are sufficiently higher than the noise level to be clearly visible on the QSM data. Therefore, our approach using QSM to quantify the iron level is a reasonable approach to detect iron changes of the mammillary bodies in the progression of cognitive decline. We also explored the mean susceptibility of the mammillary body as a function of age in both the MCI group and the HC group.

However, no significant correlations between susceptibility and age were discovered.

In this study, a significant reduction in volume as a function of age was found in MCI patients but there was no statistical difference in volumes between MCI patients and HCs. The latter finding is consistent with previous research (Copenhaver et al., 2006) showing no significant volume differences between HC and MCI groups. Nevertheless, they found significant volume reductions in the mammillary bodies in patients with AD as compared with HC and MCI participants, which suggested that atrophy of the mammillary bodies became obvious at the point of conversion from MCI to AD (Copenhaver et al., 2006). Our findings confirmed the relative preservation of the mammillary bodies volume in early disease stages.

In addition, a decreased mammillary body volume in women compared to men in the HC group was found in this study. Interestingly, Falcon et al. found a greater atrophy in medial temporal areas (Papez circuit) associated with CSF p-tau and glial biomarkers in cognitively unimpaired women compared to men (Falcon et al., 2020). A greater atrophy of the structures in the Papez circuit associated with baseline CSF p-tau may partially explain women's greater susceptibility to memory complaints and AD pathology. Although a lot of evidence suggests a higher incidence of AD in women, it is still not clear whether the greater prevalence is due to their longer life expectancy or other underlying factors (Beam et al., 2018; Medeiros and Silva, 2019). In this study, we did not find volume or susceptibility differences in the mammillary body between women and men in the MCI patients, although some studies found greater medial temporal atrophy in early stages of AD in women (Apostolova et al., 2006; Hua et al., 2010; Ardekani et al., 2016). The inability of detecting the gender differences in the mammillary body in our study could be partly due to the heterogeneous conditions of MCI with different aetiologies and the relatively small sample size. Further classification of the MCI cohort showed no susceptibility or volume differences in the mammillary body between aMCI and naMCI groups. It may be interesting to further investigate the gender differences of the mammillary body in aMCI patients with a larger sample size in the future.

The APOE $\epsilon 4$ allele is recognized as the main genetic risk factor for AD and MCI as well (Krysio et al., 2006). Previous studies showed inconsistent results of volumetric analyses of APOE $\epsilon 4$ carriers focused on medial temporal lobe with some reported reduced hippocampal volumes (O'Dwyer et al., 2012), and others not (Adamson et al., 2010; Li et al., 2014). Our exploration of APOE genotypes found no susceptibility or volume differences in the mammillary body between APOE $\epsilon 4$ carriers and non-carriers. In addition to the volume studies, functional connectivity analyses of the Papez circuit with the hippocampus as a 'seed' found that APOE $\epsilon 4$ carriers had significantly decreased functional connectivity in brain areas such as the thalamus, caudate nucleus, and cingulate cortices involved in the Papez circuit (Li et al., 2014). They also found that the decreased hippocampal functional connectivity in these regions were positively correlated with the episodic memory performance (Li et al., 2014). These findings illustrate

the importance of the integrity of the Papez circuit on episodic memory.

Damage to the integrity of gray matter and their connection fibers in the Papez circuit can lead to cognition impairment in various neurodegenerative diseases including AD, behavioral variant FTD and ALS (Thomas et al., 2011). Both *in vivo* and postmortem studies suggest that subregions of the Papez circuit are differentially affected in behavioral variant FTD and AD (Hornberger et al., 2012; Bertoux et al., 2014), with behavioral variant FTD patients having more severe neural degeneration of the fornix, anterior thalamus and anterior cingulate cortex and AD patients having more significant atrophy of the posterior cingulate cortex. Clinically mild psychiatric and cognitive impairment of patients with ALS before the onset of motor symptoms can cause a concomitant diagnose of behavioral variant FTD due to their overlap of clinical, pathological and genetic characteristics (Salameh et al., 2015). Therefore, more studies have focused on the investigation of the non-invasive biomarkers for the differential diagnosis. It has been found that the entorhinal cortex and mammillary body atrophy may help to distinguish behavioral variant FTD from ALS with behavioral variant FTD patients showing more atrophy than patients with ALS (Bueno et al., 2020). In addition, Bueno et al. (2018) showed widespread structural and functional connectivity abnormalities across the structures composed of the Papez circuit, while the thalamus, mammillary bodies and fornix were preserved in ALS patients. The post-mortem study also found substantial atrophy of the mammillary bodies and anterior thalamus in behavioral variant FTD (Hornberger et al., 2012). All in all, the integrity of the Papez circuit and its entire subregions should be taken into consideration when establishing whether the memory loss observed in a patient is likely to be due to AD or other neurodegenerative diseases such as behavioral variant FTD and ALS.

Drawing strong conclusions about the iron and volume changes of the mammillary bodies in MCI subjects will require evaluating a much larger population. It would be particularly interesting to follow longitudinal changes for a given individual. As with all *in vivo* MRI studies of MCI, our study is limited by the lack of pathological confirmation of the disease state. Nevertheless, at our institute all MCI patients will eventually undergo longitudinal clinical evaluation with reassessment of their diagnosis over time. Longitudinal assessments of the volumetric reduction may be useful in determining the conversion point from MCI to AD.

CONCLUSION

MCI patients showed increased susceptibility in the right mammillary body compared to HCs. The structural volume of the mammillary bodies decreased with age in MCI patients. Women showed decreased mammillary body volume than men in the HCs. This work provides an important baseline for studying the mammillary bodies in cognitive impairment patients not only in AD but also for other neurodegenerative diseases such as FTD and ALS which affect the Papez circuit.

DATA AVAILABILITY STATEMENT

The raw data supporting the conclusions of this article will be made available by the authors, without undue reservation.

ETHICS STATEMENT

The studies involving human participants were reviewed and approved by Ruijin Hospital, Shanghai Jiao Tong University School of Medicine, Shanghai, China. The patients/participants provided their written informed consent to participate in this study.

AUTHOR CONTRIBUTIONS

EMH originally conceived of the method. ZJ and BL contributed to the data acquisition. EMH, SS, ZJ, and YL contributed to the analysis and interpretation of the data. ZJ and SS drafted the manuscript. All authors contributed to the critical revision and final presentation of the work.

REFERENCES

- Adamson, M. M., Landy, K. M., Duong, S., Fox-Bosetti, S., Ashford, J. W., Murphy, G. M., et al. (2010). Apolipoprotein E epsilon4 influences on episodic recall and brain structures in aging pilots. *Neurobiol. Aging* 31, 1059–1063. doi: 10.1016/j.neurobiolaging.2008.07.017
- Albert, M. S., Dekosky, S. T., Dickson, D., Dubois, B., Feldman, H. H., Fox, N. C., et al. (2011). The diagnosis of mild cognitive impairment due to Alzheimer's disease: recommendations from the National Institute on Aging-Alzheimer's Association workgroups on diagnostic guidelines for Alzheimer's disease. *Alzheimers Dement.* 7, 270–279. doi: 10.1016/j.jalz.2011.03.008
- Apostolova, L. G., Dinov, I. D., Dutton, R. A., Hayashi, K. M., Toga, A. W., Cummings, J. L., et al. (2006). 3D comparison of hippocampal atrophy in amnesic mild cognitive impairment and Alzheimer's disease. *Brain* 129, 2867–2873. doi: 10.1093/brain/awl274
- Ardekani, B. A., Convit, A., and Bachman, A. H. (2016). Analysis of the MIRIAD data shows sex differences in hippocampal atrophy progression. *J. Alzheimers Dis.* 50, 847–857. doi: 10.3233/JAD-150780
- Ayton, S., Faux, N. G., Bush, A. I., and Alzheimer's Disease Neuroimaging (2015). Ferritin levels in the cerebrospinal fluid predict Alzheimer's disease outcomes and are regulated by APOE. *Nat. Commun.* 6:6760. doi: 10.1038/ncomms7760
- Ayton, S., Fazlollahi, A., Bourgeat, P., Raniga, P., Ng, A., Lim, Y. Y., et al. (2017). Cerebral quantitative susceptibility mapping predicts amyloid-beta-related cognitive decline. *Brain* 140, 2112–2119. doi: 10.1093/brain/awx137
- Baloyannis, S. J., Mavroudis, I., Baloyannis, I. S., and Costa, V. G. (2016). Mammillary bodies in Alzheimer's disease: a golgi and electron microscope study. *Am. J. Alzheimers Dis. Other Dement.* 31, 247–256. doi: 10.1177/1533317515602548
- Barnes, D. E., Cenzer, I. S., Yaffe, K., Ritchie, C. S., Lee, S. J., and Alzheimer's Disease Neuroimaging (2014). A point-based tool to predict conversion from mild cognitive impairment to probable Alzheimer's disease. *Alzheimers Dement.* 10, 646–655. doi: 10.1016/j.jalz.2013.12.014
- Bassett, J. P., and Taube, J. S. (2001). Neural correlates for angular head velocity in the rat dorsal tegmental nucleus. *J. Neurosci.* 21, 5740–5751. doi: 10.1523/JNEUROSCI.21-15-05740.2001
- Beam, C. R., Kaneshiro, C., Jang, J. Y., Reynolds, C. A., Pedersen, N. L., and Gatz, M. (2018). Differences between women and men in incidence rates of dementia and Alzheimer's disease. *J. Alzheimers Dis.* 64, 1077–1083. doi: 10.3233/JAD-180141

FUNDING

This work was supported by the Clinical Research Center, Shanghai Jiao Tong University School of Medicine (DLY201603); the Science and Technology Commission of Shanghai Municipality (17411952700); the Shanghai Sailing Program (18YF1414700); the National Natural Science Fund (81801652); and the Innovative Research Team of High-level Local Universities in Shanghai.

SUPPLEMENTARY MATERIAL

The Supplementary Material for this article can be found online at: <https://www.frontiersin.org/articles/10.3389/fnins.2020.572595/full#supplementary-material>

TABLE S1 | The T1W based volume, mean susceptibility and maximum susceptibility are presented, along with paired *t*-test results between the left mammillary body and right mammillary body for MCI patients and HCs.

TABLE S2 | Independent-sample *t*-test analyses between genders, aMCI and naMCI patients, MCI patients with APOE ε4 and without APOE ε4 for total volume and mean susceptibility in the mammillary body.

- Bertoux, M., De Souza, L. C., Corlier, F., Lamari, F., Bottlaender, M., Dubois, B., et al. (2014). Two distinct amnesic profiles in behavioral variant frontotemporal dementia. *Biol. Psychiatry* 75, 582–588. doi: 10.1016/j.biopsych.2013.08.017
- Bilgic, B., Pfefferbaum, A., Rohlfing, T., Sullivan, E. V., and Adalsteinsson, E. (2012). MRI estimates of brain iron concentration in normal aging using quantitative susceptibility mapping. *Neuroimage* 59, 2625–2635. doi: 10.1016/j.neuroimage.2011.08.077
- Braak, H., Braak, E., and Bohl, J. (1993). Staging of Alzheimer-related cortical destruction. *Eur. Neurol.* 33, 403–408. doi: 10.1159/000116984
- Bueno, A. P. A., De Souza, L. C., Pinaya, W. H. L., Teixeira, A. L., De Prado, L. G. R., Caramelli, P., et al. (2020). Papez circuit gray matter and episodic memory in amyotrophic lateral sclerosis and behavioural variant frontotemporal dementia. *Brain Imaging Behav.* doi: 10.1007/s11682-020-00307-5 [Epub ahead of print].
- Bueno, A. P. A., Pinaya, W. H. L., Moura, L. M., Bertoux, M., Radakovic, R., Kiernan, M. C., et al. (2018). Structural and functional papez circuit integrity in amyotrophic lateral sclerosis. *Brain Imaging Behav.* 12, 1622–1630. doi: 10.1007/s11682-018-9825-0
- Copenhaver, B. R., Rabin, L. A., Saykin, A. J., Roth, R. M., Wishart, H. A., Flashman, L. A., et al. (2006). The fornix and mammillary bodies in older adults with Alzheimer's disease, mild cognitive impairment, and cognitive complaints: a volumetric MRI study. *Psychiatry Res.* 147, 93–103. doi: 10.1016/j.psychres.2006.01.015
- Cruce, J. A. (1975). An autoradiographic study of the projections of the mammillothalamic tract in the rat. *Brain Res.* 85, 211–219. doi: 10.1016/0006-8993(75)90072-4
- De Reuck, J. L., Deramecourt, V., Auger, F., Durieux, N., Cordonnier, C., Devos, D., et al. (2014). Iron deposits in post-mortem brains of patients with neurodegenerative and cerebrovascular diseases: a semi-quantitative 7.0 T magnetic resonance imaging study. *Eur. J. Neurol.* 21, 1026–1031. doi: 10.1111/ene.12432
- Falcon, C., Grau-Rivera, O., Suárez-Calvet, M., Bosch, B., Sánchez-Valle, R., Arenaza-Urquijo, E. M., et al. (2020). Sex differences of longitudinal brain changes in cognitively unimpaired adults. *J. Alzheimer's Dis.* [Epub ahead of print]. doi: 10.3233/JAD-200293
- Good, P. F., Perl, D. P., Bierer, L. M., and Schmeidler, J. (1992). Selective accumulation of aluminum and iron in the neurofibrillary tangles of Alzheimer's disease: a laser microprobe (LAMMA) study. *Ann. Neurol.* 31, 286–292. doi: 10.1002/ana.410310310

- Hamilton, M. (1960). A rating scale for depression. *J. Neurol. Neurosurg. Psychiatry* 23, 56–62. doi: 10.1136/jnnp.23.1.56
- Hardy, J., and Selkoe, D. J. (2002). The amyloid hypothesis of Alzheimer's disease: progress and problems on the road to therapeutics. *Science* 297, 353–356. doi: 10.1126/science.1072994
- Hildebrandt, H., Muller, S., Bussmann-Mork, B., Goebel, S., and Eilers, N. (2001). Are some memory deficits unique to lesions of the mammillary bodies? *J. Clin. Exp. Neuropsychol.* 23, 490–501. doi: 10.1076/jcen.23.4.490.1234
- Hodges, J. R., and Carpenter, K. (1991). Anterograde amnesia with fornix damage following removal of IIIrd ventricle colloid cyst. *J. Neurol. Neurosurg. Psychiatry* 54, 633–638. doi: 10.1136/jnnp.54.7.633
- Hornberger, M., Wong, S., Tan, R., Irish, M., Piguet, O., Kril, J., et al. (2012). In vivo and post-mortem memory circuit integrity in frontotemporal dementia and Alzheimer's disease. *Brain* 135, 3015–3025. doi: 10.1093/brain/aws239
- Hua, X., Hibar, D. P., Lee, S., Toga, A. W., Jack, C. R. Jr., Weiner, M. W., et al. (2010). Sex and age differences in atrophic rates: an ADNI study with n = 1368 MRI scans. *Neurobiol. Aging* 31, 1463–1480. doi: 10.1016/j.neurobiolaging.2010.04.033
- Hughes, T. F., Snitz, B. E., and Ganguli, M. (2011). Should mild cognitive impairment be subtyped? *Curr. Opin. Psychiatry* 24, 237–242. doi: 10.1097/YCO.0b013e328344696b
- Jiang, J., Haacke, E. M., and Dong, M. (2007). Dependence of vessel area accuracy and precision as a function of MR imaging parameters and boundary detection algorithm. *J. Magn. Reson. Imaging* 25, 1226–1234. doi: 10.1002/jmri.20918
- Katzman, R., Zhang, M. Y., Ouang Ya, Q., Wang, Z. Y., Liu, W. T., Yu, E., et al. (1988). A Chinese version of the Mini-Mental State Examination; impact of illiteracy in a Shanghai dementia survey. *J. Clin. Epidemiol.* 41, 971–978. doi: 10.1016/0895-4356(88)90034-0
- Kim, H. G., Park, S., Rhee, H. Y., Lee, K. M., Ryu, C. W., Rhee, S. J., et al. (2017). Quantitative susceptibility mapping to evaluate the early stage of Alzheimer's disease. *Neuroimage Clin.* 16, 429–438. doi: 10.1016/j.nicl.2017.08.019
- Krysicio, R. J., Schmitt, F. A., Salazar, J. C., Mendiondo, M. S., and Markesbery, W. R. (2006). Risk factors for transitions from normal to mild cognitive impairment and dementia. *Neurology* 66, 828–832. doi: 10.1212/01.wnl.0000203264.71880.45
- Langkammer, C., Schweser, F., Krebs, N., Deistung, A., Goessler, W., Scheurer, E., et al. (2012). Quantitative susceptibility mapping (QSM) as a means to measure brain iron? A post mortem validation study. *Neuroimage* 62, 1593–1599. doi: 10.1016/j.neuroimage.2012.05.049
- Lehrner, J., Gufler, R., Guttman, G., Maly, J., Gleiss, A., Auff, E., et al. (2005). Annual conversion to alzheimer disease among patients with memory complaints attending an outpatient memory clinic: the influence of amnesic mild cognitive impairment and the predictive value of neuropsychological testing. *Wien Klin Wochenschr.* 117, 629–635. doi: 10.1007/s00508-005-0428-6
- Li, J., Chang, S., Liu, T., Wang, Q., Cui, D., Chen, X., et al. (2012). Reducing the object orientation dependence of susceptibility effects in gradient echo MRI through quantitative susceptibility mapping. *Magn. Reson. Med.* 68, 1563–1569. doi: 10.1002/mrm.24135
- Li, W., Antuono, P. G., Xie, C., Chen, G., Jones, J. L., Ward, B. D., et al. (2014). Aberrant functional connectivity in Papez circuit correlates with memory performance in cognitively intact middle-aged APOE4 carriers. *Cortex* 57, 167–176. doi: 10.1016/j.cortex.2014.04.006
- Li, W., Wu, B., and Liu, C. (2011). Quantitative susceptibility mapping of human brain reflects spatial variation in tissue composition. *Neuroimage* 55, 1645–1656. doi: 10.1016/j.neuroimage.2010.11.088
- Li, X., Lei, P., Tuo, Q., Ayton, S., Li, Q. X., Moon, S., et al. (2015). Enduring elevations of hippocampal amyloid precursor protein and iron are features of beta-amyloid toxicity and are mediated by tau. *Neurotherapeutics* 12, 862–873. doi: 10.1007/s13311-015-0378-2
- Lim, I. A., Faria, A. V., Li, X., Hsu, J. T., Airan, R. D., Mori, S., et al. (2013). Human brain atlas for automated region of interest selection in quantitative susceptibility mapping: application to determine iron content in deep gray matter structures. *Neuroimage* 82, 449–469. doi: 10.1016/j.neuroimage.2013.05.127
- Liu, B., Moloney, A., Meehan, S., Morris, K., Thomas, S. E., Serpell, L. C., et al. (2011). Iron promotes the toxicity of amyloid beta peptide by impeding its ordered aggregation. *J. Biol. Chem.* 286, 4248–4256. doi: 10.1074/jbc.M110.158980
- Liu, T., Spincemaille, P., De Rochefort, L., Kressler, B., and Wang, Y. (2009). Calculation of susceptibility through multiple orientation sampling (COSMOS): a method for conditioning the inverse problem from measured magnetic field map to susceptibility source image in MRI. *Magn. Reson. Med.* 61, 196–204. doi: 10.1002/mrm.21828
- McMackin, D., Cockburn, J., Anslow, P., and Gaffan, D. (1995). Correlation of fornix damage with memory impairment in six cases of colloid cyst removal. *Acta Neurochir.* 135, 12–18. doi: 10.1007/BF02307408
- Medeiros, A. D. M., and Silva, R. H. (2019). Sex differences in Alzheimer's disease: where do we stand? *J. Alzheimers Dis.* 67, 35–60. doi: 10.3233/JAD-180213
- Metzler-Baddeley, C., Hunt, S., Jones, D. K., Leemans, A., Aggleton, J. P., and O'sullivan, M. J. (2012). Temporal association tracts and the breakdown of episodic memory in mild cognitive impairment. *Neurology* 79, 2233–2240. doi: 10.1212/WNL.0b013e31827689e8
- Morris, J. C. (1997). Clinical dementia rating: a reliable and valid diagnostic and staging measure for dementia of the Alzheimer type. *Int. Psychogeriatr.* 9(Suppl. 1), 173–176. doi: 10.1017/s1041610297004870
- Neave, N., Nagle, S., and Aggleton, J. P. (1997). Evidence for the involvement of the mammillary bodies and cingulum bundle in allocentric spatial processing by rats. *Eur. J. Neurosci.* 9, 941–955. doi: 10.1111/j.1460-9568.1997.tb01445.x
- O'Dwyer, L., Lamberton, F., Matura, S., Tanner, C., Scheibe, M., Miller, J., et al. (2012). Reduced hippocampal volume in healthy young ApoE4 carriers: an MRI study. *PLoS One* 7:e48895. doi: 10.1371/journal.pone.0048895
- Papez, J. W. (1995). A proposed mechanism of emotion. 1937. *J. Neuropsychiatry Clin. Neurosci.* 7, 103–112. doi: 10.1176/jnp.7.1.103
- Petersen, R. C., and Morris, J. C. (2005). Mild cognitive impairment as a clinical entity and treatment target. *Arch. Neurol.* 62, 1160–1167. doi: 10.1001/archneur.62.7.1160
- Petersen, R. C., Smith, G. E., Ivnik, R. J., Tangalos, E. G., and Kokmen, E. (1999). Mild cognitive impairment: clinical characterization and outcome. *Arch. Neurol.* 56, 303–308. doi: 10.1001/archneur.56.3.303
- Roberts, R. O., Knopman, D. S., Mielke, M. M., Cha, R. H., Pankratz, V. S., Christianson, T. J., et al. (2014). Higher risk of progression to dementia in mild cognitive impairment cases who revert to normal. *Neurology* 82, 317–325. doi: 10.1212/WNL.0000000000000055
- Salameh, J. S., Brown, R. H. Jr., and Berry, J. D. (2015). Amyotrophic lateral sclerosis: review. *Semin. Neurol.* 35, 469–476. doi: 10.1055/s-0035-1558984
- Saunders, R. C., and Aggleton, J. P. (2007). Origin and topography of fibers contributing to the fornix in macaque monkeys. *Hippocampus* 17, 396–411. doi: 10.1002/hipo.20276
- Schmidtke, K., and Hermeneit, S. (2008). High rate of conversion to Alzheimer's disease in a cohort of amnesic MCI patients. *Int. Psychogeriatr.* 20, 96–108. doi: 10.1017/S1041610207005509
- Schweser, F., Deistung, A., Lehr, B. W., and Reichenbach, J. R. (2011). Quantitative imaging of intrinsic magnetic tissue properties using MRI signal phase: an approach to in vivo brain iron metabolism? *Neuroimage* 54, 2789–2807. doi: 10.1016/j.neuroimage.2010.10.070
- Selkoe, D. J. (2001). Alzheimer's disease: genes, proteins, and therapy. *Physiol. Rev.* 81, 741–766. doi: 10.1152/physrev.2001.81.2.741
- Shin, M. S., Park, S. Y., Park, S. R., Seol, S. H., and Kwon, J. S. (2006). Clinical and empirical applications of the rey-osterrieth complex figure test. *Nat. Protoc.* 1, 892–899. doi: 10.1038/nprot.2006.115
- Shrout, P. E., and Fleiss, J. L. (1979). Intraclass correlations: uses in assessing rater reliability. *Psychol. Bull.* 86, 420–428. doi: 10.1037//0033-2909.86.2.420
- Smith, M. A., Harris, P. L., Sayre, L. M., and Perry, G. (1997). Iron accumulation in Alzheimer disease is a source of redox-generated free radicals. *Proc. Natl. Acad. Sci. U.S.A.* 94, 9866–9868. doi: 10.1073/pnas.94.18.9866
- Sun, H., Walsh, A. J., Lebel, R. M., Blevins, G., Catz, I., Lu, J. Q., et al. (2015). Validation of quantitative susceptibility mapping with Perl's iron staining for subcortical gray matter. *Neuroimage* 105, 486–492. doi: 10.1016/j.neuroimage.2014.11.010
- Thomas, A. G., Koumellis, P., and Dineen, R. A. (2011). The fornix in health and disease: an imaging review. *Radiographics* 31, 1107–1121. doi: 10.1148/rg.314105729
- Tsivilis, D., Vann, S. D., Denby, C., Roberts, N., Mayes, A. R., Montaldi, D., et al. (2008). A disproportionate role for the fornix and mammillary bodies in recall versus recognition memory. *Nat. Neurosci.* 11, 834–842. doi: 10.1038/nn.2149

- Tucker, D. M., Roeltgen, D. P., Tully, R., Hartmann, J., and Boxell, C. (1988). Memory dysfunction following unilateral transection of the fornix: a hippocampal disconnection syndrome. *Cortex* 24, 465–472. doi: 10.1016/s0010-9452(88)80010-8
- van Rooden, S., Versluis, M. J., Liem, M. K., Milles, J., Maier, A. B., Oleksik, A. M., et al. (2014). Cortical phase changes in Alzheimer's disease at 7T MRI: a novel imaging marker. *Alzheimers Dement.* 10, e19–e26. doi: 10.1016/j.jalz.2013.02.002
- Vann, S. D. (2009). Gudden's ventral tegmental nucleus is vital for memory: re-evaluating diencephalic inputs for amnesia. *Brain* 132, 2372–2384. doi: 10.1093/brain/awp175
- Vann, S. D., Erichsen, J. T., O'mara, S. M., and Aggleton, J. P. (2011). Selective disconnection of the hippocampal formation projections to the mammillary bodies produces only mild deficits on spatial memory tasks: implications for fornix function. *Hippocampus* 21, 945–957. doi: 10.1002/hipo.20796
- Vann, S. D., Saunders, R. C., and Aggleton, J. P. (2007). Distinct, parallel pathways link the medial mammillary bodies to the anterior thalamus in macaque monkeys. *Eur. J. Neurosci.* 26, 1575–1586. doi: 10.1111/j.1460-9568.2007.05773.x
- Wang, D., Zhu, D., Wei, X. E., Li, Y. H., and Li, W. B. (2013). Using susceptibility-weighted images to quantify iron deposition differences in amnesic mild cognitive impairment and Alzheimer's disease. *Neurol. India* 61, 26–34. doi: 10.4103/0028-3886.107924
- Xu, Y., Jack, C. R. Jr., O'brien, P. C., Kokmen, E., Smith, G. E., Ivnik, R. J., et al. (2000). Usefulness of MRI measures of entorhinal cortex versus hippocampus in AD. *Neurology* 54, 1760–1767. doi: 10.1212/wnl.54.9.1760
- Yamamoto, A., Shin, R. W., Hasegawa, K., Naiki, H., Sato, H., Yoshimasu, F., et al. (2002). Iron (III) induces aggregation of hyperphosphorylated tau and its reduction to iron (II) reverses the aggregation: implications in the formation of neurofibrillary tangles of Alzheimer's disease. *J. Neurochem.* 82, 1137–1147. doi: 10.1046/j.1471-4159.2002.t01-1-01061.x
- Zhao, Q., Lv, Y., Zhou, Y., Hong, Z., and Guo, Q. (2012). Short-term delayed recall of auditory verbal learning test is equivalent to long-term delayed recall for identifying amnesic mild cognitive impairment. *PLoS One* 7:e51157. doi: 10.1371/journal.pone.0051157

Conflict of Interest: SS and EMH were employed by the company Magnetic Resonance Innovations, Inc.

The remaining authors declare that the research was conducted in the absence of any commercial or financial relationships that could be construed as a potential conflict of interest.

Copyright © 2020 Jin, Sethi, Li, Tang, Li, Hsu, He, Haacke and Yan. This is an open-access article distributed under the terms of the Creative Commons Attribution License (CC BY). The use, distribution or reproduction in other forums is permitted, provided the original author(s) and the copyright owner(s) are credited and that the original publication in this journal is cited, in accordance with accepted academic practice. No use, distribution or reproduction is permitted which does not comply with these terms.



Paramagnetic Metal Accumulation in the Deep Gray Matter Nuclei Is Associated With Neurodegeneration in Wilson's Disease

Xiang-Zhen Yuan¹, Gai-Ying Li², Jia-Lin Chen², Jian-Qi Li^{2*} and Xiao-Ping Wang^{1*}

¹ Department of Neurology, Tongren Hospital, Shanghai Jiao Tong University School of Medicine, Shanghai, China,

² Shanghai Key Laboratory of Magnetic Resonance, School of Physics and Electronic Science, East China Normal University, Shanghai, China

OPEN ACCESS

Edited by:

Mark Haacke,
Wayne State University, United States

Reviewed by:

Tomasz Litwin,
Institute of Psychiatry and Neurology,
Poland
Ferdinand Schweser,
University at Buffalo, United States
Petr Dušek,
Charles University, Czechia

Xu Li,
Kennedy Krieger Institute,
United States

*Correspondence:

Jian-Qi Li
jqli@phy.ecnu.edu.cn
Xiao-Ping Wang
wangxp@ustc.edu

Specialty section:

This article was submitted to
Neurodegeneration,
a section of the journal
Frontiers in Neuroscience

Received: 17 June 2020

Accepted: 27 August 2020

Published: 16 September 2020

Citation:

Yuan X-Z, Li G-Y, Chen J-L, Li J-Q
and Wang X-P (2020) Paramagnetic
Metal Accumulation in the Deep Gray
Matter Nuclei Is Associated With
Neurodegeneration in Wilson's
Disease. *Front. Neurosci.* 14:573633.
doi: 10.3389/fnins.2020.573633

Background: Neuropathological studies have revealed copper and iron accumulation in the deep gray matter (DGM) nuclei of patients with Wilson's disease (WD). However, the association between metal accumulation and neurodegeneration in WD has not been well studied *in vivo*. The study was aimed to investigate whether metal accumulation in the DGM was associated with the structural and functional changes of DGM in neurological WD patients.

Methods: Seventeen neurological WD patients and 20 healthy controls were recruited for the study. Mean bulk susceptibility values and volumes of DGM were obtained from quantitative susceptibility mapping (QSM). Regions of interest including the head of the caudate nucleus, globus pallidus, putamen, thalamus, substantia nigra, red nucleus, and dentate nucleus were manually segmented. The susceptibility values and volumes of DGM in different groups were compared using a linear regression model. Correlations between susceptibility values and volumes of DGM and Unified Wilson's Disease Rating Scale (UWDRS) neurological subscores were investigated.

Results: The susceptibility values of all examined DGM in WD patients were higher than those in healthy controls ($P < 0.05$). Volume reductions were observed in the head of the caudate nucleus, globus pallidus, putamen, thalamus, and substantia nigra of WD patients ($P < 0.001$). Susceptibility values were negatively correlated with the volumes of the head of the caudate nucleus ($r_p = -0.657$, $P = 0.037$), putamen ($r_p = -0.667$, $P = 0.037$), and thalamus ($r_p = -0.613$, $P = 0.046$) in WD patients. UWDRS neurological subscores were positively correlated with the susceptibility values of all examined DGM. The susceptibility values of putamen, head of the caudate nucleus, and dentate nucleus could well predict UWDRS neurological subscores.

Conclusion: Our study provided *in vivo* evidence that paramagnetic metal accumulation in the DGM was associated with DGM atrophy and neurological impairment. The susceptibility of DGM could be used as a biomarker to assess the severity of neurodegeneration in WD.

Keywords: Wilson's disease, quantitative susceptibility mapping, iron, copper, neurodegeneration

INTRODUCTION

Wilson's disease (WD), also known as hepatolenticular degeneration, is a copper-overload inherited disease caused by *ATP7B* mutations on chromosome 13. *ATP7B* encodes a copper-transporting P-type ATPase ATP7B, which plays a critical role in maintaining copper homeostasis (Czlonkowska et al., 2018). The dysfunction of ATP7B causes excessive copper accumulation in the liver, and then large amount of non-ceruloplasmin-bound copper is released into the circulation, leading to secondary copper accumulation in the brain, kidney, and other organs (Bandmann et al., 2015). Liver disease and neurological symptoms are the most common clinical features of WD. Copper chelators can effectively improve the hepatic symptoms of WD patients, but they are less effective in improving neurological symptoms and even cause neurological deterioration in initial treatment (Li et al., 2016; Czlonkowska and Litwin, 2017). The pathogenesis of neurological impairment in WD is still not clear. In addition to the toxic effects of copper on the central nervous system, iron accumulation may also aggravate neural damage (Dusek et al., 2015, 2017).

Magnetic resonance imaging (MRI) is the most sensitive imaging tool in the diagnosis of WD. Abnormal signals were observed in more than 90% of the neurological WD patients (Litwin et al., 2013a). The most common brain MRI findings are symmetrical or asymmetric hyperintensities in T2-weighted images in the deep gray matter (DGM) nuclei and brain stem. Hyperintensities in T2-weighted images in the brain may reflect neuropathological changes such as edema, demyelination, and gliosis, which are largely reversible after effective anti-copper treatment (King et al., 1996; Czlonkowska et al., 2018). Brain atrophy is another common imaging feature of neurological WD patients, and both DGM and white matter are affected. Recent studies suggested that total brain volume and the volumes of white matter and gray matter were associated with the severity of neurological impairment in WD patients (Smolinski et al., 2019; Dusek et al., 2020). However, it is not clear whether this correlation still exists in single DGM nuclei. Although WD is a copper-overload disease, the correlation between copper accumulation and neuropathological changes is still controversial (Poujois et al., 2017). An increasing number of studies indicate that iron accumulation in the DGM is involved in the neuropathological changes of WD. Dusek et al. (2017) reported that increased iron content was detected in the basal ganglia of WD patients, and severe putamen (Put) pathological changes were associated with an increased number of iron-containing macrophages. In addition, hypointensities in T2/T2*-weighted images and susceptibility-weighted images (SWI) in the DGM are frequently present in WD patients, also reflecting paramagnetic metal (mainly iron) accumulation in these regions (Skowronska et al., 2013; Dusek et al., 2017). A recent MRI-histopathological study demonstrated that R2* values correlated with iron concentration in the DGM of WD patients (Dusek et al., 2017). However, R2* mapping cannot distinguish between iron and diamagnetic substances. R2* mapping also depends on factors such as field strength, homogeneity of iron distribution, and suffers from blooming artifacts (Bilgic et al., 2012).

Quantitative susceptibility mapping (QSM) is a recently developed MRI post-processing technique, which can quantitatively measure tissue susceptibility and reflect the concentrations of paramagnetic metal *in vivo* (Wang et al., 2017; Li et al., 2018). Using QSM, several recent studies found significantly increased susceptibility in the DGM of neurological WD patients, suggesting paramagnetic metal accumulation in the DGM is a character of neuropathology (Fritzsche et al., 2014; Doganay et al., 2018; Dezortova et al., 2019). In addition, QSM performed better than R2* in distinguishing WD from healthy individuals and showed excellent diagnostic accuracy in the diagnosis of WD (Li et al., 2020).

Intracellular ferritin and hemosiderin are considered as the main source of the DGM susceptibility, which has been confirmed in recent MRI-histopathology studies (Langkammer et al., 2012; Hametner et al., 2018). *In vitro* evidences indicate that the Cu²⁺ compounds are slightly paramagnetic and the Cu⁺ compounds are diamagnetic, but the magnetic features of copper *in vivo* are still unclear (Valdes Hernandez Mdel et al., 2012). Considering that a large amount of copper accumulates in the brains of WD patients, increased susceptibility in the DGM may be explained by copper and iron accumulation.

Several case reports reported that metal accumulation in the DGM changed with the progression or improvement of neurological symptoms (Dusek et al., 2018; Zaino et al., 2019). It is speculated that metal accumulation in the DGM is a surrogate indicator of oxidative stress and neuronal loss (Yan et al., 2018). However, the relationship between metal accumulation and neurodegeneration in WD has not been quantitatively studied *in vivo*. Moreover, a quantitative biomarker for the evaluation of neurodegeneration in WD is still lacking. Validated neuroimaging biomarker will be very helpful in treatment monitoring and outcome prediction.

In this study, we hypothesized that metal accumulation in the DGM was associated with the structural and functional changes of DGM in neurological WD patients. Using the recently developed MRI technique QSM, we quantitatively measured the susceptibility values of DGM, and investigated the association between metal accumulation and DGM volume changes. Furthermore, the association between metal accumulation and the severity of neurological impairment in WD was also assessed.

MATERIALS AND METHODS

Subjects

Twenty neurological WD patients were recruited from the Department of Neurology, Tongren Hospital, Shanghai Jiao Tong University School of Medicine, between December 2018 and December 2019. WD was confirmed according to the Leipzig diagnostic criteria, including low serum ceruloplasmin, presence of Kayser-Fleischer rings on slit-lamp examination, high 24-hour urine copper excretion, and genetic confirmation (Ferenci et al., 2003). All WD patients were on anti-copper treatment with D-penicillamine or dimercaptosuccinic acid (DMSA). Before MRI scans, the severity of neurological impairment in WD patients was assessed by two neurologists with consensus using

Unified Wilson's Disease Rating Scale (UWDRS) neurological subscale (27 items, 208 points) (Leinweber et al., 2008; Volpert et al., 2017). Neurological WD was defined as the presence of neurological symptoms at the time of onset or anytime during the course of the disease. Neurological WD patients aged 18 years or older were included in this study. Exclusion criteria included severe neurological impairment or severe liver decompensation, history of other neuropsychiatric disorders or liver disease, and hepatic encephalopathy. T1 hyperintensities in the lentiform nucleus of WD patients are associated with portosystemic shunting and hepatic encephalopathy (Kozic et al., 2003), which may affect regional susceptibility due to manganese accumulation and the evaluation of neurological symptoms (Lee et al., 2018). Therefore, WD patients with T1 hyperintensities in the lentiform nucleus were excluded from the study. Twenty age and gender matched healthy controls (HC) were recruited for the study. This study was approved by the Medical Ethics Committee of Tongren Hospital, Shanghai Jiao Tong University School of Medicine. All subjects were informed about the study and signed written consent before participation.

Imaging Data Acquisition and Preprocessing

Magnetic resonance imaging scans were carried out on a clinical 3T MRI system (Magnetom Prisma Fit, Siemens Healthcare, Erlangen, Germany) equipped with a 20-channel head coil. The susceptibility maps were acquired from a 3D spoiled multi-echo gradient-echo (GRE) sequence with the following imaging parameters: repetition time (TR) = 31 ms, the first echo time (TE1) = 4.07 ms, echo spacing (ΔTE) = 4.35 ms, numbers of echoes = 6, flip angle = 12° , field of view (FOV) = 240 mm \times 200 mm, in-plane resolution = 0.83 mm \times 0.83 mm, slice thickness = 0.8 mm, number of slices = 192, acquisition time = 7.22 min. A generalized auto-calibrating partially parallel acquisition (GRAPPA) with an acceleration factor of two in the right-left direction and elliptical sampling were used to reduce the acquisition time. T1-weighted, T2-weighted, and T2-weighted fluid-attenuated inversion recovery (FLAIR) images were also obtained from all subjects. T1-weighted images were acquired using a magnetization prepared rapid gradient echo (MPRAGE) sequence with TR = 2530 ms, inversion time (TI) = 1100 ms, TE = 2.98 ms, FOV = 256 mm \times 256 mm, matrix = 256 \times 256, slice thickness = 1 mm, slice number = 192, acquisition time = 6.03 min. T2-weighted images were acquired using a fast spin echo sequence with TR = 5400 ms, TE = 105 ms, FOV = 220 mm \times 220 mm, matrix = 448 \times 448, slice thickness = 3 mm, slice number = 35, acquisition time = 1.44 min. T2-weighted FLAIR were obtained with TR = 5500 ms, TI = 1920 ms, TE = 83 ms, FOV = 220 mm \times 220 mm, matrix = 320 \times 320, slice thickness = 3 mm, slice number = 35, acquisition time = 2.47 min.

T1-weighted, T2-weighted, and FLAIR images were visually assessed by two neurologists (X-ZY and X-PW). Abnormalities in the corpus striatum, thalamus (Th), midbrain, pons, and cerebellum were recorded. Abnormal signal was defined as deviation from the conventionally accepted signal intensity of a given structure. Cortical and cerebellar atrophy was assessed

according to the global cortical atrophy (GCA) score (Pasquier et al., 1996). Central atrophy was assessed by measuring the width of the third ventricle. WD patients were considered to have brain atrophy if the GCA score > 1 and/or the width of the third ventricle > 6 mm (Dusek et al., 2020). When disagreements arose, consensus was reached through discussion.

The susceptibility maps were reconstructed using the Morphology Enabled Dipole Inversion with automatic uniform cerebrospinal fluid (CSF) zero reference (MEDI + 0) algorithm (Liu et al., 2018). The reconstruction procedure involved the following steps: The field map was first estimated by performing a one-dimensional temporal unwrapping of the phase on each voxel followed by a weighted least squares fit of the temporally unwrapped phases in each voxel over TE (Liu et al., 2013). Then, a magnitude image guided spatial unwrapping algorithm was used to account for frequency aliasing on the field map (Cusack and Papadakis, 2002). Thirdly, the background field was removed using the projection onto dipole fields (PDF) method (Liu et al., 2011). Finally, the remaining tissue field was inverted to generate a susceptibility map using MEDI (Liu et al., 2012), and the susceptibility of ventricular CSF was used as zero reference (Straub et al., 2017). The ventricular CSF mask M_{CSF} was determined from the brain ROI mask M and the $R2^*$ map by taking advantage of the low $R2^*$ values of CSF and by imposing connectivity (**Supplementary Figure S1**). The parameters for MEDI + 0 used the default settings in the MEDI toolbox, λ_1 and λ_2 were 1000 and 100, respectively. The threshold of $R2^*$ was 5 s^{-1} (Liu et al., 2018).

The 3D regions of interest (ROIs) including the bilateral head of the caudate nucleus (CN), globus pallidus (GP), Put, Th, substantia nigra (SN), red nucleus (RN), and dentate nucleus (DN), were manually segmented on the susceptibility maps by a rater who was blinded to subject information using ITK-SNAP¹. ROIs were drawn according to their anatomical boundaries on all sections where the DGM was visible (**Figure 1**). The most inferior or most superior slice of ROIs were excluded to minimize partial volume effects, and voxels at the boundaries were also excluded. ROIs were confirmed by a senior neurologist (X-PW) with more than 30 years of neuroimaging experience. To account for the effect of head size variability across individuals, the volume of each ROI was normalized with the skull-scaling factor, which was obtained from T1-weighted images using FSL's SIENAX tool (Smith et al., 2002). Susceptibility values of each ROI in the left and right hemispheres were averaged for further analysis.

Statistical Analyses

Mann-Whitney U test was used to compare the age distribution between WD patients and HC. Susceptibility values and volumes of ROIs in each group were compared using a linear regression model, and age and gender were used as covariates to correct for their potential influence on susceptibility. Correlation analysis was performed between the susceptibility values and volumes of ROIs and UWDRS neurological subscores. Since the data could not completely pass the normality test (Kolmogorov-Smirnov test), Spearman rank correlation coefficients (r) were

¹<http://www.itk-snap.org>

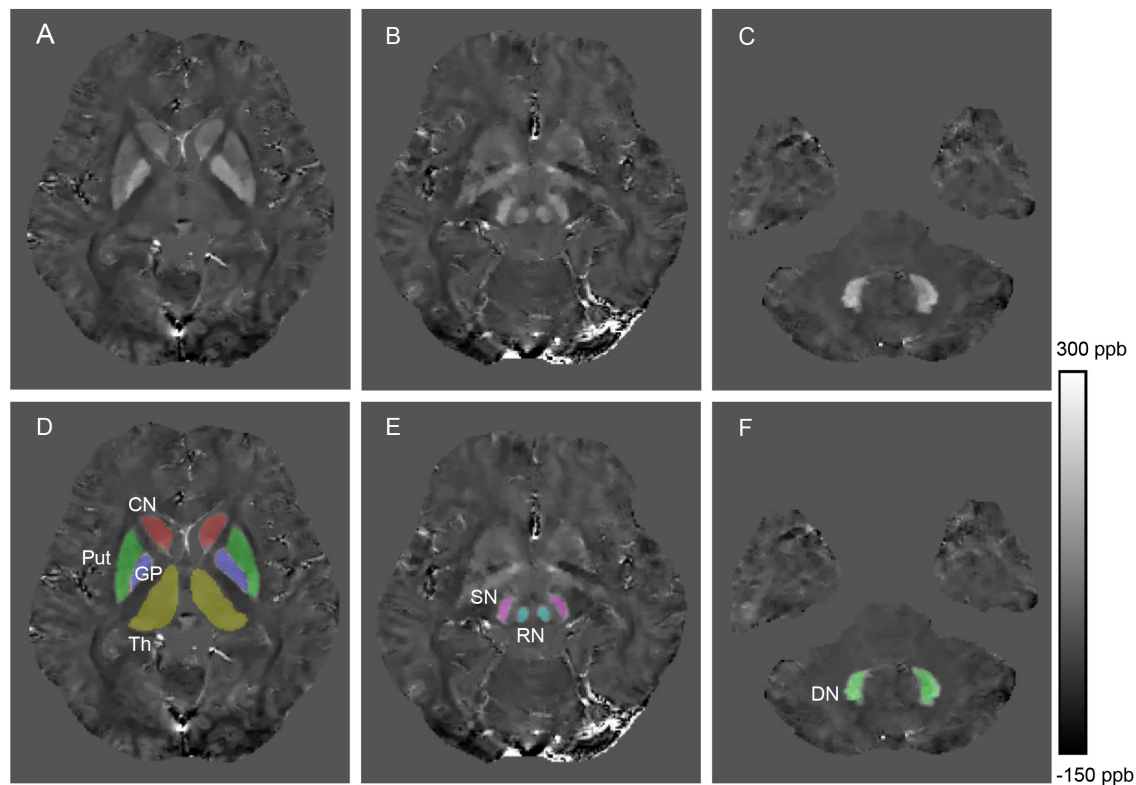


FIGURE 1 | Example images showing segmentation of regions of interest from a healthy control (28 years old, male). The QSM image (A) and example segmentations (D) include the head of the caudate nucleus (CN), globus pallidus (GP), putamen (Put) and thalamus (Th). The QSM image (B) and example segmentations (E) include the red nucleus (RN) and substantia nigra (SN). The QSM image (C) and example segmentation (F) include the dentate nucleus (DN).

calculated to quantify correlation strength. To control for the effects of age, gender, and disease duration, partial Spearman correlation coefficients (r_p) were calculated. The P -values of multiple comparisons and correlation analysis were corrected by controlling the false discovery rate (FDR) at a level of 0.05 (Benjamini and Hochberg, 1995). To test whether susceptibility values of DGM could predict the severity of neurological impairment, a multiple regression model with UWDRS neurological subscores as the dependent variable and susceptibility values of DGM as predictor variables was performed. The multiple regression model was performed using a stepwise method, which continuously increased the number of predictor variables until the best predictive model was obtained. Collinearity diagnosis was also performed by checking tolerance and variance inflation factor (VIF). Statistical analyses were conducted using SPSS Statistics 22 (SPSS Inc., Chicago, IL, United States).

RESULTS

Subjects Characteristics

Three WD patients with T1 hyperintensities in the lentiform nucleus were excluded. A total of 17 neurological WD patients (10 males and 7 females) and 20 age-matched HC (12 males and 8 females) were included for further analysis. The mean age

of WD patients and HC was 32.23 ± 7.55 (range 20–48) years and 30.4 ± 7.59 (range 18–43) years, respectively. There were no statistically differences in age distribution between the two groups ($P = 0.478$). The mean disease duration (from symptom onset to the time of MRI scans) was 10.83 ± 6.74 (range 0.5–21) years, and the mean treatment duration was 8.15 ± 6.07 (range 0.5–20) years. Four WD patients were treated with D-penicillamine and 13 WD patients were treated with DMSA.

T2/FLAIR hyperintensities in lentiform nucleus, Th, midbrain, and tegmentum of pons were the most common findings and were observed in 15 of 17 (88%) WD patients (Supplementary Figure S2). Brain atrophy was observed in 11 of 17 (65%) WD patients. Demographic and clinical characteristics of all participants are summarized in Table 1.

Susceptibility and Volume Analysis

In visual observation, high signals (increased susceptibility) could be observed in the DGM of WD patients. GP, Put, and SN had the most significant susceptibility changes in WD patients compared to HC. In addition, DGM atrophy was a common imaging feature of WD patients (Figure 2). The mean susceptibility values of all examined DGM in WD patients were higher than those in HC. Significantly increased susceptibility values were found in CN, GP, Put, Th, SN, and RN in WD patients ($P < 0.001$). The susceptibility value of DN was slightly higher in WD patients than in HC ($P = 0.031$) (Figure 3). Volume reductions were

TABLE 1 | Demographic and clinical characteristics of all subjects.

	WD patients (N = 17)	HC (N = 20)
Gender (male/female)	10/7	12/8
Age (years)*	32.23(7.55)	30.4 (7.59)
Disease duration (years)	10.83(6.74)	–
Treatment duration (years)	8.15 (6.07)	–
Kayser-Fleischer rings	16/17	–
Serum ceruloplasmin (<0.15 g/L)	17/17	–
UWDRS neurological subscores	13.71(12.14)	–
T2/FLAIR hyperintensities	15/17	0/20
Brian atrophy	11/17	0/20

Standard deviations are in parentheses. * $P = 0.478$; Mann-Whitney U test was used for age comparison. Normal reference range: serum ceruloplasmin, 0.2–0.45 g/L. FLAIR, fluid-attenuated inversion recovery; HC, healthy controls; N, number; UWDRS, Unified Wilson's Disease Rating Scale; WD, Wilson's disease.

found in CN, GP, Put, Th, and SN in WD patients ($P < 0.001$), but the volumes of RN ($P = 0.114$) and DN ($P = 0.614$) were not significantly changed (**Figure 4**). More information about the susceptibility and volumes of DGM can be found in **Supplementary Table S1**.

Correlation Between Susceptibility Values and Volumes of DGM

In WD patients, susceptibility values and volumes of DGM were negatively correlated in CN ($r = -0.757$, $P = 0.003$), GP ($r = -0.534$, $P = 0.038$), Put ($r = -0.706$, $P = 0.005$), Th ($r = -0.613$, $P = 0.021$), and RN ($r = -0.539$, $P = 0.038$). No such correlation was found in SN ($r = 0.093$, $P = 0.722$) and DN ($r = 0.235$, $P = 0.424$) (**Figure 5**). After controlling for age, gender, and disease duration, susceptibility values and volumes of DGM were still negatively correlated in CN ($r_p = -0.657$, $P = 0.037$), Put ($r_p = -0.667$, $P = 0.037$), and Th ($r_p = -0.613$, $P = 0.046$). No correlation was found between susceptibility values and volumes of DGM in GP ($r_p = -0.502$, $P = 0.118$), SN ($r_p = 0.063$, $P = 0.829$), RN ($r_p = -0.457$, $P = 0.141$), and DN ($r_p = 0.239$, $P = 0.478$).

In the group of HC, there was no correlation between susceptibility values and volumes of DGM in CN ($r = -0.302$, $P = 0.308$), GP ($r = -0.287$, $P = 0.308$), Put ($r = -0.577$, $P = 0.056$), Th ($r = -0.005$, $P = 0.985$), SN ($r = -0.477$, $P = 0.119$), RN ($r = -0.006$, $P = 0.985$), and DN ($r = 0.414$, $P = 0.163$). Similar results were obtained after controlling for age and gender: CN ($r_p = -0.313$, $P = 0.288$), GP ($r_p = -0.275$, $P = 0.315$), Put ($r_p = -0.313$, $P = 0.288$), Th ($r_p = -0.018$, $P = 0.945$), SN ($r_p = -0.381$, $P = 0.278$), RN ($r_p = -0.464$, $P = 0.256$), and DN ($r_p = 0.433$, $P = 0.256$).

Correlation Between Susceptibility Values of DGM and Neurological Impairment

Unified Wilson's Disease Rating Scale neurological subscale was used to assess the severity of neurological impairment in WD patients, with a higher score indicating a more severe condition. The susceptibility values of DGM were positively correlated with UWDRS neurological subscores in CN ($r = 0.701$, $P = 0.006$), GP

($r = 0.632$, $P = 0.011$), Put ($r = 0.727$, $P = 0.006$), Th ($r = 0.656$, $P = 0.01$), and RN ($r = 0.608$, $P = 0.014$) in WD patients. No such correlation was found in SN ($r = 0.432$, $P = 0.097$) and DN ($r = 0.374$, $P = 0.139$) (**Figure 6**). After controlling for age, gender, and disease duration, susceptibility values of DGM were positively correlated with UWDRS neurological subscores in all examined DGM: CN ($r_p = 0.669$, $P = 0.016$), GP ($r_p = 0.616$, $P = 0.026$), Put ($r_p = 0.76$, $P = 0.006$), Th ($r_p = 0.72$, $P = 0.009$), SN ($r_p = 0.588$, $P = 0.03$), RN ($r_p = 0.766$, $P = 0.006$), and DN ($r_p = 0.58$, $P = 0.03$).

The multiple regression model revealed that the susceptibility values of Put, CN, and DN could well predict UWDRS neurological subscores. The susceptibility value of Put was superior to that of other DGM nuclei in predicting the UWDRS neurological subscores. In the model with only the susceptibility value of Put as a predictor variable, UWDRS neurological subscores increased by 1 point for every 6 ppb increase in Put ($P = 0.005$; $R^2 = 0.415$). The model using the susceptibility values of CN and DN as predictor variables had the best ability in predicting the UWDRS neurological subscores. UWDRS neurological subscores increased by 1 point for every 6 ppb increase in CN ($P < 0.001$) or every 8 ppb increase in DN ($P = 0.001$; $R^2 = 0.745$). Details about the multiple regression model can be found in **Supplementary Table S2**.

Correlation Between Volumes of DGM and Neurological Impairment

There was no correlation between volumes of DGM and UWDRS neurological subscores in CN ($r = -0.432$, $P = 0.146$), GP ($r = -0.625$, $P = 0.051$), Put ($r = -0.311$, $P = 0.262$), Th ($r = -0.513$, $P = 0.082$), SN ($r = -0.549$, $P = 0.079$), RN ($r = -0.367$, $P = 0.206$), and DN ($r = 0.205$, $P = 0.43$). After controlling for age, gender, and disease duration, a negative correlation was found between the volume of Th and UWDRS neurological subscores ($r_p = -0.689$, $P = 0.045$). No such correlation was found in CN ($r_p = -0.331$, $P = 0.289$), GP ($r_p = -0.575$, $P = 0.11$), Put ($r_p = -0.335$, $P = 0.289$), SN ($r_p = -0.502$, $P = 0.118$), RN ($r_p = -0.503$, $P = 0.118$), and DN ($r_p = 0.234$, $P = 0.42$).

DISCUSSION

In this cross-sectional study, we found that the group average susceptibility values of all examined DGM in neurological WD patients were significantly higher than those in HC. Volume reductions were observed in CN, GP, Put, Th, and SN of WD patients, but RN in the midbrain and DN in the cerebellum were not affected. Susceptibility values and volumes of DGM were negatively correlated in CN, Put, and Th. In addition, increased DGM susceptibility was associated with high UWDRS neurological subscores in all examined DGM. There was only a weak correlation between volumes of DGM and UWDRS neurological subscores in Th. The results of our study were consistent with the theory that iron and copper accumulation in DGM was a character of neuropathology in neurological WD patients. To our knowledge, our study provided the first

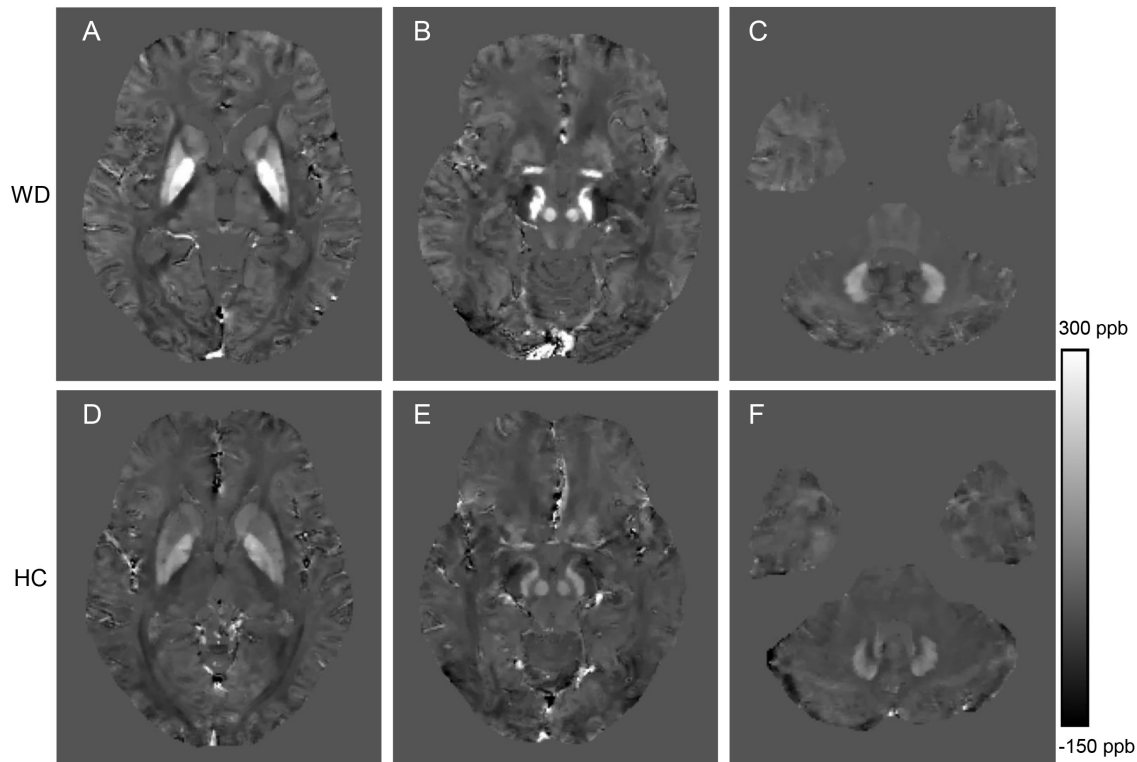


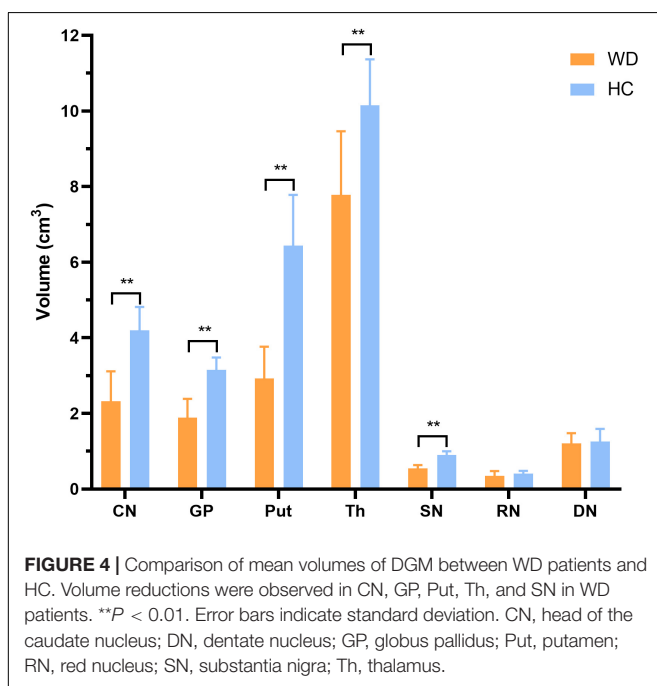
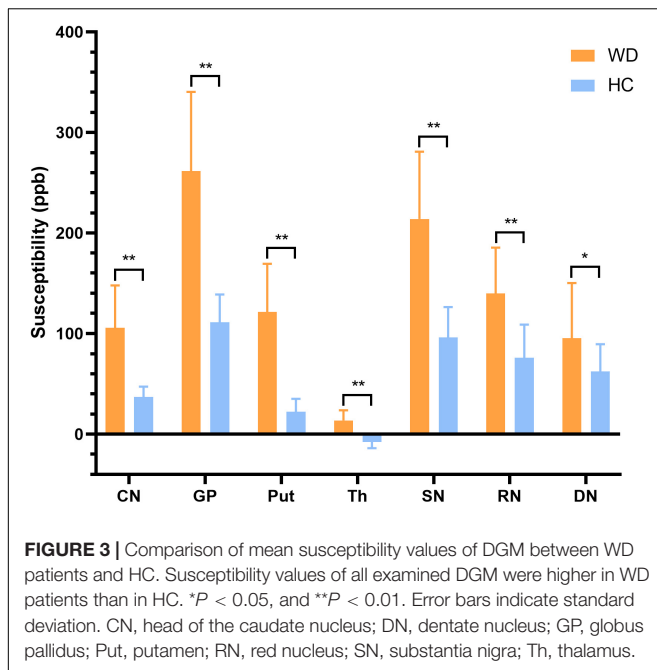
FIGURE 2 | Comparison of QSM images from a WD patient (36 years old, male, **A–C**) and a healthy control (38 years old, male, **D–F**). The QSM images (**A,D**) include head of the caudate nucleus, globus pallidus, putamen and thalamus. The QSM images (**B,E**) include the red nucleus and substantia nigra. The QSM images (**C,F**) include the dentate nucleus. Significantly increased susceptibility was observed in the deep gray matter nuclei of the WD patient.

in vivo evidence that metal accumulation in the DGM was associated with DGM atrophy and neurological impairment in neurological WD patients.

Studies using traditional GRE MRI sequences such as T2*-weighted images and SWI had identified iron accumulation in the brains of WD patients (Yang et al., 2015; Dusek et al., 2017). However, traditional GRE MRI sequences always suffer from blooming artifacts and the non-local effect (Li et al., 2012). Most importantly, traditional GRE MRI sequences cannot quantify susceptibility source without deconvolution, and phase changes cannot reflect the actual tissue susceptibility (Wang et al., 2017). QSM is a recently developed GRE MRI post-processing technique, which can quantitatively measure tissue susceptibility and is less affected by the external magnetic field (de Rochefort et al., 2010; Wang et al., 2017). Given iron content is about 3-fold higher than copper content in the DGM of neurological WD patients and the strong paramagnetism of iron species (Dusek et al., 2017; Dezortova et al., 2019), we attribute the increased susceptibility of DGM primarily to iron accumulation. However, we cannot exclude the influence of copper accumulation on susceptibility changes. In our study, significantly increased susceptibility was detected in all examined DGM nuclei, indicating metal accumulation in the DGM is common neuropathological feature of neurological WD patients. The highest susceptibilities values were observed in GP and SN, which was consistent with the distribution of iron species

in neurological WD patients (Dusek et al., 2017). Whether iron species accumulate in the dentate nucleus in WD patients is controversial. Several postmortem studies analyzed the iron content in DN in WD patients, but the results were quite different (Litwin et al., 2013b; Dusek et al., 2017). We found that the mean susceptibility value of DN in WD patients was slightly higher than that in HC. The results of our study suggested that iron species tended to accumulate in the basal ganglia and brain stem of WD patients, while DN in the cerebellum was less affected.

Interestingly, increased susceptibility was also observed in Th, which contains large amount of white matter fiber tracts. Myelin in white matter is diamagnetic, and the increased susceptibility in Th may be caused by demyelination besides metal accumulation (Hametner et al., 2018; Dezortova et al., 2019). Demyelination is a common pathological feature of white matter in WD patients. Recent studies also revealed microstructure changes in Th and white matter of WD patients using diffusion tensor imaging (DTI) (Li et al., 2014; Dong et al., 2019). However, we cannot determine whether metal accumulation or demyelination is the main factor leading to increased susceptibility in Th. In addition, an increase in the mean bulk susceptibility of DGM may be induced by DGM atrophy. Metal concentration increases with tissue atrophy, but it is unclear whether the total metal content increases (Hernandez-Torres et al., 2019). Increased susceptibility was also observed in the DGM without atrophy (RN and DN) in WD patients.



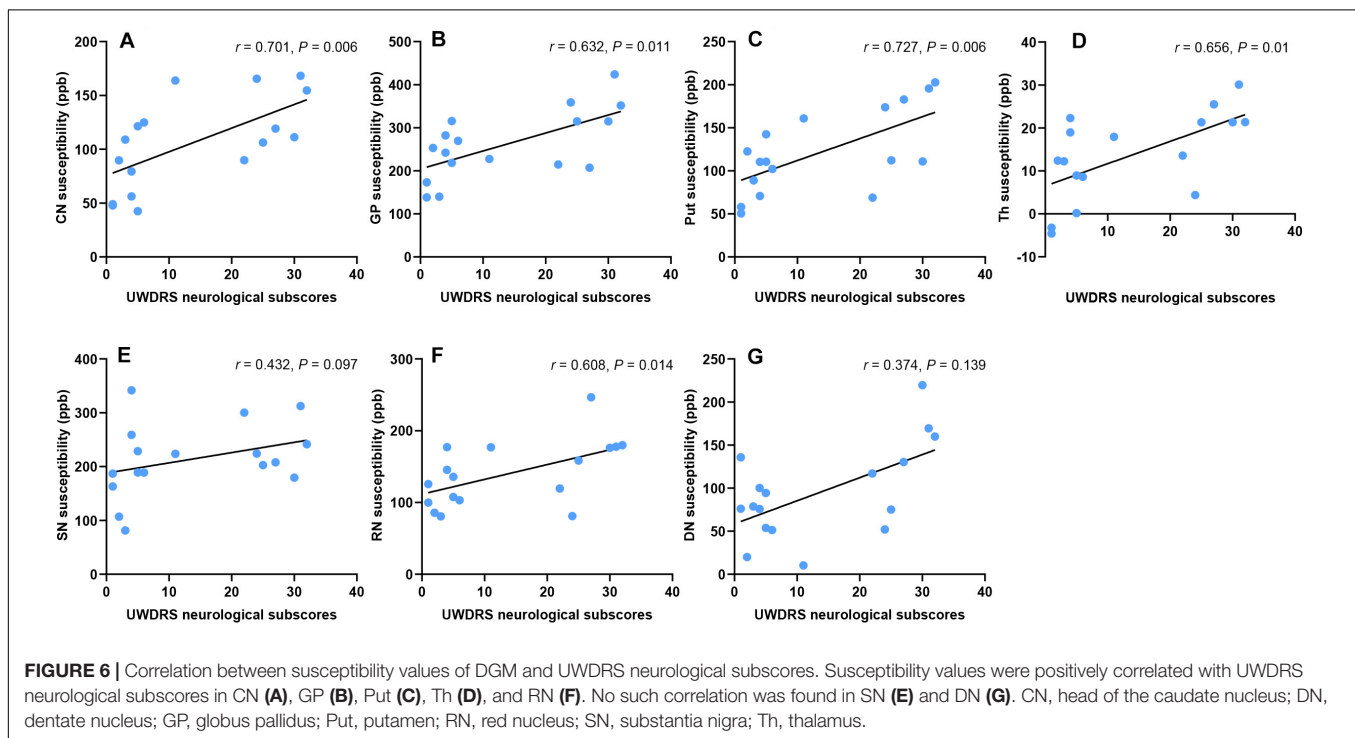
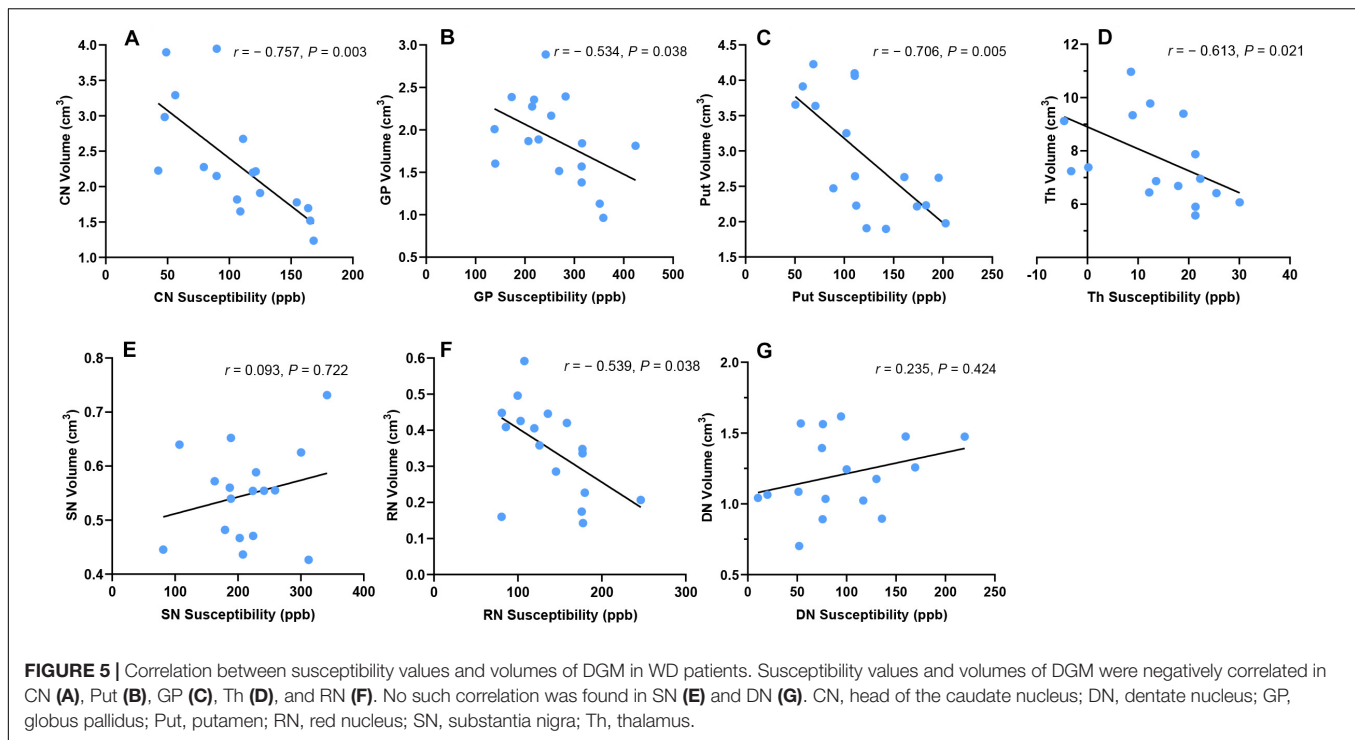
Therefore, we speculate that paramagnetic metal accumulation occurs in the DGM of WD patients. Histopathological studies are needed to confirm whether there is paramagnetic metal accumulation in the DGM of WD patients.

Brain atrophy is a common MRI feature of neurological WD patients and is associated with the severity of the neurological impairment (Smolinski et al., 2019; Dusek et al., 2020). Brain atrophy seems to be an irreversible process, but the neurological symptoms of WD patients are partly reversible after anti-copper treatment. Therefore, brain volume may be more appropriate

as an assessment for chronic treated WD patients than as a marker for treatment monitoring. In WD patients, basal ganglia and brainstem are the most vulnerable regions, especially Put, which is a softening, brownish, atrophic nuclei with cavitations at macroscopic examination (Poujois et al., 2017). In this study, we found significant DGM atrophy in CN, GP, Put, Th, and SN, but RN and DN were not affected. Furthermore, we found that susceptibility values and volumes of DGM were negatively correlated in CN, Put, and Th, suggesting that metal accumulation in the DGM was associated with neuronal loss. The results of our study were consistent with the study of Dusek et al. (2017) which found Put atrophy was accompanied with increased iron content and iron-containing macrophages. However, it is not clear whether iron accumulation was merely a biomarker of neurodegeneration or a cause or contributor to the neurodegeneration itself (Yan et al., 2018). The advantage of QSM in measuring DGM volumes is that it can show the boundaries of DGM more clearly than traditional MRI sequences, which can ensure the accuracy of segmentation (Liu et al., 2013). To our knowledge, this study is the first one to investigate the DGM volume changes in WD using QSM.

Brain atrophy and iron accumulation is a common feature of neurodegenerative diseases such as Alzheimer's disease and Parkinson's disease (Lane et al., 2018; Jiang et al., 2019). Increased iron accumulation in the DGM may be explained by the influx of iron-containing phagocytic cells (macrophages), mitochondria damage and energy production failure, or decreased iron efflux due to ceruloplasmin dysfunction (Dusek et al., 2017, 2018). Ceruloplasmin is a ferroxidase that plays a critical role in maintaining iron homeostasis and preventing the formation of free radicals (Wang and Wang, 2019). Decreased serum ceruloplasmin may aggravate iron accumulation in WD, which is similar to the pathogenesis of aceruloplasminemia (Piperno and Alessio, 2018). As mentioned above, iron accumulation may be caused by neurodegeneration in WD, and iron accumulation also exacerbates neurodegeneration due to its redox properties.

We assessed the severity of neurological impairment of WD patients using UWDRS neurological subscale, and found that the susceptibility values of DGM were positively correlated with the severity of neurological impairment in all examined DGM. The correlation between iron accumulation and neuropathological changes of Put has been confirmed by a histopathological study (Dusek et al., 2017). Brain atrophy and brain MRI abnormalities reflecting iron accumulation, such as T2* and SWI hypointensities, were proposed as a part of imaging scale to assess the severity of MRI changes in WD. These chronic brain abnormalities were considered irreversible overtime, and showed positive correlation with the severity of neurological impairment (Dusek et al., 2020). Our study provided *in vivo* evidence that metal accumulation in the DGM was associated with DGM atrophy and neurological impairment in neurological WD patients. In addition, we found the susceptibility values of Put, CN, and DN could well predict the severity of neurological impairment. The susceptibility value of Put was superior to that of other DGM nuclei in predicting the UWDRS neurological subscores. The model using the susceptibility values of CN and



DN as predictor variables had the best ability in predicting the UWDRS neurological subscores.

Few studies focused on the correlations between DGM atrophy and severity of neurological impairment in WD. Zou et al. (2019) reported that the volumes of bilateral Put and left GP were associated with the severity of neurological impairment in

WD, which was assessed using modified Young scale. However, in this study, we only found a weak correlation between the volumes of DGM and the UWDRS neurological subscores in Th. The method of DGM volume assessment (manual or automatic segmentation), the selection of neurological scales, the small number of WD patients, and the high heterogeneity of WD

patients may be the reasons for different results of the two studies. More studies are needed to determine the relationship between DGM atrophy and the severity of neurological impairment in WD. Compared with the volumes of DGM, the susceptibility values of DGM showed better correlations with UWDRS neurological subscores. The results of our study suggested that the susceptibility values of DGM could be used as a biomarker to assess the severity of neurodegeneration, which would be helpful in the diagnosis of WD, treatment monitoring, and as a surrogate outcome for clinical trials.

Several limitations in this study have to be mentioned. In some WD patients, DGM atrophy and local high susceptibility make the boundaries of DGM unclear, which may affect the accuracy of DGM segmentation. WD patients included in this study were treated patients with mild or moderate neurological symptoms. Patients with severe neurological impairment were excluded because they could not cooperate or remain still during MRI scans. It is unclear whether the susceptibility of DGM is still associated with neurological impairment in patients with severe neurological symptoms or in untreated patients. Due to limited sample size, the results of our study need to be confirmed in a larger cohort. In addition, a longitudinal study is required to determine whether the susceptibility of DGM changes with disease progression or symptom improvement.

In conclusion, our study found paramagnetic metal accumulation in the DGM of neurological WD patients, and provided *in vivo* evidence that metal accumulation in the DGM was associated with DGM atrophy and neurological impairment. The susceptibility of DGM could be used as a biomarker to assess the severity of neurodegeneration in WD.

DATA AVAILABILITY STATEMENT

The raw data supporting the conclusions of this article will be made available by the authors, without undue reservation.

REFERENCES

- Bandmann, O., Weiss, K. H., and Kaler, S. G. (2015). Wilson's disease and other neurological copper disorders. *Lancet Neurol.* 14, 103–113. doi: 10.1016/S1474-4422(14)70190-5
- Benjamini, Y., and Hochberg, Y. (1995). Controlling the false discovery rate: a practical and powerful approach to multiple testing. *J. R. Stat. Soc. Ser. B Methodol.* 57, 289–300.
- Bilgic, B., Pfefferbaum, A., Rohlfing, T., Sullivan, E. V., and Adalsteinsson, E. (2012). MRI estimates of brain iron concentration in normal aging using quantitative susceptibility mapping. *Neuroimage* 59, 2625–2635. doi: 10.1016/j.neuroimage.2011.08.077
- Cusack, R., and Papadakis, N. (2002). New robust 3-D phase unwrapping algorithms: application to magnetic field mapping and undistorting echoplanar images. *Neuroimage* 16(3 Pt 1), 754–764. doi: 10.1006/nimg.2002.1092
- Czlonkowska, A., and Litwin, T. (2017). Wilson disease - currently used anticopper therapy. *Handb. Clin. Neurol.* 142, 181–191. doi: 10.1016/B978-0-444-63625-6.00015-X

ETHICS STATEMENT

The studies involving human participants were reviewed and approved by Medical Ethics Committee of Tongren Hospital, Shanghai Jiao Tong University School of Medicine. The patients/participants provided their written informed consent to participate in this study.

AUTHOR CONTRIBUTIONS

X-ZY and J-LC developed the conception and design of the study, collected clinical and imaging data, and analyzed and interpreted the data. G-YL analyzed and interpreted the data, and revised the manuscript. J-QL and X-PW developed the conception and design of the study, and revised the manuscript. X-ZY wrote the first draft, and all of the authors critically reviewed the manuscript. All authors contributed to the article and approved the submitted version.

FUNDING

This study was supported by grants from the National Natural Science Foundation of China (81671103) and Shanghai Jiao Tong University Medical School Innovative Research Plan 2015 (TM201520).

ACKNOWLEDGMENTS

We thank all participants involved in this study.

SUPPLEMENTARY MATERIAL

The Supplementary Material for this article can be found online at: <https://www.frontiersin.org/articles/10.3389/fnins.2020.573633/full#supplementary-material>

- Czlonkowska, A., Litwin, T., Dusek, P., Ferenci, P., Lutsenko, S., Medici, V., et al. (2018). Wilson disease. *Nat. Rev. Dis. Primers* 4:21. doi: 10.1038/s41572-018-0018-3
- de Rochefort, L., Liu, T., Kressler, B., Liu, J., Spincemille, P., Lebon, V., et al. (2010). Quantitative susceptibility map reconstruction from MR phase data using bayesian regularization: validation and application to brain imaging. *Magn. Reson. Med.* 63, 194–206. doi: 10.1002/mrm.22187
- Dezortova, M., Lescinskij, A., Dusek, P., Herynek, V., Acosta-Cabronero, J., Bruha, R., et al. (2019). Multiparametric quantitative brain MRI in neurological and hepatic forms of Wilson's disease. *J. Magn. Reson. Imaging* 51, 1829–1835. doi: 10.1002/jmri.26984
- Doganay, S., Gumus, K., Koc, G., Bayram, A. K., Dogan, M. S., Arslan, D., et al. (2018). Magnetic susceptibility changes in the basal ganglia and brain stem of patients with wilson's disease: evaluation with quantitative susceptibility mapping. *Magn. Reson. Med. Sci.* 17, 73–79. doi: 10.2463/mrms.mp.2016-0145
- Dong, T., Yang, W. M., Wu, M. C., Zhang, J., Huang, P., Xu, C. S., et al. (2019). Microstructure changes in whiter matter relate to cognitive impairment in Wilson's disease. *Biosci. Rep.* 39:BSR20181651. doi: 10.1042/BSR20181651

- Dusek, P., Bahn, E., Litwin, T., Jablonka-Salach, K., Luciuk, A., Huelnhagen, T., et al. (2017). Brain iron accumulation in Wilson disease: a post mortem 7 Tesla MRI - histopathological study. *Neuropathol. Appl. Neurobiol.* 43, 514–532. doi: 10.1111/nan.12341
- Dusek, P., Roos, P. M., Litwin, T., Schneider, S. A., Flaten, T. P., and Aaseth, J. (2015). The neurotoxicity of iron, copper and manganese in Parkinson's and Wilson's diseases. *J. Trace Elem. Med. Biol.* 31, 193–203. doi: 10.1016/j.jtemb.2014.05.007
- Dusek, P., Skoloudik, D., Maskova, J., Huelnhagen, T., Bruha, R., Zahorakova, D., et al. (2018). Brain iron accumulation in Wilson's disease: a longitudinal imaging case study during anticopper treatment using 7.0T MRI and transcranial sonography. *J. Magn. Reson. Imaging* 47, 282–285. doi: 10.1002/jmri.25702
- Dusek, P., Smolinski, L., Redzia-Ogrodnik, B., Golebiowski, M., Skowronska, M., Poujois, A., et al. (2020). Semiquantitative scale for assessing brain MRI abnormalities in wilson disease: a validation study. *Mov. Disord.* 35, 994–1001. doi: 10.1002/mds.28018
- Ferenci, P., Caca, K., Loudianos, G., Mieli-Vergani, G., Tanner, S., Sternlieb, I., et al. (2003). Diagnosis and phenotypic classification of Wilson disease. *Liver Int.* 23, 139–142. doi: 10.1034/j.1600-0676.2003.00824.x
- Fritzsche, D., Reiss-Zimmermann, M., Trampel, R., Turner, R., Hoffmann, K. T., and Schafer, A. (2014). Seven-tesla magnetic resonance imaging in Wilson disease using quantitative susceptibility mapping for measurement of copper accumulation. *Invest. Radiol.* 49, 299–306. doi: 10.1097/RLI.000000000000010
- Hametner, S., Endmayr, V., Deistung, A., Palmrich, P., Prihoda, M., Haimburger, E., et al. (2018). The influence of brain iron and myelin on magnetic susceptibility and effective transverse relaxation - A biochemical and histological validation study. *Neuroimage* 179, 117–133. doi: 10.1016/j.neuroimage.2018.06.007
- Hernandez-Torres, E., Wiggermann, V., Machan, L., Sadovnick, A. D., Li, D. K. B., Traboulsee, A., et al. (2019). Increased mean R2* in the deep gray matter of multiple sclerosis patients: have we been measuring atrophy? *J. Magn. Reson. Imaging* 50, 201–208. doi: 10.1002/jmri.26561
- Jiang, H., Song, N., Jiao, Q., Shi, L., and Du, X. (2019). Iron pathophysiology in Parkinson diseases. *Adv. Exp. Med. Biol.* 1173, 45–66. doi: 10.1007/978-981-13-9589-5_4
- King, A. D., Walshe, J. M., Kendall, B. E., Chinn, R. J., Paley, M. N., Wilkinson, I. D., et al. (1996). Cranial MR imaging in Wilson's disease. *AJR Am. J. Roentgenol.* 167, 1579–1584. doi: 10.2214/ajr.167.6.8956601
- Kozic, D., Svetel, M., Petrovic, B., Dragasevic, N., Semnic, R., and Kostic, V. S. (2003). MR imaging of the brain in patients with hepatic form of Wilson's disease. *Eur. J. Neurol.* 10, 587–592. doi: 10.1046/j.1468-1331.2003.00661.x
- Lane, D. J. R., Ayton, S., and Bush, A. I. (2018). Iron and Alzheimer's disease: an update on emerging mechanisms. *J. Alzheimers Dis.* 64, S379–S395. doi: 10.3233/JAD-179944
- Langkammer, C., Schweser, F., Krebs, N., Deistung, A., Goessler, W., Scheurer, E., et al. (2012). Quantitative susceptibility mapping (QSM) as a means to measure brain iron? A post mortem validation study. *Neuroimage* 62, 1593–1599. doi: 10.1016/j.neuroimage.2012.05.049
- Lee, S., Nam, Y., Jang, J., Na, G. H., Kim, D. G., Shin, N. Y., et al. (2018). Deep gray matter iron measurement in patients with liver cirrhosis using quantitative susceptibility mapping: relationship with pallidal T1 hyperintensity. *J. Magn. Reson. Imaging* 47, 1342–1349. doi: 10.1002/jmri.25841
- Leinweber, B., Moller, J. C., Scherag, A., Reuner, U., Gunther, P., Lang, C. J., et al. (2008). Evaluation of the unified wilson's disease rating scale (UWDRS) in German patients with treated Wilson's disease. *Mov. Disord.* 23, 54–62. doi: 10.1002/mds.21761
- Li, G., Wu, R., Tong, R., Bo, B., Zhao, Y., Gillen, K. M., et al. (2020). Quantitative measurement of metal accumulation in brain of patients with wilson's disease. *Mov. Disord.* doi: 10.1002/mds.28141 [Epub ahead of print].
- Li, G., Zhou, X., Xu, P., Pan, X., and Chen, Y. (2014). Microstructure assessment of the thalamus in Wilson's disease using diffusion tensor imaging. *Clin. Radiol.* 69, 294–298. doi: 10.1016/j.crad.2013.10.016
- Li, J., Chang, S., Liu, T., Wang, Q., Cui, D., Chen, X., et al. (2012). Reducing the object orientation dependence of susceptibility effects in gradient echo MRI through quantitative susceptibility mapping. *Magn. Reson. Med.* 68, 1563–1569. doi: 10.1002/mrm.24135
- Li, J., Lin, H., Liu, T., Zhang, Z., Prince, M. R., Gillen, K., et al. (2018). Quantitative susceptibility mapping (QSM) minimizes interference from cellular pathology in R2* estimation of liver iron concentration. *J. Magn. Reson. Imaging* 48, 1069–1079. doi: 10.1002/jmri.26019
- Li, W. J., Chen, C., You, Z. F., Yang, R. M., and Wang, X. P. (2016). Current drug managements of Wilson's disease: from west to east. *Curr. Neuropharmacol.* 14, 322–325. doi: 10.2174/1570159x14666151130222427
- Litwin, T., Gromadzka, G., Czlonkowska, A., Golebiowski, M., and Poniatowska, R. (2013a). The effect of gender on brain MRI pathology in Wilson's disease. *Metab. Brain Dis.* 28, 69–75. doi: 10.1007/s11011-013-9378-2
- Litwin, T., Gromadzka, G., Szpak, G. M., Jablonka-Salach, K., Bulska, E., and Czlonkowska, A. (2013b). Brain metal accumulation in Wilson's disease. *J. Neurol. Sci.* 329, 55–58. doi: 10.1016/j.jns.2013.03.021
- Liu, T., Eskreis-Winkler, S., Schweitzer, A. D., Chen, W., Kaplitt, M. G., Tsiouris, A. J., et al. (2013). Improved subthalamic nucleus depiction with quantitative susceptibility mapping. *Radiology* 269, 216–223. doi: 10.1148/radiol.13121991
- Liu, T., Khalidov, I., de Rochefort, L., Spincemaille, P., Liu, J., Tsiouris, A. J., et al. (2011). A novel background field removal method for MRI using projection onto dipole fields (PDF). *NMR Biomed.* 24, 1129–1136. doi: 10.1002/nbm.1670
- Liu, T., Xu, W., Spincemaille, P., Avestimehr, A. S., and Wang, Y. (2012). Accuracy of the morphology enabled dipole inversion (MEDI) algorithm for quantitative susceptibility mapping in MRI. *IEEE Trans. Med. Imaging* 31, 816–824. doi: 10.1109/TMI.2011.2182523
- Liu, Z., Spincemaille, P., Yao, Y., Zhang, Y., and Wang, Y. (2018). MEDI+0: morphology enabled dipole inversion with automatic uniform cerebrospinal fluid zero reference for quantitative susceptibility mapping. *Magn. Reson. Med.* 79, 2795–2803. doi: 10.1002/mrm.26946
- Pasquier, F., Leys, D., Weerts, J. G., Mounier-Vehier, F., Barkhof, F., and Scheltens, P. (1996). Inter- and intraobserver reproducibility of cerebral atrophy assessment on MRI scans with hemispheric infarcts. *Eur. Neurol.* 36, 268–272. doi: 10.1159/000117270
- Piperno, A., and Alessio, M. (2018). Aceruloplasminemia: waiting for an efficient therapy. *Front. Neurosci.* 12:903. doi: 10.3389/fnins.2018.00903
- Poujois, A., Mikol, J., and Woimant, F. (2017). Wilson disease: brain pathology. *Handb. Clin. Neurol.* 142, 77–89. doi: 10.1016/B978-0-444-63625-6.00008-2
- Skowronska, M., Litwin, T., Dziezyc, K., Wierchowska, A., and Czlonkowska, A. (2013). Does brain degeneration in Wilson disease involve not only copper but also iron accumulation? *Neurol. Neurochir. Pol.* 47, 542–546. doi: 10.5114/ninp.2013.39071
- Smith, S. M., Zhang, Y., Jenkinson, M., Chen, J., Matthews, P. M., Federico, A., et al. (2002). Accurate, robust, and automated longitudinal and cross-sectional brain change analysis. *Neuroimage* 17, 479–489. doi: 10.1006/nimg.2002.1040
- Smolinski, L., Litwin, T., Redzia-Ogrodnik, B., Dziezyc, K., Kurkowska-Jastrzebska, I., and Czlonkowska, A. (2019). Brain volume is related to neurological impairment and to copper overload in Wilson's disease. *Neurol. Sci.* 40, 2089–2095. doi: 10.1007/s10072-019-03942-z
- Straub, S., Schneider, T. M., Emmerich, J., Freitag, M. T., Ziener, C. H., Schlemmer, H. P., et al. (2017). Suitable reference tissues for quantitative susceptibility mapping of the brain. *Magn. Reson. Med.* 78, 204–214. doi: 10.1002/mrm.26369
- Valdes Hernandez Mdel, C., Maconick, L. C., Tan, E. M., and Wardlaw, J. M. (2012). Identification of mineral deposits in the brain on radiological images: a systematic review. *Eur. Radiol.* 22, 2371–2381. doi: 10.1007/s00330-012-2494-2
- Volpert, H. M., Pfeiffenberger, J., Groner, J. B., Stremmel, W., Gotthardt, D. N., Schafer, M., et al. (2017). Comparative assessment of clinical rating scales in Wilson's disease. *BMC Neurol.* 17:140. doi: 10.1186/s12883-017-0921-3
- Wang, B., and Wang, X. P. (2019). Does ceruloplasmin defend against neurodegenerative diseases? *Curr. Neuropharmacol.* 17, 539–549. doi: 10.2174/1570159X16666180508113025
- Wang, Y., Spincemaille, P., Liu, Z., Dimov, A., Deh, K., Li, J., et al. (2017). Clinical quantitative susceptibility mapping (QSM): biometal imaging and its emerging roles in patient care. *J. Magn. Reson. Imaging* 46, 951–971. doi: 10.1002/jmri.25693
- Yan, F., He, N., Lin, H., and Li, R. (2018). Iron deposition quantification: applications in the brain and liver. *J. Magn. Reson. Imaging* 48, 301–317. doi: 10.1002/jmri.26161

- Yang, J., Li, X., Yang, R., Yu, X., Yu, C., Qian, Y., et al. (2015). Susceptibility-weighted imaging manifestations in the brain of Wilson's disease patients. *PLoS One* 10:e0125100. doi: 10.1371/journal.pone.0125100
- Zaino, D., Chiarotti, I., Battisti, C., Salvatore, S., Federico, A., and Cerase, A. (2019). Six-year clinical and MRI quantitative susceptibility mapping (QSM) follow-up in neurological Wilson's disease under zinc therapy: a case report. *Neurol. Sci.* 40, 199–201. doi: 10.1007/s10072-018-3557-1
- Zou, L., Song, Y., Zhou, X., Chu, J., and Tang, X. (2019). Regional morphometric abnormalities and clinical relevance in Wilson's disease. *Mov. Disord.* 34, 545–554. doi: 10.1002/mds.27641

Conflict of Interest: The authors declare that the research was conducted in the absence of any commercial or financial relationships that could be construed as a potential conflict of interest.

Copyright © 2020 Yuan, Li, Chen, Li and Wang. This is an open-access article distributed under the terms of the Creative Commons Attribution License (CC BY). The use, distribution or reproduction in other forums is permitted, provided the original author(s) and the copyright owner(s) are credited and that the original publication in this journal is cited, in accordance with accepted academic practice. No use, distribution or reproduction is permitted which does not comply with these terms.



Multi-Echo Quantitative Susceptibility Mapping for Strategically Acquired Gradient Echo (STAGE) Imaging

Sara Gharabaghi^{1,2}, Saifeng Liu³, Ying Wang^{3,4}, Yongsheng Chen⁵, Sagar Buch⁴, Mojtaba Jokar², Thomas Wischgoll¹, Nasser H. Kashou⁶, Chunyan Zhang⁷, Bo Wu⁸, Jingliang Cheng⁷ and E. Mark Haacke^{2,3,4,5,9*}

¹ Department of Computer Science and Engineering, Wright State University, Dayton, OH, United States, ² Magnetic Resonance Innovations, Inc., Bingham Farms, MI, United States, ³ The MRI Institute for Biomedical Research, Bingham Farms, MI, United States, ⁴ Department of Radiology, Wayne State University, Detroit, MI, United States, ⁵ Department of Neurology, Wayne State University, Detroit, MI, United States, ⁶ Department of Biomedical, Industrial and Human Factors Engineering, Wright State University, Dayton, OH, United States, ⁷ Department of MRI, The First Affiliated Hospital of Zhengzhou University, Zhengzhou, Henan, China, ⁸ Shanghai Zhu Yan Medical Technology Ltd., Shanghai, China, ⁹ Department of Biomedical Engineering, Wayne State University, Detroit, MI, United States

OPEN ACCESS

Edited by:

Tolga Cukur,
Bilkent University, Turkey

Reviewed by:

David Rudko,
McGill University, Canada
Yi Zhang,
Zhejiang University, China
Thanh D. Nguyen,
Cornell University, United States

*Correspondence:

E. Mark Haacke
nmrimaging@aol.com

Specialty section:

This article was submitted to
Brain Imaging Methods,
a section of the journal
Frontiers in Neuroscience

Received: 14 July 2020

Accepted: 16 September 2020

Published: 23 October 2020

Citation:

Gharabaghi S, Liu S, Wang Y,
Chen Y, Buch S, Jokar M, Wischgoll T,
Kashou NH, Zhang C, Wu B, Cheng J
and Haacke EM (2020) Multi-Echo
Quantitative Susceptibility Mapping
for Strategically Acquired Gradient
Echo (STAGE) Imaging.
Front. Neurosci. 14:581474.
doi: 10.3389/fnins.2020.581474

Purpose: To develop a method to reconstruct quantitative susceptibility mapping (QSM) from multi-echo, multi-flip angle data collected using strategically acquired gradient echo (STAGE) imaging.

Methods: The proposed QSM reconstruction algorithm, referred to as “structurally constrained Susceptibility Weighted Imaging and Mapping” scSWIM, performs an ℓ_1 and ℓ_2 regularization-based reconstruction in a single step. The unique contrast of the T1 weighted enhanced (T1WE) image derived from STAGE imaging was used to extract reliable geometry constraints to protect the basal ganglia from over-smoothing. The multi-echo multi-flip angle data were used for improving the contrast-to-noise ratio in QSM through a weighted averaging scheme. The measured susceptibility values from scSWIM for both simulated and *in vivo* data were compared to the: original susceptibility model (for simulated data only), the multi orientation COSMOS (for *in vivo* data only), truncated k-space division (TKD), iterative susceptibility weighted imaging and mapping (iSWIM), and morphology enabled dipole inversion (MEDI) algorithms. Goodness of fit was quantified by measuring the root mean squared error (RMSE) and structural similarity index (SSIM). Additionally, scSWIM was assessed in ten healthy subjects.

Results: The unique contrast and tissue boundaries from T1WE and iSWIM enable the accurate definition of edges of high susceptibility regions. For the simulated brain model without the addition of microbleeds and calcium, the RMSE was best at 5.21ppb for scSWIM and 8.74ppb for MEDI thanks to the reduced streaking artifacts. However, by adding the microbleeds and calcium, MEDI’s performance dropped to 47.53ppb while scSWIM performance remained the same. The SSIM was highest for scSWIM (0.90) and then MEDI (0.80). The deviation from the expected susceptibility in deep gray matter structures for simulated data relative to the model (and for the *in vivo* data relative to COSMOS) as measured by the slope was lowest for scSWIM + 1%(–1%); MEDI + 2%(–11%) and then iSWIM –5%(–10%). Finally, scSWIM measurements in the basal ganglia of healthy subjects were in agreement with literature.

Conclusion: This study shows that using a data fidelity term and structural constraints results in reduced noise and streaking artifacts while preserving structural details. Furthermore, the use of STAGE imaging with multi-echo and multi-flip data helps to improve the signal-to-noise ratio in QSM data and yields less artifacts.

Keywords: quantitative susceptibility mapping (QSM), constrained image reconstruction, gradient recalled echo (GRE) phase data, ill-posed inverse problem, strategically acquired gradient echo (STAGE) imaging

INTRODUCTION

Magnetic resonance imaging (MRI) offers many different contrast mechanisms. Today, it is possible to obtain magnetic susceptibility maps, $\chi(\vec{r})$, of the human brain (and other parts of the body) that show the underlying tissue susceptibility distribution. Quantitative susceptibility mapping (QSM) data are reconstructed from phase information, which represents the magnetic field variations caused by the magnetization of an object in the presence of an external magnetic field (Haacke et al., 2015). The resulting susceptibility maps can be used to assess bleeding (Bilgic et al., 2012), calcium deposits (Deistung et al., 2013; Chen et al., 2014) and oxygen saturation (Haacke et al., 2010). The knowledge of the susceptibility source and the quantity of either iron or calcium can help improve the diagnosis of neurodegenerative diseases such as multiple sclerosis, Parkinson's disease, stroke, Sturge-Weber syndrome and traumatic brain injury (Haacke et al., 2015) to name a few.

Extracting the susceptibility, χ , from Gradient Recalled Echo (GRE) phase data is an ill-posed problem because the dipole kernel has zeroes along a conical surface and, therefore, under-samples k-space (Haacke et al., 2015). Many studies have attempted to solve this problem. A fast and direct method to reconstruct χ is the Thresholded K-space Division (TKD) approach (Wharton et al., 2010) that uses a threshold to ignore the smaller values near the zeroes in the inversion process. However, the TKD reconstructed susceptibility map suffers from streaking artifacts and underestimates χ . An alternative approach referred to as iterative Susceptibility Weighted Imaging and mapping (iSWIM) has been used to fill in the missing parts of k-space to overcome these artifacts (Tang et al., 2013). This was accomplished by constraining the susceptibility values in regions with high susceptibility. However, the final images are still noisy in regions of uniform susceptibility. A better approach, in theory, but one that requires multiple scans, is the Calculation Of Susceptibility through Multiple Orientation Sampling (COSMOS) (Liu et al., 2009). This method utilizes the phase images from multiple orientations to stabilize the inversion process and remove the singularities by weighted linear least squares. This method is usually used as a gold standard in the evaluation of any QSM reconstruction method.

A number of other approaches use regularization techniques with different *a priori* information to reconstruct the susceptibility. Although, these methods are computationally more expensive than TKD approaches, the reconstruction times are still reasonable, and they are designed to smooth over regions that have homogeneous susceptibilities. For example, morphology enabled dipole inversion (MEDI) exploits the

structural consistency between χ and the magnitude image in the form of an ℓ_1 -norm (Liu et al., 2012). However, this constraint can cause errors in regions where there are inconsistencies between the magnitude images and the susceptibility maps. Homogeneity Enabled Incremental Dipole Inversion (HEIDI) (Schweser et al., 2012) is another method that uses structural information from both magnitude and phase images to correct this issue. An alternative approach, structural feature based collaborative reconstruction (SFCR) (Bao et al., 2016), argues that the edge information from either magnitude or phase images does not reflect all the structural features in χ and the reconstructed image suffers from over-smoothed edges. The key steps in this approach are to include a structural feature-based ℓ_1 -norm constraint and a voxel fidelity-based ℓ_2 -norm constraint. This allows both edges and small objects to be recovered while still minimizing artifacts. Furthermore, most of these methods find the total field through a linear fitting of multi-echo phase data. However, the inclusion of long echo times can lead to blooming artifact, an increase in signal loss at the edges of the object and, potentially, an underestimation of χ .

Strategically acquired gradient echo imaging (STAGE) is a rapid multi-contrast multi-parametric imaging approach that employs two fully flow compensated double-echo GRE scans using low and high flip angles (FAs) relative to the Ernst angle of white matter. It provides not only a variety of qualitative images such as the T1weighted enhanced (T1WE) image, but also provides multiple quantitative information such as R_2^* , T1, and susceptibility maps (Chen et al., 2018b; Wang et al., 2018; Haacke et al., 2020). The T1WE image is generated from the combination of two GRE scans with low and high FAs (Chen et al., 2018b) where the radiofrequency (RF) transmit field variation is corrected (Wang et al., 2018). When compared with conventional T1W or T2*W images, the T1WE images derived from STAGE have improved contrast between cortical gray matter and white matter, and between deep gray matter and white matter (Chen et al., 2018b). The improved contrast in the T1WE image benefits structural segmentation. STAGE has also become more broadly tested for a number of neurodegenerative diseases (Haacke et al., 2020). Therefore, in this study, we propose a “structurally constrained Susceptibility Weighted Imaging and Mapping” (scSWIM) method that reconstructs the susceptibility using multiple echo, multiple flip angle STAGE data. Similar to SFCR, scSWIM utilizes the structural information from both magnitude data and the susceptibility maps but in a single step. The scSWIM approach specifically uses the enhanced contrast available in STAGE imaging to define prior information about the edges of the white matter and gray matter. In this paper, we

introduce scSWIM, evaluate it on simulated data and test it on *in vivo* brain data.

MATERIALS AND METHODS

Calculating the Susceptibility From an L1 and L2 Norm Cost Function

Based on Maxwell's equations, the relationship between the phase image $\varphi(r)$ (obtained from a 3D GRE imaging approach) and susceptibility $\chi(r)$ in ppm (parts per million) can be written as (Haacke and Reichenbach, 2011):

$$\varphi(r) = \gamma B_0 TE F^{-1} \{D(k) F\{\chi(r)\}\}, \quad (1)$$

where r , B_0 and TE are the voxel position vector in image domain, the main magnetic field strength (in T) and the echo time, respectively; $\gamma = 2.675 \times 10^8 \text{ rad/s/T}$ is the gyromagnetic ratio; F and F^{-1} denote the Fourier and inverse Fourier transform operators, respectively; and $D(k)$ is the Fourier transform of the unit dipole kernel at the position $k = [k_x, k_y, k_z]$ in k -space and is defined as:

$$D(k) = \frac{k_x^2 + k_y^2 - 2k_z^2}{3(k_x^2 + k_y^2 + k_z^2)} = \frac{1}{3} - \frac{k_z^2}{|k|^2}. \quad (2)$$

The objective function of scSWIM is similar to the S-step of SFCR (Bao et al., 2016) with changes in constraint definitions and is given as:

$$f(\chi(r)) = \frac{1}{2} \|W(r) (F^{-1}D(k) F\chi(r) - \delta B(r))\|_2^2 + \lambda_1 \|P(r)G\chi(r)\|_1 + \frac{\lambda_2}{2} \|R(r)\chi(r)\|_2^2, \quad (3)$$

and the final solution for the susceptibility is given by:

$$\chi_{\text{scSWIM}}(r) = \underset{\chi(r)}{\operatorname{argmin}} f(\chi(r)), \quad (4)$$

where $\delta B(r) = \varphi(r)/(\gamma B_0 TE)$ and W in the data fidelity term is a weighting matrix proportional to the image magnitude that defines the reliability of the magnetic field shift for each voxel and G denotes the gradient operator.

In the S-step of the SFCR method, the edge matrix, P , is a binary mask that is derived from the initial susceptibility, $\hat{\chi}$ (where for convenience we have now dropped the dependence on r). This initial $\hat{\chi}$ (which is reconstructed from the first regularized minimization step of the SFCR, called the M-step) is based on an objective function that is similar to Eq. [3] but its constraints are based on the magnitude image. Also, R in the S-step of the SFCR method is a fidelity mask where voxels with high signal-to-noise ratio (SNR) are mapped to zero, low SNR to one and voxels corresponding to susceptibility artifact to two. However, the choice of R , P and the starting input are different for scSWIM as described below.

In scSWIM, we replaced the SFCR first regularized minimization (M-step) with iSWIM (Tang et al., 2013) since it

has no smoothing, provides an initial susceptibility map with sharp vessels and the reconstruction times are short. Then, in the l_1 regularization term of Eq. [3], we used the edge matrix, P , which is the binary mask that is derived from the product of the thresholded gradients of the T1WE image, P_{T1WE} , and the initial susceptibility map, $P_{\hat{\chi}}$:

$$P_{\text{T1WE},i} = \begin{cases} 0, & |G_i \rho| \geq \mu_1 \\ 1, & |G_i \rho| < \mu_1 \end{cases} \quad \text{and} \quad P_{\hat{\chi},i} = \begin{cases} 0, & |G_i \hat{\chi}| \geq \mu_2 \\ 1, & |G_i \hat{\chi}| < \mu_2 \end{cases}, \quad (5)$$

where G_i denotes the gradient operator, i is an indicator to the x , y or z directions, and ρ denotes the T1WE image. Both μ_1 and μ_2 are threshold values chosen to be 2.5 times the noise level of the derivatives of ρ and $\hat{\chi}$, respectively, in order to maintain the edges of the gray/white matter, veins and other structures in the brain. Essentially, P_{T1WE} excludes the edges of the white matter and gray matter and $P_{\hat{\chi}}$ excludes the edges of the vessels and basal ganglia including the globus pallidus (GP), caudate nucleus (CN), putamen (PT), thalamus (THA), substantia nigra (SN), and red nucleus (RN) and $P = P_{\text{T1WE}} \times P_{\hat{\chi}}$.

In the l_2 regularization term, we have used a structural matrix R to protect voxels in the regions of high susceptibility, such as veins and basal ganglia structures, from being over-smoothed while still smoothing other regions. The matrix R is generated from the normalized T1WE image excluding the regions detected in the R_{DGM} (where DGM stands for "deep gray matter") and $R_{\hat{\chi}}$ masks defined next. The R_{DGM} mask is calculated using an atlas-based segmentation method developed in-house (Wang et al., 2019). This method segments the deep gray matter structures from the high flip angle magnitude image (T1W), initial susceptibility map $\hat{\chi}$ and STAGE T1 weighted data and T1 maps. The $R_{\hat{\chi}}$ mask is generated from the method used in Tang et al. (2013) by applying a threshold to the homodyne filtered $\hat{\chi}$ map. Finally, the constants λ_1 and λ_2 are found using the L-curve approach (Hansen and O'Leary, 1992).

The single-echo scSWIM approach just described was then adopted to handle the multiple echo, multiple flip angle STAGE data. For this purpose, iSWIM was used as the initial input into scSWIM for the low flip angle, short echo data ($\text{FA}_L \text{TE}_1$). Then for the other three echoes ($\text{FA}_H \text{TE}_1$, $\text{FA}_L \text{TE}_2$, and $\text{FA}_H \text{TE}_2$), the reconstructed scSWIM from the previous echo was used as the initial guess for processing the scSWIM of the next echo. Finally, an averaged scSWIM was generated by an R_2^* -based weighted average of the individual echo scSWIMs (χ_i):

$$\chi = \sum_i w_i^2 \chi_i / \sum_i w_i^2, \quad (6)$$

where $w_i = TE_i e^{-TE_i R_2^*}$ and R_2^* is from the STAGE data and is created from averaging the R_2^* maps from each of the flip angle images (Chen et al., 2018b; Wang et al., 2018):

$$R_2^* = \frac{1}{TE_1 - TE_2} \ln(\rho_2/\rho_1), \quad (7)$$

where ρ_1 and ρ_2 are the magnitudes of the first (TE_1) and second (TE_2) echoes, respectively.

This multi-echo approach has three advantages: first, each echo can be reviewed; second, the weighted scSWIM will have a better SNR; and third, loss of tissues associated with the use of a phase quality control map (especially at longer echoes) will be, to a large degree, replaced with the shorter echo scSWIM value. This weighting automatically ensures that wherever there is a measured susceptibility from one echo it will contribute to the final QSM result (while echoes with zeroes will not make a contribution). **Figure 1** shows the block diagram of the proposed multi-echo, multi-flip angle scSWIM processing steps for STAGE.

Simulated Data

The 3D isotropic susceptibility model developed in this laboratory (Buch et al., 2012) was used to test the algorithm. This model includes the general structures of the human brain such as gray matter (GM), white matter (WM), basal ganglia and midbrain structures [PT, GP, CN, THA, RN, SN, and crus cerebri (CC)], cerebrospinal fluid (CSF) and the major veins. The susceptibility values for these structures are summarized in the first row of **Table 1**.

To test the performance of the reconstruction in the presence of cerebral microbleeds (CMB) or calcium deposits (CaD), two spherical objects with susceptibility values (radius) of 1000 ppb (5 mm) and 3000 ppb (3 mm), respectively, were added to the frontal white matter and two spherical objects with susceptibility values of -1000 ppb (5 mm) and -3000 ppb (3 mm) were added to the posterior white matter. Additionally, one spherical object with a radius of 3 mm with a susceptibility of -3000 ppb was added to the model to mimic the pineal gland (PG). The values for CMBs were taken from our experience in the field of traumatic brain injury and stroke where we usually see CMBs with susceptibilities as large as 1000 ppb but on occasion higher values up to 2000 ppb and 3000 ppb have been seen so we used both 1000 ppb and 3000 ppb to test the metal of the method. For the CaD, the values are around -3000 ppb but can range lower and slightly higher than this as the calcium is highly diamagnetic (Buch et al., 2015).

This final susceptibility model, χ_{ideal} , was used to generate the magnitude and phase images using the STAGE imaging parameters: $FA = 6^\circ/24^\circ$, $TE_1 = 7.5/8.75\text{ms}$, $TE_2 = 17.5/18.75\text{ms}$, and $TR = 25\text{ms}$. The phase images were simulated from the forward model in Equations [1] and [2] at $B_0 = 3\text{T}$. To

TABLE 1 | Susceptibility, T_1 relaxation time, and relative proton density (ρ_0) values for different structures in the simulated brain model.

	WM	GM	GP	PT	THA	CN	SN	RN	CC	V	VNT/CSF
χ (ppb)	0	20	180	90	10	60	160	130	-30	450	-14
T_1 (ms)	837	1607	888	1140	1218	1226	1147	833	780	1932	4163
ρ_0	0.73	0.80	0.72	0.82	0.79	0.82	0.79	0.80	0.79	0.85	1.00

WM, white matter; GM, gray matter; GP, Globus Pallidus; PT, Putamen; THA, Thalamus; CN, Caudate Nucleus; SN, Substantia Nigra; RN, Red Nucleus; CC, Crus Cerebri; V, Veins; VNT, Ventricles; CSF, Cerebrospinal Fluid; and ppb, parts per billion.

create the magnitude images, first an $R2^*$ map was generated from χ_{ideal} using the relationship $R2^* = 20/s + 0.125\chi$ (Ghassaban et al., 2019b) assuming $R2^* = 40/s$ for CMB, PG, and CaD objects. Then, the magnitude image was calculated using the Ernst equation (Brown et al., 2014). The proton density and T_1 relaxation times for different brain structures are summarized in **Table 1** while they are assumed to be zero for CMB, PG, and CaD objects. These values were adopted from the literature (Lee et al., 2006; Brown et al., 2014) or manually measured from the *in vivo* STAGE PD-map and T_1 -map.

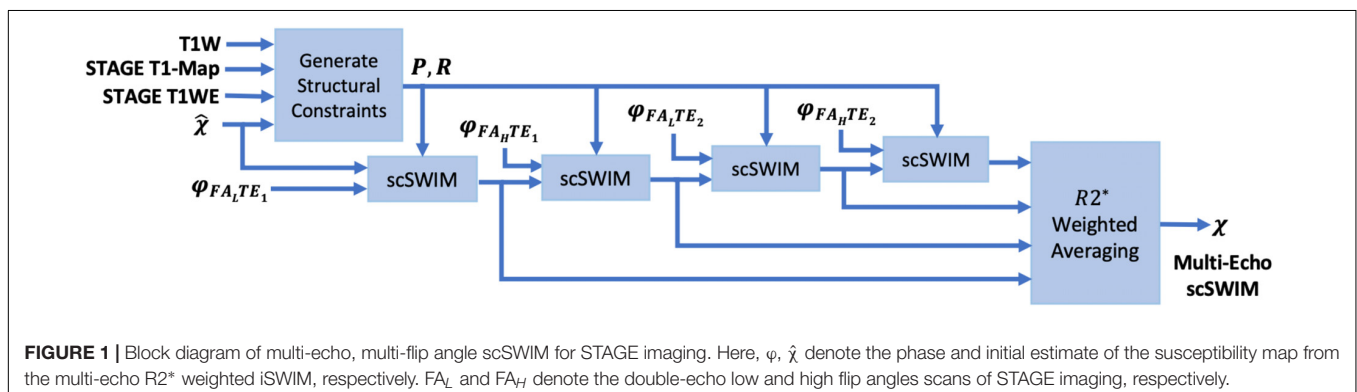
Finally, Gaussian noise was added to the complex signal to produce an SNR of 10:1. The reconstructed susceptibility map using the proposed method was compared with the TKD, iSWIM, and MEDI methods. The original simulated susceptibility model (χ_{ideal}) was used as the gold standard to measure the performance of each method using RMSE and SSIM as measures of goodness of fit (Wang et al., 2004) where SSIM = 1 corresponds to the perfect structural similarity while SSIM = 0 indicates no similarity between the two images.

In vivo Data

The proposed scSWIM method was tested on two sets of *in vivo* datasets that are discussed below. All subjects involved in this study signed a consent form to be part of this IRB approved research.

Single Test Case Including COSMOS

The *in vivo* MRI data for this single test case was acquired from a 29-year old male volunteer on a 3T Siemens scanner (Siemens Healthcare, Erlangen, Germany) at Wayne State University. The imaging parameters were: 6° and 24° for



the low and high flip angle scans with $TR = 25$ ms, $TE_1 = 6.5/7.5$ ms, $TE_2 = 17.5/18.5$ ms, bandwidth: 277 Hz/pixel, and GRAPPA = 2. The matrix size, voxel resolution, and FOV were $384 \times 288 \times 104$, $0.67 \times 0.67 \times 1.33$ mm³, and $256 \times 192 \times 139$ mm³, respectively. The total scan time for the high-resolution STAGE is about 10 min. For the purpose of generating COSMOS, two additional orientations with the same imaging parameters were collected for this subject. The reconstructed susceptibility map using the proposed scSWIM method was compared with those from the TKD, iSWIM and MEDI methods and compared to COSMOS as the reference image.

Evaluation on a Set of Healthy Human Subjects

Additionally, we tested scSWIM for ten healthy subjects acquired using a Siemens 3T Prisma scanner with lower resolution compared to the above-mentioned *in vivo* case. The imaging parameters were the same for the sample used above in the simulated data except the matrix size, voxel resolution, and FOV were $384 \times 144 \times 64$, $0.67 \times 1.33 \times 2$ mm³ (interpolated to $0.67 \times 0.67 \times 2$ mm³) and $256 \times 192 \times 128$ mm³, respectively, $TE_1 = 7.5/8.5$ ms, and a bandwidth of 240 Hz/pixel. The total scan time for this resolution is about 5 min.

Data Pre-processing

The entire processing pipeline was implemented in MATLAB (The Mathworks, Inc., Natick, MA, United States) on a workstation with Windows 10, Intel CPU i7-3770 with 4 cores and 16GB RAM. The phase image was first unwrapped using the bootstrapping (Chen et al., 2018a) and quality guided 3D phase unwrapping (Abdul-Rahman et al., 2007) methods in the simulated and *in vivo* data, respectively.

For the *in vivo* data, the induced background field from the air/tissue interfaces was removed from the unwrapped phase using the Sophisticated Harmonic Artifact Reduction for Phase data (SHARP) algorithm (Schweser et al., 2011) with a kernel size of 6 pixels. Next, the brain mask for the *in vivo* data was extracted from the magnitude images using BET (Brain Extraction Tool) (Smith, 2002). Finally, the resulting phase was zero-padded symmetrically in the spatial domain to a matrix size of $256 \times 256 \times 256$ or $512 \times 512 \times 512$ for simulated and *in vivo* datasets, respectively.

Susceptibility Map Reconstruction

In Eq. [3], the parameters λ_1 and λ_2 were determined by plotting the measured residual errors of the data fidelity and the two regularization terms for each of the individual STAGE scans using the L-curve method (Hansen and O'Leary, 1992). In theory, λ_1 controls the spatial smoothness and λ_2 helps to preserve the high susceptibility regions and small objects such as vessels from being over-smoothed. As mentioned in section "Calculating the Susceptibility From an L1 and L2 Norm Cost Function," an atlas-based segmentation method developed in-house (Wang et al., 2019) was used to generate the R_{DGM} mask. This method provided the labeled mask segmenting the right and left subcortical deep gray matter structures from the T1W, STAGE T1WE, T1 map, and $\hat{\chi}$. This labeled mask was carefully

reviewed and if needed fine-tuned manually (this was done on 3 cases for the GP and SN structures which sometimes were smaller than what would have been drawn manually). If these regions had not been corrected, the algorithm would have smoothed that part of the GP not protected. Finally, the R_{DGM} mask is generated from binarizing the labeled mask.

Several algorithms were chosen to compare with scSWIM, including TKD, iSWIM, and MEDI. In generating the MEDI results, a regularization parameter of 250 (350) was used for the simulated (*in vivo*) data. For TKD processing, a threshold of 0.1 was used and iSWIM was performed with 4 iterations. All of these parameters were adjusted to give the lowest RMSE. Additionally, COSMOS was used as the gold standard for the *in vivo* data. Multi orientation images for the COSMOS data were co-registered using ANTs (Avants et al., 2009, 2012). In the TKD, iSWIM, and scSWIM methods, the final multiple echo, multiple flip angle QSM data were generated using a multi-echo R_2^* -based weighted averaging of the individual QSM images from each echo and each flip angle data. In MEDI, the final QSM was generated by averaging the reconstructed QSM images from the fitted phases in each of the multi-echo low and high flip angle scans.

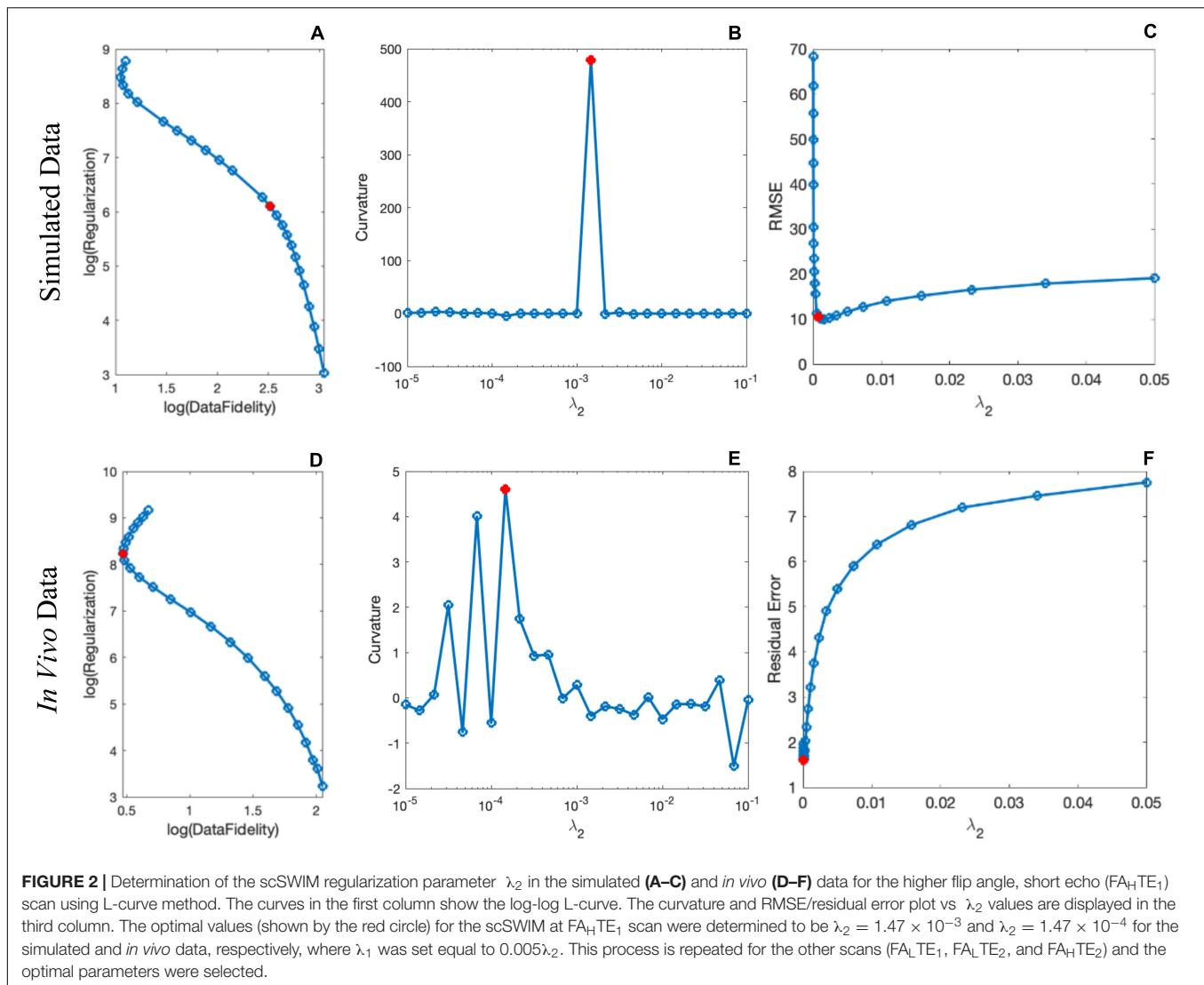
Quantitative Analysis for Susceptibility Map

For the quantitative analysis of the data, the susceptibility mean and standard deviation were found from the entire 3D structure of interest. In the simulated model, all the structures of interest were measured automatically (since we know the location of each structure). For the *in vivo* data, the susceptibility of the midbrain structures were also automatically measured since they have been determined in creating the R_{DGM} masks for the boundaries of these structures as described earlier. On the other hand, the susceptibility of the CSF, WM, and major veins [SSV and internal cerebral vein (ICV)] were measured manually by tracing the ROIs on the QSM data using SPIN (SpinTech, Inc., Bingham Farms, MI, United States). The manual tracing was performed in the axial view for CSF and WM, but veins were traced in the sagittal view for easier localization. A linear regression model was used to compare the measured susceptibility values from each reconstruction method with those from the susceptibility model and COSMOS to assess the accuracy of midbrain structures in the simulated and *in vivo* data, respectively.

RESULTS

Simulated Data

By comparing the P and R masks for the simulated data (discussed in Section "Simulated Data") and also the first and second regularization terms, and for the purpose of bringing the two terms to the same order, we set $\lambda_1 = 0.005\lambda_2$. This is further reviewed in the Discussion section. Based on this assumption and simulations in the human brain model, $\lambda_2 = \{6.81, 1.47, 3.16, 1.00\} \times 10^{-3}$ provided the best results in terms of residual errors for the four different scans ($FA_L TE_1$, $FA_H TE_1$, $FA_L TE_2$, and $FA_H TE_2$), respectively (see **Figures 2A–C** for $FA_H TE_1$). A comparison of scSWIM with TKD, iSWIM, and



MEDI along with their absolute errors and structural similarity maps relative to the simulation model are shown in **Figure 3**. In the simulated data (**Figures 3A–C**), we have used the exact known edge and structural matrices from χ_{ideal} to create P_{ideal} (**Figure 3D**) and R_{ideal} (**Figure 3E**). The TKD results (**Figures 3F–J**) show severe streaking artifacts while the iSWIM results have much less streaking (**Figures 3K–O**). MEDI does an excellent job (**Figures 3P–T**) as does scSWIM (**Figures 3U–Y**) in reproducing the model with minimal artifacts and noise. In both these last two reconstructions, the streaking artifact is highly reduced compared to both TKD and iSWIM and the images look much better in terms of SNR. However, MEDI does not resolve the streaking artifact from the CMB, pineal gland, or calcified objects with higher susceptibility values.

In the simulated data with (or without) CMBs, PG and CaDs, the RMSE for TKD, iSWIM, MEDI, and scSWIM were 32.91 (22.09), 24.61 (18.21), 47.53 (8.74) and 5.01 (5.21) ppb, respectively. Also, the SSIM index was measured as 0.52 (0.59), 0.62 (0.63), 0.80 (0.86) and 0.90 (0.91) for TKD, iSWIM,

MEDI, and scSWIM, respectively, for these two conditions. Based on these results, scSWIM has the lowest error and the highest similarity to the model compared to the other methods. The measured susceptibility values in different structures are summarized in **Table 2** showing that the measured susceptibilities in the midbrain structures for both MEDI and scSWIM are closer to the expected susceptibilities in the model while scSWIM has smaller standard deviations. The measured susceptibilities of the straight sinus vein, calcium deposition and CMB objects show that scSWIM provides the most accurate results in these structures as well.

***In vivo* Data**

Based on the L-curve analysis using the single high resolution human *in vivo* data (discussed in Section “Single Test Case Including COSMOS”) and by assuming $\lambda_1 = 0.005\lambda_2$ for the purpose of bringing two regularization terms to the same scale, $\lambda_2 = \{1, 1.47, 1.00, 1.00\} \times 10^{-4}$ provided the best results in terms of residual errors for $FA_L TE_1$, $FA_H TE_1$, $FA_L TE_2$, and

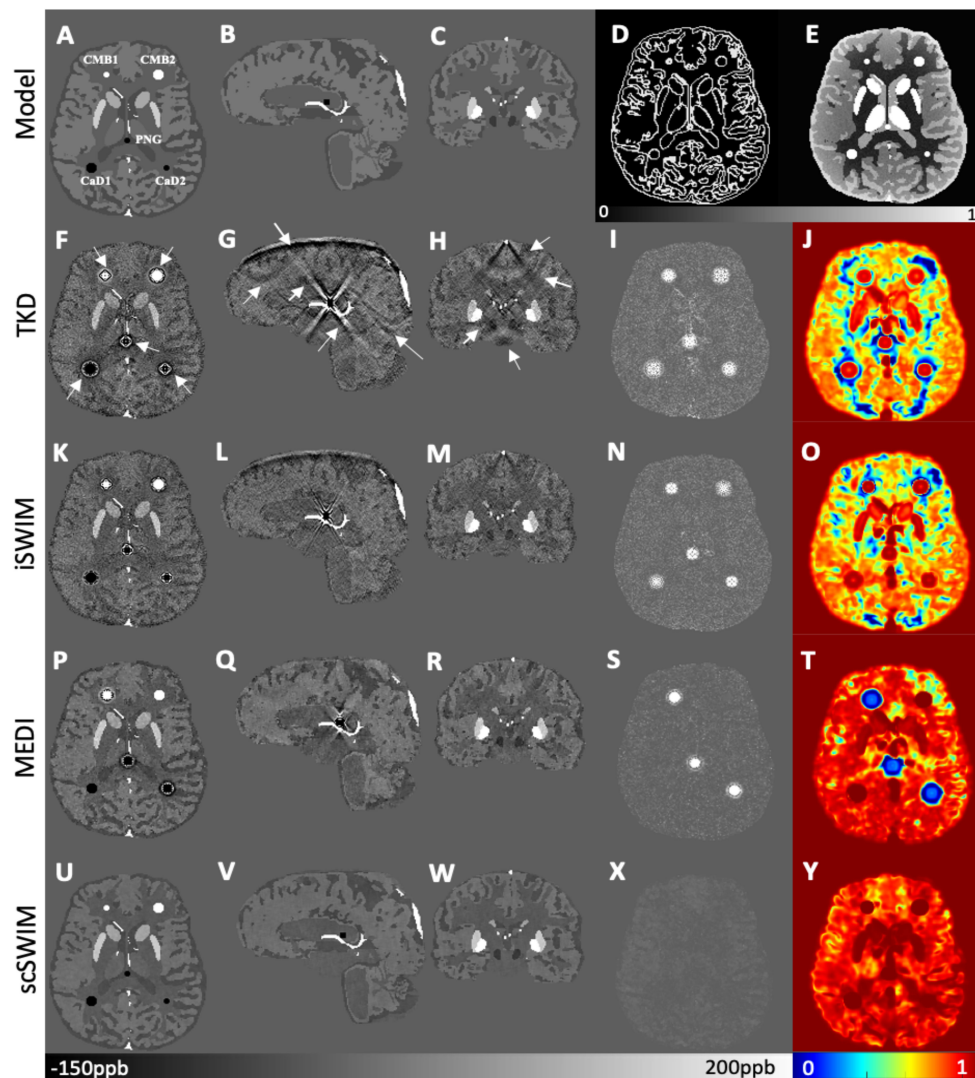


FIGURE 3 | Depiction of multi-echo, multi-flip angle QSM images using different methods for the simulated data. This figure shows the orthogonal views of the susceptibility model (A–C), and reconstructed QSM images from TKD (F–H), iSWIM (K–M), MEDI (P–R) and scSWIM (U–W) along with the scSWIM constraints P_{ideal} (D) and R_{ideal} (E). The cerebral microbleeds (CMB), pineal gland (PG) and calcium deposits (CaD) are labeled on the model (A). Streaking artifacts are indicated by the arrows. The last two columns show the corresponding susceptibility absolute error map (I, N, S, X) and structural similarity map (J, O, T, Y) for the different methods. In this simulated data, scSWIM provides better reconstruction with less artifacts, less error and higher similarity relative to the numerical model. Please note the complements of the P and R mask are shown in this figure (D, E) for better visualization.

FA_{HTE_2} , respectively (see Figures 2D–F). The structural terms used in the scSWIM cost function are illustrated in Figure 4. Specifically, Figures 4A–D show the edge and structural matrices P (includes P_x , P_y , and P_z) and R . The binary matrix P , excludes the extracted edges from the enhanced T1-weighted and initial susceptibility while the binary mask R excludes the deep gray matter structures, vessels and other high susceptibility regions (the complement of P and R masks are shown in the figure for better visualization). Figures 4E–H show the conventional T1-weighted (Figure 4E) and T1WE (Figure 4H) from STAGE and their corresponding extracted edges (final P representation of extracted edges in three directions). It can be seen visually that the contrast between gray matter and white matter of the T1WE

is higher than the conventional T1W image and its corresponding edge matrix, P_{T1WE} , provides more information about the edge.

Figure 5 shows three orthogonal views of the reconstructed multi-echo, multi-flip angle susceptibility images for this high-resolution human data set using the TKD (Figures 5A–C), iSWIM (Figures 5D–F), MEDI (Figures 5G–I), scSWIM (Figures 5J–L), and COSMOS (Figures 5M–O) methods. It can be seen in these images that scSWIM has less noise while the sharpness of the vessels and other brain structures are well-preserved. MEDI also provides a smooth reconstruction but in the regions that are close to the veins there are still some remaining artifacts. The measured susceptibility values in different structures are summarized in Table 3.

TABLE 2 | Measured susceptibility values (mean \pm standard deviation) in ppb for different structures in the reconstructed QSM images using TKD, iSWIM, MEDI, and scSWIM methods for the simulated human dataset along with the reference values.

Regions	TKD	iSWIM	MEDI	scSWIM	Model
CN-L	44.17 \pm 18.22	49.65 \pm 15.46	54.55 \pm 9.46	55.92 \pm 2.41	60.00
CN-R	44.19 \pm 18.67	49.19 \pm 15.24	53.74 \pm 9.94	55.42 \pm 2.23	60.00
GP-L	152.17 \pm 22.03	167.80 \pm 18.41	172.06 \pm 9.64	177.50 \pm 2.74	180.00
GP-R	151.02 \pm 20.65	166.44 \pm 17.05	174.20 \pm 9.93	175.94 \pm 2.39	180.00
PT-L	74.77 \pm 17.67	80.10 \pm 14.94	84.66 \pm 9.72	86.55 \pm 2.42	90.00
PT-R	74.80 \pm 17.78	78.84 \pm 15.10	85.90 \pm 9.28	85.51 \pm 2.57	90.00
THA-L	3.31 \pm 35.86	4.40 \pm 24.97	3.44 \pm 19.24	5.50 \pm 2.35	10.00
THA-R	2.48 \pm 30.50	3.36 \pm 19.63	2.67 \pm 14.17	5.11 \pm 2.36	10.00
WM	-7.43 \pm 14.35	-5.95 \pm 12.33	-5.44 \pm 7.31	-2.59 \pm 1.66	0.00
RN-L	95.66 \pm 36.19	129.41 \pm 22.95	133.49 \pm 10.63	131.22 \pm 2.32	130.00
RN-R	95.96 \pm 44.40	126.67 \pm 22.72	135.58 \pm 11.81	129.79 \pm 2.51	130.00
SN-L	158.49 \pm 32.41	151.66 \pm 24.95	158.15 \pm 11.43	159.16 \pm 3.98	160.00
SN-R	139.56 \pm 30.15	144.07 \pm 22.01	154.88 \pm 9.65	159.43 \pm 4.71	160.00
CC-L	-30.85 \pm 23.38	-28.67 \pm 17.24	-36.24 \pm 10.14	-31.28 \pm 2.45	-30.00
CC-R	-32.08 \pm 24.01	-26.41 \pm 18.83	-37.56 \pm 10.39	-30.50 \pm 2.36	-30.00
CSF	-20.74 \pm 19.21	-17.81 \pm 13.12	-33.31 \pm 11.31	-15.40 \pm 2.25	-14.00
SSV	420.43 \pm 61.28	447.76 \pm 23.11	442.70 \pm 12.95	450.83 \pm 2.52	450.00
V	369.52 \pm 85.28	408.74 \pm 58.89	446.65 \pm 48.29	446.90 \pm 4.33	450.00
CMB1	3604.8 \pm 709.84	2784.73 \pm 772.89	958.42 \pm 37.07	2992.54 \pm 2.68	3000.00
CMB2	837.13 \pm 97.45	922.31 \pm 83.85	990.91 \pm 12.36	995.58 \pm 1.26	1000.00
CaD1	-855.56 \pm 98.61	-970.63 \pm 85.75	-995.38 \pm 17.41	-1002.92 \pm 1.42	-1000.00
CaD2	-3617.62 \pm 715.04	-3914.88 \pm 770.67	-1084.43 \pm 8.72	-3002.70 \pm 2.30	-3000.00
PG	-3605.53 \pm 692.29	-3885.88 \pm 760.06	-1053.80 \pm 47.14	-2998.92 \pm 1.97	-3000.00

The susceptibilities for the left and right CN, GP, PT, THA, RN, SN, and CC were measured. CN, Caudate Nucleus; GP, Globus Pallidus; PT, Putamen; THA, Thalamus; WM, White Matter; RN, Red Nucleus; SN, Substantia Nigra; CC, Crus Cerebri; CSF, Cerebrospinal Fluid; SSV, Straight Sinus Vein; V, mean of all Veins; CMB, Cerebral Micro Bleed; CaD, Calcium Deposit; PG, Pineal Gland; L, Left; R, Right; and ppb, parts per billion unit.

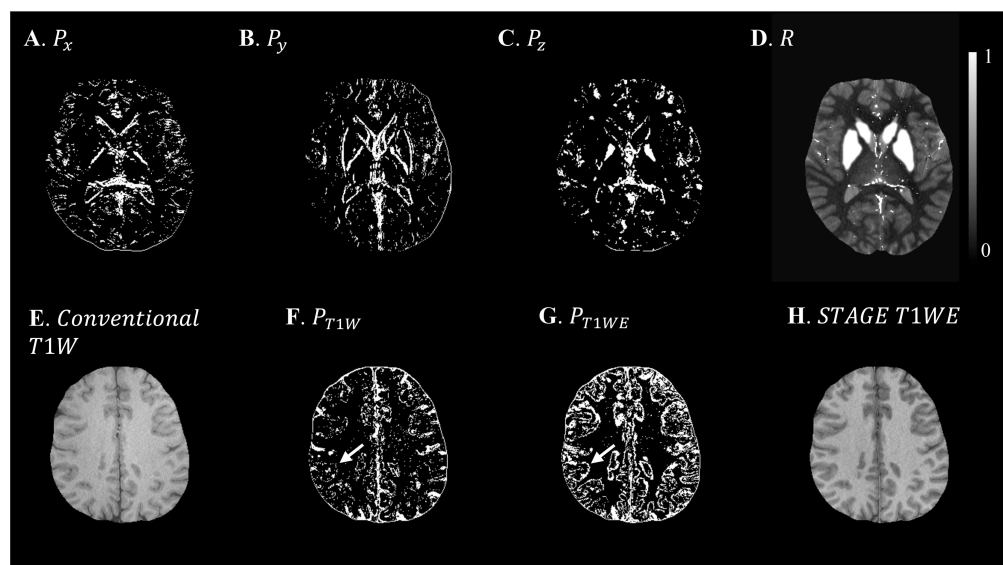


FIGURE 4 | Illustration of scSWIM constraints and comparison of constraints extracted from conventional T1W and STAGE T1WE for the single high-resolution *in vivo* data. The first row shows the scSWIM structural constraints for the single high-resolution *in vivo* data: edge matrix, P , in the x , y , and z directions (A–C), and the structural matrix, R (D). The second row shows the advantage of extracting the constraints from STAGE versus conventional GRE data: conventional T1W (G), STAGE T1WE (H), and the extracted edges (product of three directions) from conventional T1W (F) and STAGE T1WE (G). As seen, (G) provides more information about the white and gray matter edges (white arrow) and is less noisy than (F). Please note the complement of the P and R mask is shown in this figure for better visualization.

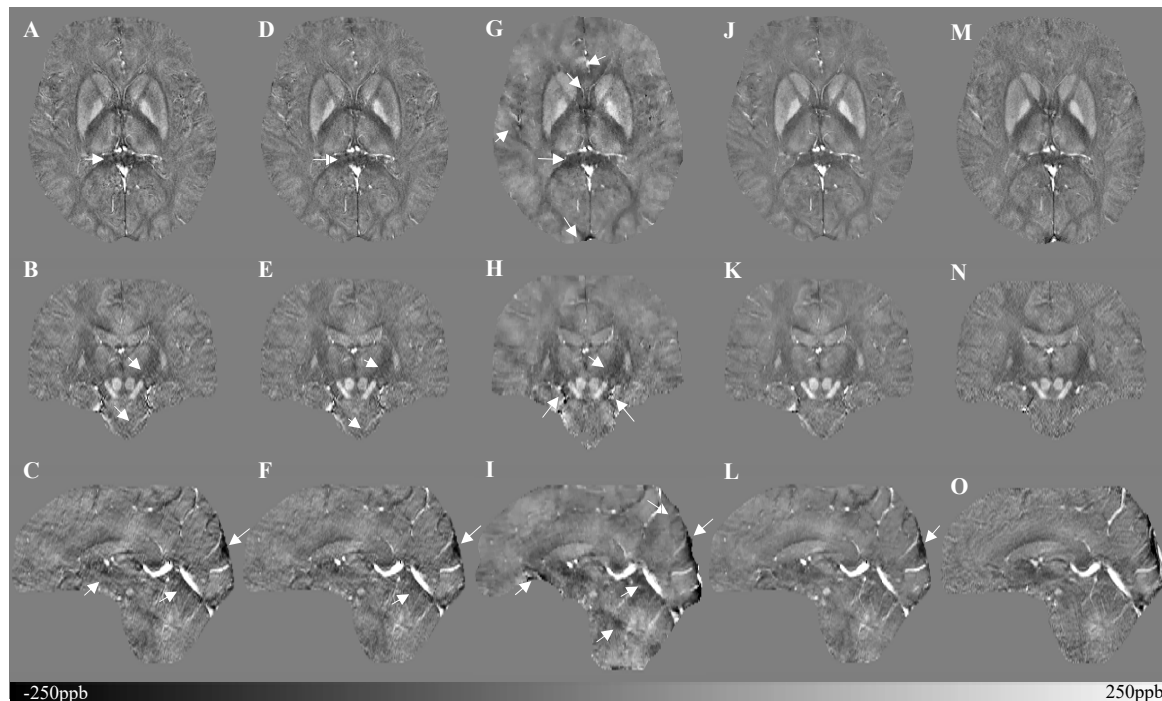


FIGURE 5 | Depiction of multi-echo, multi-flip angle QSM images using different methods for the single high-resolution *in vivo* data. This figure shows three orthogonal views of the reconstructed multi-echo, multi-flip angle susceptibility maps from TKD (A–C), iSWIM (D–F), MEDI (G–I), scSWIM (J–L), and COSMOS (M–O) for the single high-resolution *in vivo* data. All of the images are displayed with the same window/level settings. White arrows show streaking artifacts. The SNR and image quality are best in the scSWIM images while the sharpness of the vessels and other brain structures are preserved.

TABLE 3 | Measured susceptibility values (mean \pm standard deviation) in ppb for different structures in the reconstructed QSM images using TKD, iSWIM, MEDI, scSWIM, and COSMOS methods for the multi-echo, multi-flip angle in the single high-resolution *in vivo* data.

Regions	TKD	iSWIM	MEDI	scSWIM	COSMOS
CN-L	39.54 \pm 29.34	39.13 \pm 29.66	53.52 \pm 33.58	50.63 \pm 26.11	37.5 \pm 34.1
CN-R	39.87 \pm 29.36	38.11 \pm 29.32	47.85 \pm 28.98	51.95 \pm 24.38	38.2 \pm 32.5
GP-L	90.22 \pm 48.18	98.32 \pm 53.86	120.52 \pm 59.17	125.28 \pm 53.14	115.3 \pm 66.3
GP-R	90.67 \pm 42.59	98.92 \pm 48.95	115.29 \pm 43.19	123.89 \pm 45.48	111.3 \pm 55.0
PT-L	30.19 \pm 32.36	29.58 \pm 33.22	43.10 \pm 35.50	50.24 \pm 27.44	42.0 \pm 32.0
PT-R	29.37 \pm 32.43	29.31 \pm 33.08	33.89 \pm 34.56	47.45 \pm 30.06	36.43 \pm 32.95
THA-L	5.85 \pm 32.00	2.82 \pm 28.89	3.34 \pm 39.32	6.72 \pm 25.29	−1.89 \pm 38.25
THA-R	7.47 \pm 32.31	2.92 \pm 30.28	7.16 \pm 37.38	8.84 \pm 25.41	−2.49 \pm 38.77
RN-L	66.04 \pm 28.71	66.63 \pm 32.08	84.80 \pm 35.88	99.46 \pm 34.00	91.04 \pm 48.14
RN-R	101.68 \pm 35.38	113.07 \pm 43.18	114.85 \pm 39.88	120.85 \pm 39.22	95.18 \pm 53.17
SN-L	114.78 \pm 67.60	129.69 \pm 72.71	124.34 \pm 78.56	140.86 \pm 73.14	129.00 \pm 81.30
SN-R	111.97 \pm 58.00	124.66 \pm 69.93	127.47 \pm 69.16	147.67 \pm 69.67	144.25 \pm 79.86
DN-L	83.69 \pm 36.22	86.79 \pm 42.45	82.11 \pm 36.57	93.37 \pm 38.73	95.39 \pm 44.07
DN-R	74.97 \pm 35.69	82.21 \pm 40.28	63.23 \pm 39.63	92.17 \pm 38.63	84.70 \pm 47.20
SSV	424.62 \pm 43.73	422.32 \pm 43.65	395.39 \pm 50.01	411.93 \pm 42.46	404.95 \pm 38.53
ICV	281.52 \pm 59.40	298.13 \pm 54.02	302.49 \pm 54.77	326.07 \pm 53.94	316.82 \pm 67.50
CSF	16.96 \pm 28.67	20.83 \pm 26.19	26.65 \pm 25.56	28.40 \pm 22.33	18.54 \pm 43.16
WM	9.67 \pm 15.88	9.74 \pm 15.48	13.12 \pm 11.14	10.46 \pm 9.71	1.06 \pm 18.13

The susceptibilities for the left and right CN, PT, GP, RN, and SN were measured. CN, Caudate Nucleus; GP, Globus Pallidus; PT, Putamen; THA, Thalamus; RN, Red Nucleus; SN, Substantia Nigra; DN, Dentate Nucleus; SSV, Straight Sinus Vein; ICV, Internal Cerebral Vein; CSF, Cerebrospinal Fluid; WM, White Matter; L, Left; R, Right; and ppb, parts per billion unit.

The structural terms used in the scSWIM cost function for two selected healthy subjects with lower resolution data (discussed in Section “Evaluation on a Set of Healthy Human Subjects”) are illustrated in **Figure 6**. Here it can be seen that the edges are still well preserved with this *in vivo* STAGE approach. **Figure 7** shows the reconstructed multi-echo, multi-flip angle susceptibility

images using TKD (**Figures 7A,E**), iSWIM (**Figures 7B,F**), MEDI (**Figures 7C,G**) and scSWIM (**Figures 7D,H**) methods for two examples of this data. There are artifacts around the basal ganglia structures and larger veins in the TKD, iSWIM and MEDI (shown with white arrows). Furthermore, in the second slice (**Figures 7E–H**), the PG looks dilated in MEDI compared to the

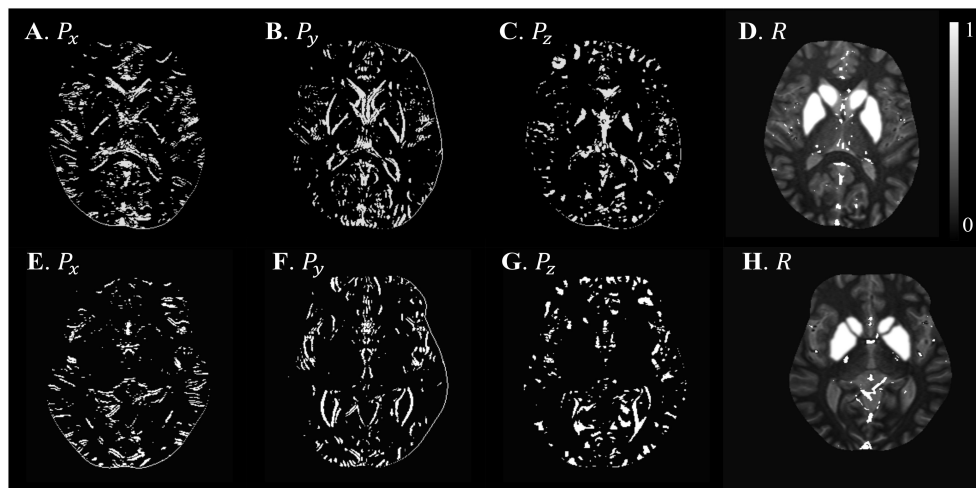


FIGURE 6 | Illustration of scSWIM structural constraints for the two healthy subjects from the low-resolution dataset. The scSWIM structural constraints, edge matrix, P , in the x , y , and z , and structural matrix, R , are shown for the low-resolution *in vivo* data from a 62-year old healthy subject (**A–D**) and a 54-year old healthy subject (**E–H**). Please note the complement of the P and R mask is shown in this figure for better visualization.

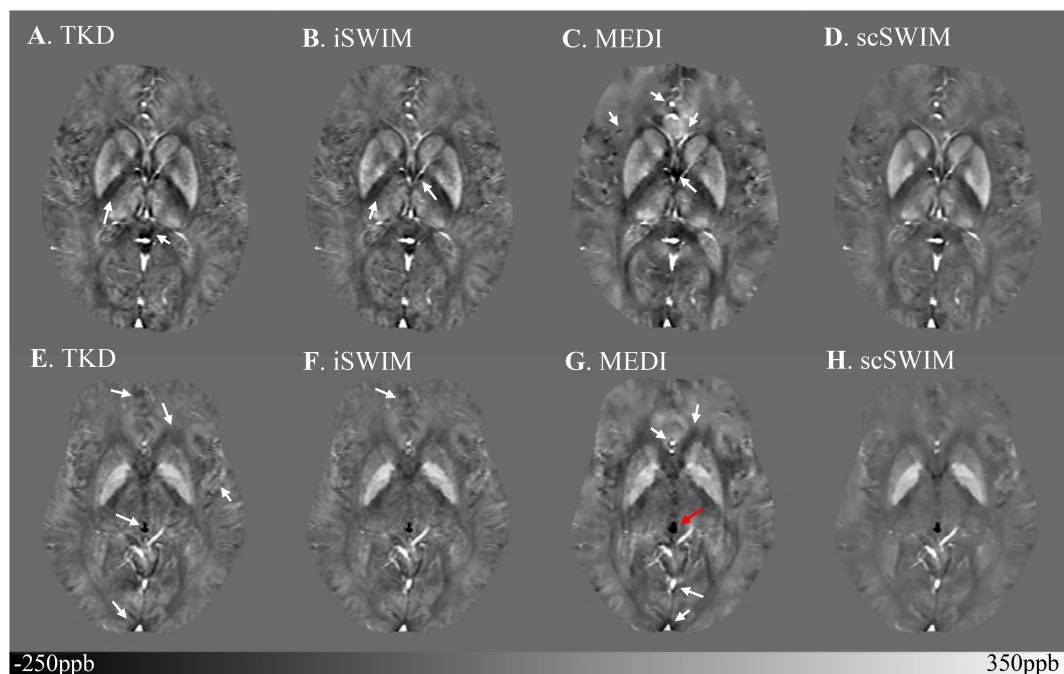


FIGURE 7 | Depiction of multi-echo, multi-flip angle QSM images using different methods for the two healthy subjects from the low-resolution dataset. Multi-echo, multi-flip angle susceptibility maps from TKD (**A,E**), iSWIM (**B,F**), MEDI ($\lambda = 350$) (**C,G**), and scSWIM (**D,H**) are shown for the two healthy subjects from **Figure 6**. The artifacts around the basal ganglia and larger veins in the TKD, iSWIM, and MEDI are shown by the white arrows. In the second row (**E–H**), the pineal gland looks dilated in MEDI compared to other methods (red arrow).

other methods (marked by a red arrow). **Table 4** summarizes the averaged measured susceptibility values (mean \pm standard deviation) in the reconstructed QSM images from the four different methods for the ten healthy subjects.

Figure 8 shows the correlation between the zero-referenced estimated susceptibility for deep gray matter structures from different reconstruction methods with the actual susceptibility from the numerical model for the simulated data and reconstructed COSMOS for the *in vivo* data. The measured CSF susceptibility for each method is used to zero-reference the

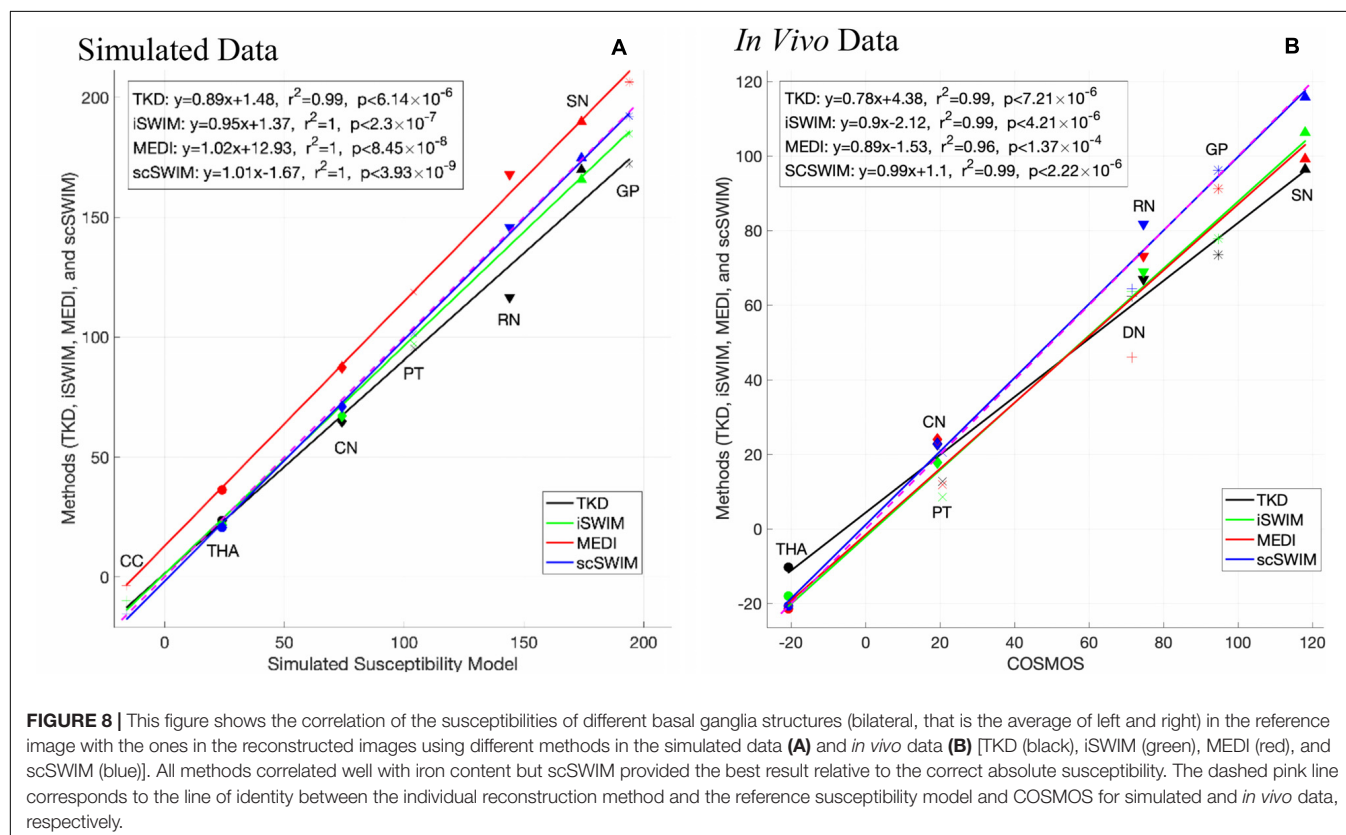
measurements. Among these methods, scSWIM (in blue color) has the closest values to the reference image in both datasets. The slope of scSWIM is 1.01(0.99) while TKD, iSWIM and MEDI are 0.89(0.78), 0.95(0.90), and 1.02(0.89) for simulated (and *in vivo*) data, respectively. The correlation coefficients in all methods are close to one and p-values to zero.

The current implementation of scSWIM for a single echo, converges in less than 3 and 5 iterations for the simulated and *in vivo* data, respectively. Each iteration consists of a minimization process that uses a preconditioned conjugate

TABLE 4 | Averaged susceptibility values (mean \pm standard deviation) in ppb for midbrain structures in the reconstructed QSM images using TKD, iSWIM, MEDI, and scSWIM for ten healthy subjects from the low-resolution *in vivo* dataset from a Siemens 3T PRISMA scanner.

Regions	TKD	iSWIM	MEDI	scSWIM	HC from Ghassaban et al. (2019a)
CN-L	45.84 \pm 9.05	44.22 \pm 9.92	59.10 \pm 13.33	52.77 \pm 9.16	52.4 \pm 7.6
CN-R	42.35 \pm 9.16	40.76 \pm 9.11	48.87 \pm 13.62	50.93 \pm 9.39	54.6 \pm 6.6
GP-L	105.63 \pm 16.15	118.45 \pm 19.04	115.97 \pm 20.53	129.13 \pm 19.69	127.8 \pm 7.8
GP-R	114.13 \pm 21.33	126.85 \pm 25.61	130.03 \pm 24.41	136.12 \pm 23.49	133.1 \pm 10.1
PT-L	52.56 \pm 17.32	54.82 \pm 19	54.05 \pm 19.39	68.71 \pm 20.84	72.8 \pm 7
PT-R	53.65 \pm 22.91	56.19 \pm 24.06	53.69 \pm 22.51	67.50 \pm 24.74	68.7 \pm 6.4
RN-L	99.82 \pm 21.34	109.65 \pm 27.26	98.26 \pm 17.49	111.51 \pm 16.62	102.9 \pm 12.9
RN-R	97.58 \pm 25.33	106.64 \pm 31.64	101.73 \pm 26.64	108.91 \pm 22.72	108.1 \pm 13.0
SN-L	111.57 \pm 14.12	123.87 \pm 17.91	122.62 \pm 11.74	128.05 \pm 6.67	127.5 \pm 10.8
SN-R	108.37 \pm 18.54	120.58 \pm 22.20	120.31 \pm 24.55	123.83 \pm 13.51	115.4 \pm 11.6

Also, the results from Ghassaban et al. (2019a) are summarized in the last column where the DGM structures are measured in both hemispheres in 24 healthy subjects from a GE 3T scanner. CN, Caudate Nucleus; GP, Globus Pallidus; PT, Putamen; RN, Red Nucleus; SN, Substantia Nigra; L, Left; R, Right; and ppb, parts per billion unit.



gradient solver. For the zero-padded *in vivo* data with a matrix size of $512 \times 512 \times 128$, the total processing time for each single-echo scSWIM is currently 2~5 minutes depending on the number of iterations using a Windows 10, Intel CPU i7-3770 with 4 cores and 16GB RAM.

DISCUSSION

The quantitative and qualitative analysis on both simulated data and human *in vivo* data showed that the reconstructed TKD suffers from streaking artifacts and underestimates the susceptibility values of deep gray matter and veins. The streaking artifact is reduced in iSWIM by using constraints from high susceptibility structures, but the final image is still noisy in the homogeneous regions. Thanks to the use of an ℓ_1 -norm regularization MEDI creates high SNR results. However, some streaking artifacts remain in regions where magnitude data is inconsistent with the susceptibility map. On the other hand, scSWIM uses both ℓ_1 and ℓ_2 regularization terms to protect edges and structures while also allowing smoothing to increase SNR in regions without structure and it successfully reduces streaking artifacts leading to less noise and faithful estimates of the susceptibility. Furthermore, scSWIM outperforms other methods in reconstructing the susceptibility map in the presence of CMBs and CaDs with high susceptibilities. In simulated data, both microbleeds with susceptibilities of 1000 ppb and 3000 ppb and calcium objects with susceptibilities of -1000 ppb and -3000 ppb were reconstructed accurately using scSWIM compared to other methods. Also, in scSWIM, the standard deviation of the measured susceptibilities (Table 2) in all structures even in the CMB or CaD with the highest susceptibility values are much lower than other methods showing the strengths of this multi-echo approach. Although, MEDI provides a smooth QSM image under normal circumstances it appears to have trouble in reconstructing the data in the presence of high susceptibilities such as seen with the CMB and CaD in the simulated model and for the pineal gland in the *in vivo* data (which appeared dilated compared to that in scSWIM). This could be due to the fact that MEDI uses phase fitting across multiple echoes and high susceptibilities can cause both signal loss at the edge of the object and severe aliasing at longer echoes. Furthermore, in the *in vivo* data, one could observe slight streaking with MEDI around the large veins that could be due to the inconsistency between the magnitude and susceptibility data.

The *in vivo* results for scSWIM showed average susceptibilities for the ten healthy subjects very close to the reported values in the literature (Ghassaban et al., 2019a). Also, the measured susceptibilities in the reconstructed COSMOS (Table 3) were not as close to scSWIM and MEDI as one would have hoped because it can contain errors due to registration of the different orientation data and noise in the data. The registration error is higher and more noticeable in the regions near the surface of the brain. Luckily most of the regions of interest (the deep gray matter) in this paper are near the core of the brain where the registration error is smaller therefore this

central region can still be used as a baseline to compare different methods.

Structural Constraints in scSWIM

The cost function of scSWIM includes two regularization terms. The ℓ_1 -norm regularization term is based on a P mask to penalize the noisy non-edge pixels and the ℓ_2 -norm regularization term is based on the R mask that prevents smoothing in the excluded high susceptibility regions. If the pre-processing fails to extract the edges of a true structure, then the P mask will penalize and smooth them. On the other hand, if R fails to exclude a high susceptibility structure, the streaking artifacts from this structure will remain and its mean susceptibility will be reduced due to smoothing. This is because the R mask protects the structures of high susceptibility from being over smoothed by the ℓ_1 -norm regularization term. The overall performance of the cost function works well when the edges and structures are best defined.

Optimal Parameter Selection for scSWIM

In the regularization-based approaches, there is always a trade-off between obtaining accurate susceptibility values, reducing streaking artifacts, and increasing SNR. In scSWIM, the λ_1 parameter controls the spatial smoothness by applying the sparsity constraint on the gradient of the susceptibility map. The larger the λ_1 , the smoother the non-edge regions will be for both the background and basal ganglia (basically increasing the SNR). On the other hand, λ_2 also controls smoothing the background but protects the objects defined by the R mask. Smaller λ_2 reduces the effect of the regularization term and increases the effect of the data fidelity term and the streaking artifact will not be handled as well. On the other hand, larger λ_2 will increase the effect of the regularization term and reduce the effect of the data fidelity term and will result in an over-smoothed image where the background such as WM and GM and smaller objects would be washed out.

Therefore, the challenging part of scSWIM is to find the optimal parameters to keep sharp edges, smooth where appropriate, and satisfy the data fidelity condition. However, finding optimal values for more than one parameter in regularization problems is still a difficult problem. With the admission of sub-optimality, we assumed that the ratio of λ_1 and λ_2 is fixed. For this purpose, we compared the P and R masks and also the first and second regularization terms and observed that $\lambda_1 = 0.005\lambda_2$ will bring the two terms to the same order. The final step was to determine the optimal value for λ_2 . This was accomplished using the L-curve approach that plots the residual data fidelity versus the regularization for different regularization parameters and selecting the value that results in the maximum curvature. For multi-echo, multi-flip angle scSWIM, the L-curves were analyzed for each individual scan separately and the optimal λ_2 values selected accordingly.

Multi-Echo, Multi-Flip Angle scSWIM

As mentioned before, STAGE imaging uses double-flip angle, double-echo GRE scans. The multi-echo, multi-flip angle scSWIM, or STAGE scSWIM is generated by an R_2^* -based weighted averaging of the individual echo scSWIM data sets. Besides having higher SNR in the STAGE scSWIM results,

each individual scSWIM dataset can be reviewed separately if desired. It would be of interest to compare the QSM results with those from the $R2^*$ maps or even the T1maps given that iron can affect the T1 of tissue. Recently, there has been more interest in multi-contrast quantitative mapping in diseases such as Parkinson's disease and dementia where a more systemic quantitative approach is being taken with 3D data. Iron has played a key role in these studies not just in the basal ganglia but also in the hippocampus, motor cortex and cortical gray matter in general.

More importantly, the final STAGE scSWIM will keep regions that have been removed by the phase quality control map at longer echo times. An alternate approach would be reconstructing QSM from the linear fit to the phase as done in MEDI. However, regions of high susceptibility phase aliasing can be severe and phase fitting may not be successful. Furthermore, severe loss of signal in and around the object (blooming artifacts) will occur for high susceptibilities that will result in a significantly under-estimated susceptibility. The use of shorter echo times and the weighting factors can favor the short echo data replacing the long echo data when the susceptibilities are very high as in the case of the CMBs and CaD as shown in the results section.

STAGE uses the conventional SWI with two flip angles and is effectively available at any site that can run 3D GRE imaging. It is a 5 min scan (2.5 min for each flip angle) that provides eight qualitative and seven quantitative clinically useful images such as T1maps, spin density maps, QSM, $R2^*$, B1 field corrections and etc. Although, the high resolution STAGE scan time may take longer (~10 min), using a compressed sense factor of 3 to 4 the scan times can be brought back to a time frame of 5 to 7 min. The proposed scSWIM method achieved the best results when processing double-echo, double-flip angle STAGE data by using the derived T1WE images to extract reliable geometry constraints, but it can also be performed on a single-echo T1W SWI dataset.

CONCLUSION

In this paper, we have proposed a constraint based QSM reconstruction algorithm scSWIM which uses STAGE and iSWIM inputs to reconstruct the susceptibility map from multiple flip angle, multiple echo data. The results show for both simulated and *in vivo* human brain data that streaking artifacts are suppressed, and SNR is increased. Further, the measured susceptibilities are accurate relative to the brain model used and

scSWIM works well even for regions with high susceptibility such as microbleeds and calcifications.

DATA AVAILABILITY STATEMENT

The data analyzed in this study is subject to the following licenses/restrictions: The data is currently not available. The data is from a collaboration with a clinical site. Requests to access these datasets should be directed to Nmrimaging@aol.com.

ETHICS STATEMENT

The studies involving human participants were reviewed and approved by Ethics Committee of Wayne State University and Ethics Committee of The First Affiliated Hospital of Zhengzhou University. The patients/participants provided their written informed consent to participate in this study.

AUTHOR CONTRIBUTIONS

SG and SL designed, executed, and implemented the research project under the supervision of EMH. SB, YC, YW, and MJ helped in designing the experiments. CZ and BW helped with data acquisition. JC was the senior supporter of the data acquisition. SG wrote the first draft of the manuscript. EMH, SL, and SB critically discussed the results and reviewed the manuscript. EMH, TW, YC, and NK provided feedback and helped shape the manuscript. All authors contributed to the article and approved the submitted version.

FUNDING

This research was supported in part by the NIH/NHLBI grant R44HL145826. The content is solely the responsibility of the authors and does not necessarily represent the official views of the National Institutes of Health.

SUPPLEMENTARY MATERIAL

The Supplementary Material for this article can be found online at: <https://www.frontiersin.org/articles/10.3389/fnins.2020.581474/full#supplementary-material>

REFERENCES

- Abdul-Rahman, H. S., Gdeisat, M. A., Burton, D. R., Lalor, M. J., Lilley, F., and Moore, C. J. (2007). Fast and robust three-dimensional best path phase unwrapping algorithm. *Appl. Opt.* 46, 6623–6635. doi: 10.1364/AO.46.006623
- Avants, B. B., Tustison, N., and Song, G. (2009). Advanced normalization tools (ANTS). *Insight J.* 2, 1–35.
- Avants, B. B., Tustison, N. J., Song, G., Cook, P. A., Klein, A., and Gee, C. (2012). A reproducible evaluation of ANTs similarity metric performance in brain image registration. 54, 2033–2044. doi: 10.1016/j.neuroimage.2010.09.025.A
- Bao, L., Li, X., Cai, C., Chen, Z., and Van Zijl, P. C. M. (2016). Quantitative susceptibility mapping using structural feature based collaborative reconstruction (SFCR) in the human brain. *IEEE Trans. Med. Imaging* 35, 2040–2050. doi: 10.1109/TMI.2016.2544958
- Bilgic, B., Pfefferbaum, A., Rohl, T., Sullivan, E. V., and Adalsteinsson, E. (2012). NeuroImage MRI estimates of brain iron concentration in normal aging using quantitative susceptibility mapping. *Neuroimage* 59, 2625–2635. doi: 10.1016/j.neuroimage.2011.08.077

- Brown, R. W., Cheng, Y. C. N., Haacke, E. M., Thompson, M. R., and Venkatesan, R. (2014). *Magnetic Resonance Imaging: Physical Principles and Sequence Design*. Hoboken, NY: Wiley-Blackwell.
- Buch, S., Liu, S., Haacke, E. M., and Neelavalli, J. (2012). "Simulated 3D brain model to study the phase behavior of brain structures," in *Proceedings of the 20th Annual Meeting of ISMRM* Melbourne, 2332.
- Buch, S., Liu, S., Ye, Y., Cheng, Y. C. N., Neelavalli, J., and Haacke, E. M. (2015). Susceptibility mapping of air, bone, and calcium in the head. *Magn. Reson. Med.* 73, 2185–2194. doi: 10.1002/mrm.25350
- Chen, W., Zhu, W., Kovanlikaya, I., Kovanlikaya, A., Liu, T., Wang, S., et al. (2014). Intracranial calcifications and hemorrhages: characterization with quantitative susceptibility mapping. *Radiology* 270, 496–505. doi: 10.1148/radiol.13122640
- Chen, Y., Liu, S., Kang, Y., and Haacke, E. M. (2018a). "A rapid, robust multi-echo phase unwrapping method for quantitative susceptibility mapping (QSM) using strategically acquired gradient echo (STAGE) data acquisition," in *Proceedings of the SPIE 10573, Medical Imaging 2018: Physics of Medical Imaging* (Washington, DC: SPIE), doi: 10.1117/12.2292951
- Chen, Y., Liu, S., Wang, Y., Kang, Y., and Haacke, E. M. (2018b). STrategically acquired gradient echo (STAGE) imaging, part I: creating enhanced T1 contrast and standardized susceptibility weighted imaging and quantitative susceptibility mapping. *Magn. Reson. Imaging* 46, 130–139. doi: 10.1016/j.mri.2017.10.005
- Deistung, A., Schweser, F., Wiestler, B., Abello, M., Roethke, M., Sahm, F., et al. (2013). Quantitative susceptibility mapping differentiates between blood depositions and calcifications in patients with glioblastoma. *PLoS One* 8:e57924. doi: 10.1371/journal.pone.0057924
- Ghassaban, K., He, N., Sethi, S. K., Huang, P., and Chen, S. (2019a). Regional high iron in the substantia nigra differentiates parkinson's disease patients from healthy controls. *Front. Aging Neurosci.* 11:106. doi: 10.3389/fnagi.2019.00106
- Ghassaban, K., Liu, S., Jiang, C., and Haacke, E. M. (2019b). Quantifying iron content in magnetic resonance imaging. *Neuroimage* 187, 77–92. doi: 10.1016/j.neuroimage.2018.04.047
- Haacke, E. M., Chen, Y., Utriainen, D., Wu, B., Wang, Y., Xia, S., et al. (2020). STrategically acquired gradient echo (STAGE) imaging, part III: technical advances and clinical applications of a rapid multi-contrast multi-parametric brain imaging method. *Magn. Reson. Imaging* 65, 15–26. doi: 10.1016/j.mri.2019.09.006
- Haacke, E. M., Liu, S., Buch, S., Zheng, W., Wu, D., and Ye, Y. (2015). Quantitative susceptibility mapping: current status and future directions. *Magn. Reson. Imaging* 33, 1–25. doi: 10.1016/j.mri.2014.09.004
- Haacke, E. M., and Reichenbach, J. R. (2011). *Susceptibility Weighted Imaging in MRI: Basic Concepts and Clinical Applications*. Hoboken, NY: Wiley Blackwell.
- Haacke, E. M., Tang, J., Neelavalli, J., and Cheng, Y. C. N. (2010). Susceptibility mapping as a means to visualize veins and quantify oxygen saturation. *J. Magn. Reson. Imaging* 32, 663–676. doi: 10.1002/jmri.22276
- Hansen, P. C., and O'Leary, D. P. (1992). The use of the L-curve in the regularization of discrete ill-posed problems. *SIAM J. Sci. Comput.* 14, 1487–1503. doi: 10.1137/0914086
- Lee, C., Baker, E., and Thomasson, D. (2006). Normal regional T1 and T2 relaxation times of the brain at 3T. *Proc. Intl. Soc. Magn. Reson. Med.* 14:2006.
- Liu, J., Liu, T., De Rochefort, L., Ledoux, J., Khalidov, I., Chen, W., et al. (2012). Morphology enabled dipole inversion for quantitative susceptibility mapping using structural consistency between the magnitude image and the susceptibility map. *Neuroimage* 59, 2560–2568. doi: 10.1016/j.neuroimage.2011.08.082
- Liu, T., Spincemaille, P., De Rochefort, L., Kressler, B., and Wang, Y. (2009). Calculation of susceptibility through multiple orientation sampling (COSMOS): a method for conditioning the inverse problem from measured magnetic field map to susceptibility source image in MRI. *Magn. Reson. Med.* 61, 196–204. doi: 10.1002/mrm.21828
- Schweser, F., Deistung, A., Lehr, B. W., and Reichenbach, J. R. (2011). Quantitative imaging of intrinsic magnetic tissue properties using MRI signal phase: an approach to in vivo brain iron metabolism? *Neuroimage* 54, 2789–2807. doi: 10.1016/j.neuroimage.2010.10.070
- Schweser, F., Sommer, K., Deistung, A., and Reichenbach, J. R. (2012). Quantitative susceptibility mapping for investigating subtle susceptibility variations in the human brain. *Neuroimage* 62, 2083–2100. doi: 10.1016/j.neuroimage.2012.05.067
- Smith, S. M. (2002). Fast robust automated brain extraction. *Hum. Brain Mapp.* 17, 143–155. doi: 10.1002/hbm.10062
- Tang, J., Liu, S., Neelavalli, J., Cheng, Y. C. N., Buch, S., and Haacke, E. M. (2013). Improving susceptibility mapping using a threshold-based k-space/image domain iterative reconstruction approach. *Magn. Reson. Med.* 69, 1396–1407. doi: 10.1038/jid.2014.371
- Wang, Y., Chen, Y., Utriainen, D. T., and Haacke, E. M. (2019). "Automatic segmentation of deep grey matter structures for iron quantification," in *Proceedings of the 27th Annual Meeting of ISMRM* Montréal, QC.
- Wang, Y., Chen, Y., Wu, D., Wang, Y., Sethi, S. K., Yang, G., et al. (2018). STrategically Acquired gradient echo (STAGE) imaging, part II: correcting for RF inhomogeneities in estimating T1 and proton density. *Magn. Reson. Imaging* 46, 140–150. doi: 10.1016/j.mri.2017.10.006
- Wang, Z., Bovik, A. C., Sheikh, H. R., and Simoncelli, E. P. (2004). Image quality assessment: From error visibility to structural similarity. *IEEE Trans. Image Process.* 13, 600–612. doi: 10.1109/TIP.2003.819861
- Wharton, S., Schäfer, A., and Bowtell, R. (2010). Susceptibility mapping in the human brain using threshold-based k-space division. *Magn. Reson. Med.* 63, 1292–1304. doi: 10.1002/mrm.22334

Conflict of Interest: SG, MJ, and EMH are employees of the Magnetic Resonance Innovations Inc., Bingham Farms, MI, United States. YW and EMH are employees of The MRI Institute for Biomedical Research, Bingham Farms, MI, United States.

The remaining authors declare that the research was conducted in the absence of any commercial or financial relationships that could be construed as a potential conflict of interest.

Copyright © 2020 Gharabaghi, Liu, Wang, Chen, Buch, Jokar, Wischgoll, Kashou, Zhang, Wu, Cheng and Haacke. This is an open-access article distributed under the terms of the Creative Commons Attribution License (CC BY). The use, distribution or reproduction in other forums is permitted, provided the original author(s) and the copyright owner(s) are credited and that the original publication in this journal is cited, in accordance with accepted academic practice. No use, distribution or reproduction is permitted which does not comply with these terms.



Iron Content in Deep Gray Matter as a Function of Age Using Quantitative Susceptibility Mapping: A Multicenter Study

Yan Li^{1†}, Sean K. Sethi^{2,3,4†}, Chunyan Zhang⁵, Yanwei Miao⁶, Kiran Kumar Yerramsetty⁷, Vinay Kumar Palutia⁷, Sara Gharabaghi³, Chengyan Wang⁸, Naying He^{1*}, Jingliang Cheng⁵, Fuhua Yan^{1*} and Ewart Mark Haacke^{1,2,3,4}

¹ Department of Radiology, Ruijin Hospital, Shanghai Jiao Tong University School of Medicine, Shanghai, China,

² Department of Radiology, Wayne State University, Detroit, MI, United States, ³ MR Innovations, Inc., Bingham Farms, MI, United States, ⁴ SpinTech, Inc., Bingham Farms, MI, United States, ⁵ Department of Magnetic Resonance Imaging, The First Affiliated Hospital of Zhengzhou University, Zhengzhou, China, ⁶ Department of Radiology, First Affiliated Hospital of Dalian Medical University, Dalian, China, ⁷ MR Medical Imaging Innovations India Pvt., Ltd., Madhapur, India, ⁸ Human Phenome Institute, Fudan University, Shanghai, China

OPEN ACCESS

Edited by:

Domenico De Berardis,
Azienda USL Teramo, Italy

Reviewed by:

Alan Wilman,
University of Alberta, Canada
Federica Vellante,
University of Studies G. d'Annunzio
Chieti and Pescara, Italy
Marianna Mazza,
Catholic University of the Sacred
Heart, Italy

*Correspondence:

Naying He
hny12267@rjh.com.cn
Fuhua Yan
yfh11655@rjh.com.cn

[†]These authors have contributed
equally to this work

Specialty section:

This article was submitted to
Neurodegeneration,
a section of the journal
Frontiers in Neuroscience

Received: 17 September 2020

Accepted: 07 December 2020

Published: 06 January 2021

Citation:

Li Y, Sethi SK, Zhang C, Miao Y, Yerramsetty KK, Palutia VK, Gharabaghi S, Wang C, He N, Cheng J, Yan F and Haacke EM (2021) Iron Content in Deep Gray Matter as a Function of Age Using Quantitative Susceptibility Mapping: A Multicenter Study. *Front. Neurosci.* 14:607705. doi: 10.3389/fnins.2020.607705

Purpose: To evaluate the effect of resolution on iron content using quantitative susceptibility mapping (QSM); to verify the consistency of QSM across field strengths and manufacturers in evaluating the iron content of deep gray matter (DGM) of the human brain using subjects from multiple sites; and to establish a susceptibility baseline as a function of age for each DGM structure using both a global and regional iron analysis.

Methods: Data from 623 healthy adults, ranging from 20 to 90 years old, were collected across 3 sites using gradient echo imaging on one 1.5 Tesla and two 3.0 Tesla MR scanners. Eight subcortical gray matter nuclei were semi-automatically segmented using a full-width half maximum threshold-based analysis of the QSM data. Mean susceptibility, volume and total iron content with age correlations were evaluated for each measured structure for both the whole-region and RII (high iron content regions) analysis. For the purpose of studying the effect of resolution on QSM, a digitized model of the brain was applied.

Results: The mean susceptibilities of the caudate nucleus (CN), globus pallidus (GP) and putamen (PUT) were not significantly affected by changing the slice thickness from 0.5 to 3 mm. But for small structures, the susceptibility was reduced by 10% for 2 mm thick slices. For global analysis, the mean susceptibility correlated positively with age for the CN, PUT, red nucleus (RN), substantia nigra (SN), and dentate nucleus (DN). There was a negative correlation with age in the thalamus (THA). The volumes of most nuclei were negatively correlated with age. Apart from the GP, THA, and pulvinar thalamus (PT), all the other structures showed an increasing total iron content despite the reductions in volume with age. For the RII regional high iron content analysis, mean susceptibility in most of the structures was moderately to strongly correlated with age. Similar to the global analysis, apart from the GP, THA, and PT, all structures showed an increasing total iron content.

Conclusion: A reasonable estimate for age-related iron behavior can be obtained from a large cross site, cross manufacturer set of data when high enough resolutions are used. These estimates can be used for correcting for age related iron changes when studying diseases like Parkinson's disease, Alzheimer's disease, and other iron related neurodegenerative diseases.

Keywords: magnetic resonance imaging, quantitative susceptibility mapping, age-related brain iron, deep gray matter, multicenter study

INTRODUCTION

Iron is ubiquitous in numerous biological processes in normal aging as well as in neurodegeneration. It is distributed throughout the brain in the form of ferritin and its concentration is highest in the deep gray matter (DGM) (Haacke et al., 2005). Iron plays an important role in many brain cellular processes, including oxygen transport, electron transfer, neurotransmitter synthesis, myelination, and mitochondrial function (Drayer, 1986; Connor et al., 1990). Despite this positive role for iron utilization, it is toxic in the form of free iron. In that case, iron can react with oxygen to produce neurotoxic free radicals, which could lead to membrane lipid peroxidation and accumulation of lipofuscin in neurons (Koeppen, 2003). Excessive iron accumulation has been associated with various neuro-degenerative diseases, such as Parkinson's disease (Ghassaban et al., 2019), atypical parkinsonian disorders (Lee and Lee, 2019), Alzheimer's disease (Nikseresht et al., 2019), pantothenate kinase-associated neurodegeneration (Álvarez-Córdoba et al., 2019), aceruloplasminemia (Zhou et al., 2020), and different types of hereditary cerebellar ataxias (Deistung et al., 2016). Brain iron deposition is also linked with cognitive severity in Parkinson's disease (Thomas et al., 2020). For these reasons, probing and quantifying the presence of iron in the brain is very important.

With the common use of 3D multi-echo gradient echo (GRE) imaging methods, the ability to collect whole brain $R2^*$ and quantitative susceptibility mapping (QSM) data has become feasible clinically. QSM is an emerging MRI technique that is sensitive to magnetic susceptibility differences between tissues. The signal phase of GRE sequences can be used to detect the local variations in iron content (Schwarz et al., 2014; Langkammer et al., 2016). $R2^*$ depends on water content as well as iron content and field strength, while QSM is, in principle, independent of water content, echo time, and field strength. QSM has become a complementary method to $R2^*$ for measuring iron content (Liu et al., 2017; Santin et al., 2017). Kofi (2015) assessed the reproducibility of brain QSM in healthy controls (HC) and

patients with multiple sclerosis (MS) on both 1.5T and 3T scanners. Brain QSM measurements have good inter-scanner and same-scanner reproducibility for HC and patients, respectively. Ippoliti et al. (2018) also evaluated the reproducibility and consistency of QSM across 1.5T and 3.0T field strengths and optimized the contrast-to-noise ratio (CNR) at 1.5T through bandwidth tuning. Feng et al. (2018) evaluated the repeatability of QSM on a 3.0T scanner using 8 subjects and found that QSM results were highly reproducible across the four time scans. Although the reliability and stability of QSM have been verified in these papers with a small number of cases, a standard from which to calculate the age dependency of iron across manufacturers that also includes the effect of resolution has not been presented or evaluated.

In addition, most current clinical applications of QSM look for differences between patients and HCs in specific brain regions or nuclei (Mostile et al., 2017). Therefore, it is important to be able to correct for age to make a diagnosis relative to patients with a specific neurodegenerative disease. An increase in age-related iron deposition has been reported in many studies. In Hallgren's landmark work studying brain iron (Hallgren, 1958), histochemical methods were used to show the non-heme iron concentration as a function of age in the brain. Acosta-Cabrero et al. (2016) used QSM to provide insight into iron accumulation in the brain across the adult lifespan (20–79 years old). Whole-brain and ROI analyses confirmed that the propensity of brain cells to accumulate excessive iron as a function of age largely depends on their exact anatomical location. Whereas only patchy signs of iron scavenging were observed in white matter (WM), strong, bilateral, and confluent QSM-age associations were identified in several deep-brain nuclei, chiefly the striatum and midbrain- as well as across motor, premotor, posterior insular, superior prefrontal, and cerebellar cortices. The validity of QSM as a suitable *in vivo* imaging technique with which to monitor iron dysregulation in the human brain was demonstrated by confirming age-related increases in several subcortical nuclei that are known to accumulate iron with age. Their study indicated that, in addition to these structures, there is a predilection for iron accumulation in the frontal lobes, which, when combined with the subcortical findings, suggests that iron accumulation with age predominantly affects brain regions related to motor/cognition/output functions. Keuken et al. (2017) included 30 young, 14 middle-age, and 10 elderly healthy subjects scanned at 7.0T. They investigated volumetric, spatial, and quantitative MRI parameter ($T1$, $T2^*$, and QSM) changes associated with healthy aging in subcortical nuclei (basal ganglia, red nucleus, and the periaqueductal gray

Abbreviations: QSM, quantitative susceptibility mapping; DGM, deep gray matter; GRE, gradient echo; HC, healthy controls; MS, multiple sclerosis; CNR, contrast-to-noise ratio; WM, white matter; FOV, field-of-view; SNR, signal to noise ratio; BET, brain extraction tool; 3DSRNCP, 3D phase unwrapping algorithm; SHARP, sophisticated harmonic artifact reduction; TKD, truncated k-space division; CN, caudate nucleus; GP, globus pallidus; PUT, putamen; THA, thalamus; PT, pulvinar thalamus; RN, red nucleus; SN, substantia nigra; DN, dentate nucleus; FWHM, full-width half maximum; SPIN, Signal Processing in Nmr; ROI, region of interest; ANOVA, analysis of variance; GMD, gray matter density; GMV, gray matter volume; STAGE, STrategically Acquired Gradient Echo.

matter). They concluded that aging has a heterogeneous effect across regions. Numerous papers have recently shown a similar relationship with age and iron content using QSM (Aquino et al., 2009; Haacke et al., 2010; Daugherty and Raz, 2013; Hare et al., 2013; Liu et al., 2016; Ghassaban et al., 2018; Yan et al., 2018). However, the number of subjects in these studies was generally small with the largest being 174 (Liu et al., 2016).

Hence, in the present work, our goal was to evaluate the effect of resolution on the QSM quantification; verify the consistency of QSM across field strengths and manufacturers in evaluating the DGM of the human brain using 623 subjects from multiple imaging sites; and establish an iron content baseline (using QSM) as a function of age for each DGM structure using both a global and a regional iron analysis (Liu et al., 2016). Using a normative database of iron content related to age may be useful in categorizing and predicting neurological diseases especially movement and cognition disorder diseases, or conditions which affect motor or cognitive function.

MATERIALS AND METHODS

Data Acquisition

A total of 623 healthy adults were included from 3 sites: The First Affiliated Hospital of Dalian Medical University (Site 1: Dalian), Ruijin Hospital, Shanghai Jiao Tong University School of Medicine (Site 2: Ruijin), and The First Affiliated Hospital of Zhengzhou University (Site 3: Zhengzhou), equipped with a GE HDX 1.5T scanner (173 cases, 85 females, 88 males; age, 45.1 ± 14.2 years; range, 20–69 years), a Philips Ingenia 3.0T scanner (336 cases, 219 females, 117 males; age, 62.3 ± 6.5 years; range, 40–79 years), and a Siemens Prisma 3.0T scanner (114 cases, 61 females, 53 males; age, 60.3 ± 9.3 years; range, 40–90 years), respectively. All the participants provided written informed consent to participate in this study. Data were acquired using the following parameters: TR = 53/25/25 ms, TE = 40/17.5/17.5 ms, and voxel size = $0.6 \text{ mm} \times 0.75 \text{ mm} \times 3 \text{ mm} = 1.35 \text{ mm}$; $0.67 \text{ mm} \times 1.34 \text{ mm} \times 2 \text{ mm} = 1.80 \text{ mm}$, and $0.67 \text{ mm} \times 1.34 \text{ mm} \times 2 \text{ mm} = 1.80 \text{ mm}$ for each scanner, respectively.

Simulation Model

For the purpose of studying the effect of resolution on the QSM data, a digitized model of the brain was used (Buch, 2012). This 3D isotropic model included the general structures of the human brain including the gray/white matter, basal ganglia, and midbrain structures as well as the major veins. The matrix size, voxel resolution and field-of-view (FOV) for this model were: $504 \text{ mm} \times 504 \text{ mm} \times 504 \text{ mm}$, $0.5 \text{ mm} \times 0.5 \text{ mm} \times 0.5 \text{ mm}$, and $252 \text{ mm} \times 252 \text{ mm} \times 252 \text{ mm}$, respectively.

The phase images, $\varphi(\vec{r})$, were simulated from the susceptibility model, $\chi(\vec{r})$, using the expression (Haacke et al., 2010):

$$\varphi(\vec{r}) = \gamma B_0 TE d(\vec{r}) \otimes \chi(\vec{r}), [1]$$

where $\gamma = 2.675 \times 10^8 \text{ rad/s/T}$ is the gyromagnetic ratio and $B_0 = 3 \text{ T}$ is the main magnetic field strength along the z-direction (the slice select direction in this case); \vec{r} and TE are the voxel position vector and the echo time, respectively. Also, \otimes denotes the convolution operation between $d(\vec{r})$, the unit dipole kernel, and the susceptibility model.

Magnitude images were generated from the Ernst equation (Brown, 2014) assuming that $R2^*(\vec{r}) = 20/s + 0.125 \chi(\vec{r})$ (Ghassaban et al., 2019). Then, the complex signal was generated from the simulated magnitude and phase images, and Gaussian noise was added to each of the real and imaginary components to produce a signal-to-noise ratio (SNR) of 10:1 at a TE = 7.5 ms. The resulting complex data were then truncated in the slice direction to produce images with the following resolutions: $0.5 \text{ mm} \times 0.5 \text{ mm} \times 0.5 \text{ mm}$, $0.5 \text{ mm} \times 0.5 \text{ mm} \times 1 \text{ mm}$, $0.5 \text{ mm} \times 0.5 \text{ mm} \times 2 \text{ mm}$, and $0.5 \text{ mm} \times 0.5 \text{ mm} \times 3 \text{ mm}$. **Figure 1** shows the simulated model in three different views with labels for the main DGM analyzed and **Table 1** summarizes the susceptibility values, proton density, T_1 relaxation times, and the size of the different brain structures in the model.

Resampling of the Data to Create a Single Resolution Common to All Sites

In order to create a comparison with the same resolution, the original data in Site 1 was k-space cropped in-plane to create a resolution of $0.67 \text{ mm} \times 1.34 \text{ mm} \times 3 \text{ mm}$ to mimic the in-plane resolution of the other two sites. Likewise, to make the slice thicknesses the same for all sites, the data from the other two sites were k-space cropped through-plane to increase the slice thickness to 3 mm and therefore create an image with the same resolution of $0.67 \text{ mm} \times 1.34 \text{ mm} \times 3 \text{ mm}$.

Quantitative Analysis

Quantitative susceptibility mapping data were reconstructed using our in-house MATLAB-based toolbox SMART 2.0 (MRI Institute for Biomedical Research, Detroit, MI, United States). The brain extraction tool (BET) (Smith, 2002) was used to isolate the brain tissue (threshold = 0.2, erode = 4, and island = 2000) using the first echo where the signal intensity is highest; a 3D phase unwrapping algorithm (3DSRNCP) (Abdul-Rahman et al., 2007) to unwrap the original phase data; and the sophisticated harmonic artifact reduction (SHARP) (Schweser et al., 2011) to remove unwanted background fields (threshold = 0.05 and deconvolution kernel size = 6). Both BET and SHARP steps were skipped for the simulated data. Finally, a truncated k-space division (TKD) based inverse filtering technique (threshold = 0.1) with an iterative approach (iteration threshold = 0.1, and number of iterations = 4) was used to reconstruct the susceptibility maps (Tang et al., 2013).

Eight subcortical gray matter nuclei, inclusive of caudate nucleus (CN), globus pallidus (GP), putamen (PUT), thalamus (THA), pulvinar thalamus (PT), red nucleus (RN), substantia nigra (SN), and dentate nucleus (DN) were semi-automatically segmented using a full-width half maximum (FWHM) threshold based analysis of the susceptibility maps using Signal Processing in Nmr (SPIN) software (SpinTech, Inc., Bingham Farms, MI,

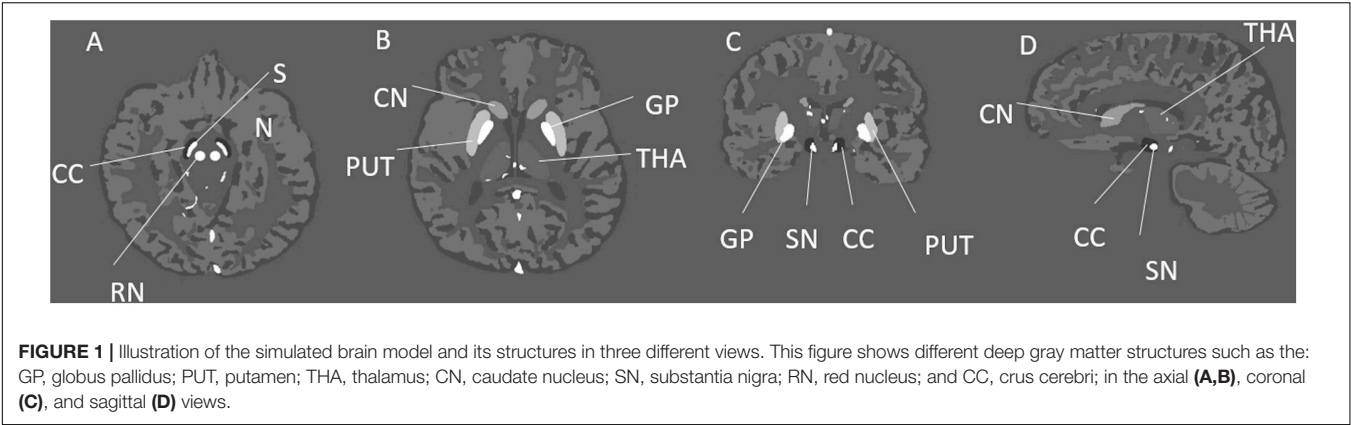


FIGURE 1 | Illustration of the simulated brain model and its structures in three different views. This figure shows different deep gray matter structures such as the: GP, globus pallidus; PUT, putamen; THA, thalamus; CN, caudate nucleus; SN, substantia nigra; RN, red nucleus; and CC, crus cerebri; in the axial (A), coronal (B), and sagittal (C) views.

TABLE 1 | The susceptibility (ppb), T_1 relaxation time, relative proton density (ρ_0), and the size (mm^3) of different structures for the simulated brain model.

	χ (ppb)	T_1 (ms)	ρ_0	Size (mm^3)
WM	0	837	0.73	~
GM	20	1607	0.80	~
VNT/CSF	-14	4163	1.00	~
CN	60	1226	0.82	$42.5 \times 14.5 \times 20.5$
GP	180	888	0.72	$20.5 \times 14.5 \times 13.5$
PUT	90	1140	0.82	$33.5 \times 14.5 \times 21$
SN	160, 200	1147	0.79	$9.5 \times 8.5 \times 7, 9.5 \times 7.5 \times 6$
RN	130	833	0.80	$6 \times 10 \times 6$
CC	-30	780	0.79	$14.5 \times 10 \times 10.5$
THA	10	1218	0.79	$29.5 \times 26.5 \times 17.5$
V	450	1932	0.85	~

The size is described in row \times column \times slice directions format. Please note that SN in the model is composed of two parts. WM, white matter; GM, gray matter; GP, globus pallidus; PUT, putamen; THA, thalamus; CN, caudate nucleus; SN, substantia nigra; RN, red nucleus; CC, crus cerebri; V, veins; VNT, ventricles; CSF, cerebrospinal fluid; and ppb, parts per billion.

United States). The mean susceptibility values and volumes of the regions of interest (ROIs) were then assessed. Representative images from each site and segmentation outlines are shown in **Figure 2**. The raters had an intraclass coefficient of >0.9 for the susceptibility measurement of all structures, and these averages are reported in this study. The product of the mean susceptibility and the volume of each GM nuclei was used to represent the total iron deposition in the structure. During the ROI drawing, the readers were blinded to the subject type and age to reduce the impact of ROI selection on evaluating the susceptibility-age relationship. The 3D whole-structural measurements (global) were used to determine age-related thresholds, which were applied to calculate the local iron deposition [RII: portion of the structure that contains high iron concentrations, that is, those regions with iron content higher than two standard deviations above the mean as a function of age as taken from the paper of Liu et al. (2016)]. Age-susceptibility, age-volume and age-total iron correlations were determined for each measured structure for both the whole-region and the high iron content region RII.

Statistical Analysis

The statistical analyses were performed using MATLAB R2019a (MathWorks, Natick, MA, United States) and SPSS 22.0.

Participant demographics were compared between groups with an analysis of variance (ANOVA) or Welch's ANOVA in the case of nonparametric variables as determined by Levene's test. Distribution of sex was compared using a χ^2 test. The mean susceptibility/nuclei volume/total iron content (volume \times mean susceptibility) data were fitted using linear regression models (Liu et al., 2016) and Pearson correlation analysis was applied to investigate the relationship between each measure and age in each structure. Strength of the Pearson correlation coefficient (r) was determined using the following guide for the absolute value: 0.00–0.19 “very weak,” 0.20–0.39 “weak,” 0.40–0.59 “moderate,” 0.60–0.79 “strong,” and 0.80–1.0 “very strong.” p -values less than 0.05 were considered statistically significant.

RESULTS

Participant Characteristics

Group subject demographics are shown in **Table 2**. Sex distribution ($\chi^2 = 13.6$, $p < 0.05$) and age (Welch's $F = 190$, $p < 0.05$) differed significantly across the three sites. The average age of the subjects in Site 1 was smaller than that of Site 2 or Site 3, and the distribution of each age group was relatively uniform.

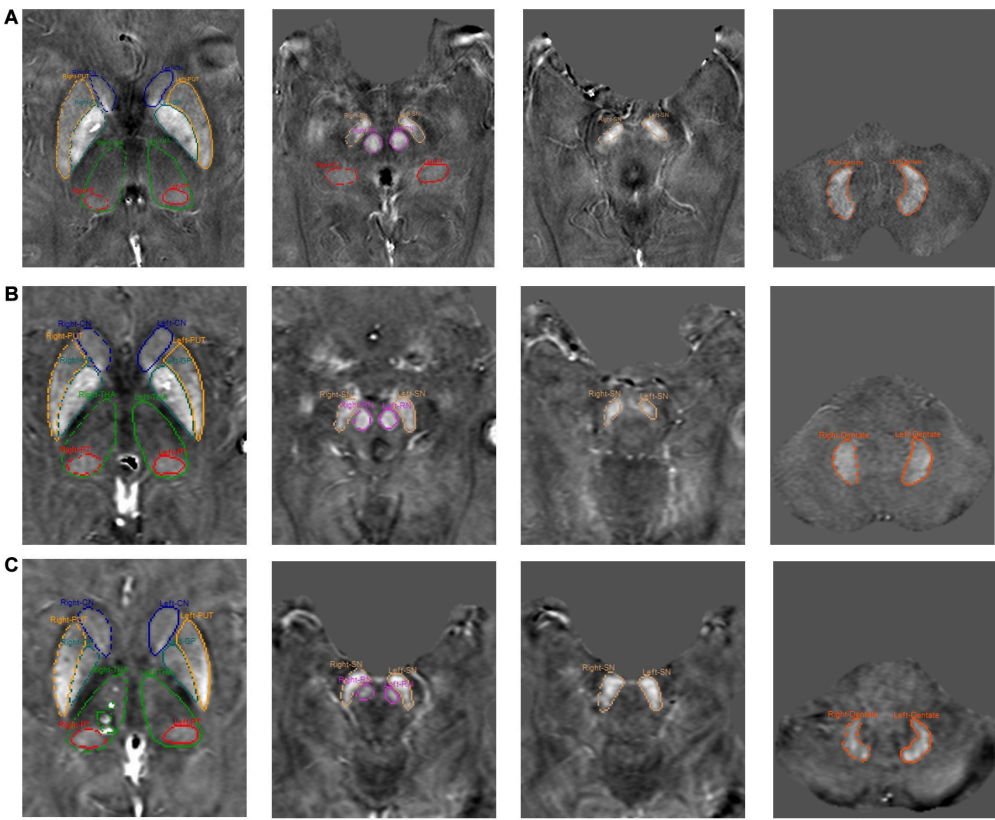


FIGURE 2 | Representative images from each site and segmentation outlines of 8 ROIs. **(A)** Site 1, **(B)** Site 2, and **(C)** Site 3.

TABLE 2 | Demographic data of the subjects and the scanning parameters in three sites.

	Site 1	Site 2	Site 3	<i>p</i> -value
Sample size	173	336	114	/
Age range (years)	20–69	40–79	40–90	/
Age (years, mean ± SD)	45.1 ± 14.2	62.3 ± 6.5	60.3 ± 9.3	<0.05
Sex (male/female)	88/85	117/219	53/61	<0.05
MRI scanner	GE HDX	Philips Ingenia	Siemens Prisma	
Field strength (Tesla)	1.5	3.0	3.0	
TR (ms)	53	20	20	
TE (ms)	40	17.5	17.5	
Voxel size (mm)	0.6 × 0.75 × 3	0.67 × 1.34 × 2	0.67 × 1.34 × 2	

SD, standard deviation.

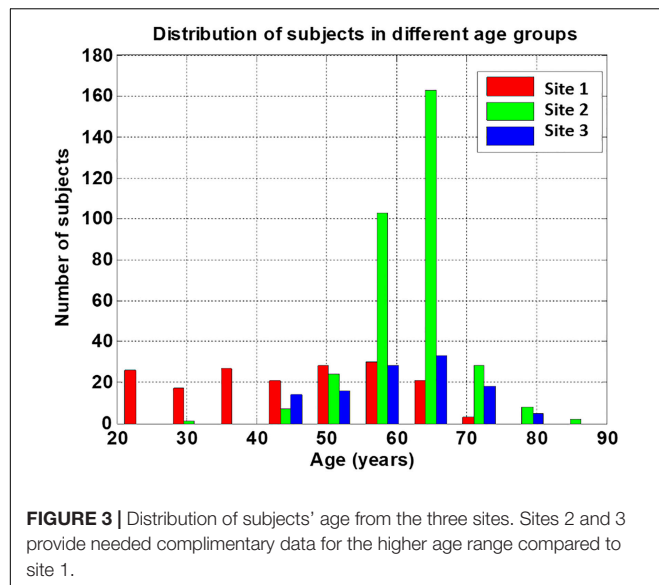
The subjects in both sites 2 and 3 were mainly between 55 and 65 years old, as shown in **Figure 3**.

Effect of Resolution on QSM in the Simulated Data

Figure 4 shows the plots of the measured susceptibility values in the various structures of interest in the simulated model for different resolutions. The measured susceptibility values in these plots are zero-referenced with respect to the measured susceptibility in the THA. As seen in these plots, the mean susceptibilities of CN, GP, and PUT are not significantly affected

by changing the slice thickness from 0.5 to 3 mm, but for the small structures, such as the SN and RN, the susceptibility is reduced about 10% for 2 mm thick slices and nearly 25% for 3 mm thick slices.

The iron content for the k-space cropped lower resolutions were compared to the original iron content measurements (**Figure 5**). Three representative structures were chosen to highlight in the Figure: the putamen because it is a large structure and the red nucleus and substantia nigra because they are small structures where we expect to see the biggest effect. We found that the R^2 values of the correlations were very high, on the order of 0.9 or higher indicating the closeness of the measurements.



The values of all the slopes and correlation measures are given in **Supplementary Table 1**. For those data that were originally cropped to lower resolution and retraced, the R values were in the range of 0.7 to 0.9 for site 1, 0.8 to 0.9 for site 2 and 0.7 to 0.9 for site 3 for most structures. However, despite not having as high R values as the original data, all the data points in the remeasured lower resolution still fell within the 95% confidence intervals determined by the higher resolution data.

Relationship Between Mean Susceptibility and Age

Global Analysis

For the global mean susceptibility analysis of iron content, the slopes (ppb/year) and intercepts (ppb) across the sites overlapped for all structures as shown in **Figures 6A,B**. Further, as shown in **Supplementary Table 2**, the mean values in the dominant age range (55–65 years) of sites 02 and 03 agree very well with those from site 1 suggesting that the 95% CI projections of site 1 to higher ages should match sites 2 and 3 well. With these two facts in mind, we have merged the data from all 3 sites into a single large dataset to assess the relationship between the mean magnetic susceptibility and age. As shown in **Supplementary Table 3** and **Figure 7**, the mean susceptibility correlated with age (with a positive slope) for the CN, PUT, RN, SN, and DN, all $p < 0.001$. For the THA, there was a strong negative correlation with age ($p < 0.001$). The mean susceptibility in the GP had a negative slope but it was not significantly different from zero ($p = 0.49$) while the PT had a small negative slope that was significant ($p < 0.01$).

RII Analysis

For the RII regional high iron content analysis, the slopes ranges (ppb/year) and intercepts (ppb) across the sites also overlapped for all structures (except for the PUT and RN) and are shown in **Figures 6C,D**. Further, as shown in **Supplementary Table 2**, the mean values in the dominant age range (55–65 years) of sites 2

and 3 agree very well with those from site 1 suggesting that the 95% CI projections of site 1 to higher ages should match sites 2 and 3 well. This allows for the data from the 3 sites to be merged into a single dataset to assess the relationship between the mean magnetic susceptibility and age for RII. For the RII analysis, as shown in **Table 3** and **Figure 8**, mean susceptibility in all the structures was moderately to strongly correlated with age (all $p < 0.001$) except for the THA. For the THA, there was a slight negative slope with age ($p < 0.001$).

Relationship Between Nuclei Volume and Age

Global Analysis

The parameters of the linear fitting equations for the global nuclei volumes versus age are given in **Supplementary Table 4**. The volumes of most nuclei, including the CN, GP, PUT, THA, PT, and RN were negatively correlated with age (all $p < 0.001$). Of interest is the fact that volumes for the SN and DN both increase with age. Volumes for the global analysis are shown in **Supplementary Figure 1**.

RII Analysis

There was a negative correlation between the volume of the RII region for the THA with age ($p < 0.001$) as shown in **Supplementary Table 5**. RII volumes of SN and DN increased with age significantly, but correlation between RII volume of RN and age was not significantly different from zero ($p = 0.14$). All the volumes for the RII analysis are shown in **Supplementary Figure 2**.

Relationship Between Total Iron Content (Volume × Mean Susceptibility) and Age

Global Analysis

The parameters of the linear fitting equations for total iron content globally versus age is given in **Supplementary Table 6** and **Supplementary Figure 3**. Apart from the GP, THA, and PT all the other structures showed an increasing total iron content despite the reductions in volume with age.

RII Analysis

The parameters of the linear fitting equations for RII analysis total iron versus age is given in **Supplementary Table 7** and **Supplementary Figure 4**. Like the global analysis, apart from the GP, THA, and PT all structures showed an increasing total iron content (despite the reductions in RII volume with age) as well as a much tighter distribution than the global iron dependence with age.

DISCUSSION

In this study, the effect of image resolution on the QSM quantification was evaluated based on a simulation model, as well as resampled original data. The consistency of QSM across field strengths and manufacturers in evaluating the DGM of the human brain was verified using a total of 623 subjects from multiple imaging sites, and a QSM baseline as a function of

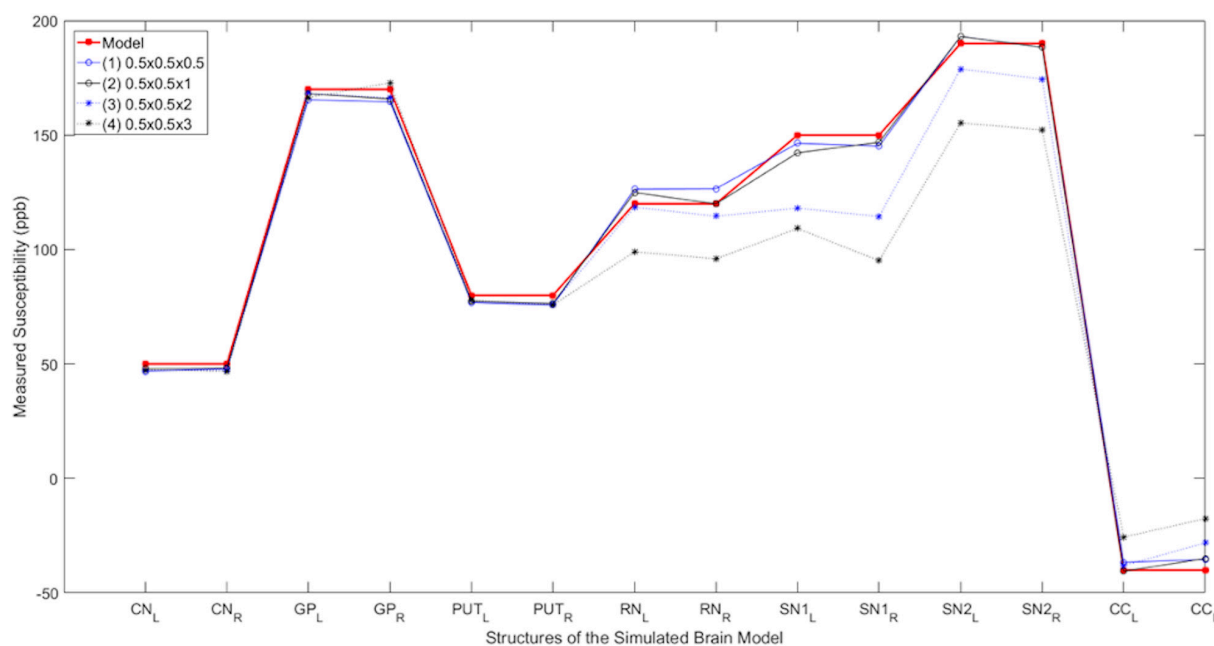


FIGURE 4 | Susceptibility as a function of slice thickness. Comparison of the measured susceptibility values (ppb) of different structures for both left (L) and right (R) sides in the reconstructed QSM data from the simulated noisy phase with different resolutions. The plot in red is the true susceptibility in the original high-resolution model and the other plots show the reconstructed QSM data with different resolutions. As seen in this figure, as the resolution reduces, the measured susceptibility values in smaller structures such as the RN, SN, and CC are negatively affected.

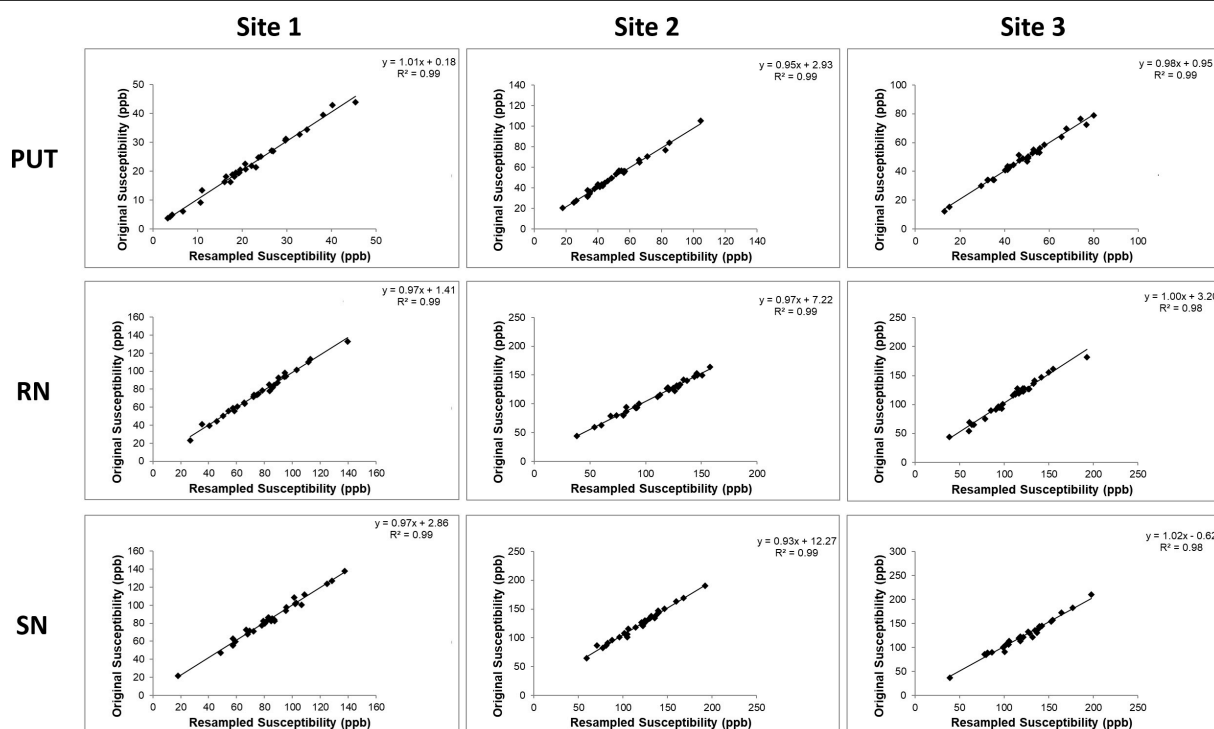


FIGURE 5 | Comparisons between the iron content of the PUT, RN, and SN in the k-space cropped lower resolution images and the original images. These correlations are very high because the same ROIs were used in the cropped and re-interpolated data. When the boundaries are redrawn on the lower resolution data (see **Supplementary Figure S5**), the correlations are not as good as those shown here, but the data still lies within the 95% confidence intervals as noted in the results section.

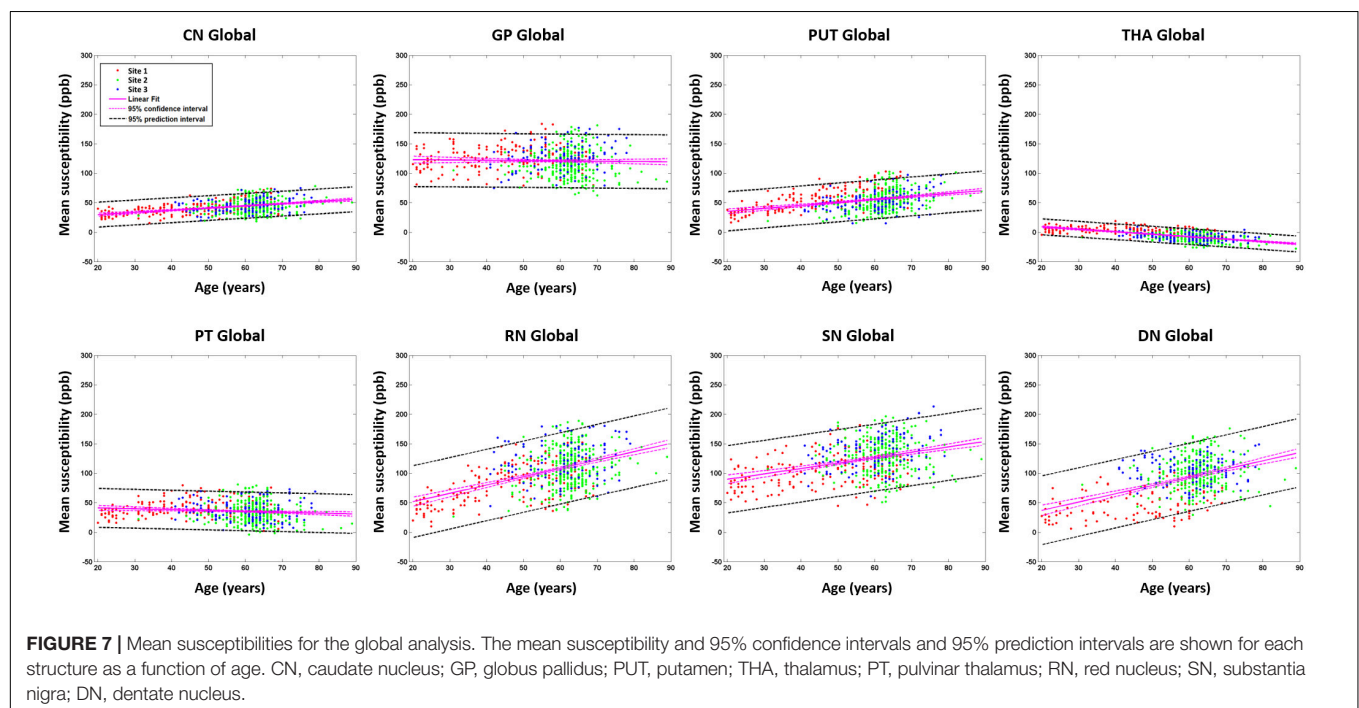
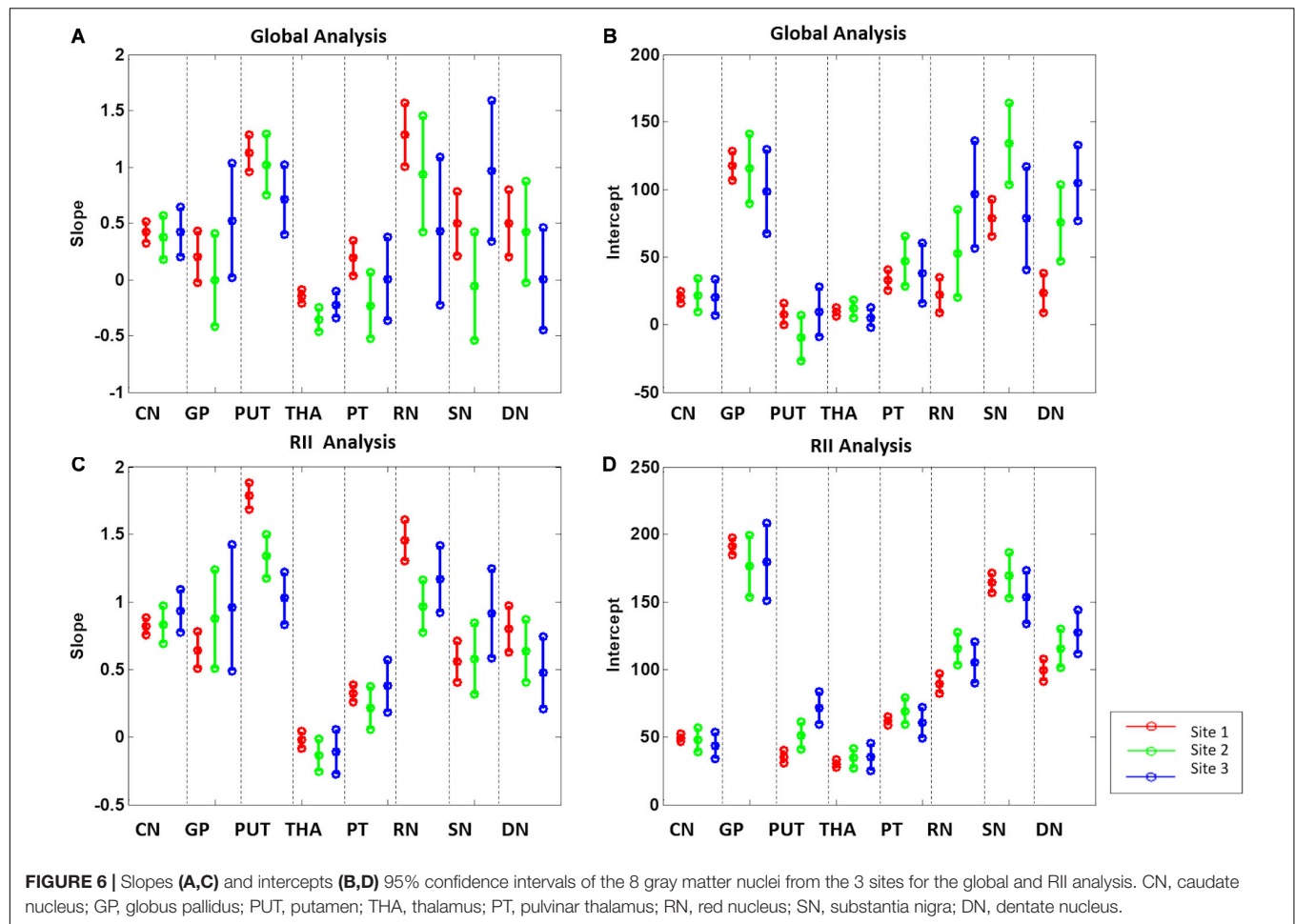
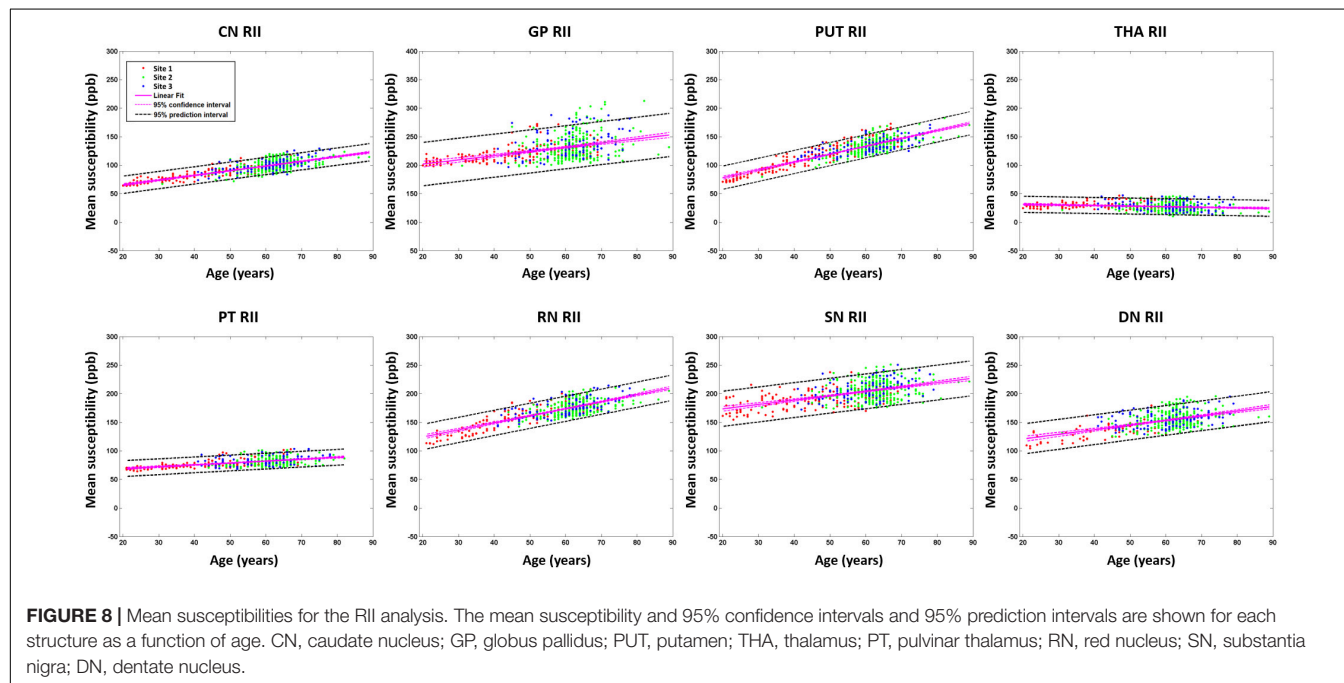


TABLE 3 | Linear fitting equations for mean susceptibility (χ) (ppb) versus age for the RII analysis.

	$\chi = A \times \text{age} + B$	Error in A (ppb/year)	Error in B (ppb)	r	r -CI	p -value
CN	$\chi = 0.82 \times \text{age} + 49$	0.05	2.89	0.80	(0.77, 0.83)	<0.001
GP	$\chi = 0.74 \times \text{age} + 187$	0.13	7.62	0.43	(0.36, 0.5)	<0.001
PUT	$\chi = 1.38 \times \text{age} + 50$	0.07	3.88	0.86	(0.83, 0.88)	<0.001
THA	$\chi = -0.1 \times \text{age} + 33$	0.05	2.70	-0.17	(-0.25, -0.09)	<0.001
PT	$\chi = 0.33 \times \text{age} + 62$	0.05	2.87	0.52	(0.45, 0.58)	<0.001
RN	$\chi = 1.23 \times \text{age} + 100$	0.09	5.14	0.77	(0.74, 0.81)	<0.001
SN	$\chi = 0.77 \times \text{age} + 158$	0.11	6.18	0.51	(0.45, 0.57)	<0.001
DN	$\chi = 0.81 \times \text{age} + 105$	0.12	6.98	0.53	(0.46, 0.59)	<0.001

R , Pearson correlation coefficient; r -CI, confidence interval of r .



age for each DGM structure for both global and regional iron analysis was determined. The RII analysis showed a much tighter correlation with age and a higher slope than the global analysis for all structures, providing an additional source of information outside whole structure mean iron or total iron for a reliable and sensitive reference for age-related changes. The age related data generated for each structure including susceptibility, volume, or total iron content for both the global and regional analysis can be used to correct for age dependence of each of these measures for monitoring abnormal global and regional iron deposition. The literature and data for RII is scant as it is a relatively new technique for measuring iron on QSM (Habib et al., 2012; Ghassaban et al., 2019; Sethi et al., 2019).

As for the RII analysis findings, the correlations of iron with age are moderate to strong in almost all structures other than the THA, which is consistent with the work of Liu et al. (2016). Even in the GP, which usually shows no iron content change over the lifespan after the age of 20 years (Hallgren, 1958; Xu et al., 2008; Li et al., 2014), we found the Pearson correlation coefficient for age and RII susceptibility greater than 0.40. Data from all

major DGM nuclei fell well within the calculated 95% confidence intervals derived from the merged data except for some outliers in the GP. These are likely due to high levels of mineralization in the caudal part of the structure. An added advantage to the RII analysis is that it is less dependent on an accurate drawing of the structure since much of the higher iron content regions are inside the boundaries of these structures. Finally, the slopes and intercepts found by merging the RII data from all three sites agrees with the iron trends with age in other studies (Liu et al., 2010, 2016; Ghassaban et al., 2019).

Iron Changes With Age

When considering the global analysis for all structures, susceptibility values for the subjects aged 55–65 years are accordance with values recorded by Acosta-Cabrero et al. (2016) on subjects aged 59–79 years. They delineated ROIs of the deep gray matter automatically (CN, PUT, and GP) and manually (RN, SN, and DN) on QSM. When comparing the regression slope and intercepts, there were differences between our study and theirs. One reason may be due to a 3D erosion function being

performed to remove spurious pixels whereas our study used a FWHM boundary for our global analysis. But the more likely reason is too narrow an age range without subjects in the 20 to 30 year decade to anchor the data properly. Their team did not report volumetric measurements. The susceptibility versus age plot for the thalamus was flat and similar to our plot, but with a shift in the intercept. Several of the structures have iron content in agreement with recent work by Zhang et al. (2018), who collected data across the human lifespan. The age-related increases in iron affect the morphology and contrast of the structure with the surrounding tissue which is particularly true for the DN. This may have applications to iron rich structures like the SN and GP. Further, we report similar global susceptibility changes with age to a recent work by Ghassaban et al. (2019), who recently used $0.86 \text{ mm} \times 0.86 \text{ mm} \times 1 \text{ mm}$ resolution at 3T.

Hallgren and Sourander (Hallgren, 1958) stated that in younger and middle-aged brains, advanced age was associated with greater iron concentrations in the basal ganglia than in subcortical WM, but noted that the association between age and iron content was attenuated after middle age. Much of the recent MR data actually show that there is a continued slow increase in age and the quantity and quality of the published data now by far supersedes the limited results in Hallgren and Sourander.

Of note in these results are the following observations. At any given age, there is a wide range of “normal” iron content. This makes it very hard to give a narrow range of age if one were to be given the iron content. This is less of a problem for the RII analysis because the results are more tightly bound. One might ask what causes this large variation of iron content and if it is related to some disease state like hypertension or vascular disease. This, in itself, would be an intriguing finding to ascertain why some elderly people have the same low iron content as younger people. Furthermore, there is strong neuropathologic evidence that iron overload is a hallmark of many neurodegenerative processes. Outcomes relating to progression of cognitive impairment are of particular interest (Belaidi and Bush, 2016; Moon et al., 2016; Lane et al., 2018; Chang, 2019). Many central nervous system disorders have also been associated with an excessive deposition of iron in specific brain locales as reported in Huntington’s disease (Chen et al., 2013) (caudate, putamen), Parkinson’s disease and multisystem atrophy (Lee et al., 2013; Péran et al., 2018; Seki et al., 2019) (putamen, globus pallidus), multiple sclerosis (Haacke et al., 2009; Mahad et al., 2015; Ropele et al., 2017; Zivadinov et al., 2018) (associated with the MS plaques), and intracerebral hematoma periphery (Garton et al., 2016). An understanding of the normal brain-iron distribution may also help interpret the pathophysiology of the brain damage that occurs in association with neurodegenerative, demyelinating, and vascular disorders.

Another interesting finding is the negative slope of the thalamus. To understand this effect, one has to look back at what QSM actually provides; it provides only changes in susceptibility. The positive and negative values represent more or less magnetic susceptibility relative to the reference region, respectively (Doring et al., 2016). So, if the WM remains the zero mark of QSM then the negative slope of the THA really represents an increasing iron content of the WM with age. Now WM is

diamagnetic relative to GM because it is myelinated. However, it has been shown that demyelinated WM has effectively the same susceptibility as GM (about 50 ppb) which makes sense because its overall iron content is about the same as that of gray matter (Haacke et al., 2005; Langkammer et al., 2012). Therefore, an increasing susceptibility of WM with age could represent a general demyelination over time. Since the THA susceptibility changes from roughly 10 ppb to -20 ppb over the age range of 20 years to 90 years, this suggests an increase of WM susceptibility of 30 ppb or a little over half of the difference between healthy WM and GM.

Another consideration is determining the total iron content from susceptibility by estimating the iron concentration from the age equations provided in Hallgren and Sourander’s work as done in other studies (Aquino et al., 2009; Liu et al., 2016). On the assumption that the gray matter density (GMD) remains constant with age, the total iron content is proportional to gray matter volume (GMV). In fact, GMD changes with age, sex, and is not easily quantified (Gennatas et al., 2017). There are a variety of methods that can be used in the future to determine absolute water content and thereby solving this problem; one such method is STrategically Acquired Gradient Echo (STAGE) imaging (Haacke et al., 2020).

Volume Changes With Age

Our volumetric results for the subjects in the 55-year age range and up are in accordance with recent work by He et al. (2017). Also, Ghassaban et al. (2019) showed volumes decreased with age for all structures (except for SN and DN), suggesting brain atrophy occurs with age. Fjell et al. (2013) measured segmented brain volumes over time for adults 18–94 years of age; while they fit the volumes with an exponential function for age, they noted corresponding decreases in GM volume with age. In another study assessing volumes at 1.5T, Raz et al. (2003) also noted decreases in GM volume in the CN and PUT in a cohort of 55 subjects aged 20–77 years, but not the GP which is highly subject to perivascular spaces and mineralization. Areas of mineralization and large veins were not measured in our ROIs, however, perivascular spaces are not as easily visualized on magnitude on which our tracings were performed and may contribute to the discrepancy in the age versus volume plots between these studies.

For SN and DN, there is a small positive correlation with age, possibly because the increased iron content makes the structures clearer on the QSM data. Our volumetric results, nevertheless, are in accordance with a work which involved 38 subjects, aged 64.1 ± 7.5 years, with DN volumes ranging between 600 and 800 mm^3 (He et al., 2017). For the SN, the volumes for our analysis overlap well with data for 20 controls (mean age, 60.8 ± 8.3 years, SN volume = $400\text{--}650 \text{ mm}^3$) (Pyatigorskaya et al., 2018). Likewise, total iron content followed the same trends.

Resolution Effects

As far as resolution is concerned, the large structures are not much affected by slices as thick as 3 mm but the SN, RN and DN are expected to have lower susceptibilities for slices that are too thick. The final effects of these thicker slices also

depend to some degree on how the structures are drawn and if partial volume effects are considered. The advantage of tracing the DN on QSM, instead of T2W or SWI, is that the variability of the structural volume is reduced (He et al., 2017). Our group opted to use FWHM to trace the structures which may confer a high reliability between the raters, however, for structures which have smaller size and more intricate detail like the DN, it may be a drawback. Ideally, an automated means to assess the structures may improve the agreement between all structures, field strengths and manufacturers. Both our simulations and the restructuring of the data show that even with resolutions as low as $0.67 \text{ mm} \times 1.34 \text{ mm} \times 3 \text{ mm}$, iron content with age still follows the pattern as shown in this paper, although some minor deviations can occur for smaller objects such as the RN and SN. Nevertheless, for sufficient SNR, higher resolution is always desirable for better edge definition and volume measurements (such as the higher resolution used for sites 2 and 3: $0.67 \times 1.34 \times 2 \text{ mm}^3$).

Limitations

There are several limitations to this study. First, the distribution of subject age was different between site 1 and the other two sites as was the slice thickness. Nevertheless, for larger structures this did not affect the susceptibilities significantly. Second, other QSM methods may provide slightly higher absolute levels of susceptibility by 5 to 10% but, as long as any one method is used consistently across sites and imaging parameters, then the results should be consistent with those presented herein (Liu et al., 2016).

CONCLUSION

Although QSM has the potential to be a robust technology, care must be taken in assessing some smaller structures like the DN, the RN and the SN to avoid reconstruction bias based on slice thickness. We recommend using a slice thickness no greater than 2 mm to avoid a resolution-related reduction in susceptibility values. RII iron analysis showed a tighter age-related behavior than global iron analysis and appeared to be less susceptible to imaging parameters, field strength, or region drawing. For the first time, we showed that the local iron content in the GP increases with age (range 20–90 years) despite the global iron remaining roughly constant. Almost all structures showed a reduction in iron containing volumes with age except for the SN and DN. Finally, the results of this work show that a reasonable estimate for age-related iron behavior can be obtained from a large cross site, cross manufacturer set of data and can be used for correcting for age related iron changes when

studying diseases like Parkinson's disease and other iron related neurodegenerative diseases.

DATA AVAILABILITY STATEMENT

The raw data supporting the conclusions of this article will be made available by the authors, without undue reservation.

ETHICS STATEMENT

The studies involving human participants were reviewed and approved by the First Affiliated Hospital of Dalian Medical University, Ruijin Hospital, Shanghai Jiao Tong University School of Medicine, and the First Affiliated Hospital of Zhengzhou University. The patients/participants provided their written informed consent to participate in this study.

AUTHOR CONTRIBUTIONS

YL: conceptualization, methodology, formal analysis, investigation, data curation, and writing – original draft. SS: conceptualization, software, validation, writing – original draft, and visualization. CZ, YM, and JC: investigation. KY and VP: methodology and software. SG: data curation and writing – review and editing. CW: writing – review and editing. NH: investigation and funding acquisition. FY: resources, supervision, project administration, and funding acquisition. EH: conceptualization, supervision, and writing – review and editing. All authors agreed to be accountable for the content of the work.

FUNDING

This work was supported by the Science and Technology Commission of Shanghai Municipality (17411952700), Shanghai Sailing Program (18YF1414700), National Natural Science Foundation of China (81971576 and 81801652), Shanghai Science and Technology Committee (18DZ1930103), and Innovative research team of high-level local universities in Shanghai.

SUPPLEMENTARY MATERIAL

The Supplementary Material for this article can be found online at: <https://www.frontiersin.org/articles/10.3389/fnins.2020.607705/full#supplementary-material>

REFERENCES

- Abdul-Rahman, H. S., Gdeisat, M. A., Burton, D. R., Lalor, M. J., Lilley, F., and Moore, C. J. (2007). Fast and robust three-dimensional best path phase unwrapping algorithm. *Appl. Opt.* 46, 6623–6635. doi: 10.1364/AO.46.006623
- Acosta-Cabronero, J., Betts, M. J., Cardenas-Blanco, A., Yang, S., and Nestor, P. J. (2016). In vivo MRI mapping of brain iron deposition across the adult lifespan. *J. Neurosci.* 36, 364–374. doi: 10.1523/JNEUROSCI.1907-15.2016
- Álvarez-Córdoba, M., Fernández Khoury, A., Villanueva-Paz, M., Gómez-Navarro, C., Villalón-García, I., Suárez-Rivero, J. M., et al. (2019). Pantothenate Rescues Iron Accumulation in Pantothenate Kinase-Associated Neurodegeneration

- Depending on the Type of Mutation. *Mol. Neurobiol.* 56, 3638–3656. doi: 10.1007/s12035-018-13331330
- Aquino, D., Bizzi, A., Grisoli, M., Barbara, G., Maria Grazia, B., and Nardo, N. (2009). Age-related Iron Deposition in the Basal Ganglia: Quantitative Analysis in Healthy Subjects. *Radiology* 252, 165–172. doi: 10.1148/radiol.2522081399
- Belaïdi, A. A., and Bush, A. I. (2016). Iron neurochemistry in Alzheimer's disease and Parkinson's disease: targets for therapeutics. *J. Neurochem.* 2016, 179–197. doi: 10.1111/jnc.13425
- Brown, R. (2014). *Magnetic resonance imaging: physical principles and sequence design*. New Jersey: Wiley-Blackwell.
- Buch, S. (2012). *A Brain Model For The Study Of MR Susceptibility Induced Phase Behavior*. New Jersey: Wiley-Blackwell.
- Chang, Y. (2019). *Advances in Experimental Medicine and Biology 1173 Brain Iron Metabolism and CNS Diseases*. Available at <http://www.springer.com/series/5584> New York: Springer.
- Chen, J., Marks, E., Lai, B., Zhang, Z., Duce, J. A., Lam, L. Q., et al. (2013). Iron Accumulates in Huntington's Disease Neurons: Protection by Deferoxamine. *PLoS One* 8, 1–12. doi: 10.1371/journal.pone.0077023
- Connor, J. R., Menzies, S. L., Martin, S. M. S., and Mufson, E. J. (1990). Cellular Distribution of Transferrin, Ferritin, and Iron in Normal and Aged Human Brains. *J. Neurosci. Res.* 27, 595–611. doi: 10.1002/jnr.490270421
- Daugherty, A., and Raz, N. (2013). NeuroImage Age-related differences in iron content of subcortical nuclei observed in vivo: A meta-analysis. *Neuroimage* 70, 113–121. doi: 10.1016/j.neuroimage.2012.12.040
- Deistung, A., Stefanescu, M. R., Ernst, T. M., Schlamann, M., Ladd, M. E., Reichenbach, J. R., et al. (2016). Structural and Functional Magnetic Resonance Imaging of the Cerebellum: Considerations for Assessing Cerebellar Ataxias. *Cerebellum* 15, 21–25. doi: 10.1007/s12311-015-0738739
- Doring, T. M., Granado, V., Rueda, F., Deistung, A., Reichenbach, J. R., Tukamoto, G., et al. (2016). Quantitative susceptibility mapping indicates a disturbed brain iron homeostasis in Neuromyelitis Optica - A pilot study. *PLoS One* 11, 1–14. doi: 10.1371/journal.pone.0155027
- Drayer, P. (1986). Imaging of the aging brain. Part I. Normal findings. *Radiology* 166, 785–796. doi: 10.1148/radiology.166.3.3277247
- Feng, X., Deistung, A., and Reichenbach, J. R. (2018). Quantitative susceptibility mapping (QSM) and R2* in the human brain at 3 T: Evaluation of intra-scanner repeatability. *Z. Med. Phys.* 28, 36–48. doi: 10.1016/j.zemedi.2017.05.003
- Fjell, A. M., Westlye, L. T., Grydeland, H., Amlie, I., Espeseth, T., Reinvang, I., et al. (2013). Critical ages in the life course of the adult brain: Nonlinear subcortical aging. *Neurobiol. Aging* 34, 2239–2247. doi: 10.1016/j.neurobiolaging.2013.04.006
- Garton, T., Keep, R. F., Hua, Y., and Xi, G. (2016). Brain iron overload following intracranial haemorrhage. *Stroke Vasc. Neurol.* 1, 172–184. doi: 10.1136/svn-20162042
- Gennatas, E. D., Avants, B. B., Wolf, D. H., Satterthwaite, T. D., Ruparel, K., Ciric, R., et al. (2017). Age-related effects and sex differences in gray matter density, volume, mass, and cortical thickness from childhood to young adulthood. *J. Neurosci.* 37, 5065–5073. doi: 10.1523/JNEUROSCI.3550-16.2017
- Ghassaban, K., He, N., Sethi, S. K., Huang, P., Chen, S., Yan, F., et al. (2019). Regional high iron in the substantia nigra differentiates Parkinson's disease patients from healthy controls. *Front. Aging Neurosci.* 11, 1–10. doi: 10.3389/fnagi.2019.00106
- Ghassaban, K., Liu, S., Jiang, C., and Haacke, E. M. (2018). Quantifying iron content in magnetic resonance imaging Kiarash. *Neuroimage* 187, 77–92. doi: 10.1016/j.neuroimage.2018.04.047
- Haacke, E. M., Chen, Y., Utraiainen, D., Wu, B., Wang, Y., Xia, S., et al. (2020). STrategically Acquired Gradient Echo (STAGE) imaging, part III: Technical advances and clinical applications of a rapid multi-contrast multi-parametric brain imaging method. *Magn. Reson. Imag.* 65, 15–26. doi: 10.1016/j.mri.2019.09.006
- Haacke, E. M., Cheng, N. Y. C., House, M. J., Liu, Q., Neelavalli, J., Ogg, R. J., et al. (2005). Imaging iron stores in the brain using magnetic resonance imaging. *Magn. Reson. Imag.* 23, 1–25. doi: 10.1016/j.mri.2004.10.001
- Haacke, E. M., Makki, M., Ge, Y., Maheshwari, M., Sehgal, V., Hu, J., et al. (2009). Characterizing iron deposition in multiple sclerosis lesions using susceptibility weighted imaging. *J. Magn. Reson. Imag.* 29, 537–544. doi: 10.1002/jmri.21676
- Haacke, E. M., Miao, Y., Liu, M., Habib, C. A., Katkuri, Y., Liu, T., et al. (2010). Correlation of Putative Iron Content as Represented by Changes in R2* and Phase With Age in Deep Gray Matter of Healthy Adults. *J. Magn. Reson. Imag.* 32, 561–576. doi: 10.1002/jmri.22293
- Habib, C. A., Liu, M., Bawany, N., Garbern, J., Krumbein, L., Mentzel, H. J., et al. (2012). Assessing abnormal iron content in the deep gray matter of patients with multiple sclerosis versus healthy controls. *Am. J. Neuroradiol.* 33, 252–258. doi: 10.3174/ajnr.A2773
- Hallgren, B. (1958). The Effect Of Age On The Non-Haemin Iron In The Human Brain. *J. Neurochem.* 3, 41–51. doi: 10.1111/j.1471-4159.1958.tb12607.x
- Hare, D., Ayton, S., Bush, A., and Lei, P. (2013). A delicate balance: iron metabolism and diseases of the brain. *Front. Aging Neurosci.* 5, 1–19. doi: 10.3389/fnagi.2013.00034
- He, N., Langley, J., Huddleston, D. E., Ling, H., Xu, H., Liu, C., et al. (2017). Improved Neuroimaging Atlas of the Dentate Nucleus. *Cerebellum* 16, 951–956. doi: 10.1007/s12311-017-0872877
- Ippoliti, M., Adams, L. C., Winfried, B., Hamm, B., Spincemaille, P., Wang, Y., et al. (2018). Quantitative susceptibility mapping across two clinical field strengths: Contrast-to-noise ratio enhancement at 1.5T. *J. Magn. Reson. Imag.* 48, 1410–1420. doi: 10.1002/jmri.26045
- Keuken, M. C., Bazin, P. L., Backhouse, K., Beekhuizen, S., Himmer, L., Kandola, A., Lafeber, J. J. (2017). Effects of aging on T1, T2*, and QSM MRI values in the subcortex. *Brain Struct. Funct.* 222, 2487–2505. doi: 10.1007/s00429-016-13521354
- Koeppen, A. H. (2003). A brief history of brain iron research. *J. Neurol. Sci.* 207, 95–97. doi: 10.1016/s0022-510x(02)00429-x
- Kofi, D. (2015). Reproducibility of quantitative susceptibility mapping in the brain at two field strengths from two vendors. *IPSI SIG Tech.* 42, 1592–1600. doi: 10.1002/jmri.24943
- Lane, D. J. R., Ayton, S., and Bush, A. I. (2018). Iron and Alzheimer's Disease: An Update on Emerging Mechanisms. *J. Alzheimer's Dis.* 64, S379–S395. doi: 10.3233/JAD-179944
- Langkammer, C., Pirpamer, L., Seiler, S., Deistung, A., Schweser, F., Franthal, S., et al. (2016). Quantitative Susceptibility Mapping in Parkinson's Disease. *PLoS One* 11:e0162460. doi: 10.1371/journal.pone.0162460
- Langkammer, C., Schweser, F., Krebs, N., Deistung, A., Goessler, W., Scheurer, E., et al. (2012). Quantitative susceptibility mapping (QSM) as a means to measure brain iron: A post mortem validation study. *Neuroimage* 62, 1593–1599. doi: 10.1016/j.neuroimage.2012.05.049
- Lee, J. H., and Lee, M. S. (2019). Brain iron accumulation in atypical parkinsonian syndromes: In vivo MRI evidences for distinctive patterns. *Front. Neurol.* 10, 1–9. doi: 10.3389/fneur.2019.00074
- Lee, J. H., Han, Y. H., Kang, B. M., Mun, C. W., Lee, S. J., and Baik, S. K. (2013). Quantitative assessment of subcortical atrophy and iron content in progressive supranuclear palsy and parkinsonian variant of multiple system atrophy. *J. Neurol.* 260, 2094–2101. doi: 10.1007/s00415-013-6951-x
- Li, W., Wu, B., Batrachenko, A., Bancroft-wu, V., Morey, R. A., Shashi, V., et al. (2014). Differential Developmental Trajectories of Magnetic Susceptibility in Human Brain Gray and White Matter Over the Lifespan. *Hum. Brain Mapp.* 35, 2698–2713. doi: 10.1002/hbm.22360
- Liu, J., Liu, T., Rochefort, L., De, Khalidov, I., Prince, M., et al. (2010). Quantitative susceptibility mapping by regulating the field to source inverse problem with a sparse prior derived from the Maxwell Equation: validation and application to brain. *Proc. Annu. Meet. ISMRM* 18:4996.
- Liu, M., Liu, S., Ghassaban, K., Zheng, W., Diccio, D., Miao, Y., et al. (2016). Assessing Global and Regional Iron Content in Deep Gray Matter as a Function of Age Using Susceptibility Mapping. *J. Magn. Reson. Imag.* 144, 59–71. doi: 10.1002/jmri.25130
- Liu, S., Buch, S., Chen, Y., Choi, H., Dai, Y., Hu, J., et al. (2017). Susceptibility Weighted Imaging: Current Status and Future Directions. *NMR Biomed.* 30, 1–46. doi: 10.1002/nbm.3552
- Mahad, D. H., Trapp, B. D., and Lassmann, H. (2015). Pathological mechanisms in progressive multiple sclerosis. *Lancet Neurol.* 14, 183–193. doi: 10.1016/S1474-4422(14)70256-X
- Moon, Y., Han, S. H., and Moon, W. J. (2016). Patterns of Brain Iron Accumulation in Vascular Dementia and Alzheimer's Dementia Using Quantitative Susceptibility Mapping Imaging. *J. Alzheimer's Dis.* 51, 737–745. doi: 10.3233/JAD-151037

- Mostile, G., Cicero, C. E., Giuliano, L., Zappia, M., and Nicoletti, A. (2017). Iron and Parkinson's disease: A systematic review and meta-analysis. *Mol. Med. Rep.* 15, 3383–3389. doi: 10.3892/mmr.2017.6386
- Nikseresht, S., Bush, A. I., and Ayton, S. (2019). Treating Alzheimer's disease by targeting iron. *Br. J. Pharmacol.* 176, 3622–3635. doi: 10.1111/bph.14567
- Péran, P., Barbagallo, G., Nemmi, F., Sierra, M., Galitzky, M., Traon, A. P., et al. (2018). MRI supervised and unsupervised classification of Parkinson's disease and multiple system atrophy. *Mov. Disord.* 33, 600–608. doi: 10.1002/mds.27307
- Pyatigorskaya, N., Magnin, B., Mongin, M., Yahia-Cherif, L., Valabregue, R., Arnaldi, D., et al. (2018). Comparative study of MRI biomarkers in the substantia nigra to discriminate idiopathic Parkinson disease. *Am. J. Neuroradiol.* 39, 1460–1467. doi: 10.3174/ajnr.A5702
- Raz, N., Rodrigue, K. M., Kennedy, K. M., Head, D., Gunning-Dixon, F., and Acker, J. D. (2003). Differential Aging of the Human Striatum: Longitudinal Evidence. *Am. J. Neuroradiol.* 24, 1849–1856.
- Ropele, S., Enzinger, C., and Fazekas, F. (2017). Iron Mapping in Multiple Sclerosis. *Neuroimage. Clin. N. Am.* 27, 335–342. doi: 10.1016/j.nic.2016.12.003
- Santin, M. D., Didier, M., Valabrègue, R., Yahia Cherif, L., García-Lorenzo, D., Loureiro, et al. (2017). Reproducibility of R2* and quantitative susceptibility mapping (QSM) reconstruction methods in the basal ganglia of healthy subjects. *NMR Biomed.* 30:3491. doi: 10.1002/nbm.3491
- Schwarz, S. T., Afzal, M., Morgan, P. S., Bajaj, N., and Auer, D. P. (2014). Nigrosome imaging with T2*-weighted 3T MRI as a diagnostic marker of Parkinson's disease: a case-control and cross-sectional study of diagnostic accuracy. *Lancet* 383:S94. doi: 10.1016/S0140-6736(14)6035760353
- Schweser, F., Deistung, A., Lehr, B. W., and Reichenbach, J. R. (2011). Quantitative imaging of intrinsic magnetic tissue properties using MRI signal phase: An approach to in vivo brain iron metabolism? *Neuroimage* 54, 2789–2807. doi: 10.1016/j.neuroimage.2010.10.070
- Seki, M., Seppi, K., Mueller, C., Potrusil, T., Goebel, G., Reiter, E., et al. (2019). Diagnostic Potential of Multimodal MRI Markers in Atypical Parkinsonian Disorders. *J. Parkinsons. Dis.* 9, 681–691. doi: 10.3233/JPD-181568
- Sethi, S. K., Kisch, S. J., Ghassaban, K., Rajput, A., Rajput, A., Babyn, P. S., et al. (2019). Iron quantification in Parkinson's disease using an age-based threshold on susceptibility maps: The advantage of local versus entire structure iron content measurements. *Magn. Reson. Imag.* 55, 145–152. doi: 10.1016/j.mri.2018.10.001
- Smith, S. M. (2002). Fast robust automated brain extraction. *Hum. Brain Mapp.* 17, 143–155. doi: 10.1002/hbm.10062
- Tang, J., Liu, S., Neelavalli, J., Cheng, Y. C. N., Buch, S., and Haacke, E. M. (2013). Improving susceptibility mapping using a threshold-based K-space/image domain iterative reconstruction approach. *Magn. Reson. Med.* 69, 1396–1407. doi: 10.1002/mrm.24384
- Thomas, G. E. C., Leyland, L. A., Schrag, A. E., Lees, A. J., Acosta-Cabronero, J., and Weil, R. S. (2020). Brain iron deposition is linked with cognitive severity in Parkinson's disease. *J. Neurol. Neurosurg. Psych.* 91, 418–425. doi: 10.1136/jnnp-2019322042
- Xu, X., Wang, Q., and Zhang, M. (2008). Age, gender, and hemispheric differences in iron deposition in the human brain: An in vivo MRI study. *Neuroimage* 40, 35–42. doi: 10.1016/j.neuroimage.2007.11.017
- Yan, F., He, N., Lin, H., and Li, R. (2018). Iron deposition quantification: Applications in the brain and liver. *J. Magn. Reson. Imag.* 48, 301–317. doi: 10.1002/jmri.26161
- Zhang, Y., Wei, H., Cronin, M. J., He, N., Yan, F., and Liu, C. (2018). Longitudinal data for magnetic susceptibility of normative human brain development and aging over the lifespan. *Data Br.* 20, 623–631. doi: 10.1016/j.dib.2018.06.005
- Zhou, L., Chen, Y., Li, Y., Gharabaghi, S., Chen, Y., and Sethi, S. K. (2020). Intracranial iron distribution and quantification in aceruloplasminemia: A case study. *Magn. Reson. Imag.* 70, 29–35. doi: 10.1016/j.mri.2020.02.016
- Zivadinov, R., Tavazzi, E., Bergsland, N., Hagemeyer, J., Lin, F., Dwyer, M. G., et al. (2018). Brain iron at quantitative MRI is associated with disability in multiple sclerosis. *Radiology* 289, 487–496. doi: 10.1148/radiol.2018180136

Conflict of Interest: SS, SG, and EH were employed by Magnetic Resonance Innovations, Inc., and SpinTech, Inc. KY and VP were employed by MR Medical Imaging Innovations India.

The remaining authors declare that the research was conducted in the absence of any commercial or financial relationships that could be construed as a potential conflict of interest.

Copyright © 2021 Li, Sethi, Zhang, Miao, Yerramsetty, Palutla, Gharabaghi, Wang, He, Cheng, Yan and Haacke. This is an open-access article distributed under the terms of the Creative Commons Attribution License (CC BY). The use, distribution or reproduction in other forums is permitted, provided the original author(s) and the copyright owner(s) are credited and that the original publication in this journal is cited, in accordance with accepted academic practice. No use, distribution or reproduction is permitted which does not comply with these terms.



Increased Brain Iron Detection by Voxel-Based Quantitative Susceptibility Mapping in Type 2 Diabetes Mellitus Patients With an Executive Function Decline

Jing Li^{1†}, Qihao Zhang^{2†}, Nan Zhang^{3†} and Lingfei Guo^{3*†}

¹ Department of Radiology, Beijing Friendship Hospital, Capital Medical University, Beijing, China, ² Department of Radiology, Weill Cornell Medical College, New York, NY, United States, ³ Shandong Medical Imaging Research Institute, Cheeloo College of Medicine, Shandong University, Jinan, China

OPEN ACCESS

Edited by:

Mark Haacke,
Wayne State University, United States

Reviewed by:

Niels Bergsland,
University at Buffalo, United States
Sean K. Sethi,
Wayne State University, United States

*Correspondence:

Lingfei Guo
glfsci@163.com

†ORCID:

Jing Li
orcid.org/0000-0001-9392-6600
Qihao Zhang
orcid.org/0000-0002-8054-5849
Nan Zhang
orcid.org/0000-0002-6202-9349
Lingfei Guo
orcid.org/0000-0002-4885-625X

Specialty section:

This article was submitted to
Brain Imaging Methods,
a section of the journal
Frontiers in Neuroscience

Received: 15 September 2020

Accepted: 07 December 2020

Published: 15 January 2021

Citation:

Li J, Zhang Q, Zhang N and
Guo L (2021) Increased Brain Iron
Detection by Voxel-Based
Quantitative Susceptibility Mapping
in Type 2 Diabetes Mellitus Patients
With an Executive Function Decline.
Front. Neurosci. 14:606182.
doi: 10.3389/fnins.2020.606182

Purpose: Brain iron accumulation has been suggested as a pathomechanism in patients with type 2 diabetes mellitus (T2DM) with cognitive impairment. This research aims to examine the total-brain pattern of iron accumulation in relation to executive function decline in patients with T2DM by voxel-based quantitative susceptibility mapping (QSM) analysis.

Materials and Methods: A total of 32 patients with T2DM and 34 age- and sex-matched healthy controls (HCs) were enrolled in this study. All participants underwent brain magnetic resonance examination, and 48 individuals underwent cognitive function assessments. Imaging data were collected with three-dimensional fast low-angle shot sequences to achieve magnitude as well as phase images. Using voxel-based QSM analysis, we compared the voxel-wise susceptibility values of the whole brain among groups and explored whether the susceptibility values had correlations with cognitive data.

Results: Among the 66 participants, cognitive function was estimated in 23 patients with T2DM (11 males and 12 females; average age, 64.65 ± 8.44 years) and 25 HCs (13 males and 12 females; average age, 61.20 ± 7.62 years). T2DM patients exhibited significantly ($t = 4.288$, $P < 0.001$) lower Montreal Cognitive Assessment (MoCA) scores [T2DM, 27 (27, 28); HCs, 29 (28, 29); normal standard ≥ 26] and higher Trail-making Test (TMT)-A/TMT-B scores [71 (51, 100)/185 (149, 260)] than HCs [53 (36.5, 63.5)/150 (103, 172.5)] ($Z = 2.612$, $P = 0.009$; $Z = 2.797$, $P = 0.005$). Subjects with T2DM showed significantly higher susceptibility values than HCs in the caudate/putamen/pallidum, frontal inferior triangular gyrus, and precentral gyrus on the right hemisphere. In contrast (HC > T2DM), no region showed a significant difference in susceptibility values between the groups. The correlation analysis between susceptibility values and cognitive function scores was tested by voxel-based susceptibility value with sex and age as covariates. After multiple comparison correction, in T2DM patients, the left thalamus showed a significant relationship with TMT-A ($R^2 = 0.53$, $P = 0.001$). The right thalamus and left

thalamus showed a significant relationship with TMT-B ($R^2 = 0.35$, $P = 0.019$; and $R^2 = 0.38$, $P = 0.017$, respectively). In HCs, the cluster of right precentral/middle frontal gyrus/inferior frontal gyrus/inferior triangular gyrus showed a significant relationship with TMT-B ($R^2 = 0.59$, $P = 0.010$). No relationship was found between the susceptibility values with MoCA in the brain region in both two groups.

Conclusion: Patients with T2DM presented declined cognitive assessments and elevated iron deposition in the striatum and frontal lobe, suggesting that executive function decline in T2DM might be associated with the cerebral iron burden and that changes in susceptibility values may represent a latent quantitative imaging marker for early assessment of cognitive decline in patients with T2DM.

Keywords: type 2 diabetes mellitus, magnetic resonance imaging, quantitative susceptibility mapping, iron deposition, executive function

BACKGROUND

In type 2 diabetes mellitus (T2DM), peripheral insulin resistance together with compensatory insulin hypersecretion from pancreatic islets likely results in some complications, such as neuropathy, nephropathy, atherosclerosis, and retinopathy (Forbes and Cooper, 2013). Insulin resistance in the brain will lead to subsequent sequelae, which might result in tau hyperphosphorylation and/or amyloid accretion. Insulin functions through the distribution of iron in neuronal tissue; nonetheless, an insulin-resistant state has a disruptive role in the process, consequently resulting in detrimental iron overload (Medhi and Chakrabarty, 2013). Additionally, insulin resistance leads to high permeability of the blood–brain barrier (BBB), and increased permeability with leakage of material into the vessel wall and perivascular tissue will cause inflammation (Wardlaw et al., 2013; Takechi et al., 2017). The inflammatory status of the brain can influence brain iron metabolism and lead to iron deposition (McCarthy et al., 2018). The accumulation of iron in neurons will induce damage by apoptosis (Ward et al., 2014). Therefore, we speculated that the iron excess caused by T2DM can generate damage within the central nervous system.

T2DM patients suffer from cognitive deficits of memory, executive function (EF), attention, visuospatial capabilities, and other domains (McCrimmon et al., 2012). According to one proposal, an early onset of T2DM and weak glycemic control together with microvascular and macrovascular complications may lead to combined cognitive impairment. T2DM can be applied as an individual independent risk factor for Alzheimer's disease (AD), vascular dementia (VD), and mild cognitive impairment (MCI) (Moon et al., 2016). Patients with T2DM have more executive dysfunction than individuals without diabetes (Minami et al., 2020), which is related to mild-to-moderate EF decreases (Vincent and Hall, 2015). EF decreases in T2DM patients than in healthy older controls but at a smaller scale in AD patients suffering from impairments in executive processing, and T2DM patients may be at a higher risk of developing AD (Redondo et al., 2016).

Heretofore, to image biomarkers, several magnetic resonance imaging (MRI) techniques have been proposed in T2DM patients

with cognitive impairment (Zilliox et al., 2016). Because it is easy to provide precise location information of the brain regions for voxel-based morphometry (VBM) (Chen et al., 2017), VBM has been used widely, and gray matter structural and volume alterations of the brain have been revealed to be related to cognitive impairment (Liu et al., 2017). On the basis of a growing number of studies on MRI, brain iron overload has been observed in various neurodegenerative illnesses and is related to cognitive decline (Ward et al., 2014; Del et al., 2015; Daglas and Adlard, 2018; Chai et al., 2019). Quantitative susceptibility mapping (QSM) represents an updated MRI strategy that facilitates quantification of materials by changing susceptibility and enables non-invasive quantitative analysis of brain iron deposition (de Rochefort et al., 2010; Schweser et al., 2012; Wang et al., 2017). The functions of iron in DNA synthesis, gene expression, neurotransmission, myelination of neurons, and the mitochondrial system are considered crucial components in the brain. Therefore, the brain's iron balance requires strict regulation. Abnormal iron metabolism is relevant to many brain illnesses or disorders. However, the abnormal mode of brain iron accumulation in patients with T2DM has not been fully elucidated *in vivo*. The relationship between iron accumulation and EF decline in T2DM has not been revealed and publicized. Therefore, this research focuses on assessing the whole-brain pattern of iron accumulation in relation to EF decline in patients with T2DM by voxel-based QSM analysis.

MATERIALS AND METHODS

Participants

This cross-sectional research consisted of 32 T2DM patients (20 males; average age, 61.09 ± 9.99 years; age range 39–75 years) and 34 age- and sex-matched healthy control (HC) volunteers (15 males; average age, 58.50 ± 10.07 years; age range, 35–73 years) who were registered from December 2018 to April 2020. The patients all met the diagnostic criteria of T2DM (the diagnosis was based on the American Diabetes Association criteria). In this research, no special selection of

T2DM patients according to metabolic control, the existence of micro- or macrovascular complications, neuropathy, the disease duration or treatment type for hyperglycemia, vascular risk factors, or arterial hypertension was applied. The HC volunteers without T2DM had no history of elevated blood glucose levels, and their blood glucose levels were maintained in the normal range (fasting glucose < 5.5 mmol/L). Patients who had a greater than 1-year history of T2DM and willing to undergo the MRI scan were enrolled. The exclusion criteria included a history of psychiatric or neurological disorders (including cerebrovascular accidents), which may affect cognitive functioning, a history of alcohol or substance abuse, acute complications of T2DM (ketoacidosis and severe hypoglycemia) within the 3 months preceding the examination, and MRI scan contraindications. The research obtained approval from the Institutional Review Board of Shandong Medical Imaging Research Institute Affiliated to Shandong University. All of the participants were given information about the experimental procedures and signed consent forms. In consideration of the likely cognitive impairment of the participants, all of the subjects were invited to perform cognitive function assessments according to their educational levels. Finally, 48 people (23 T2DM patients and 25 HCs) completed the questionnaire.

Clinical Data Collection

The participants underwent an elaborate interview as well as a clinical examination. Age, education level (the number of years in elementary school, high school, and college), and the duration and medical treatment of diabetes were registered and recorded. Systolic blood pressure (BP) and diastolic BP were measured. Arterial hypertension was defined as an average systolic BP > 140 mm Hg and a diastolic BP > 90 mm Hg or self-reported use of medication to lower BP, and fasting glucose, HbA1c, fasting triglycerides, and fasting cholesterol were determined by laboratory testing of venous blood samples. Weight and height were measured and used to calculate body mass index (BMI). After the above medical history collection, blood sample collection, and clinical examinations were finished, the participants were invited to visit the clinic on separate days for cognitive tests and MRI scans. The following items were evaluated on the same day, and the interval was 1–4 days between these two visits. The severity of cerebral small vessel disease (CSVD) was assessed using the Fazekas scale (0–3) oriented with periventricular hyperintensity (PVH) together with deep white matter hyperintensity (DWMH) lesions (Fazekas et al., 1987) and by a combined simple CSVD score (0–3 scale, calculated based on the severity of cerebral microbleeds, lacunes, and WMH) (Amin Al Olama et al., 2020).

Neuropsychological Tests

Standardized general and detailed neurological examinations were conducted on the participants, 48 of whom (23 T2DM patients and 25 HCs) underwent the cognitive assessment, and the assessment tools included the Montreal Cognitive Assessment (MoCA) and the Chinese version of the Trail-making Test (TMT). The MoCA is a one-page 30-point test administered in

10 min (Nasreddine et al., 2005; Bergeron et al., 2017). A score of 13/14 was used as the optimal cutoff point for illiterate individuals, a score of 19/20 was used for individuals with 1–6 years of education, a score of 24/25 was used for individuals with 7 or more years of education, and scores below these cutoff values indicated cognitive impairment (Lu et al., 2011). The subjects also completed the Chinese version of the TMT, which includes two parts: TMT-A to assess cognitive processing speed and TMT-B to measure executive functioning (Woods et al., 2015; Wei et al., 2018). A practice trial with eight items was administered before the actual test to ensure that the individuals understood the tasks. The time required to complete the tasks (in seconds) was recorded as the test score (higher scores indicated lower cognitive function). The test conductor, who had been trained in a professional manner, did not have knowledge about the grouping assignments.

Image Acquisition

All of the subjects were imaged on a MAGNETOM Skyra 3.0-T MR scanner (Siemens Healthcare, Erlangen, Germany) using a 32-channel head coil for signal reception. The brain scanning protocol consisted of a 3D T1-weighted (T1W) magnetization-prepared rapid gradient echo (MPRAGE) sequence for anatomic structure [repetition time (TR) = 7.3 ms, echo time (TE) = 2.4 ms, inversion time (TI) = 900 ms, flip angle = 9°, and isotropic voxel size = 1 mm³] and a 3D multi-echo gradient echo (ME-GRE) sequence for QSM (TR = 50 ms, first TE = 6.8 ms, TE interval = 4.1 ms, number of echoes = 10, flip angle = 15°, and voxel size = 1 × 1 × 2 mm³). Additionally, the required sequences also included T2-weighted (T2W) turbo spin echo (TSE), T2W fluid-attenuated inversion recovery (FLAIR), diffusion-weighted (DW), and susceptibility-weighted (SW) imaging to detect brain abnormalities.

Quantitative Susceptibility Mapping Preprocessing and Quantitative Analysis

Brain QSM maps were computed from complex ME-GRE image data using morphology-enabled dipole inversion with an automatic uniform cerebrospinal fluid (CSF) zero reference algorithm (MEDI + 0) (Liu et al., 2018). Briefly, a non-linear fitting of the multi-echo data was performed to estimate the total field. The total field was spatially unwrapped using a quality-guided region-growing algorithm (Cusack and Papadakis, 2002). Background field removal using the projection onto dipole fields (PDF) algorithm was then applied to compute the local field, which was then inverted to obtain the final susceptibility map. Structural priors (edges) derived from the magnitude image and a regularization term enforcing a uniform susceptibility distribution of the CSF within the lateral ventricles were used in the numerical inversion to improve QSM quality and to provide CSF as an automatic susceptibility reference. The CSF mask was determined by thresholding the R2* map computed from the GRE magnitude data and imposing voxel connectivity (Liu et al., 2018).

We first acquired gray matter volume images by segmenting the T1 anatomical image through Statistical Parametric Mapping

version 12¹ and resliced QSM images to the same resolution ($1 \times 1 \times 1 \text{ mm}^3$) as the gray matter volume images. Next, a study-specific brain template was generated on the Diffeomorphic Anatomical Registration Through Exponentiated Lie Algebra (DARTEL) toolbox (Ashburner, 2007). The gray matter volume and QSM maps were then normalized to the Montreal Neurological Institute (MNI) space and smoothed using a Gaussian kernel with an 8-mm full width with half maximum (Pengas et al., 2009).

Statistical Analysis

The enrolled subjects were separated into two groups (T2DM and HCs). To compare voxel-based QSM values, we used a two-sample *t*-test with sex and age as covariates. A significance cluster-level $P = 0.05$ was applied with correction for multiple comparisons using the family-wise error (FWE) method, and only clusters with sizes > 100 voxels were included. The correlation analysis between susceptibility values and cognitive function scores was tested by voxel-based susceptibility value with sex and age as covariates. A significance cluster-level $P = 0.05$ was applied with correction for multiple comparisons using the FWE method, and only clusters with sizes > 100 voxels were included. The Statistical Package for the Social Sciences (IBM SPSS Statistics for Macintosh, Version 19.0) was used for the statistical analysis. First, descriptive analyses on 32 T2DM patients and 34 HCs were carried out. The measurement data were expressed as the mean \pm standard deviation or the median and interquartile range if the data were not normally distributed. The count data were expressed as *n* (%). The chi-square test was used to compare count data. To compare the clinical data and cognitive assessment scores of the patients with T2DM and HCs, the independent sample *t*-test or the Mann–Whitney *U*-test was used.

RESULTS

Participant Characteristics

This research included 32 patients with T2DM (20 males and 12 females with an average age of 61.09 ± 9.99 years) and 34 HCs (15 males and 19 females with an average age of 58.50 ± 10.07 years). These participants showed no significant difference in age or sex ($t = 1.049$, $P = 0.298$; $\chi^2 = 2.236$, $P = 0.133$, respectively). **Table 1** shows the participants' clinical features. Of all 66 participants, 23 patients with T2DM (11 males and 12 females; average age, 64.65 ± 8.44 years) and 25 HCs (13 males and 12 females; average age, 61.20 ± 7.62 years) received an assessment of cognitive function. T2DM patients exhibited significantly ($t = 4.288$, $P < 0.001$) lower MoCA scores [T2DM, 27 (27, 28); HCs, 29 (28, 29); normal standard ≥ 26] and higher TMT-A/TMT-B scores [71 (51, 100)/185 (149, 260)] than HCs [53 (36.5, 63.5)/150. (103, 172.5)] ($Z = 2.612$, $P = 0.009$; $Z = 2.797$, $P = 0.005$). **Table 2** and **Figure 1** show the scores for each cognitive assessment subindex within these tests and evaluations.

¹<http://www.fil.ion.ucl.ac.uk/spm/>

TABLE 1 | Clinical features of the participants.

	HC (<i>n</i> = 34)	T2DM (<i>n</i> = 32)	Statistical value (χ^2 or <i>t</i>)	<i>P</i>
Sex (male)	15 (44.12%)	20 (62.50%)	2.236 ^a	0.133
Age (years)	58.50 \pm 10.07	61.09 \pm 9.99	1.049	0.298
Risk factors for cardiovascular disease				
BMI (kg/m ²)	25.3 \pm 4.7	27.5 \pm 5.6	1.315 ^b	0.104
Fasting serum cholesterol (mmol/L)	5.3 \pm 0.9	5.4 \pm 1.1	0.398 ^b	0.634
Fasting serum triglycerides (mmol/L)	2.2 \pm 0.6	2.6 \pm 0.8	1.324 ^b	0.117
Hypertension	13 (38.24%)	15 (46.88%)	0.504 ^b	0.478 ^b
Use of antihypertensive medication	11 (32.35%)	12 (37.50%)	0.192 ^b	0.661 ^b
History of myocardial infarction	0	0		
CSVD scores	1.1 \pm 0.34	1.3 \pm 0.45	1.291 ^c	0.208 ^c
Type 2 diabetes-related factors				
Fasting plasma glucose (mmol/L)	5.2 \pm 1.26	9.2 \pm 2.44	3.551 ^b	<0.001
HbA1c (mmol/ml)	–	61.1 \pm 10.3		
HbA1c (%)	–	7.9 \pm 1.3		
Diabetes duration (years)	–	11.2 \pm 6.5		
Insulin use	–	16 (50.00%)		

HC, healthy control; T2DM, type 2 diabetes mellitus; BMI, body mass index; CSVD, cerebral small vessel disease. ^aChi-square test. ^bIndependent samples *t*-test. ^cMann–Whitney *U*-test.

TABLE 2 | Cognitive functioning assessment of the participants.

Variables	HC (<i>n</i> = 25)	T2DM (<i>n</i> = 23)	Statistical value	<i>P</i>
Gender (male)	13 (52.00%)	12 (52.17%)	0.000 ^a	0.990
Age, years	61.20 \pm 7.62	64.65 \pm 8.44	1.847 ^b	0.071
Education, years	12.60 \pm 2.41	11.34 \pm 2.26	1.488 ^b	0.144
MoCA	29 (28, 29)	27 (27, 28)	4.288 ^c	<0.001
TMT-A	53.00 (36.50, 63.50)	71.00 (51.00, 100.00)	2.612 ^c	0.009
TMT-B	150.00 (103.00, 172.50)	185.00 (149.00, 260.00)	2.797 ^c	0.005

HC, healthy control; T2DM, type 2 diabetes mellitus; MoCA, Montreal Cognitive Assessment; TMT, Trail-making Test. ^aChi-square test. ^bIndependent samples *t*-test. ^cMann–Whitney *U*-test.

Susceptibility Value Analysis Across Regions of Interest

Table 3 and **Figure 2** show the comparison of susceptibility values within whole-brain voxel-based analyses between patients

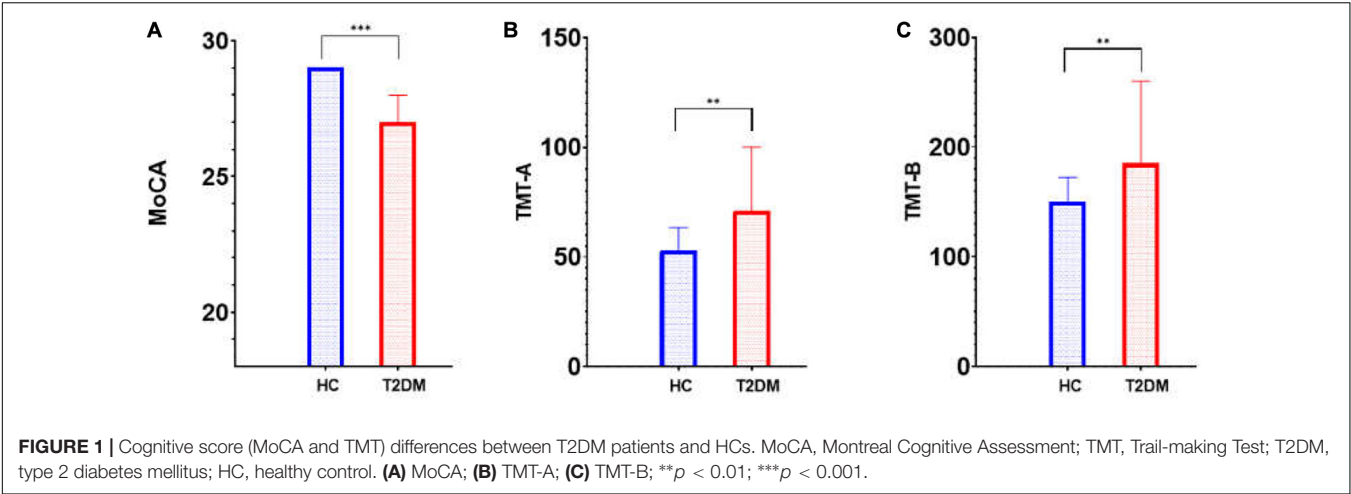
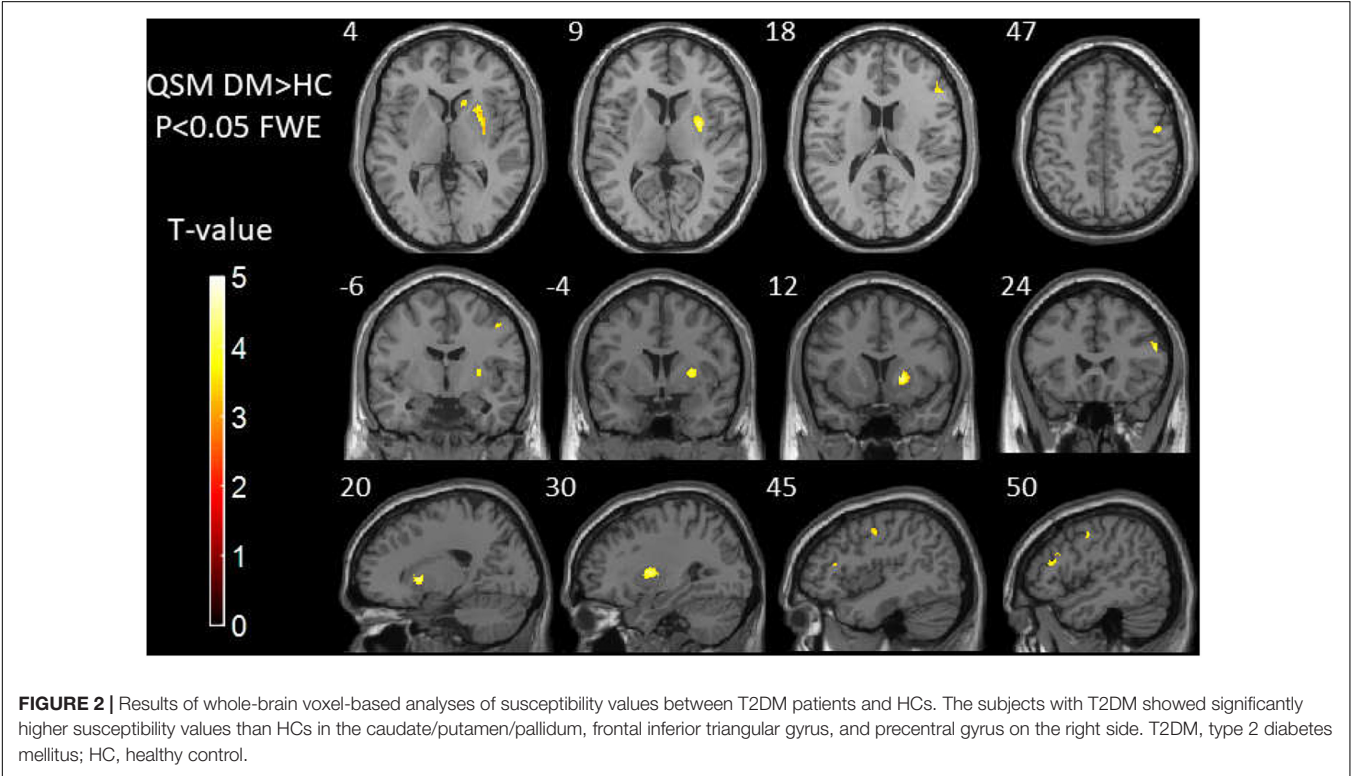


TABLE 3 | Results of whole-brain voxel-based analyses of susceptibility values between T2DM patients and HCs.

Brain regions	Peak MNI (X, Y, Z)			Cluster voxels	T	Z	P [#]	Susceptibility value [ppb ($\times 10^{-9}$)]	
								T2DM	HCS
Right caudate/putamen/pallidum	30	4	9	1,348	−4.52	4.03	0.018	87.84 ± 19.57	63.23 ± 26.02
Right frontal inferior triangular gyrus	53	25	20	591	−4.48	3.99	0.021	15.74 ± 14.44	4.47 ± 9.25
Right precentral gyrus	49	−5	46	221	−3.77	3.37	0.041	8.46 ± 13.00	−3.39 ± 14.19

T2DM, type 2 diabetes mellitus; HC, healthy control; MNI, Montreal Neurological Institute. [#]The family-wise error (FWE) method for correction.



with T2DM and HCs. The subjects with T2DM showed significantly higher susceptibility values than HCs in the caudate/putamen/pallidum, frontal inferior triangular gyrus, and precentral gyrus on the right side. In contrast (HC > T2DM), no region showed a significant difference in susceptibility values between the groups.

Correlations of Neuropsychological Test Results With Susceptibility Values

Correlation analysis between voxel-based susceptibility value and cognitive scores with sex and age as covariates was conducted. A significance cluster-level $P = 0.05$ was applied with correction for multiple comparisons using the FWE method. We found that in T2DM patients, the left thalamus showed a significant relationship with TMT-A ($R^2 = 0.53$, $P = 0.001$). The right thalamus and left thalamus showed a significant relationship with TMT-B ($R^2 = 0.35$, $P = 0.019$; and $R^2 = 0.38$, $P = 0.017$, respectively). In HCs, the cluster of right precentral/middle frontal gyrus/inferior frontal gyrus/inferior triangular gyrus showed a significant relationship with TMT-B ($R^2 = 0.59$, $P = 0.010$). No relationship was found between the susceptibility values with MoCA in the brain region in both two groups (see **Tables 4, 5** and **Figure 3**).

DISCUSSION

In this study, we found that brain iron in T2DM patients compared with HCs was significantly increased in the striatum containing the caudate/putamen/pallidum and in the frontal

lobe (frontal inferior triangular gyrus and precentral gyrus) (**Figures 4–6**). The increased iron content in multiple brain regions is likely to be related to iron ions, which affect the synthesis of neurotransmitters as well as various metabolic components throughout regions as well as types of neurons (Provost et al., 2015). These brain regions contain major structures that are closely correlated with cognitive, emotional, and motor functions. We also found that T2DM patients exhibited lower MoCA scores and higher TMT-A/TMT-B scores and that the susceptibility values of some brain regions showed significant correlation with TMT-A or TMT-B. These phenomena suggest that the synergy of these changes might have an influence on fronto-striato-thalamic circuits of the brain and then impact EF (Lee et al., 2019; Wu et al., 2020). The results suggest that an increase in iron deposition within the brain might function as a risk factor for the seriousness of brain injury in patients with T2DM.

QSM is a new MRI technique that can measure susceptibility-changing materials quantitatively and accurately. It has the ability to non-invasively analyze the brain iron deposition (de Rochefort et al., 2010; Schweser et al., 2012). QSM is more selective for iron than $T2^*$ relaxometry and can be employed to data from standard acquisition sequences available in most commercial

TABLE 4 | The correlation using whole-brain voxel-based analyses of susceptibility values in the patients with T2DM.

	Brain regions	Peak MNI (X, Y, Z)			Cluster voxels	T	R^2	$P^{\#}$
TMT-A	Left thalamus	−4	−8	19	1,035	4.84	0.53	0.001
TMT-B	Right thalamus	9	−17	14	239	4.28	0.35	0.019
	Left thalamus	−9	−14	14	104	4.49	0.38	0.017

T2DM, type 2 diabetes mellitus; MNI, Montreal Neurological Institute; TMT, Trail-making Test. $^{\#}$ The family-wise error (FWE) method for correction.

TABLE 5 | The correlation using whole-brain voxel-based analyses of susceptibility values in the healthy participants.

	Brain regions	Peak MNI (X, Y, Z)			Cluster voxels	T	R^2	$P^{\#}$
TMT-B	Right precentral/middle frontal gyrus/inferior frontal gyrus/inferior triangular gyrus	61	23	27	1,533	4.21	0.59	0.010

MNI, Montreal Neurological Institute; TMT, Trail-making Test. $^{\#}$ The family-wise error (FWE) method for correction.

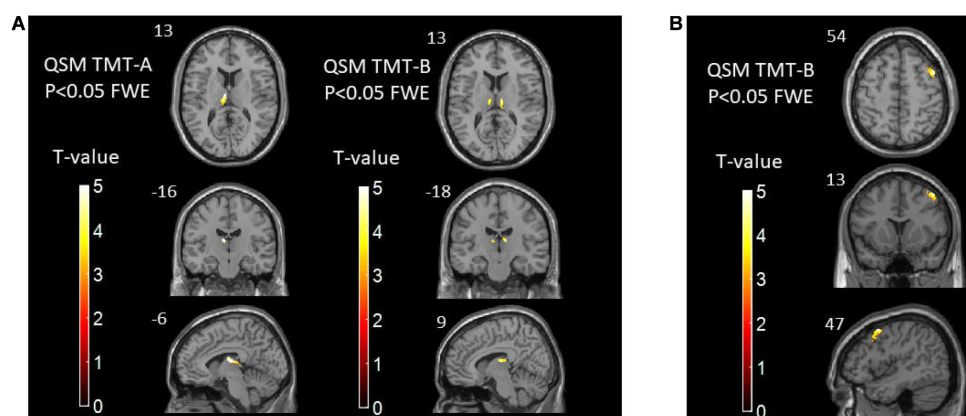
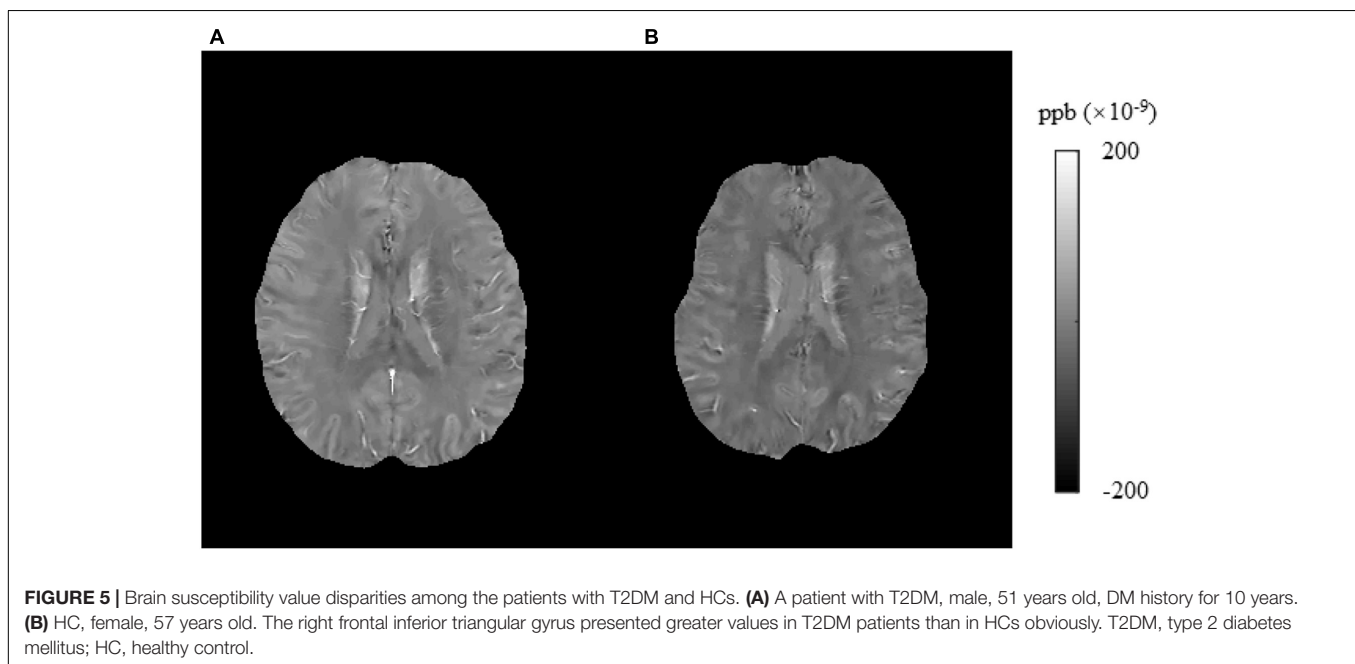
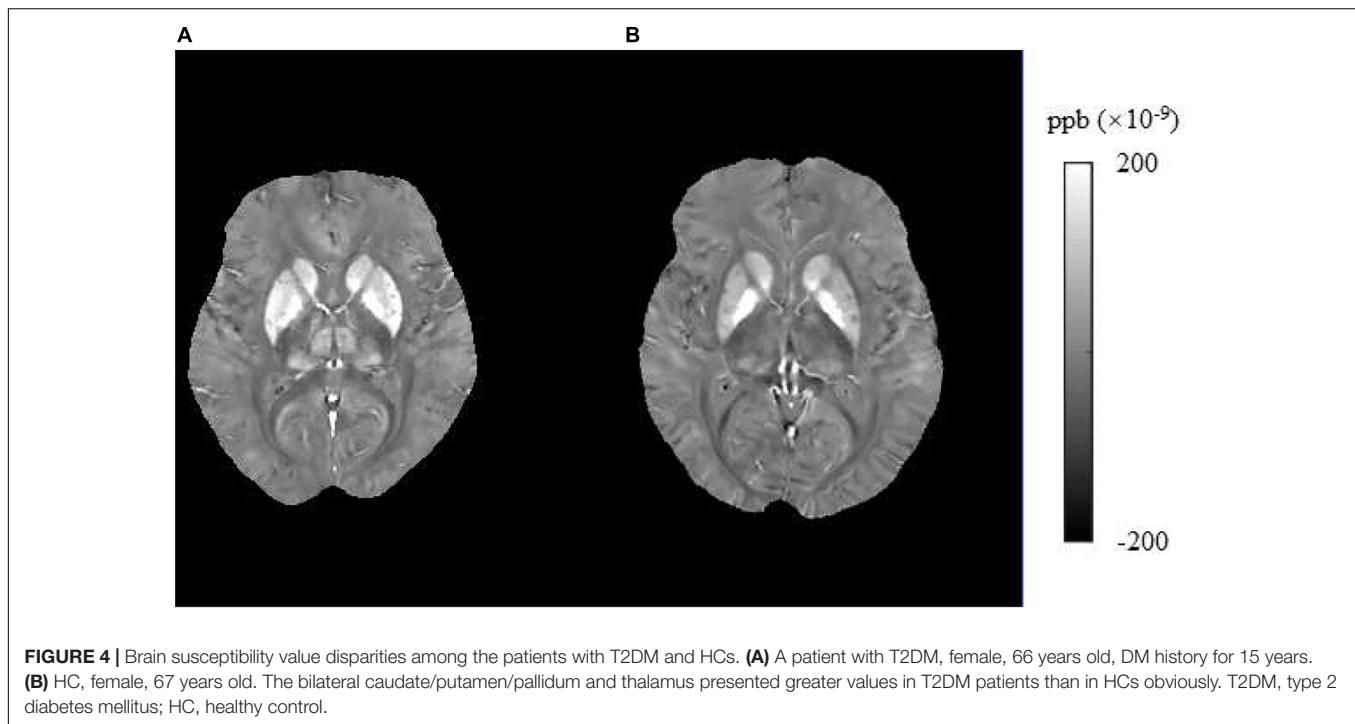
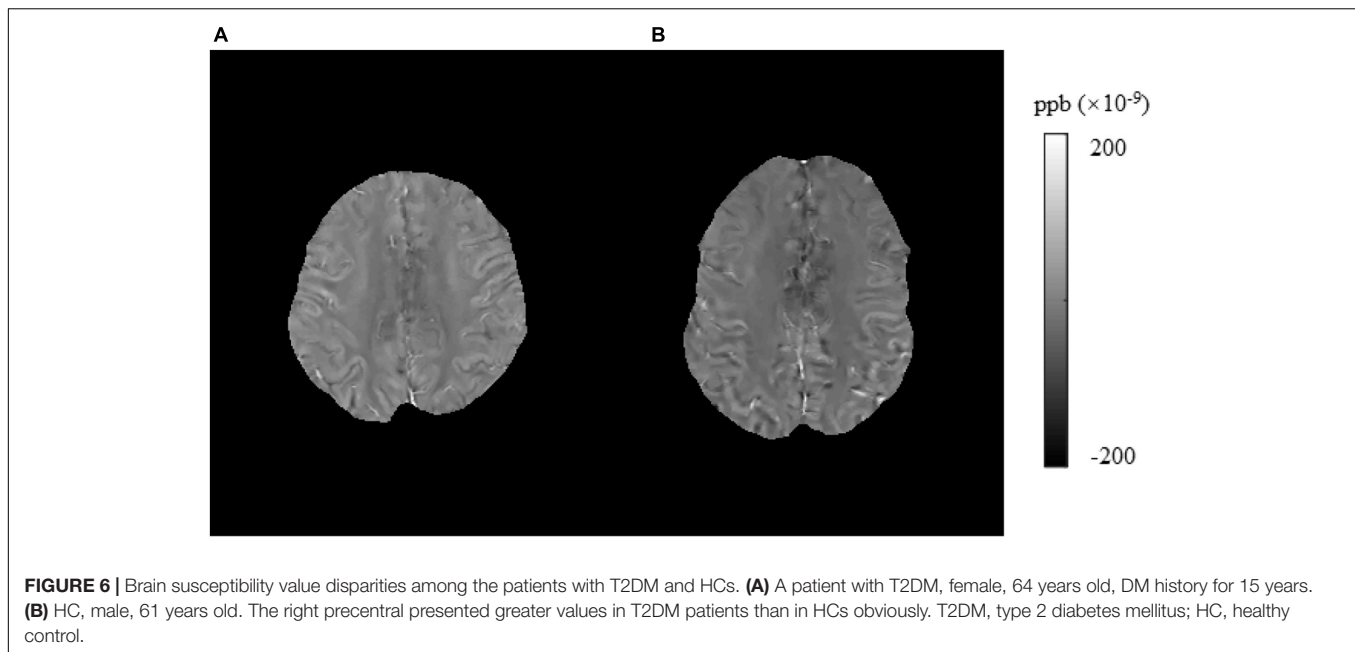


FIGURE 3 | (A) The correlations between susceptibility values and TMT-A/TMT-B scores in T2DM patients. **(B)** The correlations between susceptibility values and TMT-B scores in healthy controls. TMT, Trail-making Test; T2DM, type 2 diabetes mellitus.



scanners. It is also a computer algorithm that can derive values sensitive to the levels of iron from suitable MRI data (Wang and Liu, 2015; Wang et al., 2017). Iron is an indispensable auxiliary factor involved in oxygen binding and transportation, and energy and material metabolism in the body, which can influence oxygen transportation, cell growth regulation, electron transport, and DNA synthesis. If iron homeostasis is impaired, reactive oxygen species will be excessively produced, resulting in apoptosis (Hubler et al., 2015; Apostolakis and Kypraiou, 2017).

Insulin resistance can lead to higher permeability of the BBB. Then, perivascular edema and extravasation of toxic plasma components caused by BBB disruption contribute to localized damage to the brain parenchyma and cognitive dysfunction (Li et al., 2018). T2DM can lead to cerebral small vascular atherosclerosis, which is characterized by smooth muscle cell loss in the tunica media, degeneration of the internal elastic lamina, deposits of fibro-hyaline material and collagens, vessel wall thickening, microatheroma formation, and the



obstruction of the lumen (Pantoni, 2010). The occlusion of the arterial lumen leads to lacunar infarction, and the rupture of microatheroma leads to microbleeds. Iron accumulation could occur as an epiphenomenon of demyelination, axonal damage, and/or neurodegeneration (Raz et al., 2015). Histopathologically, microbleeds represent focal accumulations of hemosiderin-containing macrophages (Haller et al., 2018). Therefore, we speculate that cerebral iron overload in patients with T2DM and QSM could reflect this change. Finally, our results confirmed this hypothesis. In this study, we used voxel-based QSM analysis because we consider that a voxel-based analysis is more sensitive than a region of interest (ROI)-based analysis. In our previous study, the differences of the QSM data between T2DM patients and HCs were investigated by ROI-based comparisons using the independent sample *t*-test analysis. Although we found that the brain iron deposits in patients with T2DM had an increasing trend than in healthy elderly individuals in all selected iron-rich gray matter nuclei, after multiple comparison correction, only the susceptibility values of putamen had significant difference (Li et al., 2020).

In this study, using voxel-based QSM analysis, more affected areas were detected, including the striatum containing the caudate/putamen/pallidum and the frontal lobe (frontal inferior triangular gyrus and precentral gyrus). In a previous research, the difference of susceptibility changes caused by iron accumulation was compared among three groups, cognitive normal (CN) elderly, patients with amnesic MCI (aMCI), and patients with early state AD. The differences of the QSM data among the three groups were investigated by voxel-based and ROI-based comparisons. The results of the voxel-based analysis demonstrated more regions with significant difference than the ROI-based analysis (Kim et al., 2017). Therefore, according to the above results, we consider that the voxel-based analysis is more sensitive.

In our study, the affected areas were the striatum containing the caudate/putamen/pallidum and the frontal lobe (frontal inferior triangular gyrus and precentral gyrus). In T2DM patients, the right thalamus and left thalamus showed a significant relationship with TMT scores. In subcortical structures, the thalamus and striatum play key roles in sustaining normal cognitive function. The thalamus functions as an integration center for subcortical and cortical regions; hence, it is a critical component of functions such as awareness and sensory, motor, and cognitive functions. The striatum is one of the main neural structures of the extrapyramidal motor system, which includes the caudate nucleus and lentiform nucleus, the latter of which is divided into the putamen and pallidum (Hedden and Gabrieli, 2010). The striatum plays an indispensable role in various brain functions, including motor control and learning, language, cognitive functioning, and addiction, through functional cortico-striato-thalamocortical neural pathways (Koikkalainen et al., 2007; Fazl and Fleisher, 2018). Therefore, a pathologic state in the striatum may engender a wide range of clinical manifestations such as motor dysfunction and psychiatric disorders (Uono et al., 2017). The frontal inferior triangular gyrus and precentral gyrus are also closely related to the executive control network (Kozlova et al., 2019; Syan et al., 2019). Previous studies have shown that the impaired biophysical completeness of brain macromolecular protein pools and their local microenvironments in the fronto-striato-thalamic circuits in T2DM patients might provide insights into the neurological pathophysiological potential of diabetes-related clinical and cognitive deficits (Yang et al., 2015). According to this information, we thought that the iron overload areas detected in our study could explain the cognitive decline in patients with T2DM.

According to a prior investigation on iron deposition in T2DM patients' brains using QSM as well as the relevant

cognitive impairments, T2DM patients with MCI exhibited significantly increased susceptibility values in the left putamen than T2DM patients without MCI. The susceptibility values of the left putamen showed a close connection to neuropsychological cognitive scores (Yang et al., 2018). Our research also revealed that the susceptibility values of the putamen in T2DM patients were significantly greater than those in healthy elderly individuals. We also found that the MoCA and TMT scores of T2DM patients were markedly lower and higher, respectively, than those of HCs, suggesting that these related cognitive functions of T2DM patients were significantly decreased. Additionally, using voxel-based data, we found in T2DM patients that the left thalamus showed a significant relationship with TMT-A. The right thalamus and left thalamus showed a significant relationship with TMT-B, while in HCs, the cluster of right precentral/middle frontal gyrus/inferior frontal gyrus/inferior triangular gyrus showed a significant relationship with TMT-B. In a large sample research, involving more than 600 older individuals with a mean age of 73 years, the associations between iron deposits and cognitive ability remained consistent significant after controlling for the presence or absence of five health risk conditions that relate to vascular health (hypertension, diabetes, hypercholesterolemia, cardiovascular disease, and occurrence of a previous stroke) (Del et al., 2015). This result and our results strengthen the hypothesis that brains with iron overload have a close relationship with cognitive decline (Fernández-Real and Manco, 2014). Our discoveries suggest that enhanced iron deposition within the brain might be a risk factor for brain injury severity in patients with T2DM. With the use of T1W structural MRI scanning, shape analysis revealed that T2DM is associated with focal atrophy in the bilateral caudate head and dorso-medial part of the thalamus. ROI-based volumetry detected thalamic volume reduction in T2DM when compared with the controls. Furthermore, worse performance of cognitive processing speed correlated with more severe GM atrophy in the bilateral dorso-medial part of the thalamus (Chen et al., 2017). With the use of diffusion kurtosis imaging, a study found that mean kurtosis (MK) decreased in bilateral thalamus and caudate in atlas-based analysis and that MK values correlated with neuropsychological scores in the cingulum (hippocampus) (Xiong et al., 2019). These discoveries and our results clarify that the thalamus is a critical structure for cognitive functions in T2DM patients. In HCs, we found that the cluster of right precentral/frontal middle frontal gyrus/inferior frontal gyrus/inferior triangular gyrus showed a significant relationship with TMT-B. EF is a collection of cognitive processes essential for higher order mental function. Processes involved in EF include working memory, attention, cognitive flexibility, and impulse control. These complex behaviors are largely mediated by prefrontal cortical function (Logue and Gould, 2014). Our result also illustrated that the brain damage in frontal cortex could cause worse EF.

Our study has several limitations. First, there exists background error and white noise in the original susceptibility maps. Therefore, the cluster in the precentral gyrus with susceptibility value close to 0 is subject to the systematic

error of QSM reconstruction or white noise. Second, the susceptibility maps normalized to MNI space may suffer from error introduced in VBM pipeline. We found a slightly lower susceptibility values of deep gray matter (DGM) as compared with other studies. Low susceptibility in DGM is also reported in two previous voxel-based QSM analyses (Kim et al., 2017; Uchida et al., 2019). One possible reason is the data smoothing procedure when normalizing to MNI space in the VBM pipeline. This normalization step may introduce other errors. In this study, the individual QSM images are first aligned to individual T1 images and then registered to the study-specific T1 template, which may decrease the contrast in regions such as the basal ganglia and thalamus, where QSM images show high contrast. A study-specific QSM template generated with the T1 template by merging these two modalities may help to solve this problem (Hanspach et al., 2017). Third, this research included an initial cross-sectional investigation of brain iron changes in T2DM patients in a relatively small sample size; on this basis, we should observe iron deposition dynamics by examining longitudinal brain iron levels in patients with T2DM in larger samples at various phases. Prospective research with larger sample sizes is required to confirm the regional susceptibility changes and for in-depth exploration of the latent mechanism to confirm the role of iron deposition in whole-brain pathology.

CONCLUSION

In sum, those suffering from with T2DM presented enhanced iron deposition within the striatum and frontal lobe, suggesting that the EF decline in T2DM might be associated with the cerebral iron burden. Using voxel-based data, we identified that the mean susceptibility values of the thalamus, striatum, and frontal lobe had significant correlation with TMT scores, which might reflect a key role of iron deposition during the T2DM process. The changes in susceptibility values throughout these areas likely represent quantitative imaging markers of central nervous system injury among patients with T2DM. Furthermore, QSM might be a beneficial tool for the detection and evaluation of such injuries.

DATA AVAILABILITY STATEMENT

The raw data supporting the conclusions of this article will be made available by the authors, without undue reservation, to any qualified researcher.

ETHICS STATEMENT

The studies involving human participants were reviewed and approved by the Institutional Review Board of Shandong Medical Imaging Research Institute Affiliated to Shandong University. The patients/participants provided their written informed consent to participate in this study.

AUTHOR CONTRIBUTIONS

JL and LG wrote the main manuscript text. QZ prepared imaging data and **Figures 1–4**. NZ prepared the clinical data. LG revised the main manuscript text. All authors reviewed the manuscript.

FUNDING

This work was supported by grants from the National Natural Science Foundation of China (81800840), the Natural Science Foundation of Shandong Province (ZR2020MH288), the

Technology Development Plan of Jinan (201302049, 201602206, and 201907052), Medical and Health Science and Technology Development Project of Shandong Province (2016WS0529), and Funding for Study Abroad Program by Shandong Province (No. 201803059).

SUPPLEMENTARY MATERIAL

The Supplementary Material for this article can be found online at: <https://www.frontiersin.org/articles/10.3389/fnins.2020.606182/full#supplementary-material>

REFERENCES

- Amin Al Olama, A., Wason, J. M. S., Tuladhar, A. M., van Leijssen, E. M. C., Koini, M., Hofer, E., et al. (2020). Simple MRI score aids prediction of dementia in cerebral small vessel disease. *Neurology* 94, e1294–e1302.
- Apostolakis, S., and Kypraiou, A. M. (2017). Iron in neurodegenerative disorders: being in the wrong place at the wrong time? *Rev. Neurosci.* 28, 893–911. doi: 10.1515/revneuro-2017-0020
- Ashburner, J. (2007). A fast diffeomorphic image registration algorithm. *Neuroimage* 38, 95–113. doi: 10.1016/j.neuroimage.2007.07.007
- Bergeron, D., Flynn, K., Verret, L., Poulin, S., Bouchard, R. W., Bocti, C., et al. (2017). Multicenter validation of an MMSE-MoCA conversion table. *J. Am. Geriatr. Soc.* 65, 1067–1072. doi: 10.1111/jgs.14779
- Chai, C., Wang, H., Liu, S., Chu, Z. Q., Li, J., Qian, T., et al. (2019). Increased iron deposition of deep cerebral gray matter structures in hemodialysis patients: a longitudinal study using quantitative susceptibility mapping. *J. Magnet. Reson. Imaging* 49, 786–799. doi: 10.1002/jmri.26226
- Chen, J., Zhang, J., Liu, X., Wang, X., Xu, X., Li, H., et al. (2017). Abnormal subcortical nuclei shapes in patients with type 2 diabetes mellitus. *Eur. Radiol.* 27, 4247–4256. doi: 10.1007/s00330-017-4790-3
- Cusack, R., and Papadakis, N. (2002). New robust 3-D phase unwrapping algorithms: application to magnetic field mapping and undistorting echoplanar images. *Neuroimage* 16(3 Pt 1), 754–764. doi: 10.1006/nimg.2002.1092
- Daglas, M., and Adlard, P. A. (2018). The involvement of iron in traumatic brain injury and neurodegenerative disease. *Front. Neurosci.* 12:981. doi: 10.3389/fnins.2018.00981
- de Rochefort, L., Liu, T., Kressler, B., Liu, J., Spincemaille, P., Lebon, V., et al. (2010). Quantitative susceptibility map reconstruction from MR phase data using bayesian regularization: validation and application to brain imaging. *Magnet. Resonan. Med.* 63, 194–206. doi: 10.1002/mrm.22187
- Del, C. V. H. M., Ritchie, S., Glatz, A., Allerhand, M., Muñoz Maniega, S., Gow, A. J., et al. (2015). Brain iron deposits and lifespan cognitive ability. *Age* 37:100.
- Fazekas, F., Chawluk, J. B., Alavi, A., Hurtig, H. I., and Zimmerman, R. A. (1987). MR signal abnormalities at 1.5 T in Alzheimer's dementia and normal aging. *Am. J. Roentgenol.* 149, 351–356. doi: 10.2214/ajr.149.2.351
- Fazl, A., and Fleisher, J. (2018). Anatomy, physiology, and clinical syndromes of the basal ganglia: a brief review. *Semin. Pediatr. Neurol.* 25, 2–9. doi: 10.1016/j.spen.2017.12.005
- Fernández-Real, J. M., and Manco, M. (2014). Effects of iron overload on chronic metabolic diseases. *Lancet* 2, 513–526. doi: 10.1016/s2213-8587(13)70174-8
- Forbes, J. M., and Cooper, M. E. (2013). Mechanisms of diabetic complications. *Physiol. Rev.* 93, 137–188.
- Haller, S., Vernooij, M. W., Kuijper, J. P. A., Larsson, E. M., Jäger, H. R., and Barkhof, F. (2018). Cerebral microbleeds: imaging and clinical significance. *Radiology* 287, 11–28. doi: 10.1148/radiol.2018170803
- Hanspach, J., Dwyer, M. G., Bergsland, N. P., Feng, X., Hagemeier, J., Bertolino, N., et al. (2017). Methods for the computation of templates from quantitative magnetic susceptibility maps (QSM): toward improved atlas- and voxel-based analyses (VBA). *J. Magnet. Resonan. Imaging* 46, 1474–1484. doi: 10.1002/jmri.25671
- Hedden, T., and Gabrieli, J. D. E. (2010). Shared and selective neural correlates of inhibition, facilitation, and shifting processes during executive control. *Neuroimage* 51, 421–431. doi: 10.1016/j.neuroimage.2010.01.089
- Hubler, M. J., Peterson, K. R., and Hasty, A. H. (2015). Iron homeostasis: a new job for macrophages in adipose tissue? *Trends Endocrinol. Metab.* 26, 101–109. doi: 10.1016/j.tem.2014.12.005
- Kim, H. G., Park, S., Rhee, H. Y., Lee, K. M., Ryu, C. W., Rhee, S. J., et al. (2017). Quantitative susceptibility mapping to evaluate the early stage of Alzheimer's disease. *Neuroimage Clin.* 16, 429–438. doi: 10.1016/j.nicl.2017.08.019
- Koikkalainen, J., Hirvonen, J., Nyman, M., Lötjönen, J., Hietala, J., and Ruotsalainen, U. (2007). Shape variability of the human striatum—effects of age and gender. *Neuroimage* 34, 85–93. doi: 10.1016/j.neuroimage.2006.08.039
- Kozlova, L. I., Petrovskii, E. D., Verevkin, E. G., Mel'nikov, M. E., Savelov, A. A., and Shtark, M. B. E. E. G. (2019). Alpha-rhythm-related changes in BOLD fMRI signal in neurofeedback training. *Bull. Exper. Biol. Med.* 168, 199–204. doi: 10.1007/s10517-019-04674-y
- Lee, C. Y., Chen, H. L., Chen, P. C., Chen, Y. S., Chiang, P. L., Wang, C. K., et al. (2019). Correlation between executive network integrity and sarcopenia in patients with Parkinson's disease. *Intern. J. Environ. Res. Public Health* 16:4884. doi: 10.3390/ijerph16244884
- Li, J., Zhang, Q., Zhang, N., and Guo, L. (2020). Increased brain iron deposition in the putamen in patients with Type 2 diabetes mellitus detected by quantitative susceptibility mapping. *J. Diabetes Res.* 2020:7242530.
- Li, Q., Yang, Y., Reis, C., Tao, T., Li, W., Li, X., et al. (2018). Cerebral small vessel disease. *Cell Transplant.* 27, 1711–1722.
- Liu, J., Liu, T., Wang, W., Ma, L., Ma, X., Shi, S., et al. (2017). Reduced gray matter volume in patients with Type 2 diabetes mellitus. *Front. Aging Neurosci.* 9:161. doi: 10.3389/fnagi.2017.00161
- Liu, Z., Spincemaille, P., Yao, Y., Zhang, Y., and Wang, Y. M. E. D. I. (2018). +0: Morphology enabled dipole inversion with automatic uniform cerebrospinal fluid zero reference for quantitative susceptibility mapping. *Magnet. Resonan. Med.* 79, 2795–2803. doi: 10.1002/mrm.26946
- Logue, S. F., and Gould, T. J. (2014). The neural and genetic basis of executive function: attention, cognitive flexibility, and response inhibition. *Pharmacol. Biochem. Behav.* 123, 45–54. doi: 10.1016/j.pbb.2013.08.007
- Lu, J., Li, D., Li, F., Zhou, A., Wang, F., Zuo, X., et al. (2011). Montreal cognitive assessment in detecting cognitive impairment in Chinese elderly individuals: a population-based study. *J. Geriatr. Psychiatry Neurol.* 24, 184–190. doi: 10.1177/0891988711422528
- McCarthy, R. C., Sosa, J. C., Gardeck, A. M., Baez, A. S., Lee, C. H., and Wessling-Resnick, M. (2018). Inflammation-induced iron transport and metabolism by brain microglia. *J. Biol. Chem.* 293, 7853–7863. doi: 10.1074/jbc.ra118.001949
- McCrimmon, R. J., Ryan, C. M., and Frier, B. M. (2012). Diabetes and cognitive dysfunction. *Lancet* 379, 2291–2299.
- Medhi, B., and Chakrabarty, M. (2013). Insulin resistance: an emerging link in Alzheimer's disease. *Neurol. Sci.* 34, 1719–1725. doi: 10.1007/s10072-013-1454-1
- Minami, T., Ito, Y., Yamada, M., Furuta, R., Minagawa, F., Kamata, K., et al. (2020). The effect of long-term past glycemic control on executive function among patients with type 2 diabetes mellitus. *Diabetol. Intern.* 11, 114–120. doi: 10.1007/s13340-019-00411-y

- Moon, Y., Han, S. H., and Moon, W. J. (2016). Patterns of brain iron accumulation in vascular dementia and Alzheimer's dementia using quantitative susceptibility mapping imaging. *J. Alzheimers Dis.* 51, 737–745. doi: 10.3233/jad-151037
- Nasreddine, Z. S., Phillips, N. A., Bäckström, V. R., Charbonneau, S., Whitehead, V., Collin, I., et al. (2005). The montreal cognitive assessment, MoCA: a brief screening tool for mild cognitive impairment. *J. Am. Geriatr. Soc.* 53, 695–699. doi: 10.1111/j.1532-5415.2005.53221.x
- Pantoni, L. (2010). Cerebral small vessel disease: from pathogenesis and clinical characteristics to therapeutic challenges. *Lancet Neurol.* 9, 689–701. doi: 10.1016/s1474-4422(10)70104-6
- Pengas, G., Pereira, J. M., Williams, G. B., and Nestor, P. J. (2009). Comparative reliability of total intracranial volume estimation methods and the influence of atrophy in a longitudinal semantic dementia cohort. *J. Neuroimage.* 19, 37–46. doi: 10.1111/j.1552-6569.2008.00246.x
- Provost, J.-S., Hanganu, A., and Monchi, O. (2015). Neuroimaging studies of the striatum in cognition Part I: healthy individuals. *Front. Syst. Neurosci.* 9:140. doi: 10.3389/fnsys.2015.00140
- Raz, E., Branson, B., Jensen, J. H., Bester, M., Babb, J. S., Herbert, J., et al. (2015). Relationship between iron accumulation and white matter injury in multiple sclerosis: a case-control study. *J. Neurol.* 262, 402–409. doi: 10.1007/s00415-014-7569-3
- Redondo, M. T., Beltrán-Brotóns, J. L., Reales, J. M., and Ballesteros, S. (2016). Executive functions in patients with Alzheimer's disease, type 2 diabetes mellitus patients and cognitively healthy older adults. *Exper. Gerontol.* 83, 47–55. doi: 10.1016/j.exger.2016.07.013
- Schweser, F., Sommer, K., Deistung, A., and Reichenbach, J. R. (2012). Quantitative susceptibility mapping for investigating subtle susceptibility variations in the human brain. *Neuroimage* 62, 2083–2100. doi: 10.1016/j.neuroimage.2012.05.067
- Syan, S. K., Owens, M. M., Goodman, B., Epstein, L. H., Meyre, D., Sweet, L. H., et al. (2019). Deficits in executive function and suppression of default mode network in obesity. *Neuroimage Clin.* 24:102015. doi: 10.1016/j.nicl.2019.102015
- Takechi, R., Lam, V., Brook, E., Giles, C., Fimognari, N., Mooradian, A., et al. (2017). Blood-brain barrier dysfunction precedes cognitive decline and neurodegeneration in diabetic insulin resistant mouse model: an implication for causal link. *Front. Aging Neurosci.* 9:399. doi: 10.3389/fnagi.2017.00399
- Uchida, Y., Kan, H., Sakurai, K., Arai, N., Kato, D., Kawashima, S., et al. (2019). Voxel-based quantitative susceptibility mapping in Parkinson's disease with mild cognitive impairment. *Mov. Disord.* 34, 1164–1173. doi: 10.1002/mds.27717
- Uono, S., Sato, W., Kochiyama, T., Kubota, Y., Sawada, R., Yoshimura, S., et al. (2017). Putamen volume is negatively correlated with the ability to recognize fearful facial expressions. *Brain Topogr.* 30, 774–784. doi: 10.1007/s10548-017-0578-7
- Vincent, C., and Hall, P. A. (2015). Executive function in adults with Type 2 diabetes: a meta-analytic review. *Psychosom. Med.* 77, 631–642. doi: 10.1097/psy.0000000000000103
- Wang, Y., and Liu, T. (2015). Quantitative susceptibility mapping (QSM): decoding MRI data for a tissue magnetic biomarker. *Magnet. Resonan. Med.* 73, 82–101. doi: 10.1002/mrm.25358
- Wang, Y., Spincemaille, P., Liu, Z., Dimov, A., Deh, K., Li, J., et al. (2017). Clinical quantitative susceptibility mapping (QSM): biometal imaging and its emerging roles in patient care. *J. Magnet. Resonan. Imaging* 46, 951–971. doi: 10.1002/jmri.25693
- Ward, R. J., Zucca, F. A., Duyn, J. H., Crichton, R. R., and Zecca, L. (2014). The role of iron in brain ageing and neurodegenerative disorders. *Lancet Neurol.* 13, 1045–1060. doi: 10.1016/s1474-4422(14)70117-6
- Wardlaw, J. M., Smith, C., and Dichgans, M. (2013). Mechanisms of sporadic cerebral small vessel disease: insights from neuroimaging. *Lancet Neurol.* 12, 483–497. doi: 10.1016/s1474-4422(13)70060-7
- Wei, M., Shi, J., Li, T., Ni, J., Zhang, X., Li, Y., et al. (2018). Diagnostic accuracy of the chinese version of the trail-making test for screening cognitive impairment. *J. Am. Geriatr. Soc.* 66, 92–99. doi: 10.1111/jgs.15135
- Woods, D. L., Wyma, J. M., Herron, T. J., and Yund, E. W. (2015). The effects of aging, malingering, and traumatic brain injury on computerized trail-making test performance. *PLoS One* 10:e0124345. doi: 10.1371/journal.pone.0124345
- Wu, W., McAnulty, G., Hamoda, H. M., Sarill, K., Karmacharya, S., Gagoski, B., et al. (2020). Detecting microstructural white matter abnormalities of frontal pathways in children with ADHD using advanced diffusion models. *Brain Imaging Behav.* 14, 981–997. doi: 10.1007/s11682-019-00108-5
- Xiong, Y., Sui, Y., Zhang, S., Zhou, X. J., Yang, S., Fan, Y., et al. (2019). Brain microstructural alterations in type 2 diabetes: diffusion kurtosis imaging provides added value to diffusion tensor imaging. *Eur. Radiol.* 29, 1997–2008. doi: 10.1007/s00330-018-5746-y
- Yang, Q. F., Zhou, L. N., Liu, C., Liu, D. H., Zhang, Y., Li, C., et al. (2018). Brain iron deposition in type 2 diabetes mellitus with and without mild cognitive impairment in vivo susceptibility mapping study. *Brain Imag. Behav.* 12, 1479–1487. doi: 10.1007/s11682-017-9815-7
- Yang, S., Ajilore, O., Wu, M., Lamar, M., and Kumar, A. (2015). Impaired macromolecular protein pools in fronto-striato-thalamic circuits in type 2 diabetes revealed by magnetization transfer imaging. *Diabetes* 64, 183–192. doi: 10.2337/db14-0316
- Zilliox, L. A., Chadrasekaran, K., Kwan, J. Y., and Russell, J. W. (2016). Diabetes and cognitive impairment. *Curr. Diabetes Rep.* 16:87.

Conflict of Interest: The authors declare that the research was conducted in the absence of any commercial or financial relationships that could be construed as a potential conflict of interest.

Copyright © 2021 Li, Zhang, Zhang and Guo. This is an open-access article distributed under the terms of the Creative Commons Attribution License (CC BY). The use, distribution or reproduction in other forums is permitted, provided the original author(s) and the copyright owner(s) are credited and that the original publication in this journal is cited, in accordance with accepted academic practice. No use, distribution or reproduction is permitted which does not comply with these terms.



Correlation Between Cerebral Venous Oxygen Level and Cognitive Status in Patients With Alzheimer's Disease Using Quantitative Susceptibility Mapping

YangYingQiu Liu^{1†}, JunYi Dong^{1†}, QingWei Song¹, Nan Zhang¹, WeiWei Wang¹, BingBing Gao¹, ShiYun Tian¹, ChunBo Dong², ZhanHua Liang², LiZhi Xie³ and YanWei Miao^{1*}

¹ Department of Radiology, First Affiliated Hospital of Dalian Medical University, Dalian, China, ² Department of Neurology, First Affiliated Hospital of Dalian Medical University, Dalian, China, ³ GE Healthcare, MR Research China, Beijing, China

OPEN ACCESS

Edited by:

Fuhua Yan,

Shanghai Jiao Tong University, China

Reviewed by:

Maria Eugenia Caligiuri,

University of Magna Graecia, Italy

Xiaojun Guan,

Zhejiang University, China

*Correspondence:

YanWei Miao

ywmiao716@163.com

[†]These authors have contributed equally to this work

Specialty section:

This article was submitted to Neurodegeneration, a section of the journal Frontiers in Neuroscience

Received: 09 June 2020

Accepted: 17 December 2020

Published: 18 January 2021

Citation:

Liu Y, Dong J, Song Q, Zhang N, Wang W, Gao B, Tian S, Dong C, Liang Z, Xie L and Miao Y (2021) Correlation Between Cerebral Venous Oxygen Level and Cognitive Status in Patients With Alzheimer's Disease Using Quantitative Susceptibility Mapping. *Front. Neurosci.* 14:570848. doi: 10.3389/fnins.2020.570848

Purpose: To quantitatively assess the blood oxygen levels of the cerebral vein using quantitative susceptibility mapping (QSM), and to analyze the correlation between magnetic susceptibility value (MSV) and clinical laboratory indicators/cognitive scores in patients with Alzheimer's disease (AD).

Materials and Methods: Fifty-nine patients (21 males and 38 females) with clinically confirmed AD (AD group) and 22 control subjects (12 males, 10 females; CON group) were recruited. Clinical data and laboratory examination indexes were collected. All patients underwent Mini-mental State Examination, Montreal Cognitive Assessment, Clock Drawing Task, and Activity of Daily Living Scale test, as well as a routine MRI and enhanced gradient echo T2 star weighted angiography (ESWAN).

Results: Higher cerebral venous MSV was observed in AD group compared to CON group, significant differences were observed for bilateral thalamus veins and left dentate nucleus veins. The MSV of bilateral thalamus veins, bilateral internal cerebral veins, and bilateral dentate nucleus veins had significant negative correlation with Mini-mental State Examination score; the MSV of bilateral thalamus veins, bilateral dentate nucleus veins, right septal vein had a significant negative correlation with Montreal Cognitive Assessment scores; a significant negative correlation between the MSV of bilateral thalamus veins, left dentate nucleus vein, right septal vein and the Clock Drawing Task score; the MSV of bilateral thalamus veins, left dentate nucleus vein had a significant negative correlation with Activity of Daily Living Scale score. The MSV of left dentate nucleus vein was positively correlated with the course of the disease, the MSV of bilateral septal vein were positively correlated with the total cholesterol, and the MSV of left septal vein had a positive correlation with LDL.

Conclusion: Decreasing cerebral venous oxygen level in AD patients may affect cognitive status, and associated with the deterioration of the disease in AD patients.

Keywords: Alzheimer's disease, susceptibility weighted imaging, magnetic susceptibility value, cerebral vein, magnetic resonance imaging

INTRODUCTION

Alzheimer's disease (AD) is a progressive neurodegenerative disease and the most prevalent type of dementia in the elderly (Gong et al., 2019). AD is characterized by progressive cognitive and functional deficits and behavioral changes. Neuropathological features of AD include neuronal loss caused by neurofibrillary tangles (NFTs) and senile plaques formed by the deposition of β -amyloid protein ($A\beta$) in the brain (Harrington, 2012).

Previous studies have shown that cerebral blood flow is decreased in AD patients (Mak et al., 2014). Cerebral metabolic ratio of oxygen may decrease with the long-term cerebral blood perfusion insufficiency, which may affect the metabolism of neurons. Nevertheless, it remains unclear whether the decrease of cerebral oxygen content is associated with the cognitive decline in patient with AD. Different MRI sequences are currently applied to quantify the changes in cerebral oxygen and calculate oxygen extraction fraction (OEF) (An et al., 2001). Local OEF can be calculated based on the changes in venous phase values of susceptibility weighted imaging (SWI), which has just been applied to clinical work (Barnes and Haacke, 2009; Kesavadas et al., 2010; Zaitzu et al., 2011; Li et al., 2013; Messina et al., 2014).

Over the recent years, it has been found that SWI has some shortcomings in quantitative measurement. ϕ value is a parameter reflecting the magnetic susceptibility of tissues. Yet, due to the effect of "dipole field," the accuracy and repeatability of measurement of ϕ value are not high enough (Liu et al., 2015). In order to improve the shortcomings related to quantitative measurement of SWI, a new sequence known as quantitative susceptibility mapping (QSM) was designed. It is a non-invasive magnetic resonance imaging technique that generates a linearly proportional, volumetric image based on the magnetic susceptibility of the subject tissue (Derry and Kent, 2017). This sequence measures the magnetic susceptibility of tissues rather than the ϕ value, which solves the problem of measuring the ϕ value in algorithm. The intensity of QSM signal depends on the amount and concentration of deoxyhemoglobin in tissues and the diameter of blood vessels (Mukherjee et al., 2003), QSM can reliably calculate the oxygen saturation of human cerebral veins (Fan et al., 2014) and obtain the magnetic susceptibility value (MSV), provide information on oxygen metabolism (Jensen-Kondering and Böhm, 2013). To our previous literature review, there was no studies reported were found on cerebral venous oxygen level for patients with AD.

Based on the above factors, the purpose of this study was to quantitatively evaluate the cerebral venous oxygen level

in AD patients by using QSM magnetic susceptibility. We also further analyzed the correlation between cerebral venous oxygen level and cognitive status in order to understand the mechanisms underlying changes of cerebral oxygen level in AD patients, and hoping to identify the imaging indicators for monitoring the evaluation of AD patients and further clinical intervention therapy.

MATERIALS AND METHODS

Subjects

Fifty-nine patients with clinically confirmed AD (AD group) were recruited in the Neurology Department between September 2015 and December 2018. Subjects were enrolled based on National Institute of Neurological and Communicative Disorders and Stroke and the Alzheimer's disease and Related Disorders Association (NINCDS/ADRDA) criteria for probable AD (McKhann et al., 1984, 2011). The exclusion criteria: (a) other forms of dementia, such as frontotemporal dementia, dementia with Lewy bodies, vascular dementia and Parkinson's disease dementia; (b) a history of stroke, brain tumor, serious head trauma, smoking, alcohol or drug dependence, and neurologic or psychiatric diseases; (c) large-vessel disease and diseases with white matter lesions. In addition, 22 elderly without cognitive impairment were recruited as control group (CON group). In this group of patients, the high signal intensity of white matter on MRI was below Fazekas-scale grade 2 or less than 2 static lacunar infarctions in the brain. Both AD group and CON group were right-handed.

Clinical data including gender, age, level of education were collected from all subjects. Course of the disease and laboratory examination indexes, including total cholesterol, triglycerides, high-density lipoprotein (HDL), low density lipoprotein (LDL), and homocysteine levels were collected from AD patients.

This retrospective study was approved by the hospital ethics committee. In addition, all patients signed the informed consent.

MR Image Acquisition

Routine MRI and enhanced gradient echo T2 star weighted angiography (ESWAN) were performed using the GE signa HDXT 3.0T MRI system with 8-channel head coil. All the scan sequence parameters were set the same. The specific scanning sequence and parameters are shown in **Table 1**.

Image Post-processing

The ESWAN raw data was saved and transmitted to a personal computer in DICOM format. Image post-processing was performed by using signal processing in nuclear magnetic resonance (SPIN) software provided by Wayne State University. Firstly, the original phase map and magnitude map of ESWAN were further processed by susceptibility weighted imaging mapping (SWIM) module in SPIN software to obtain QSM. The processing steps were as follows: (1) brain extraction: skull removal were carried out, and the artifacts on phase map were eliminated by compound threshold: $BET = 0.2$; (2) phase unwrapping; (3) phase quality map: kernel size = 6,

Abbreviations: AD, Alzheimer's disease; NFTs, neurofibrillary tangles; $A\beta$, β -amyloid protein; OEF, oxygen extraction fraction; SWI, susceptibility weighted imaging; QSM, quantitative susceptibility mapping; HDL, high-density lipoprotein; LDL, low-density lipoprotein; ESWAN, enhanced gradient echo T2 star weighted angiography; SPIN, signal processing in nuclear magnetic resonance; SWIM, susceptibility weighted imaging mapping; SHARP, sophisticated harmonic artifact reduction for phase data; MSV, magnetic susceptibility value; ROI, region of interest; IGV, internal cerebral vein; SV, septal vein; TV, thalamus vein; BV, basal vein; DNV, dentate nucleus vein; MMSE, Mini-mental State Examination; MoCA, Montreal Cognitive Assessment; CDT, Clock Drawing Task; ADL, Activity of Daily Living Scale; FDR, false discovery rate; BBB, blood-brain barrier.

TABLE 1 | MRI scan parameters.

Sequence	TR (ms)	TE (ms)	Interval (mm)	FOV (cm × cm)	Matrix	Flip angle (°)	Bandwidth (kHz)
T1WI	2500	25	1	22 × 19.8	320 × 256	/	31.25
T2WI	5000	118	1	22 × 19.8	320 × 256	/	31.25
ESWAN	36	3.6; 7.8; 11.9; 16.1; 20.3; 24.4; 28.6; 32.8	0	24 × 24	256 × 256	20	31.25

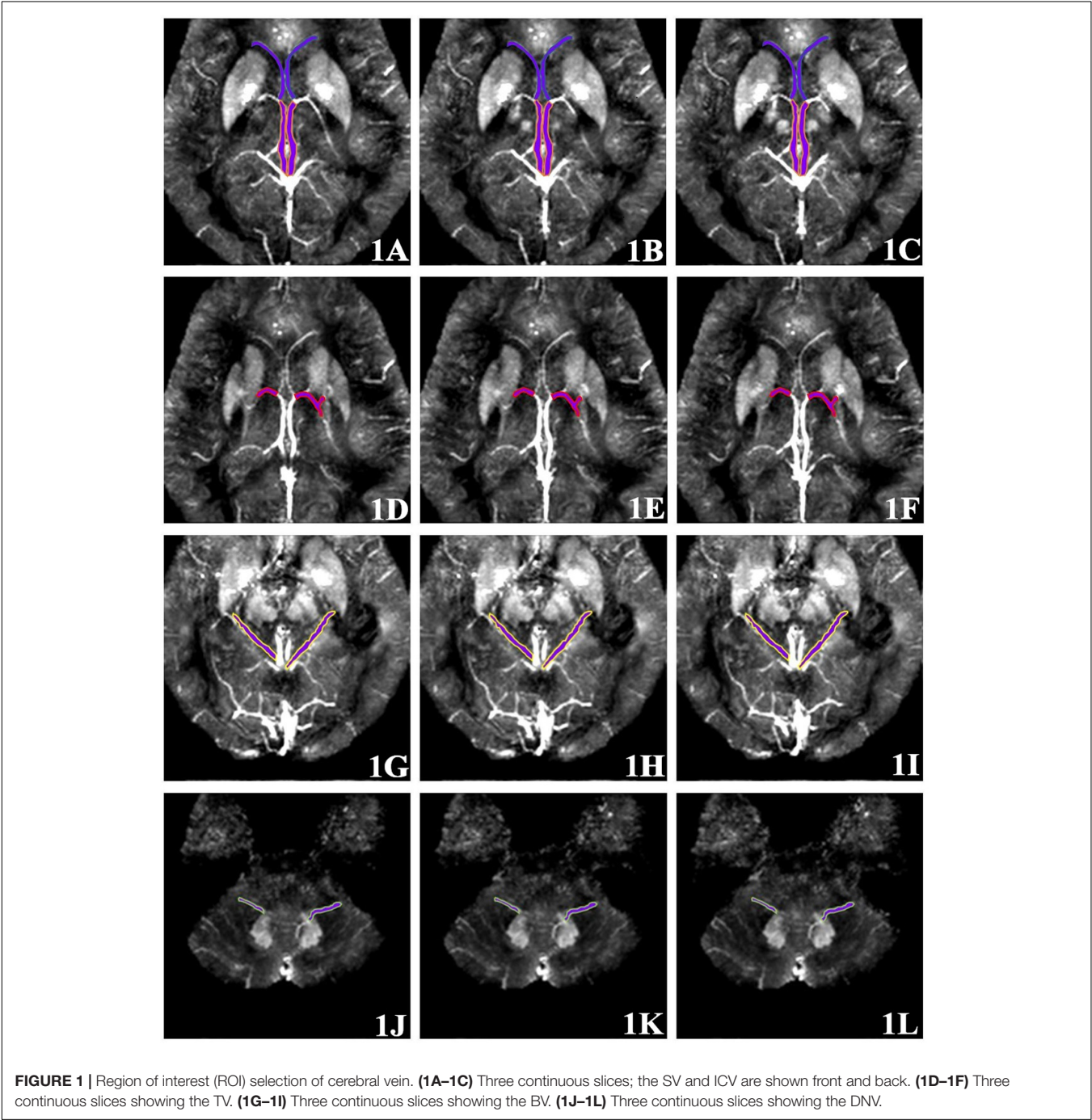


TABLE 2 | Clinical data.

Characteristics	AD group (n = 59)	CON group (n = 22)	p-value
Gender (M/F)	21/38	12/10	0.123
Age ^a	71.12 ± 9.21	67.86 ± 8.60	0.154
Years of education ^b	9.00 (3.00)	9.00 (6.00)	0.534
Course of the disease ^a	3.68 ± 2.42	–	–
MMSE ^b	19.00 (9.00)	30.00 (0.00)	<0.001*
MoCA ^b	14.00 (8.00)	30.00 (0.25)	<0.001*
CDT ^b	2.00 (2.00)	4.00 (0.00)	<0.001*
ADL ^b	27.00 (11.00)	14.00 (0.00)	<0.001*
Total cholesterol ^b	5.29 (1.42)	–	–
Triglycerides ^b	1.02 (0.60)	–	–
HDL ^a	1.46 ± 0.36	–	–
LDL ^a	2.86 ± 0.87	–	–
Homocysteine ^b	14.23 (5.60)	–	–

^aData are expressed as mean value ± standard deviations. ^bData are expressed as median (inter-quartile range). *P < 0.05.

threshold = 0.05; (4) background field removal: sophisticated harmonic artifact reduction for phase data (SHARP); (5) the standard inversion filtering was applied to Fourier transform of high-pass filter phase map.

ROI Selection

Quantitative measurement of MSV of region of interest (ROI) in magnetic sensitive maps was analyzed using SPIN software. As shown in **Figure 1**, the ROI included bilateral internal cerebral

veins (ICV), septal veins (SV), thalamus veins (TV), basal veins (BV) and dentate nucleus veins (DNV). Briefly, the ROIs were manually drawn along the boundary of the full length of the vein at the maximum slice that clearly displayed the vein. Three consecutive slices were then measured at the same location and averaged, avoiding the influence of air-cranial junction and ventricular system. Due to the small range of the SV and DNV in some patients, it could not be clearly displayed at three consecutive slices, then the same part was repeatedly measured three times and averaged. In order to ensure maneuverability of measurement, the ROI should select vessels with clear display and relatively fixed. The ROIs were manually drawn by two neuro-radiologists (neuro-radiologist 1 with 10 years of experience, neuro-radiologist 2 with 5 years of experience) in the same manner. To evaluate inter-observer reliability, the intra-class correlation coefficients (ICCs) were calculated, ICC > 0.75 was considered with inter-observer stability.

Cognitive Scale

Neurological and cognitive functions in all subjects, including Mini-mental State Examination (MMSE), Montreal Cognitive Assessment (MoCA), Clock Drawing Task (CDT), and Activity of Daily Living Scale (ADL) were analyzed by a senior neurologist.

Statistical Analysis

Data analyses were performed using statistical package for social science (SPSS) version 20.0 and R version 3.5.3. ICC test was

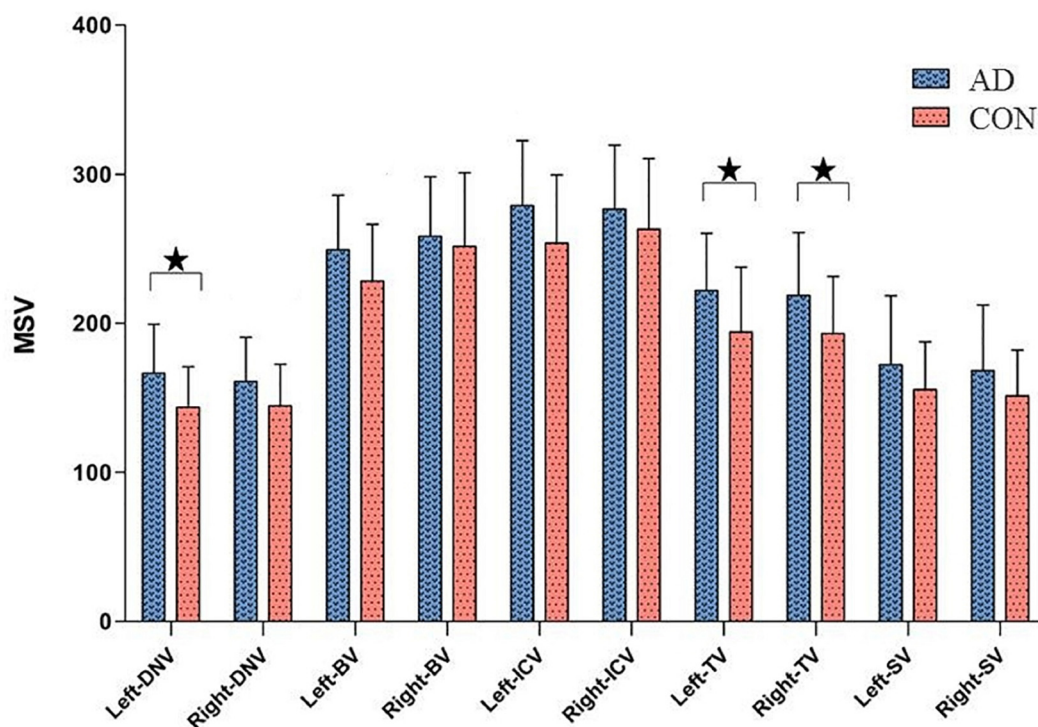


FIGURE 2 | Comparisons of cerebral vein MSV between AD group and CON group, *P < 0.05.

calculated to evaluate inter-observer reliability. Independent-samples *t*-test (for normally distributed data) or Mann–Whitney *U* test (for non-normally distributed data) was used to compare the MSV of cerebral venous between AD group and CON group.

Spearman correlation analysis was performed on the MSV of cerebral venous and the MMSE score, MoCA score, CDT score, and ADL score. The correlation between clinical and laboratory data of the AD group and MSV were performed by Pearson

TABLE 3 | Cerebral vein MSV between AD group and CON group.

Region	AD group	CON group	Original <i>p</i> -value	FDR corrected <i>p</i> -value
Left-DNV ^a	166.44 ± 32.88	143.65 ± 27.13	0.002	0.028*
Right-DNV ^a	161.12 ± 29.37	144.64 ± 27.91	0.025	0.059
Left-BV ^a	249.37 ± 36.54	228.23 ± 38.35	0.032	0.059
Right-BV ^b	260.00 (54.00)	232.00 (61.75)	0.199	0.249
Left-ICV ^b	283.00 (59.50)	243.50 (75.75)	0.036	0.059
Right-ICV ^a	276.58 ± 43.04	263.14 ± 47.30	0.252	0.252
Left-TV ^a	221.93 ± 38.57	194.14 ± 43.69	0.013	0.043*
Right-TV ^a	218.80 ± 42.11	193.10 ± 38.30	0.012	0.043*
Left-SV ^b	165.00 (55.00)	156.50 (20.75)	0.226	0.251
Right-SV ^b	156.00 (61.00)	147.00 (42.75)	0.130	0.186

^aData are expressed as mean value ± standard deviations. ^bData are expressed as median (inter-quartile range). **P* < 0.05.

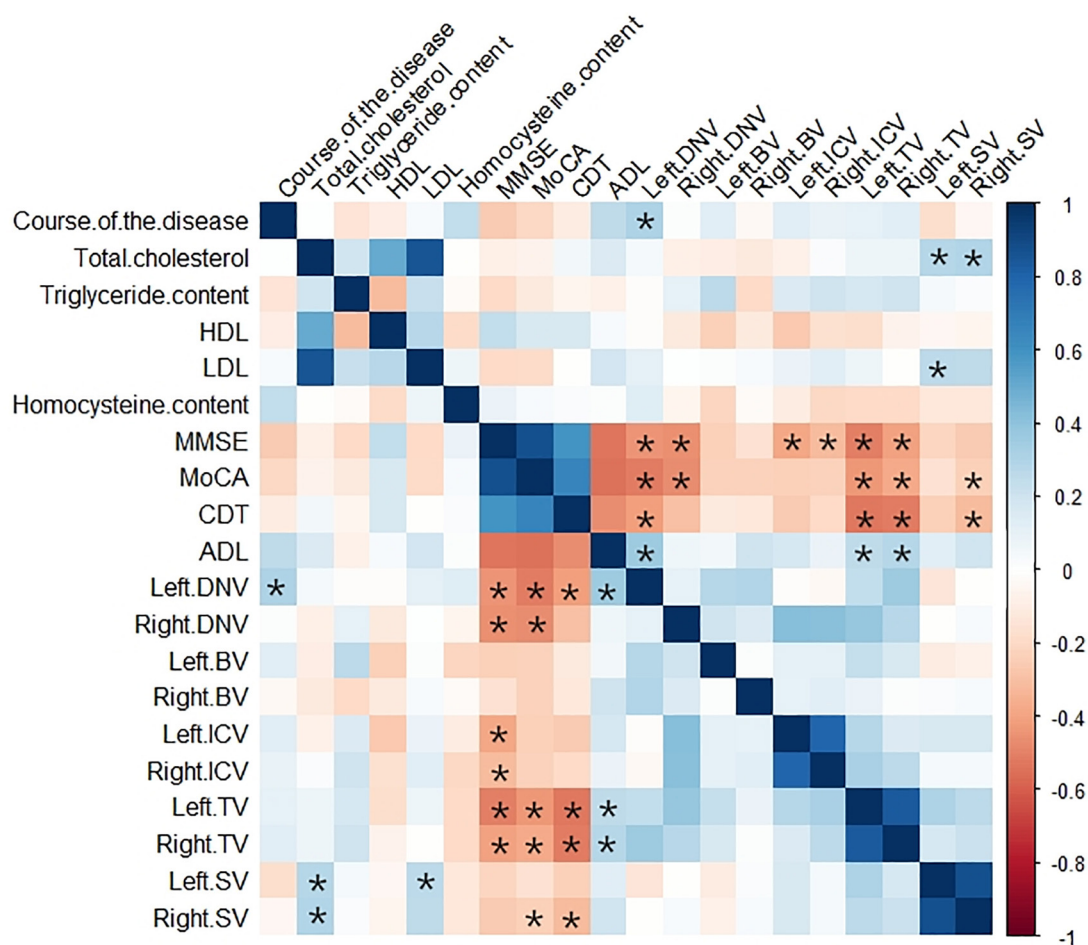


FIGURE 3 | Heat map showing the correlation analysis between MSV of cerebral veins and clinical data, laboratory examination indexes, MMSE score, MoCA score, CDT score, ADL score in AD group. Color bar on the right side displays the value of the correlation coefficient (higher from -1 to 1, and from red to blue). *Significant correlation.

correlation analysis (for normally distributed data) or Spearman correlation analysis (for non-normally distributed data). False discovery rate (FDR) (Benjamini-Hochberg method) was further adopted to correct for multiple comparisons. $P < 0.05$ was considered statistically significant.

RESULTS

Subject Characteristics

The clinical and cognitive data were summarized in **Table 2**. There was no significant difference in gender, age or years of education between the two groups ($p > 0.05$). The MMSE score, MoCA score, CDT score and ADL score in AD group were significantly different from that in CON group ($p < 0.001$).

Cerebral Vein MSV in AD Group and CON Group

The ICC of the two neuro-radiologists were 0.809~0.929. As shown in **Figure 2** and **Table 3**, higher cerebral vein MSV were detected in AD group compared to CON group; significant differences were observed in bilateral TV ($p_L = 0.043$, $p_R = 0.043$), and left DNV ($p = 0.028$).

Correlation Analysis Between the MSV of Bilateral Cerebral Veins and the Cognitive Scores in AD Group

The correlation analysis results between MSV of cerebral veins and MMSE score, MoCA score, CDT score, and ADL score were represented by heat maps (**Figure 3**), and the significant correlation were represented by scatter plots (**Figure 4**). The MSV of bilateral TV ($r_L = -0.537$, $p < 0.001$; $r_R = -0.445$, $p < 0.001$), bilateral ICV ($r_L = -0.399$, $p = 0.002$; $r_R = -0.327$, $p = 0.011$) and bilateral DNV ($r_L = -0.398$, $p = 0.002$; $r_R = -0.468$, $p < 0.001$) were all negatively correlated with the MMSE scores. Among these, the MSV of left TV showed moderate correlation, while others showed low correlation with MMSE. Furthermore, the MSV of bilateral TV ($r_L = -0.463$, $p < 0.001$; $r_R = -0.401$, $p = 0.003$), bilateral DNV ($r_L = -0.454$, $p < 0.001$; $r_R = -0.460$, $p < 0.001$) and right SV ($r = -0.311$, $p = 0.026$) were negatively correlated with the MoCA scores. In addition, there was a significant negative correlation between the MSV of bilateral TV ($r_L = -0.526$, $p < 0.001$; $r_R = -0.505$, $p < 0.001$), left DNV ($r = -0.398$, $p = 0.002$), the right SV ($r = -0.343$, $p = 0.009$) and the CDT score; moderate correlation was observed between bilateral TV and CDT score, while the MSV of left DNV and right SV displayed low correlation with CDT score. Additionally, the MSV of bilateral TV ($r_L = 0.332$, $p = 0.017$; $r_R = 0.342$, $p = 0.017$), and the left DNV ($r = 0.323$, $p = 0.017$) were positively correlated with ADL score.

Correlation Analysis Between MSV of Cerebral Veins and Clinical and Laboratory Data in AD Group

The correlation analysis results between MSV of cerebral veins and clinical and laboratory data in AD group were represented by

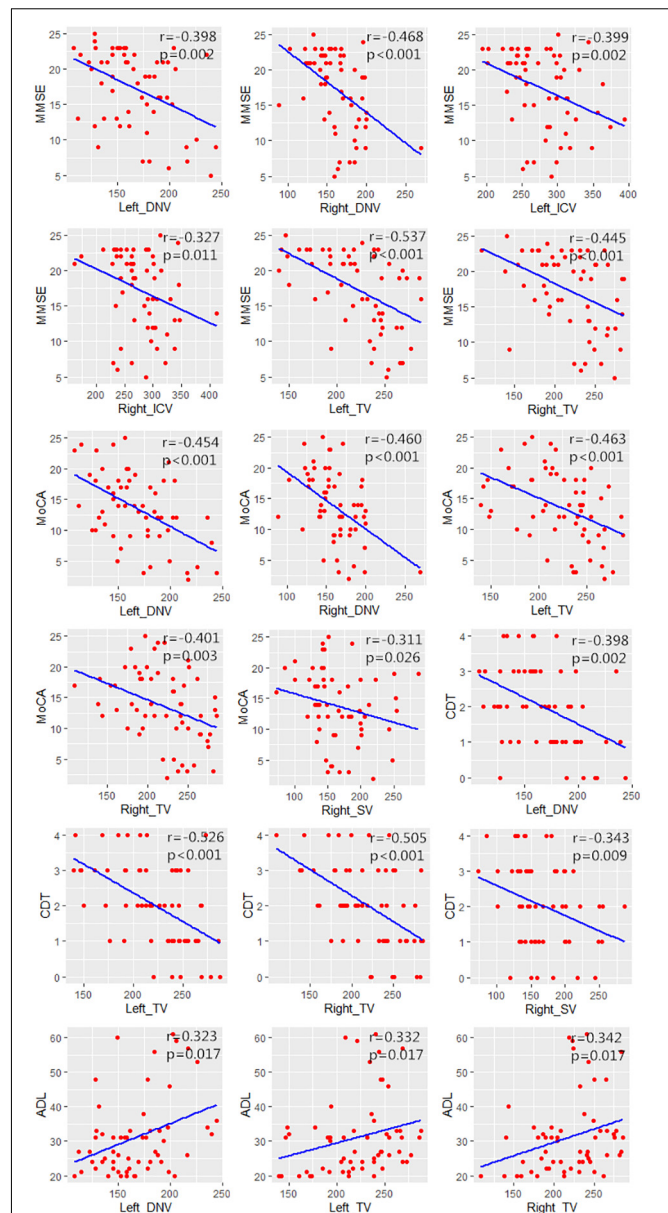


FIGURE 4 | Scatter plots showing the significant correlation between MSV of cerebral veins and MMSE score, MoCA score, CDT score, ADL score.

heat map (**Figure 3**). The MSV of left DNV ($r = 0.307$, $p = 0.031$) had a positive correlation with the course of the disease. The MSV of bilateral SV ($r_L = 0.280$, $p = 0.030$; $r_R = 0.290$, $p = 0.025$) were positively correlated with the total cholesterol, and the MSV of left SV ($r = 0.260$, $p = 0.045$) had a positive correlation with LDL (**Figure 5**). However, no correlation was found between MSV of cerebral veins and HDL, homocysteine levels ($p > 0.05$).

DISCUSSION

Venous oxygen level is an important factor for evaluating brain development and function. Under normal conditions,

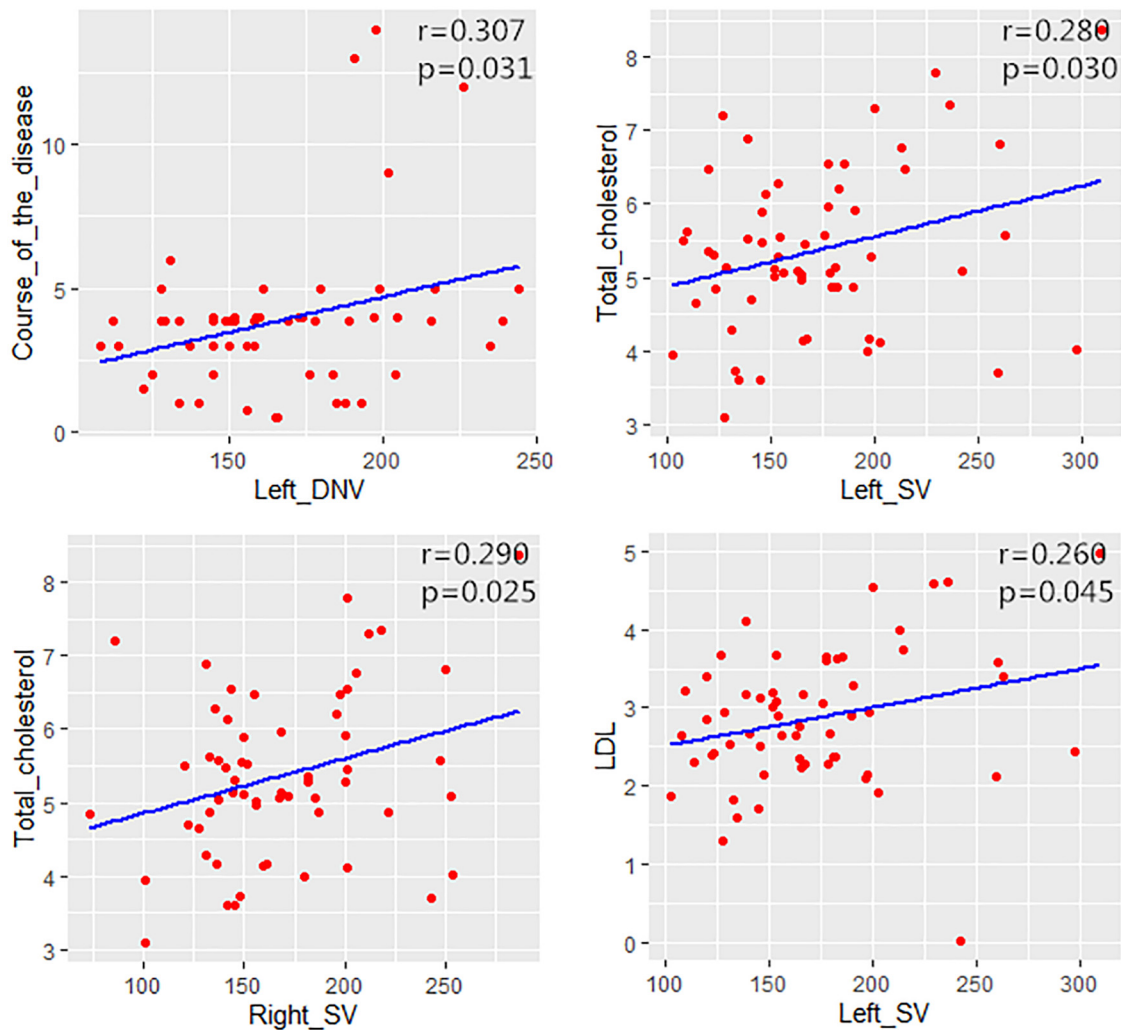


FIGURE 5 | Scatter plots showing the correlation between MSV of cerebral veins and the course of the disease, total cholesterol and LDL in AD group.

the brain consumes 20% of the total energy of the body through oxidative metabolism (Gallagher et al., 1998). The measurement of venous oxygen is crucial for analyzing the neuronal activity and brain physiology during aging and regulation of brain disease status (Donahue et al., 2009). Under normal conditions, blood oxygen level is in a relatively constant state. Nevertheless, abnormal condition, such as cerebrovascular and neurodegenerative diseases or brain trauma can affect brain oxygen levels, which may further lead to a decline of cognitive level. Previous studies have shown that vascular risk factors can participate in the pathogenesis and progression of AD (Li et al., 2011; Zhu et al., 2014; Inzelberg et al., 2015).

Previous studies have found that AD is associated with blood–brain barrier (BBB) dysfunction. BBB is an important structure that maintains the microenvironment homeostasis of the central nervous system. It can prevent pathogens and other macromolecules from entering the brain through blood circulation, excrete metabolites from brain tissues, and

participate in the cerebrospinal fluid regulation and immune response (Halliday et al., 2016). BBB dysfunction leads to the accumulation of metabolites in blood vessels, increases oxygen consumption, and further reduces the venous oxygen levels. Structural alterations, atherosclerotic lesions, and impaired hemodynamic may occur in the cerebral vessels of AD patients (Meyer et al., 2008), and the peripheral nerve tissue is accompanied by axonal loss and myelin dissolution (Gouw et al., 2008), which put the brain tissue of AD patients in a hypoxic state.

In this study, QSM was first used to quantify blood oxygen levels in cerebral veins of AD patients. We found that the oxygen level of bilateral cerebral veins in AD group was generally lower than that in CON group, in addition, the proportion of deoxyhemoglobin increased, which is consistent with previous studies. However, significant differences were observed only for left DNV and bilateral TV, thus suggesting that besides the relationship between MSV and the content of deoxyhemoglobin in blood vessel, diameter of blood vessel is another important

factor for the diagnosis of AD patients. Blood vessels with the small diameter are easily affected by the slice and partial volume effect during the measurement process, which leads to some deviations in the measurement results.

Furthermore, our data indicated that the MSV of bilateral TV, bilateral ICV and bilateral DNV were all negatively correlated with MMSE scores, and there was negative correlation between the MSV of bilateral TV, bilateral DNV, right SV and the MoCA scores. In addition, the MSV of bilateral TV, left DNV and right SV were all negatively correlated with CDT scores; while the MSV of bilateral TV, left DNV were positively correlated with ADL scores. Thus, to sum up, higher MSV indicates lower venous oxygen level, the lower the cognitive scores, and the worse the cognitive level. Because AD patients have low venous oxygen level and AD is a chronic progressive disease, the brain tissue may be in a state of long-term hypoxia, which will inevitably lead to the decline of brain function and consequently reduce the cognitive level.

Our findings showed the MSV of the left DNV was positively correlated with the course of disease, indicating that the longer course of disease led to lower oxygen levels of the left DNV. The development of AD is an irreversible pathological process. Consequently, the longer course of AD, leads to more serious conditions, while the decrease of cerebral venous oxygen level is positively correlated with the deterioration of the disease.

In this study, the MSV of bilateral SV were positively correlated with the total cholesterol, and the MSV of left SV had a positive correlation with LDL. We suggested that dyslipidemia influences the cerebral blood perfusion through vascular disease, further leads to decreasing of cerebral oxygen level. Previous studies have reported that, dyslipidemia was a key factor of metabolic syndrome, and increases the risk of AD (Gentile et al., 2020). Wingo et al. (2019) found that elevated LDL levels were associated with higher probability of having early-onset AD, this novel findings highlight the important role of LDL in AD pathogenesis. Besides, increased plasma homocysteine level is a strong, independent risk factor for the development of AD (Seshadri et al., 2002). However, no correlation was found between MSV of cerebral veins and homocysteine levels.

The present study has some limitations: (1) this study was a retrospective study and our subjects were all inpatients, who consulted our hospital due to obvious symptoms. The course of the disease was relatively long and the symptoms were relatively severe. Also, there were few patients with mild cognitive impairment who were not included in this study, which should be addressed by further research. (2) The AD group and CON group were of different size, thus, larger sample size is needed to reduce

errors. (3) The ROI in this study was manually placed, which will inevitably lead to certain errors.

CONCLUSION

Decreasing cerebral venous oxygen level in AD patients may affect cognitive status, and associated with the deterioration of the disease in AD patients.

DATA AVAILABILITY STATEMENT

The original contributions presented in the study are included in the article/**Supplementary Material**, further inquiries can be directed to the corresponding author/s.

ETHICS STATEMENT

The studies involving human participants were reviewed and approved by the Ethics Committee of First Affiliated Hospital of Dalian Medical University. The patients/participants provided their written informed consent to participate in this study. Written informed consent was obtained from the individual(s) for the publication of any potentially identifiable images or data included in this article.

AUTHOR CONTRIBUTIONS

YL, JD, and YM conceived the study and participated in its design, data collection, and drafting of the manuscript. WW, BG, and ST participated in statistical analysis and software. QS and NZ participated in image reconstruction and data analysis. CD, ZL, and LX participated in the manuscript revise. The authors read and approved the final manuscript.

FUNDING

This study was supported by the National Natural Science Foundation of China (Nos. 81671646 and 81801657).

SUPPLEMENTARY MATERIAL

The Supplementary Material for this article can be found online at: <https://www.frontiersin.org/articles/10.3389/fnins.2020.570848/full#supplementary-material>

REFERENCES

- An, H., Lin, W., Celik, A., and Lee, Y. Z. (2001). Quantitative measurements of cerebral metabolic rate of oxygen utilization using MRI: a volunteer study. *NMR Biomed.* 14, 441–447. doi: 10.1002/nbm.717
- Barnes, S. R. S., and Haacke, E. M. (2009). Susceptibility-Weighted Imaging: Clinical Angiographic Applications. *Magn. Reson. Imaging Clin. N. Am.* 17, 47–61. doi: 10.1016/j.mric.2008.12.002
- Derry, P. J., and Kent, T. A. (2017). Correlating quantitative susceptibility mapping with cognitive decline in Alzheimer's disease. *Brain* 140, 2069–2072. doi: 10.1093/brain/awx167

- Donahue, M. J., Blicher, J. U., Østergaard, L., Feinberg, D. A., MacIntosh, B. J., Miller, K. L., et al. (2009). Cerebral blood flow, blood volume, and oxygen metabolism dynamics in human visual and motor cortex as measured by whole-brain multi-modal magnetic resonance imaging. *J Cereb Blood Flow Metab.* 29, 1856–1866. doi: 10.1038/jcbfm.2009.107
- Fan, A., Bilgic, B., Gagnon, L., Witzel, T., Bhat, H., Rosen, B., et al. (2014). Quantitative oxygenation venography from MRI phase. *Magn Reson Med.* 72, 149–159. doi: 10.1002/mrm.24918
- Gallagher, D., Belmonte, D., Deurenberg, P., Wang, Z., Krasnow, N., Pi-Sunyer, F. X., et al. (1998). Organ-tissue mass measurement allows modeling of REE and metabolically active tissue mass. *Am. J. Physiol.* 275, E249–E258. doi: 10.1016/S0303-7207(98)00082-3
- Gentile, F., Doneddu, P. E., Riva, N., Nobile-Orazio, E., and Quattrini, A. (2020). Diet, Microbiota and Brain Health: Unraveling the Network Intersecting Metabolism and Neurodegeneration. *Int. J. Mol. Sci.* 21:7471. doi: 10.3390/ijms21207471
- Gong, N. J., Dibb, R., Bulk, M., van der Weerd, L., and Liu, C. (2019). Imaging beta amyloid aggregation and iron accumulation in Alzheimer's disease using quantitative susceptibility mapping MRI. *Neuroimage* 191, 176–185. doi: 10.1016/j.neuroimage.2019.02.019
- Gouw, A. A., Seewann, A., Vrenken, H., van der Flier, W. M., Rozemuller, J. M., Barkhof, F., et al. (2008). Heterogeneity of white matter hyperintensities in Alzheimer's disease: post-mortem quantitative MRI and neuropathology. *Brain* 131, 3286–3298. doi: 10.1093/brain/awn265
- Halliday, M. R., Rege, S. V., Zhao, Z., Miller, C. A., Winkler, E. A., et al. (2016). Accelerated pericyte degeneration and blood-brain barrier breakdown in apolipoprotein E4 carriers with Alzheimer's disease. *J. Cereb Blood Flow Metab.* 36, 216–227. doi: 10.1038/jcbfm.2015.44
- Harrington, C. R. (2012). The molecular pathology of Alzheimer's disease. *Neuroimaging Clin. N. Am.* 22, 11–22. doi: 10.1016/j.nic.2011.11.003
- Inzelberg, R., Massarwa, M., Schechtman, E., Strugatsky, R., Farrer, L., and Friedland, R. (2015). Estimating the risk for conversion from mild cognitive impairment to Alzheimer's disease in an elderly Arab community. *J. Alzheimers Dis.* 45, 865–871. doi: 10.3233/JAD-142871
- Jensen-Kondering, U., and Böhm, R. (2013). Asymmetrically hypointense veins on T2* w imaging and susceptibility-weighted imaging in ischemic stroke. *World J. Radiol.* 5, 156–165. doi: 10.4329/wjr.v5.i4.156
- Kesavadas, C., Santhosh, K., and Thomas, B. (2010). Susceptibility weighted imaging in cerebral hypoperfusion-can we predict increased oxygen extraction fraction? *Neuroradiology* 52, 1047–1054. doi: 10.1007/s00234-010-0733-2
- Li, J., Wang, Y. J., Zhang, M., Xu, Z. Q., Gao, C. Y., Fang, C. Q., et al. (2011). Vascular risk factors promote conversion from mild cognitive impairment to Alzheimer disease. *Neurology* 76, 1485–1491. doi: 10.1212/WNL.0b013e318217e7a4
- Li, M., Hu, J., Miao, Y., Shen, H., Tao, D., Yang, Z., et al. (2013). In vivo measurement of oxygenation changes after stroke using susceptibility weighted imaging filtered phase data. *PLoS One* 8:e63013. doi: 10.1371/journal.pone.0063013
- Liu, C., Li, W., Tong, K., Yeom, K., and Kuzminski, S. (2015). Susceptibility-weighted imaging and quantitative susceptibility mapping in the brain. *J. Magn. Reson. Imaging* 42, 23–41. doi: 10.1002/jmri.24768
- Mak, H. K., Qian, W., Ng, K. S., Chan, Q., Song, Y. Q., Chu, L. W., et al. (2014). Combination of MRI hippocampal volumetry and arterial spin labeling MR perfusion at 3-Tesla improves the efficacy in discriminating Alzheimer's disease from cognitively normal elderly adults. *J. Alzheimers Dis.* 41, 749–758. doi: 10.3233/JAD-131868
- McKhann, G. M., Drachman, D., Folstein, M., Katzman, R., Price, D., and Stadlan, E. M. (1984). Clinical diagnosis of Alzheimer's disease: report of the NINCDS-ADRDA Work Group under the auspices of Department of Health and Human Services Task Force on Alzheimer's Disease. *Neurology* 34, 939–944. doi: 10.1212/wnl.34.7.939
- McKhann, G. M., Knopman, D. S., Chertkow, H., Hyman, B. T., Jack, C. R., Kaas, C. H., et al. (2011). The diagnosis of dementia due to Alzheimer's disease: recommendations from the National Institute on Aging-Alzheimer's Association workgroups on diagnostic guidelines for Alzheimer's disease. *Alzheimers Dement* 7, 263–269. doi: 10.1016/j.jalz.2011.03.005
- Messina, S. A., Poretti, A., Tekes, A., Robertson, C., Johnston, M. V., and Huisman, T. (2014). Early predictive value of susceptibility weighted imaging (SWI) in pediatric hypoxic-ischemic injury. *J. Neuroimaging* 24, 528–530. doi: 10.1111/jon.12043
- Meyer, E. P., Ulmann-Schuler, A., Staufenbiel, M., and Krucker, T. (2008). Altered morphology and 3D architecture of brain vasculature in a mouse model for Alzheimer's disease. *Proc. Natl. Acad. Sci. USA* 105, 3587–3592. doi: 10.1073/pnas.0709788105
- Mukherjee, P., Kang, H., Videen, T., McKinstry, R., Powers, W. J., and Derdeyn, C. P. (2003). Measurement of cerebral blood flow in chronic carotid occlusive disease: comparison of dynamic susceptibility contrast perfusion MR imaging with positron emission tomography. *AJNR Am. J. Neuroradiol.* 24, 862–871. doi: 10.1007/s00234-002-0922-8
- Seshadri, S., Beiser, A., Selhub, J., Jacques, P. F., Rosenberg, I. H., D'Agostino, R. B., et al. (2002). Plasma homocysteine as a risk factor for dementia and Alzheimer's disease. *N. Engl. J. Med.* 346, 476–483. doi: 10.1056/NEJMoa011613
- Wingo, T. S., Cutler, D. J., Wingo, A. P., Le, N. A., Rabinovici, G. D., Miller, B. L., et al. (2019). Association of Early-Onset Alzheimer Disease With Elevated Low-Density Lipoprotein Cholesterol Levels and Rare Genetic Coding Variants of APOB. *JAMA Neurol.* 76, 809–817. doi: 10.1001/jamaneurol.2019.0648
- Zaitzu, Y., Kudo, K., Terae, S., Yazu, R., Ishizaka, K., Fujima, N., et al. (2011). Mapping of cerebral oxygen extraction fraction changes with susceptibility-weighted phase imaging. *Radiology* 261, 930–936. doi: 10.1148/radiol.11102416
- Zhu, J., Wang, Y., Li, J., Deng, J., and Zhou, H. D. (2014). Intracranial artery stenosis and progression from mild cognitive impairment to Alzheimer disease. *Neurology* 82, 842–849. doi: 10.1212/WNL.0000000000000185

Conflict of Interest: LX was employed by GE Healthcare.

The remaining authors declare that the research was conducted in the absence of any commercial or financial relationships that could be construed as a potential conflict of interest.

Copyright © 2021 Liu, Dong, Song, Zhang, Wang, Gao, Tian, Dong, Liang, Xie and Miao. This is an open-access article distributed under the terms of the Creative Commons Attribution License (CC BY). The use, distribution or reproduction in other forums is permitted, provided the original author(s) and the copyright owner(s) are credited and that the original publication in this journal is cited, in accordance with accepted academic practice. No use, distribution or reproduction is permitted which does not comply with these terms.



Alterations of Iron Level in the Bilateral Basal Ganglia Region in Patients With Middle Cerebral Artery Occlusion

Lei Du^{1,2†}, Zifang Zhao^{3†}, Xiuxiu Liu^{1†}, Yue Chen¹, Wenwen Gao¹, Yige Wang¹, Jian Liu⁴, Bing Liu¹ and Guolin Ma^{1,2*}

¹ Department of Radiology, China-Japan Friendship Hospital, Beijing, China, ² Graduate School of Peking Union Medical College, Peking Union Medical College, Chinese Academy of Medical Sciences, Beijing, China, ³ Department of Anesthesiology, Peking University First Hospital, Peking University, Beijing, China, ⁴ Department of Ultrasound Diagnosis, China-Japan Friendship Hospital, Beijing, China

OPEN ACCESS

Edited by:

Minming Zhang,
Zhejiang University, China

Reviewed by:

Falei Yuan,
Zhejiang Ocean University, China
Zhijun Zhang,
Shanghai Jiao Tong University, China

*Correspondence:

Guolin Ma
maguolin1007@qq.com

[†]These authors have contributed
equally to this work

Specialty section:

This article was submitted to
Neurodegeneration,
a section of the journal
Frontiers in Neuroscience

Received: 18 September 2020

Accepted: 17 December 2020

Published: 21 January 2021

Citation:

Du L, Zhao Z, Liu X, Chen Y, Gao W,
Wang Y, Liu J, Liu B and Ma G (2021)
Alterations of Iron Level in the Bilateral
Basal Ganglia Region in Patients With
Middle Cerebral Artery Occlusion.
Front. Neurosci. 14:608058.
doi: 10.3389/fnins.2020.608058

Background and Purpose: The purpose of this study was to explore the changes of iron level using quantitative susceptibility mapping (QSM) in the bilateral basal ganglia region in middle cerebral artery occlusion (MCAO) patients with long-term ischemia.

Methods: Twenty-seven healthy controls and nine patients with MCAO were recruited, and their QSM images were obtained. The bilateral caudate nucleus (Cd), putamen (Pt), and globus pallidus (Gp) were selected as the regions of interest (ROIs). Susceptibility values of bilateral ROIs were calculated and compared between the affected side and unaffected side in patients with MCAO and between patients with MCAO and healthy controls. In addition, receiver operating characteristic (ROC) curves were performed to evaluate the diagnostic capability of susceptibility values in differentiating healthy controls and patients with MCAO by the area under the curve (AUC).

Results: The susceptibility values of bilateral Cd were asymmetric in healthy controls; however, this asymmetry disappeared in patients with MCAO. In addition, compared with healthy controls, the average susceptibility values of the bilateral Pt in patients with MCAO were increased ($P < 0.05$), and the average susceptibility value of the bilateral Gp was decreased ($P < 0.05$). ROC curves showed that the susceptibility values of the Pt and Gp had a larger AUC (AUC = 0.700 and 0.889, respectively).

Conclusion: As measured by QSM, the iron levels of the bilateral basal ganglia region were significantly changed in patients with MCAO. Iron dyshomeostasis in the basal ganglia region might be involved in the pathophysiological process of middle cerebral artery stenosis and occlusion. These findings may provide a novel insight to profoundly address the pathophysiological mechanisms of MCAO.

Keywords: middle cerebral artery occlusion, quantitative susceptibility mapping, iron, susceptibility, basal ganglia region

INTRODUCTION

It is well-established that stroke has been one of the most common cerebrovascular diseases that could generate neuronal deaths and subsequent disability and mortality. According to pathological origins, stroke can be divided into two forms, ischemic and hemorrhagic stroke, and ischemic stroke accounts for the majority of patients (Mohan et al., 2009). Notably, middle cerebral artery stenosis and occlusion is the most frequent ischemic subtype in clinical practice and the most widely selected experimental model to elucidate the pathophysiology of cerebrovascular ischemic lesions. Although non-infectious neuroinflammation, oxidative stress, and metabolic disturbances of metal ions have been implicated in the process of middle cerebral artery occlusion (MCAO) (Fujioka et al., 2003; Kamel and Iadecola, 2012), the pathogenesis of MCAO has not been fully elucidated.

Iron, mainly stored in the form of ferritin or hemosiderin in brain tissue, is indispensable to the maintenance of normal brain function as it is an important cofactor for various enzymes involved in neurotransmitter synthesis, oxygen transport, electron transfer, and myelin generation (Connor et al., 2001; Munoz and Humeres, 2012). Regardless of the crucial roles in normal physiological functions, overloading of iron in the brain might trigger an abnormal release of toxic free radicals and consequent oxidative damage (Bolt and Marchan, 2010; Kell, 2010). Consistently, recent studies indicated that excessive iron deposition in brain tissue was closely linked to a variety of neurodegenerative diseases, such as Parkinson's disease (PD), Alzheimer's disease (AD), and stroke, which validated the underlying role of brain iron in the pathogenesis and progression of cognitive symptoms (Bishop et al., 2011; Acosta-Cabronero et al., 2013; Murakami et al., 2015; Du et al., 2016).

Compared with the traditional iron measurement techniques, susceptibility weighted imaging (SWI) (Schafer et al., 2009; Shmueli et al., 2009) and quantitative susceptibility mapping (QSM) can non-invasively and quantitatively detect the magnetic susceptibility values of brain tissue with higher specificity and sensitivity. Previous studies had found that the susceptibility value of tissue acquired by QSM was positively correlated with the iron level in deep gray matter nuclei (Langkammer et al., 2012; Deistung et al., 2013; Lim et al., 2013; Sun et al., 2015), which further verified the specific advantage in the measurements of tissue iron content. Currently, QSM has been increasingly used for the diagnosis, grading, and severity prediction of neurodegenerative diseases, both in clinical practice and experimental investigation.

The blood and oxygen in the basal ganglia regions are mostly supplied by the middle cerebral artery, and only a small part is supplied by the anterior cerebral artery and the choroid artery. Ischemia induced by MCAO could cause a variety of pathophysiological complications and subsequently result in brain function disorders and brain damage. Interestingly, the ischemic damages were found not only in the regions supplied by the MCA but also in deep regions such as the basal ganglia region, hippocampus, hypothalamus, and thalamus (Fujioka et al., 2003; El Amki et al., 2015; Pang et al., 2015). A possible explanation

is the concomitant occlusions of deep and small cerebral arteries arising directly from the internal carotid artery, at the proximity of the origin of MCA (El Amki et al., 2015). Moreover, several studies have found that long-term ischemia could result in oxidative stress, non-infectious neuroinflammation, acidosis, and metabolic disturbances of metal ions such as calcium (Siesjo, 1988; Kamel and Iadecola, 2012; Yushmanov et al., 2013; Liu et al., 2014). However, it remains unknown whether the metabolism of iron in the basal ganglia regions would change after a long-term ischemia. We speculated that the iron level in the basal ganglia regions may change along with ischemic brain damage secondary to MCAO. The purpose of this study was to explore the changes of iron level using QSM in the bilateral basal ganglia region in MCAO patients with long-term ischemia.

MATERIALS AND METHODS

Subjects

This study protocol was approved by the Ethics Committee of China-Japan Friendship Hospital and informed consent of all the participants was obtained. The severity of stroke of all the participants was measured by the NIH Stroke Scale (NIHSS) scale. A total of 27 healthy controls and 9 adult patients with MCAO were enrolled in this research. The patients with MCAO visited the Department of Neurology of China-Japan Friendship Hospital between March 2018 and March 2019. The diagnosis of MCAO was made by neurological physicians based on clinical symptoms, CT results, conventional MRI, and MR angiography. Patients with MCAO were selected if they met the following criteria: (a) the MR image has no artifacts; (b) the clinical information of the participants is complete and the participants had no other brain diseases, such as tumors or dementia; and (c) the participants had no visual and hearing impairment, capable of coordinating with the completion of scale and MRI examination. There were five cases of left middle cerebral artery occlusion and four cases of right middle cerebral artery occlusion in the patient group. There were five males and four females, with an average age of 61.7 ± 12.3 years (38–79 years). All patients had chronic ischemia and were right-handed. **Table 1** shows the detailed clinical information of the nine patients with MCAO.

Healthy controls were recruited from the local communities. Inclusion criteria were as follows: (a) ages range 54–79 (including 54 and 79 years); (b) being right-handed; (c) the patient has no basic diseases such as hypertension and diabetes, no cognitive impairment, and no family history of neurological and psychiatric illness; and (d) MRI examination reveals only small lacunar infarcts. Healthy controls suffering from cardiovascular, neurologic, metabolic, and psychiatric disorders or brain abnormalities were excluded from this study. Finally, 27 healthy controls were enrolled in the present study, 9 males and 18 females, with an average age of 65.1 ± 7.6 years (54–79 years). **Table 2** shows all the subjects' clinical information. All subjects received T1-weighted imaging, T2-weighted imaging, 3D T1-weighted imaging, and quantitative susceptibility mapping.

TABLE 1 | Detailed clinical information of nine patients with MCAO.

Patient	Sex	Age	Affected side	Smoke	Drink	Hypertension	Diabetes	Handedness	Duration (years)
1	M	38	Right	Y	N	Y	N	Right	2
2	M	61	Left	N	Y	N	N	Right	5
3	F	57	Left	N	N	Y	N	Right	6
4	F	64	Right	N	N	Y	N	Right	2
5	M	50	Left	Y	Y	Y	N	Right	1
6	F	79	Left	N	N	N	N	Right	7
7	F	71	Right	N	N	Y	N	Right	3
8	M	63	Left	N	N	Y	N	Right	4
9	M	72	Right	N	N	Y	Y	Right	6

MCAO, middle cerebral artery occlusion; M, male; F, female; Y, yes; N, no.

TABLE 2 | Demographic data of healthy controls and patients with MCAO.

	Healthy	MCAO	P-values
No.	27	9	–
Sex (male/female)	9/18	5/4	$P > 0.05$
Age (years)	65.1 ± 7.6 (54–79)	61.7 ± 12.3 (38–79)	$P > 0.05$
Educations	10.4 ± 3.8	–	–
Duration (years)	–	4.0 ± 2.1 (1–7)	–
Handedness (right)	27	9	$P > 0.05$

–, not significant or not measured; MCAO, middle cerebral artery occlusion.

MR Imaging Protocol

A 3.0-T MRI scanner (GE Healthcare, Discovery MR750, Milwaukee, USA) equipped with an eight-channel head coil was used to acquire the data. All participants underwent a T2-weighted imaging scan to exclude craniocerebral organic diseases.

A 3D gradient-echo (GRE) sequence was used for quantitative susceptibility mapping. The parameters were field of view (FOV) = 256×256 mm, matrix size = 256×256 , slice thickness = 1.0 mm, echo time (TE) = 3.2 ms, repetition time (TR) = 22.9 ms, flip angle (FA) = 12° , and scan time = 4 min 24 s.

A 3D T1WI structure image was reconstructed using three-dimensional fast spoiled gradient-echo sequences (3D FSPGR): FOV = 256×256 mm, matrix size = 256×256 , slice thickness = 1.0 mm, TR = 6.7 ms, TE = min full, FA = 12° , number of slices = 192, and scan time = 4 min 10 s.

QSM

We performed several processing steps to calculate the quantitative susceptibility mapping from the obtained MR phase images. Firstly, a Laplacian-based phase unwrapping was used to perform the phase unwrapping images. Then, we acquired a brain mask using skull-stripping the GRE magnitude image obtained at a TE of 10 ms. Secondly, the phase unwrapping images were divided by $2\pi \cdot \text{TE}$ to get images of the frequency shift in hertz for each echo. Thirdly, background fields were removed with the variable spheric kernel size sophisticated harmonic artifact decrease for the phase-data (V-SHARP) method with

a regularization parameter of 0.05 and a maximum radius of 4 mm. Compared with single-echo reconstruction, we averaged the resulting images of all five echoes to acquire a better signal-to-noise ratio after elimination of background fields. Finally, inverse dipole calculations using a least squares and QR factorization-based minimization was performed to get the QSM imaging.

Image Segmentation

In the present study, the caudate nucleus (Cd), putamen (Pt), and globus pallidus (Gp) were selected as the regions of interest (ROIs) (**Figure 1A**). Firstly, the GRE quantitative susceptibility mapping was co-registered to the 3D T1WI, which is to better define the boundaries of each gray nucleus. The ROIs were then manually segmented by two radiologists (Lei Du, 5 years of working experience; Yue Chen, 2 years of working experience) slice by slice using the FuncTool on a GE AW4.6 workstation (GE Healthcare, Milwaukee, WI). They were blinded to clinical and MR imaging information. The susceptibility value and size of three successive slices were acquired in each ROI to eliminate the effects of the occasional case. Also, the average susceptibility values of each ROI were calculated. The unit of susceptibility value was parts per million (ppm).

Statistical Analysis

Between the patient group and the healthy control group, age was compared using two-sample *t*-test, and gender and handedness were compared using the chi-square (χ^2) test. The data of age and education was shown in the form of mean \pm SD.

The interobserver agreement of two observers was assessed using the intraclass correlation coefficient (ICC), and ICC < 0.40 is poor, 0.40–0.59 is fair, 0.60–0.74 is good, and > 0.74 is excellent (Oppo et al., 1998).

The paired *t*-test was used to assess the differences of susceptibility values between the left and right hemispheres in healthy controls and between the affected side and the unaffected side in patients with MCAO. Comparisons between patients with MCAO and the healthy controls were investigated using two-sample *t*-test. Moreover, receiver operating characteristic (ROC) curves were performed to evaluate the diagnostic capability of susceptibility values in differentiating patients with MCAO and

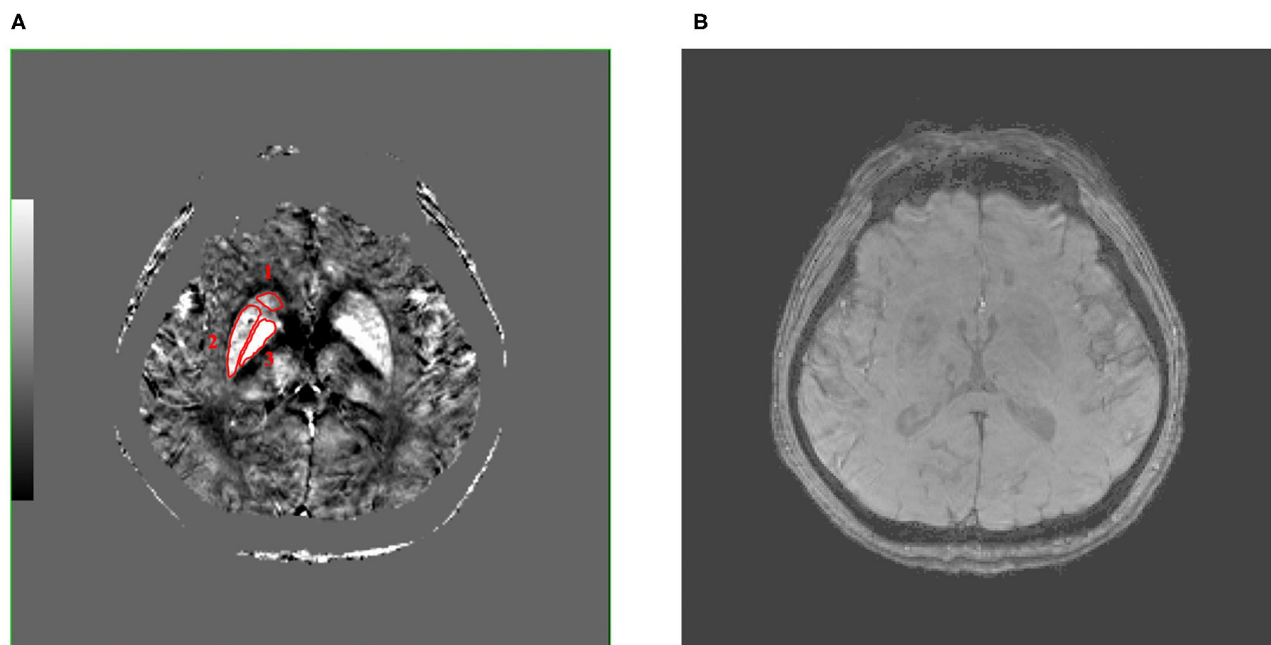


FIGURE 1 | These are QSM (A) and SWI (B) images of a 50-year-old male patient with MCAO at the same level, and the caudate nucleus (Cd), putamen (Pt), and globus pallidus (Gp) (number 1–3, separately) were selected as regions of interest (ROIs), which were encircled in red line in QSM image. Compared with SWI image, QSM image can show the boundary of the Cd, Pt, and Gp more clearly. QSM, quantitative susceptibility mapping; SWI, susceptibility weighted imaging; MCAO, middle cerebral artery occlusion; ROIs, regions of interest.

healthy controls by the area under the curve (AUC) $P < 0.05$ was considered to be statistically significant.

RESULTS

Characteristics of All the Participants

The demographic information of all the participants is summarized in **Table 2**. Finally, 9 MCAO patients (5 males and 4 females, mean age 61.7 ± 12.3 years, range 38–79 years) and 27 healthy controls (9 males and 18 females, mean age 65.1 ± 7.6 years, range 54–79 years, education 10.4 ± 3.8 years) were enrolled in this study. All participants are right-handed. There were five cases of left middle cerebral artery occlusion and four cases of right middle cerebral artery occlusion in the patient group. Then, the left and right gray nuclei in each ROI were divided into the affected side group and the unaffected side group in patients with MCAO. From **Table 2**, we knew that gender, age, and handedness between the patient group and healthy control group are matched ($P > 0.05$). The interobserver variability was assessed by ICC, and a good agreement was acquired between two radiologists for the susceptibility values (**Table 3**).

The QSM image showed the location of the bilateral Cd, Pt, and Gp in a 50-year-old male patient with MCAO (**Figure 1A**). **Figure 1A** shows that there were significant differences between the ROI and surrounding brain regions as seen by the naked eyes, indicating that the iron level in the Cd, Pt, and Gp is more than that in the surrounding brain region. **Figure 1B** displays a SWI image at the same level as QSM. Compared with the SWI image,

TABLE 3 | Intraclass correlation coefficient (ICC) of bilateral caudate nucleus (Cd), putamen (Pt), and globus pallidus (Gp) in patients with MCAO and healthy controls.

	ROIs	ICC of the left hemisphere (95% CI)	ICC of the right hemisphere (95% CI)
MCAO	Cd	0.973 (0.881 to 0.994)	0.448 (–1.446 to 0.876)
	Pt	0.987 (0.943 to 0.997)	0.313 (–2.047 to 0.845)
	Gp	0.877 (0.455 to 0.972)	0.916 (0.628 to 0.981)
Healthy controls	Cd	0.259 (–1.309 to 0.762)	0.742 (0.196 to 0.917)
	Pt	0.706 (0.085 to 0.906)	0.555 (–0.388 to 0.857)
	Gp	0.776 (0.303 to 0.928)	0.796 (0.364 to 0.934)

ICC, intraclass correlation coefficient; Cd, caudate nucleus; Pt, putamen; Gp, globus pallidus; MCAO, middle cerebral artery occlusion; ROIs, regions of interest; CI, confidence interval.

the QSM image could show the boundary of the Cd, Pt, and Gp more clearly.

Comparisons of Susceptibility Values Between the Affected Side and Unaffected Side in Patients With MCAO and Between Left and Right in Healthy Controls

The mean and SD of the susceptibility values of the Cd, Pt, and Gp in all participants are summarized in **Tables 4, 5**.

There were significant differences between the left and right susceptibility values of the Cd in the healthy controls, and the right was slightly higher than the left. Also, there were no significant differences between the left and right Pt and Gp in the healthy controls and no significant differences between the affected side and unaffected side in all ROI in patients with MCAO (Figure 2).

Comparisons of Susceptibility Values Between Patients With MCAO and Healthy Controls

To facilitate the comparison between the patient group and the healthy control group, we calculated the average susceptibility values of the left and right ROI, since there was no significant difference between the left and right ROI both in MCAO

TABLE 4 | Mean and SD of the susceptibility values of bilateral caudate nucleus (Cd), putamen (Pt), and globus pallidus (Gp) in all participants.

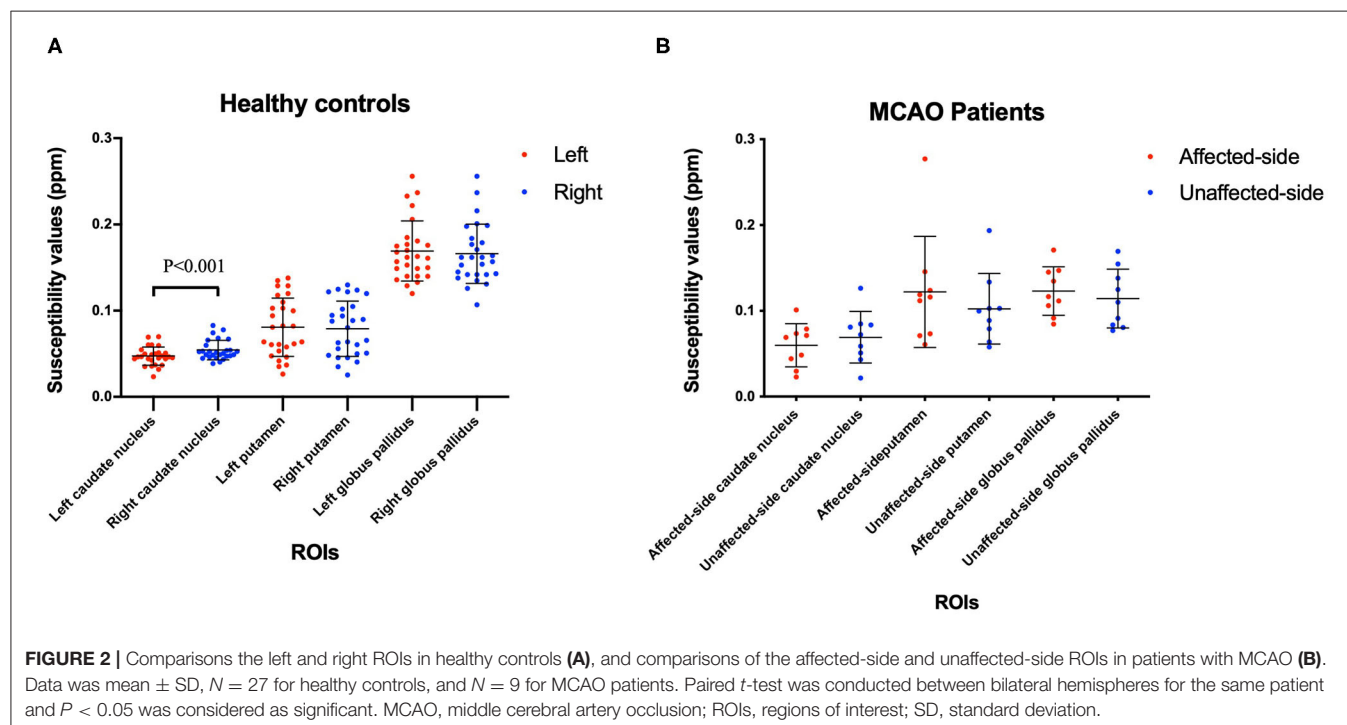
	Caudate nucleus (Cd)		Putamen (Pt)		Globus pallidus (Gp)	
	Left	Right	Left	Right	Left	Right
Healthy	0.0473 ± 0.01065	0.0543 ± 0.01137	0.0808 ± 0.03398	0.0791 ± 0.03210	0.1692 ± 0.03488	0.1660 ± 0.03443
MCAO	0.0660 ± 0.03143	0.0631 ± 0.02461	0.1004 ± 0.03240	0.1242 ± 0.06869	0.1188 ± 0.03535	0.1188 ± 0.02758

SD, standard deviation; Cd, caudate nucleus; Pt, putamen; Gp, globus pallidus; MCAO, middle cerebral artery occlusion.

TABLE 5 | Mean and SD of the susceptibility values of the affected side and unaffected side caudate nucleus (Cd), putamen (Pt), and globus pallidus (Gp) in all participants.

	Caudate nucleus (Cd)		Putamen (Pt)		Globus pallidus (Gp)	
	Affected side	Unaffected side	Affected side	Unaffected side	Affected side	Unaffected side
MCAO	0.0599 ± 0.02532	0.0692 ± 0.03014	0.1221 ± 0.06470	0.1025 ± 0.04104	0.1232 ± 0.02827	0.1144 ± 0.03418

SD, standard deviation; Cd, caudate nucleus; Pt, putamen; Gp, globus pallidus; MCAO, middle cerebral artery occlusion.



patients and healthy controls, except the Cd of the patient group. There was no significant difference between the healthy group and the MCAO patient group both in the affected side and unaffected side of the Cd. **Figure 3** shows the comparisons between the healthy group and the patient group in the Pt and Gp. **Figure 3** shows that the susceptibility values of the Pt were significantly higher in patients with MCAO than those in the controls ($P < 0.05$), and the susceptibility values of the Gp were significantly lower in patients with MCAO than those in the controls ($P < 0.05$).

The susceptibility values of the bilateral Pt in MCAO patients were significantly higher than those in the controls. **Figure 4** shows that the AUC of average susceptibility values of the bilateral Gp (AUC = 0.889) was larger than the others, including the left Cd, right Cd, and bilateral Pt (AUC = 0.761, 0.679, and 0.700, respectively). The cutoff of the susceptibility value of Pt was 0.0996. The sensitivity and specificity for identifying patients with MCAO from the controls were 66.7 and 66.7%, respectively. In contrast, the susceptibility values of the bilateral Gp in patients with MCAO were significantly lower than those in the controls ($P < 0.05$). The cutoff of the susceptibility value for Gp was 0.1408. The sensitivity and specificity for differentiating patients with MCAO from the controls were 77.8 and 81.5%.

DISCUSSION

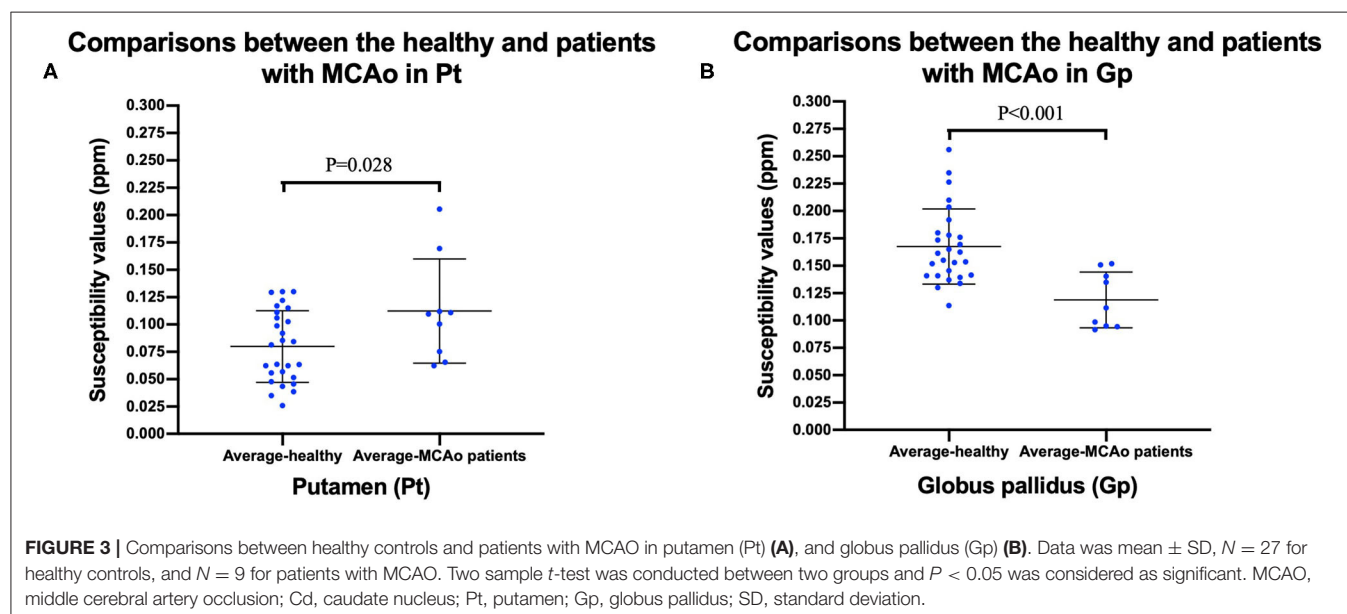
In the current study, susceptibility values acquired by QSM were used to investigate the alterations of the iron level in the bilateral basal ganglia region in patients with MCAO. We found some alterations of susceptibility values in patients with MCAO and some significant differences between patients with MCAO and healthy controls. More specifically, the susceptibility values of the Pt in patients with MCAO were significantly higher than

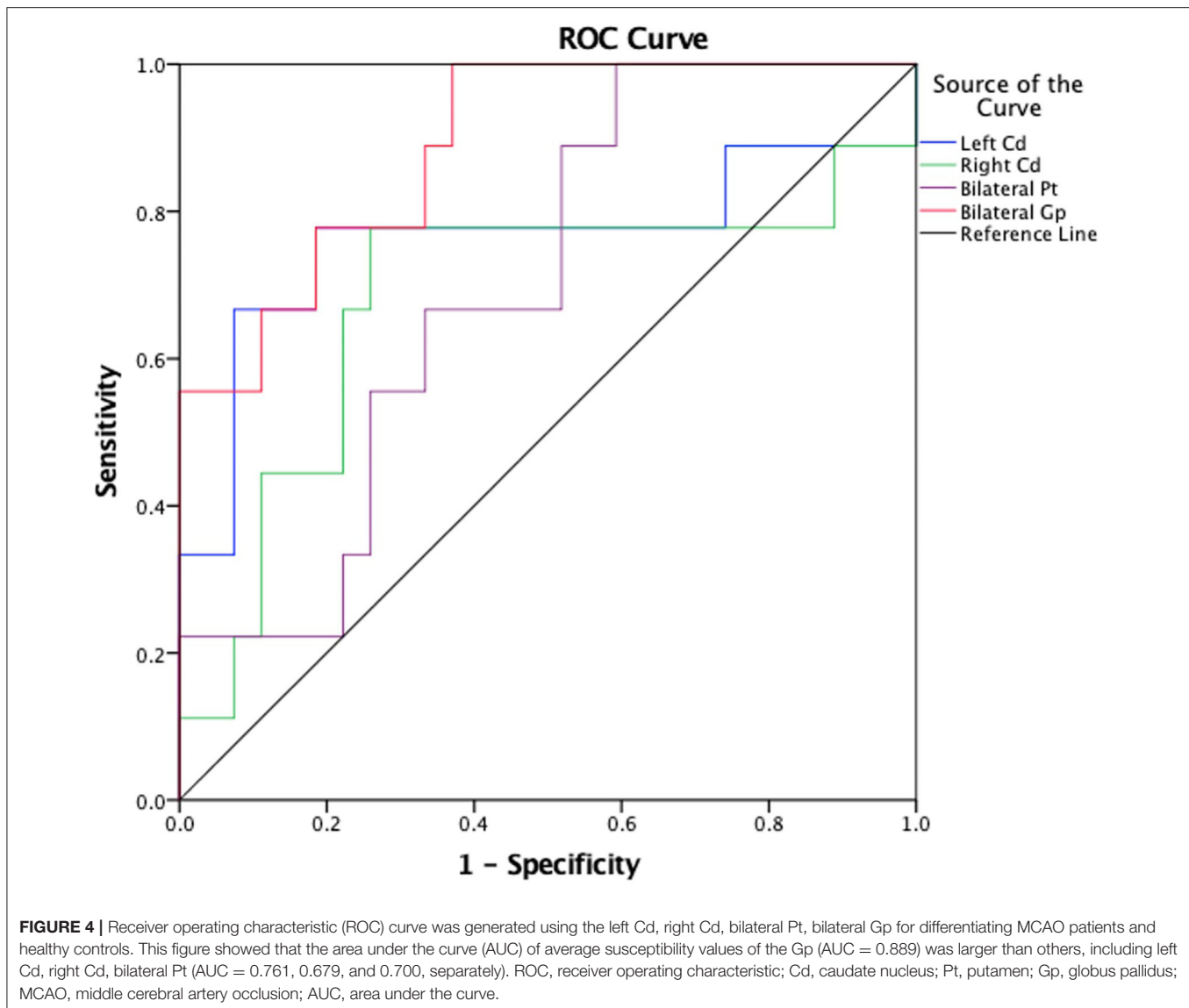
those in healthy controls, and the susceptibility values of the bilateral Gp were significantly lower in patients with MCAO than in the healthy controls. In addition, the results also showed that the susceptibility values of bilateral Cd were asymmetric in healthy controls; however, the asymmetry disappeared in patients with MCAO. There were no significant differences between the affected side and the unaffected side in patients with MCAO.

The human cerebrovascular system has several compensatory neuroprotective approaches in response to ischemic attack, which help to diminish the neuronal damage. During the disease process of middle cerebral artery stenosis or occlusion, the compensatory neuroprotective mechanisms would be automatically activated if ipsilateral cerebral blood flow is insufficient and impacts normal brain function. Principal compensation approaches include the opening of communicating branches of Willis circle, the increase of vascular internal diameter, bloodstream speeding, and so on. The above compensatory reflections may contribute to the abnormal iron metabolism and consequent alterations of iron level in the bilateral basal ganglia region, which was found in the present study. However, further research is necessary to investigate it.

Iron plays a vital role in maintaining numerous fundamental biological functions of the human brain. However, disorders of iron homeostasis or excessive iron accumulation may lead to abnormal generation of toxic free radicals and consequent oxidative damage (Bolt and Marchan, 2010; Kell, 2010), which are molecular and pathological characteristics of some neurodegenerative diseases such as Alzheimer's disease, Parkinson's disease, and Huntington's disease (Ward et al., 2014; Masaldan et al., 2019; Thomas et al., 2020).

In the current study, we found that a significant increase of iron levels in the Pt was presented in patients with MCAO,





indicating that MCAO could result in pathological changes of microscopic and molecular properties in the basal ganglia region. Possible interpretations for this pathological alteration are as follows: Firstly, inadequate blood flow and oxygen supply induced by MCAO can result in the proliferation, activation, and migration of astrocytes and microglia (Hu et al., 2015; Gulke et al., 2018; Zhang et al., 2019). Astrocytes and microglia significantly impact iron transport or storage mechanisms, which were involved in iron-mediated toxicity (Bishop et al., 2011). Secondly, ischemic stroke, including MCAO, can trigger a cascading pathological noninfectious neuroinflammation and the subsequent excessive release of proinflammatory cytokines, including interleukin-1 (IL-1), tumor necrosis factor alpha (TNF- α), and interleukin-6 (IL-6) (Fujioka et al., 2003; Wang et al., 2007; Chamorro et al., 2016). Neuroinflammation might affect the iron homeostasis in the CNS glia. Abnormal TNF- α release

could result in increased uptake and retention of iron both in astrocytes and microglia (Rathore et al., 2012). Thirdly, we speculated that injury of the blood-brain barrier induced by ischemia attack might be another reason leading to iron deposition. It is well-recognized that the blood-brain barrier plays a crucial role in regulating the physiological transportation and metabolism of various endogenous substances and ions, including iron (Khan et al., 2018; Chiou et al., 2019; Jackson et al., 2019; Linville et al., 2019). Ischemia-related damage of endothelial cells of the blood-brain barrier significantly impairs the normal absorption of iron, and excessive amounts of iron consequently cross into the brain tissue and can be absorbed by microglia and astrocytes (McCarthy and Kosman, 2015; Simpson et al., 2015; Bu et al., 2019; Yan and Zhang, 2019), which eventually leads to increased iron level in the Pt.

Accumulating studies indicated that iron overloading and the consequent spontaneous release of neurotoxic free iron in these brain regions could result in neuronal death and memory dysfunction (Rouault, 2001). It had been demonstrated that neuronal death of the Cd and Pt could result in a series of neurocognitive dysfunctions including cognition deficit (Petty et al., 1996; Du et al., 2018). Our findings in this study provided a probable explanation regarding the neurological symptoms manifested in MCAO patients.

Interestingly, the iron level in the bilateral Gp in MCAO patients was significantly decreased when compared with that in healthy controls. Possible explanations are as follows: Firstly, a significant fluctuation of brain iron may occur during the poststroke recovery. Following the ischemic attack, various endogenous brain repair processes would be activated and engaged in functional recovery (Zhang and Chopp, 2015; Zhao and Willing, 2018). Notably, it had been demonstrated that iron metabolism was involved in the spontaneous repair in chronic ischemic brain regions (Shin et al., 2018; Kim et al., 2020). We postulated that the active iron transport and the imbalance of iron metabolism along with the brain repair process may result in a decreased iron level in some brain nucleus. Secondly, the TNF- α and interferon- γ expressed by activated microglia presented an iron-mediated toxic effect on oligodendrocytes (Zhang et al., 2005), which could trigger a subsequent release of intracellular iron (Zhang et al., 2006). The liberated iron could be detoxified and cleared from the brain region, which ultimately decreased the iron level. In addition, the decrease of blood supply and iron-rich erythrocytes after MCAO might be another reason for this phenomenon. Decreased cerebral blood flow implied a significant reduction of iron coming from erythrocytes in affected brain regions, such as the Gp.

The limitations of this study should not be neglected. First, the number of patients with MCAO enrolled in this study was limited, and the conclusions need to be verified by future studies with a larger sample size. Second, the voxel of imaging was large, and a single voxel displayed an average measurement of the neuronal environment. Third, it is hard to completely avoid the slight errors when drawing the ROIs due to the undefined nucleus boundary in current images. Therefore, further study should be conducted to thoroughly explore the potential pathophysiological roles of the basal ganglia region in patients with MCAO and the correlations between the occurrence and progression of ischemia and the alterations of the iron level in the basal ganglia region.

REFERENCES

- Acosta-Cabrero, J., Williams, G. B., Cardenas-Blanco, A., Arnold, R. J., Lupson, V., and Nestor, P. J. (2013). *In vivo* quantitative susceptibility mapping (QSM) in Alzheimer's disease. *PLoS ONE* 8:e81093. doi: 10.1371/journal.pone.0081093
- Bishop, G. M., Dang, T. N., Dringen, R., and Robinson, S. R. (2011). Accumulation of non-transferrin-bound iron by neurons, astrocytes, and microglia. *Neurotox. Res.* 19, 443–451. doi: 10.1007/s12640-010-9195-x

CONCLUSIONS

As measured by QSM, iron levels of the bilateral basal ganglia region were significantly changed in patients with MCAO. Iron dyshomeostasis in the basal ganglia region might be involved in the pathophysiological process of middle cerebral artery stenosis and occlusion. These findings may provide a novel insight to profoundly address the pathophysiological mechanisms of MCAO.

DATA AVAILABILITY STATEMENT

The original contributions presented in the study are included in the article/supplementary materials, further inquiries can be directed to the corresponding author.

ETHICS STATEMENT

The studies involving human participants were reviewed and approved by China-Japan Friendship Hospital. The participants provided their written informed consent to participate in this study. Written informed consent was obtained from the individuals for the publication of any potentially identifiable images or data included in this article.

AUTHOR CONTRIBUTIONS

LD, ZZ, and XL designed this research, analyzed the MRI data, and drafted this manuscript. LD and YC drew the regions of interest. WG, YW, JL, and BL did the MRI scanning. GM revised the whole manuscript. All authors contributed to the article and approved the submitted version.

FUNDING

This study was supported by the National Key Research and Development Program of China (Grant Nos. 2020YFC2003903, 2019YFC0120903, and 2016YFC1307001) and by grants from the National Natural Science Foundation of China (NSFC) (Grant Nos. 81971585, 81571641, and 91959123).

ACKNOWLEDGMENTS

We thank all the patients and healthy controls who participated in our study. The authors thank Dr. Lizhi Xie from GE Healthcare for helping in solving MR technical problems.

- Bolt, H. M., and Marchan, R. (2010). Iron dysregulation: an important aspect in toxicology. *Arch. Toxicol.* 84, 823–824. doi: 10.1007/s00204-010-0610-0
- Bu, X. L., Xiang, Y., and Guo, Y. (2019). The role of iron in amyotrophic lateral sclerosis. *Adv Exp Med Biol.* 1173, 145–152. doi: 10.1007/978-981-13-9589-5_8
- Chamorro, A., Dirnagl, U., Urra, X., and Planas, A. M. (2016). Neuroprotection in acute stroke: targeting excitotoxicity, oxidative and nitrosative stress, and inflammation. *Lancet Neurol.* 15, 869–881. doi: 10.1016/S1474-4422(16)00114-9

- Chiou, B., Neal, E. H., Bowman, A. B., Lippmann, E. S., Simpson, I. A., and Connor, J. R. (2019). Endothelial cells are critical regulators of iron transport in a model of the human blood-brain barrier. *J. Cereb. Blood Flow Metab.* 39, 2117–2131. doi: 10.1177/0271678X18783372
- Connor, J. R., Menzies, S. L., Burdo, J. R., and Boyer, P. J. (2001). Iron and iron management proteins in neurobiology. *Pediatr. Neurol.* 25, 118–129. doi: 10.1016/S0887-8994(01)00303-4
- Deistung, A., Schafer, A., Schweser, F., Biedermann, U., Turner, R., and Reichenbach, J. R. (2013). Toward *in vivo* histology: a comparison of quantitative susceptibility mapping (QSM) with magnitude-, phase-, and R2*-imaging at ultra-high magnetic field strength. *Neuroimage* 65, 299–314. doi: 10.1016/j.neuroimage.2012.09.055
- Du, G., Liu, T., Lewis, M. M., Kong, L., Wang, Y., Connor, J., et al. (2016). Quantitative susceptibility mapping of the midbrain in Parkinson's disease. *Mov. Disord.* 31, 317–324. doi: 10.1002/mds.26417
- Du, L., Zhao, Z., Cui, A., Zhu, Y., Zhang, L., Liu, J., et al. (2018). Increased iron deposition on brain quantitative susceptibility mapping correlates with decreased cognitive function in Alzheimer's disease. *ACS Chem. Neurosci.* 9, 1849–1857. doi: 10.1021/acscchemneuro.8b00194
- El Amki, M., Clavier, T., Perzo, N., Bernard, R., Guichet, P. O., and Castel, H. (2015). Hypothalamic, thalamic and hippocampal lesions in the mouse MCAO model: potential involvement of deep cerebral arteries? *J. Neurosci. Methods* 254, 80–85. doi: 10.1016/j.jneumeth.2015.07.008
- Fujioka, M., Taoka, T., Matsuo, Y., Mishima, K., Ogoshi, K., Kondo, Y., et al. (2003). Magnetic resonance imaging shows delayed ischemic striatal neurodegeneration. *Ann Neurol.* 54, 732–747. doi: 10.1002/ana.10751
- Gulke, E., Gelderblom, M., and Magnus, T. (2018). Danger signals in stroke and their role on microglia activation after ischemia. *Ther. Adv. Neurol. Disord.* 11:1756286418774254. doi: 10.1177/1756286418774254
- Hu, X., Leak, R. K., Shi, Y., Suenaga, J., Gao, Y., Zheng, P., et al. (2015). Microglial and macrophage polarization—new prospects for brain repair. *Nat. Rev. Neurol.* 11, 56–64. doi: 10.1038/nrneurol.2014.207
- Jackson, S., Meeks, C., Vezina, A., Robey, R. W., Tanner, K., and Gottesman, M. M. (2019). Model systems for studying the blood-brain barrier: applications and challenges. *Biomaterials* 214:119217. doi: 10.1016/j.biomaterials.2019.05.028
- Kamel, H., and Iadecola, C. (2012). Brain-immune interactions and ischemic stroke: clinical implications. *Arch. Neurol.* 69, 576–581. doi: 10.1001/archneurol.2011.3590
- Kell, D. B. (2010). Towards a unifying, systems biology understanding of large-scale cellular death and destruction caused by poorly liganded iron: parkinson's, huntington's, alzheimer's, prions, bactericides, chemical toxicology and others as examples. *Arch. Toxicol.* 84, 825–889. doi: 10.1007/s00204-010-0577-x
- Khan, A. I., Liu, J., and Dutta, P. (2018). Iron transport kinetics through blood-brain barrier endothelial cells. *Biochim. Biophys. Acta. Gen. Subj.* 1862, 1168–1179. doi: 10.1016/j.bbagen.2018.02.010
- Kim, H. W., Shin, J. A., Kim, H. J., Ahn, J. H., and Park, E. M. (2020). Enhanced repair processes and iron uptake by ischemic preconditioning in the brain during the recovery phase after ischemic stroke. *Brain Res.* 1750:147172. doi: 10.1016/j.brainres.2020.147172
- Langkammer, C., Schweser, F., Krebs, N., Deistung, A., Goessler, W., Scheurer, E., et al. (2012). Quantitative susceptibility mapping (QSM) as a means to measure brain iron? a post mortem validation study. *Neuroimage* 62, 1593–1599. doi: 10.1016/j.neuroimage.2012.05.049
- Lim, I. A., Faria, A. V., Li, X., Hsu, J. T., Airan, R. D., Mori, S., et al. (2013). Human brain atlas for automated region of interest selection in quantitative susceptibility mapping: application to determine iron content in deep gray matter structures. *Neuroimage* 82, 449–469. doi: 10.1016/j.neuroimage.2013.05.127
- Linville, R. M., DeStefano, J. G., Sklar, M. B., Xu, Z., Farrell, A. M., Bogorad, M. I., et al. (2019). Human iPSC-derived blood-brain barrier microvessels: validation of barrier function and endothelial cell behavior. *Biomaterials* 190–191, 24–37. doi: 10.1016/j.biomaterials.2018.10.023
- Liu, H., Chen, R., Wang, J., Chen, S., Xiong, C., Wang, J., et al. (2014). 1,5-diaminonaphthalene hydrochloride assisted laser desorption/ionization mass spectrometry imaging of small molecules in tissues following focal cerebral ischemia. *Anal. Chem.* 86, 10114–10121. doi: 10.1021/ac5034566
- Masaldan, S., Bush, A. I., Devos, D., Rolland, A. S., and Moreau, C. (2019). Striking while the iron is hot: iron metabolism and ferroptosis in neurodegeneration. *Free Radic. Biol. Med.* 133, 221–233. doi: 10.1016/j.freeradbiomed.2018.09.033
- McCarthy, R. C., and Kosman, D. J. (2015). Iron transport across the blood-brain barrier: development, neurovascular regulation and cerebral amyloid angiopathy. *Cell Mol. Life Sci.* 72, 709–727. doi: 10.1007/s00018-014-1771-4
- Mohan, K. M., Crichton, S. L., Grieve, A. P., Rudd, A. G., Wolfe, C. D., and Heuschmann, P. U. (2009). Frequency and predictors for the risk of stroke recurrence up to 10 years after stroke: the South London stroke register. *J. Neurol. Neurosurg. Psychiatry* 80, 1012–1018. doi: 10.1136/jnnp.2008.170456
- Munoz, P., and Humeres, A. (2012). Iron deficiency on neuronal function. *Biomaterials* 25, 825–835. doi: 10.1007/s10534-012-9550-x
- Murakami, Y., Kakeda, S., Watanabe, K., Ueda, I., Ogasawara, A., Moriya, J., et al. (2015). Usefulness of quantitative susceptibility mapping for the diagnosis of Parkinson disease. *AJNR Am. J. Neuroradiol.* 36, 1102–1108. doi: 10.3174/ajnr.A4260
- Oppo, K., Leen, E., Angerson, W. J., Cooke, T. G., and McArdle, C. S. (1998). Doppler perfusion index: an interobserver and intraobserver reproducibility study. *Radiology* 208, 453–457. doi: 10.1148/radiology.208.2.9680575
- Pang, C., Cao, L., Wu, F., Wang, L., Wang, G., Yu, Y., et al. (2015). The effect of trans-resveratrol on post-stroke depression via regulation of hypothalamus-pituitary-adrenal axis. *Neuropharmacology* 97, 447–456. doi: 10.1016/j.neuropharm.2015.04.017
- Petty, R. G., Bonner, D., Mouratoglou, V., and Silverman, M. (1996). Acute frontal lobe syndrome and dyscontrol associated with bilateral caudate nucleus infarctions. *Br. J. Psychiatry* 168, 237–240. doi: 10.1192/bjp.168.2.237
- Rathore, K. I., Redensek, A., and David, S. (2012). Iron homeostasis in astrocytes and microglia is differentially regulated by TNF-alpha and TGF-beta1. *Glia* 60, 738–750. doi: 10.1002/glia.22303
- Rouault, T. A. (2001). Iron on the brain. *Nat. Genet.* 28, 299–300. doi: 10.1038/91036
- Schafer, A., Wharton, S., Gowland, P., and Bowtell, R. (2009). Using magnetic field simulation to study susceptibility-related phase contrast in gradient echo MRI. *Neuroimage* 48, 126–137. doi: 10.1016/j.neuroimage.2009.05.093
- Shin, J. A., Kim, Y. A., Kim, H. W., Kim, H. S., Lee, K. E., Kang, J. L., et al. (2018). Iron released from reactive microglia by noggin improves myelin repair in the ischemic brain. *Neuropharmacology* 133, 202–215. doi: 10.1016/j.neuropharm.2018.01.038
- Shmueli, K., de Zwart, J. A., van Gelderen, P., Li, T. Q., Dodd, S. J., and Duyn, J. H. (2009). Magnetic susceptibility mapping of brain tissue *in vivo* using MRI phase data. *Magn. Reson. Med.* 62, 1510–1522. doi: 10.1002/mrm.22135
- Siesjo, B. K. (1988). Acidosis and ischemic brain damage. *Neurochem. Pathol.* 9, 31–88.
- Simpson, I. A., Ponnuru, P., Klinger, M. E., Myers, R. L., Devraj, K., Coe, C. L., et al. (2015). A novel model for brain iron uptake: introducing the concept of regulation. *J. Cereb. Blood Flow Metab.* 35, 48–57. doi: 10.1038/jcbfm.2014.168
- Sun, H., Walsh, A. J., Lebel, R. M., Blevins, G., Catz, I., Lu, J. Q., et al. (2015). Validation of quantitative susceptibility mapping with perls' iron staining for subcortical gray matter. *Neuroimage* 105, 486–492. doi: 10.1016/j.neuroimage.2014.11.010
- Thomas, G. E. C., Leyland, L. A., Schrag, A. E., Lees, A. J., Acosta-Cabrero, J., and Weil, R. S. (2020). Brain iron deposition is linked with cognitive severity in Parkinson's disease. *J. Neurol. Neurosurg. Psychiatry* 91, 418–425. doi: 10.1136/jnnp-2019-322042
- Wang, Q., Tang, X. N., and Yenari, M. A. (2007). The inflammatory response in stroke. *J. Neuroimmunol.* 184, 53–68. doi: 10.1016/j.jneuroim.2006.11.014
- Ward, R. J., Zucca, F. A., Duyn, J. H., Crichton, R. R., and Zecca, L. (2014). The role of iron in brain ageing and neurodegenerative disorders. *Lancet Neurol.* 13, 1045–1060. doi: 10.1016/S1474-4422(14)70117-6
- Yan, N., and Zhang, J. J. (2019). The emerging roles of ferroptosis in vascular cognitive impairment. *Front. Neurosci.* 13:811. doi: 10.3389/fnins.2019.00811
- Yushmanov, V. E., Kharlamov, A., Yanovski, B., LaVerde, G., Boada, F. E., and Jones, S. C. (2013). Correlated sodium and potassium imbalances within the ischemic core in experimental stroke: a ²³Na MRI and

- histochemical imaging study. *Brain Res.* 1527, 199–208. doi: 10.1016/j.brainres.2013.06.012
- Zhang, X., Haaf, M., Todorich, B., Grosstephan, E., Schieremberg, H., Surguladze, N., et al. (2005). Cytokine toxicity to oligodendrocyte precursors is mediated by iron. *Glia* 52, 199–208. doi: 10.1002/glia.20235
- Zhang, X., Surguladze, N., Slagle-Webb, B., Cozzi, A., and Connor, J. R. (2006). Cellular iron status influences the functional relationship between microglia and oligodendrocytes. *Glia* 54, 795–804. doi: 10.1002/glia.20416
- Zhang, X., Zhao, H. H., Li, D., and Li, H. P. (2019). Neuroprotective effects of matrix metalloproteinases in cerebral ischemic rats by promoting activation and migration of astrocytes and microglia. *Brain Res. Bull.* 146, 136–142. doi: 10.1016/j.brainresbull.2018.11.003
- Zhang, Z. G., and Chopp, M. (2015). Promoting brain remodeling to aid in stroke recovery. *Trends Mol. Med.* 21, 543–548. doi: 10.1016/j.molmed.2015.07.005
- Zhao, L. R., and Willing, A. (2018). Enhancing endogenous capacity to repair a stroke-damaged brain: An evolving field for stroke research. *Prog. Neurobiol.* 163–164, 5–26. doi: 10.1016/j.pneurobio.2018.01.004

Conflict of Interest: The authors declare that the research was conducted in the absence of any commercial or financial relationships that could be construed as a potential conflict of interest.

Copyright © 2021 Du, Zhao, Liu, Chen, Gao, Wang, Liu, Liu and Ma. This is an open-access article distributed under the terms of the Creative Commons Attribution License (CC BY). The use, distribution or reproduction in other forums is permitted, provided the original author(s) and the copyright owner(s) are credited and that the original publication in this journal is cited, in accordance with accepted academic practice. No use, distribution or reproduction is permitted which does not comply with these terms.



Alterations and Associations Between Magnetic Susceptibility of the Basal Ganglia and Diffusion Properties in Alzheimer's Disease

Xiuxiu Liu^{1†}, Lei Du^{1,2†}, Bing Zhang^{3,6†}, Zifang Zhao⁴, Wenwen Gao¹, Bing Liu^{1,2}, Jian Liu⁵, Yue Chen¹, Yige Wang^{1,2}, Hongwei Yu¹ and Guolin Ma^{1*}

¹ Department of Radiology, China-Japan Friendship Hospital, Beijing, China, ² Graduate School of Peking Union Medical College, Beijing, China, ³ Department of Radiology, The Affiliated Drum Tower Hospital of Nanjing University Medical School, Nanjing, China, ⁴ Department of Anesthesiology, Peking University First Hospital, Beijing, China, ⁵ Department of Ultrasound Diagnosis, China-Japan Friendship Hospital, Beijing, China, ⁶ Institute of Brain Science, Nanjing University, Nanjing, China

OPEN ACCESS

Edited by:

Fuhua Yan,
Shanghai Jiao Tong University, China

Reviewed by:

Rodolfo Gabriel Gatto,
University of Illinois at Chicago,
United States
Maria Eugenia Caligiuri,
University of Magna Graecia, Italy

*Correspondence:

Guolin Ma
maguolin1007@qq.com

[†]These authors share first authorship

Specialty section:

This article was submitted to
Neurodegeneration,
a section of the journal
Frontiers in Neuroscience

Received: 11 October 2020

Accepted: 12 January 2021

Published: 16 February 2021

Citation:

Liu X, Du L, Zhang B, Zhao Z, Gao W, Liu B, Liu J, Chen Y, Wang Y, Yu H and Ma G (2021) Alterations and Associations Between Magnetic Susceptibility of the Basal Ganglia and Diffusion Properties in Alzheimer's Disease. *Front. Neurosci.* 15:616163. doi: 10.3389/fnins.2021.616163

This study adopted diffusion tensor imaging to detect alterations in the diffusion parameters of the white matter fiber in Alzheimer's disease (AD) and used quantitative susceptibility mapping to detect changes in magnetic susceptibility. However, whether the changes of susceptibility values due to excessive iron in the basal ganglia have correlations with the alterations of the diffusion properties of the white matter in patients with AD are still unknown. We aim to investigate the correlations among magnetic susceptibility values of the basal ganglia, diffusion indexes of the white matter, and cognitive function in patients with AD. Thirty patients with AD and nineteen healthy controls (HCs) were recruited. Diffusion indexes of the whole brain were detected using tract-based spatial statistics. The caudate nucleus, putamen, and globus pallidus were selected as regions of interest, and their magnetic susceptibility values were measured. Compared with HCs, patients with AD showed that there were significantly increased axial diffusivity (AxD) in the internal capsule, superior corona radiata (SCR), and right anterior corona radiata (ACR); increased radial diffusivity (RD) in the right anterior limb of the internal capsule, ACR, and genu of the corpus callosum (GCC); and decreased fractional anisotropy (FA) in the right ACR and GCC. The alterations of RD values, FA values, and susceptibility values of the right caudate nucleus in patients with AD were correlated with cognitive scores. Besides, AxD values in the right internal capsule, ACR, and SCR were positively correlated with the magnetic susceptibility values of the right caudate nucleus in patients with AD. Our findings revealed that the magnetic susceptibility of the caudate nucleus may be an MRI-based biomarker of the cognitive dysfunction of AD and abnormal excessive iron distribution in the basal ganglia had adverse effects on the diffusion properties of the white matter.

Keywords: diffusion tensor imaging, quantitative susceptibility mapping, basal ganglia, Alzheimer's disease, magnetic susceptibility, tract-based spatial statistics

INTRODUCTION

Alzheimer's disease (AD) is recognized as a degenerative disease characterized by cognitive dysfunction and memory disorder, and the number of patients with AD is in the first place in senile dementia (Zhong et al., 2004; Arfanakis et al., 2007; Chen et al., 2007). From 2000 to 2017, the number of deaths from AD increased by 45% (Gaugler et al., 2019). Until now, people with AD have suffered because there is no way to stop the progression of AD, so it is critical to find early pathological changes and brain imaging changes for early diagnosis and early treatment. Some studies have shown that amyloid- β (A β) plaque, phosphorylated tau protein, and pathological iron deposition in the brain cause damage to the neurons and axons (Hardy, 2006; Pena et al., 2006; Takahashi et al., 2017).

Diffusion tensor imaging (DTI) has recently emerged as a non-invasive and effective neuroimaging method that provides valuable imaging clues to detect changes in the diffusion function of the fiber fasciculus in terms of neuropsychiatric diseases. Axial diffusivity (AxD), radial diffusivity (RD), mean diffusivity (MD), and fractional anisotropy (FA) are the common and representative DTI metrics (Alexander et al., 2007; Amlen and Fjell, 2014; Alves et al., 2015). AxD indicates the velocity of water diffusion along the longitudinal axis, and FA can measure the degree of directionality of water diffusion. Previous DTI studies have explored that white matter fiber alterations are widespread in AD. Generally, the alterations of the white matter in AD exist in the corpus callosum, cingulum bundle, internal capsule, fornix, as well as prefrontal lobe, posterior parietal, and medial frontal regions of the white matter (Sun et al., 2004; Naggara et al., 2006; Mielke et al., 2009; Teipel et al., 2012; Madhavan et al., 2016; Araque Caballero et al., 2018).

Quantitative susceptibility mapping (QSM) is a non-invasive MRI technology that enables to quantify the magnetic susceptibility properties of the tissues *in vivo* (Schweser et al., 2012), and the susceptibility value can be used to reflect the iron level of the brain tissue. Several studies have shown that excessive iron deposition was found in some degenerative diseases, such as AD and Parkinson's disease (PD) (Mitsumori et al., 2009; Oshiro et al., 2011). Furthermore, studies about AD in *in vivo*, *in vitro*, postmortem, and animal models have found that the magnetic susceptibility values were increased in the basal ganglia, such as the caudate nucleus and the putamen (Acosta-Cabronero et al., 2013; Hwang et al., 2016; Moon et al., 2016).

Although previous studies have explored the brain iron overload and diffusion parameter changes, whether the changes of susceptibility values due to excessive iron in the basal ganglia have correlations with the alterations of the diffusion properties of the white matter of patients with AD are still unknown. This study aimed to detect the diffusion index changes of the white matter fibers using the tract-based spatial statistics (TBSS) and explored the magnetic susceptibility changes of the basal ganglia. We then examined the relationships between iron deposition and the changes of white matter integrity in AD patients.

MATERIALS AND METHODS

Subjects

The ethics committee of China-Japan Friendship Hospital has approved this study, and the study obtained informed consent from all subjects. Thirty patients with AD and twenty healthy controls (HCs) were recruited in this study. AD patients were recruited when they visited the Department of Neurology of China-Japan Friendship Hospital in November 2015 and March 2019. Inclusion criteria of patients with AD were as follows: (a) conforming to the diagnostic criteria of the National Institute of Neurological and Communicative Disorders and Stroke and the Alzheimer's Disease and Related Disorders Association (NINCDS-ADRDA) (Acosta-Cabronero et al., 2013; Du et al., 2018), (b) no abnormal brain changes in conventional MRI examination, (c) right-handed, and (d) the MRI images are complete and have no artifacts. Exclusion criteria of patients with AD were as follows: (a) brain organic lesions; (b) neuropsychiatric diseases; (c) alcohol and drug dependence; (d) severe history of heart, lung, liver, and kidney diseases; (e) metabolic diseases, such as hypothyroidism and vitamin B12 deficiency; and (f) MRI contraindications. HCs were recruited from the local communities. Inclusion conditions of HCs were as follows: (a) no psychoses and neurological diseases, (b) no abnormal brain changes in conventional MRI examination, (c) Mini-Mental State Examination (MMSE) scores were between 26 and 30, (d) right-handed, and (d) the MR images are complete and have no artifacts. One HC was excluded because of incomplete images. The total number of all subjects is 49, which consists of 30 patients with AD and 19 HCs. The MMSE scale and Montreal Cognitive Assessment (MoCA) scale were used to assess the cognitive performance of all patients. All participants received conventional MRI, DTI, and QSM scanning.

MRI Scan Acquisition

MRI examinations consisting of DTI and QSM were executed on a 3.0 T device using eight-channel head coils (Discovery MR750 scanner; GE Medical Systems, United States). Research sequences included a spin-echo echo-planar sequence (EPI) to acquire the DTI images with 64 encoding directions ($b = 1,000 \text{ s/mm}^2$) and eight b_0 reference images ($b = 0 \text{ s/mm}^2$) [repetition time (TR) = 8,028 ms, echo time (TE) = 81.8 ms, flip angle (FA) = 90° , slice thickness = 2 mm, matrix = 120×120 , and field of view (FOV) = $240 \times 240 \text{ mm}^2$] and a 3D gradient echo (GRE) sequence to acquire QSM images (TE = 3.2 ms, TR = 22.9 ms, FA = 12° , slice thickness = 1 mm, bandwidth = 62.5 Hz/pixel, FOV = $256 \times 256 \text{ mm}^2$, matrix size = 256×256).

Image Preprocessing

Briefly, DTI preprocessing included images format conversion using the dcm2nii tool, head motion eddy correction, gradient direction correction using the FMRIB's Diffusion Toolbox (FDT), acquisition of brain mask using the Brain Extraction Tool (BET), and diffusion tensor calculation to output AxD, MD, FA, and RD

(Lin et al., 2020). The above procedures used the FSL software¹ running in Linux.

QSM reconstruction included loading magnitude/phase images, creating brain mask based on the magnitude images, phase unwrapping based on Laplacian algorithm, background phase removing, using the streaking artifact reduction method for QSM (STAR-QSM) to reconstruct QSM images, and region of interest (ROI) drawing were implemented using the STI Suite software² in Matlab 2013b (Li et al., 2011; Schweser et al., 2011; Wei et al., 2015).

TBSS Processing

After diffusion tensor images were preprocessed, voxel-wise analysis was performed using the TBSS toolbox. Individual FA images were mapped onto the FMRIB58 FA template, performed the non-linear registration to transform into Montreal Neurological Institute 152 (MNI152) standard space, and skeletonized using standard parameters (Smith et al., 2006). The mean FA images and the mean FA skeleton maps were generated, taking a threshold of 0.2 for the mean FA skeleton. Furthermore, individual FA images, AxD images, RD images, and MD images were mapped onto the mean FA skeleton, respectively. The code `tbss_fill` was used for results expansion, which can visualize the manifestation of realistic analysis easily. FSLview was adopted to view results. Some auxiliary commands, such as `cluster`, `atlasquery`, and `fslmeans`, were used. The `atlasquery` command was used to output information about the white matter fibers in clusters with significant differences. Anatomical atlas consisting of JHU white-matter tractography atlas and JHU ICBM-DTI-81 white-matter labels could identify various fiber tracts (Wakana et al., 2004; Hua et al., 2008). Afterward, the cluster program was used to acquire the statistically significant clusters information about AxD, RD, and FA (Chen et al., 2018). The `fslmeans` command is used to extract the mean values of the diffusion indexes of the significant difference clusters for other analysis.

Basal Ganglia Segmentation and Measurement

Some raw and unprocessed DICOM images, post-processed magnitude images, and QSM images of the same slices from the same patient's brain can be seen in **Supplementary Figure 1**. After acquiring the final QSM images, we selected the basal ganglia as the ROI, and it was further divided into six ROIs: bilateral caudate nucleus, bilateral putamen, and bilateral globus pallidus as shown in **Figure 1**. The six ROIs are demarcated on the QSM axial images. Each ROI was manually segmented and measured the susceptibility values in three consecutive layers on axial QSM images by two radiologists to improve measurement accuracy and verify measurement consistency. They drew and measured ROIs independently and knew nothing about the subjects. The unit of susceptibility value was the international standard unit—parts per million (ppm).

Statistical Analysis

Statistical analysis was executed using the SPSS software package (IBM SPSS 26.0). The Shapiro–Wilk normality test was used to test data for normality. All variables were normally distributed except the magnetic susceptibility values of the bilateral caudate nucleus and right globus pallidus in the AD group. Two-sample *t*-test or non-parameter testing of two independent samples was used for intergroup comparison. Gender was compared using the chi-square (χ^2) test. The intraclass correlation coefficient (ICC) was calculated to evaluate the concordance between the two radiologists' measurements (Oppo et al., 1998; Du et al., 2018). Group differences in FA, MD, RD, and AxD were analyzed running the FSL randomise program with permutation tests (5,000 permutations) for multiple comparisons adopting the threshold-free cluster enhancement (TFCE) method (Nichols and Holmes, 2002; Winkler et al., 2014; Goodrich-Hunsaker et al., 2018). We chose gender, age, and educational years as covariates in the regression analysis (Sampedro et al., 2020). *P* value less than 0.05 was considered statistically different. Partial correlation analysis controlling age and gender was used for correlation analysis, and false discovery rate (FDR) was used for multiple comparison correction. Combining the FA values with the susceptibility values of the right caudate nucleus, the MMSE scores were used for multiple linear regression analysis to discover which imaging parameters contribute more to cognitive decline.

RESULTS

Subjects' Characteristics

Participants' demographic characteristics and the results of cognitive scales are presented in **Table 1**. MMSE and MoCA scores were used to assess the cognitive function of AD patients. The MMSE test revealed lower scores in AD patients than in HCs ($P < 0.001$). There was no significant difference in gender, age, and educational years between the AD group and the HC group.

Two experienced radiologists drew the ROIs and measured their magnetic susceptibility values on QSM images. ICC was calculated to show consistency between two observers. The susceptibility values measured by two radiologists were consistent, as shown in **Supplementary Table 1**.

Mapping Intergroup Differences of TBSS Analysis

There were statistically significant differences in AxD values between the AD group and the HC group after family wise error (FWE) correction ($P < 0.05$) (**Figure 2**). The corresponding statistically significant clusters were displayed in **Table 2**. The AD group had significantly higher AxD values than the HC group in two clusters including the bilateral superior corona radiata (SCR), bilateral posterior limb of the internal capsule (PLIC), bilateral anterior limb of the internal capsule (ALIC), and right anterior corona radiata (ACR). Higher RD values could be found in the right ACR, right ALIC, and genu of the corpus callosum (GCC) in AD patients. However, there was no significant

¹<https://fsl.fmrib.ox.ac.uk/fsl/fslwiki/FslInstallation>

²<https://people.eecs.berkeley.edu/~chunlei.liu/software.html>

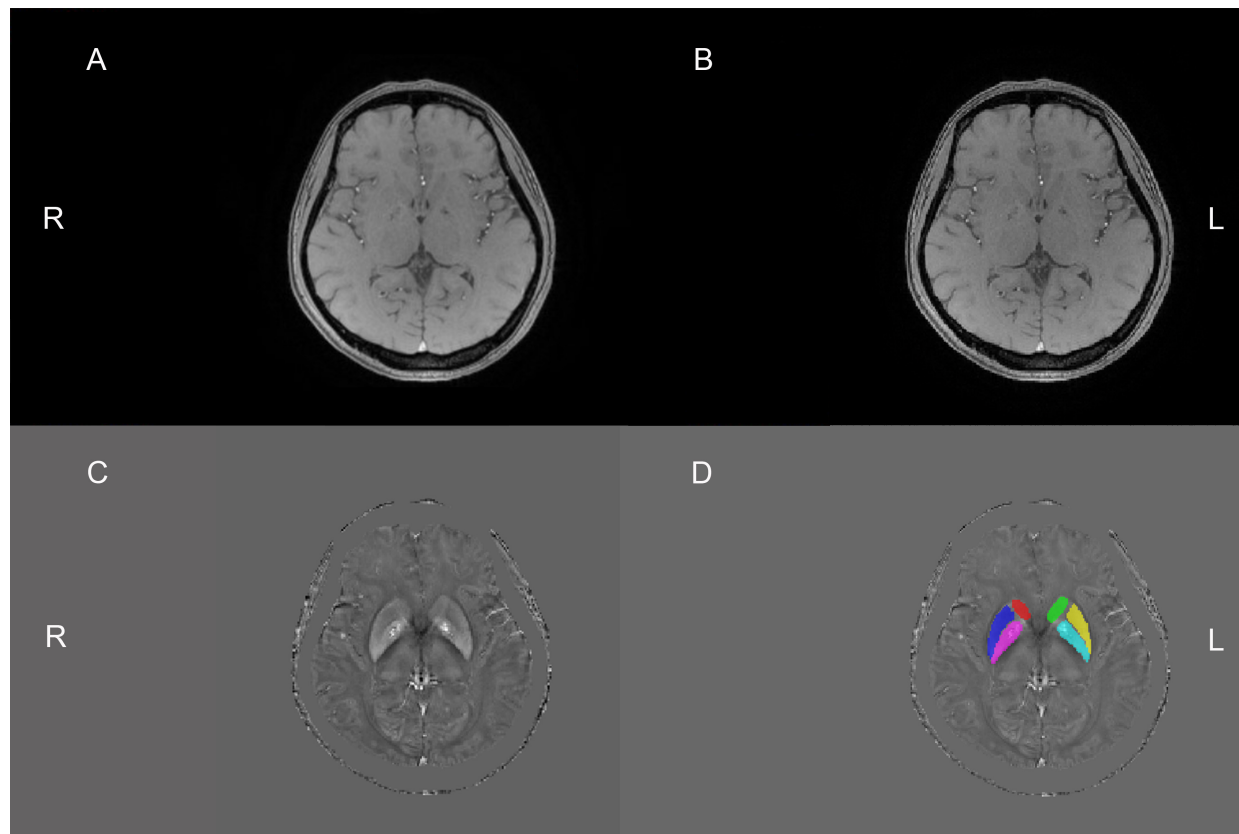


FIGURE 1 | The above four pictures are the same slice of the same patient. The raw and unprocessed DICOM image (A) obtained from the MRI machine. Sensitive information, such as the patient's name, check number, and date of birth, has been covered with black. The magnitude image (B) and QSM image (C) were obtained by the post-processing of the STI Suite software, respectively. This image (D) was obtained after drawing the regions of interest (ROIs) based on the C image. Six ROIs were drawn manually on QSM images. Red, dark blue, purple, green, yellow, and light blue are the right caudate nucleus, right putamen, right globus pallidus, left caudate nucleus, left putamen, and left globus pallidus, respectively. R, right; L, left.

TABLE 1 | Demographic and clinical characteristics.

Group	AD	Healthy controls	P
Number	30	19	–
Male/female	8/22	5/14	0.978
Age (year)	68.37 ± 6.734	66.68 ± 8.564	0.447
Education (year)	11.03 ± 3.917	9.63 ± 3.961	0.230
MMSE	19.80 ± 3.925	28.00 ± 1.856	0.000
MoCA	16.77 ± 3.857	Nm	–

MMSE, Mini-Mental State Examination; MoCA, Montreal Cognitive Assessment; Nm, not measured.

difference between the AD group and the HC group after FWE correction, which was displayed in **Supplementary Figure 2** and **Supplementary Table 2**. Lower FA values were observed in the right ACR and GCC in the AD group than in the HC group, but no significant difference after FWE multiple comparison correction, which was shown in **Supplementary Figure 3** and **Supplementary Table 3**. The regions with statistically different MD values did not exist after FWE multiple comparison correction. The mean AxD, RD, and FA values of every cluster were extracted and compared between the AD group and the HC group, and the corresponding statistically significant results

without FWE multiple comparison correction were shown in **Figure 3**.

Comparisons of Susceptibility Values in the Basal Ganglia Between Groups

Figure 4 showed the results about the comparisons of the susceptibility values in the basal ganglia between the AD group and the HC group. Compared with the HC group, the susceptibility values of the bilateral caudate nucleus were significantly increased in the AD group ($P < 0.001$).

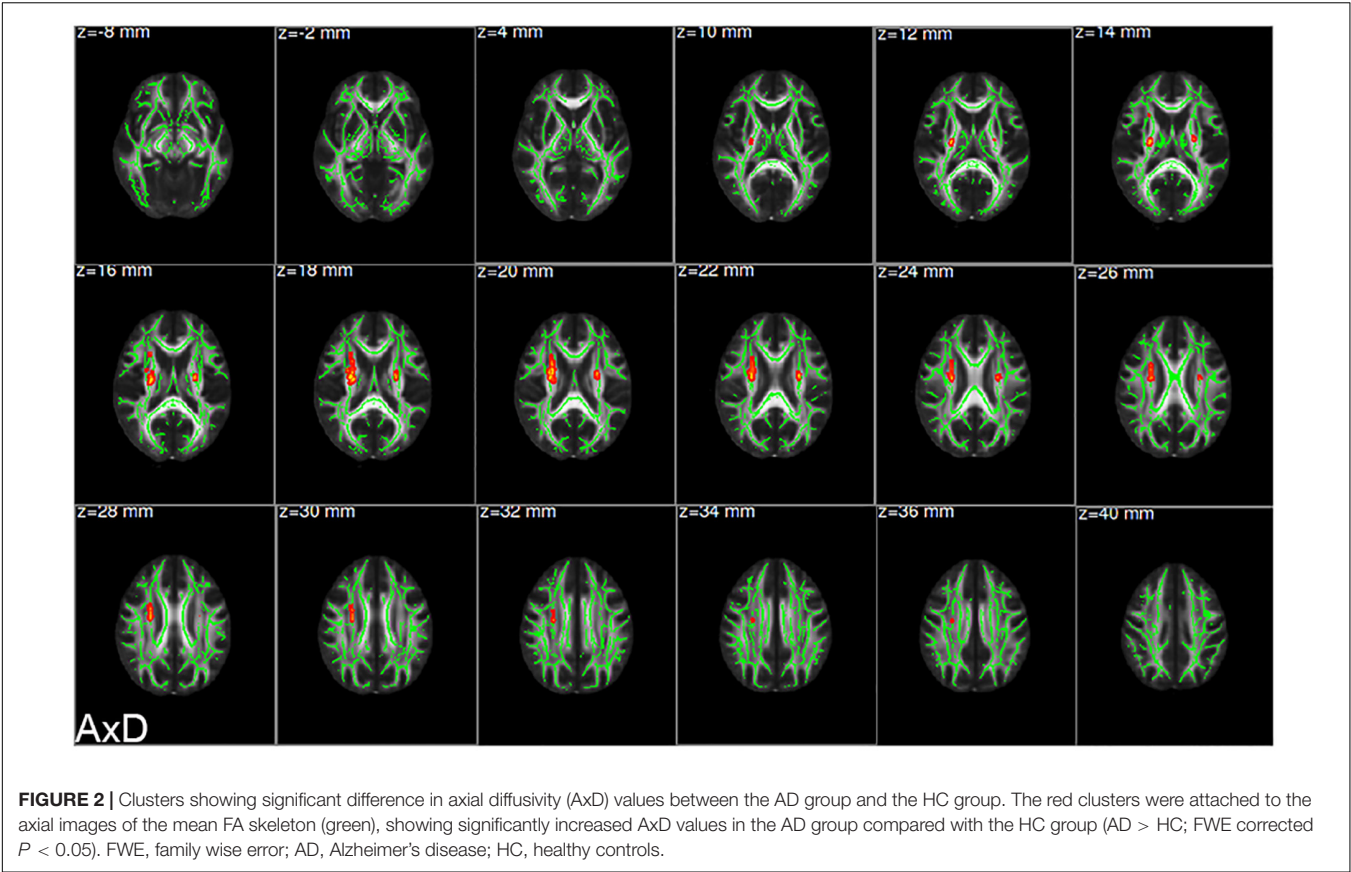


TABLE 2 | Clusters showed significant differences in AxD values.

Cluster ID	Cluster size	P-FWE	MNI coordinates			Tracts in clusters
			X	Y	Z	
AD > HC						
Cluster 1	60	0.048	114	121	91	Superior corona radiata (L) Posterior limb of the internal capsule (L) Anterior limb of the internal capsule (L)
Cluster 2	384	0.034	65	114	86	Superior corona radiata (R) Posterior limb of the internal capsule (R) Anterior corona radiata (R) Anterior limb of the internal capsule (R)

The MNI coordinate refers to the coordinate with the largest 1 - P value. AxD, axial diffusivity; AD, Alzheimer's disease; HC, healthy control; FWE, family wise error; MNI, Montreal Neurological Institute; R, right; L, left.

Correlations Between AxD Values, RD Values, FA Values, and Cognitive Scales

We found that the MMSE and MoCA scores of one patient were extremely low, so we removed the MMSE and MoCA scores of this patient in order to acquire reliable analysis results. The results of partial correlation analysis between the AxD values, RD values, and FA values and the MoCA scores and MMSE scores in patients with AD were shown in **Figure 5**. After FDR correction, the mean RD values of cluster 2 including the right ACR and GCC had significant negative correlations with the MMSE scores and the MoCA scores ($r = -0.491$, $P = 0.007$; $r = -0.532$, $P = 0.003$;

Figures 5A,B). Significant positive correlations between the mean FA values and the MMSE scores or the MoCA scores were observed in **Figures 5C,D** ($r = 0.507$, $P = 0.005$; $r = 0.528$, $P = 0.003$). There were no significant correlations between AxD values and cognitive scores.

Correlations Between Susceptibility Values of ROIs and Cognitive Scales

We found that the susceptibility value of the right caudate nucleus of one patient was extremely high and it belonged to an abnormal outlier, so we removed it in order to acquire reliable

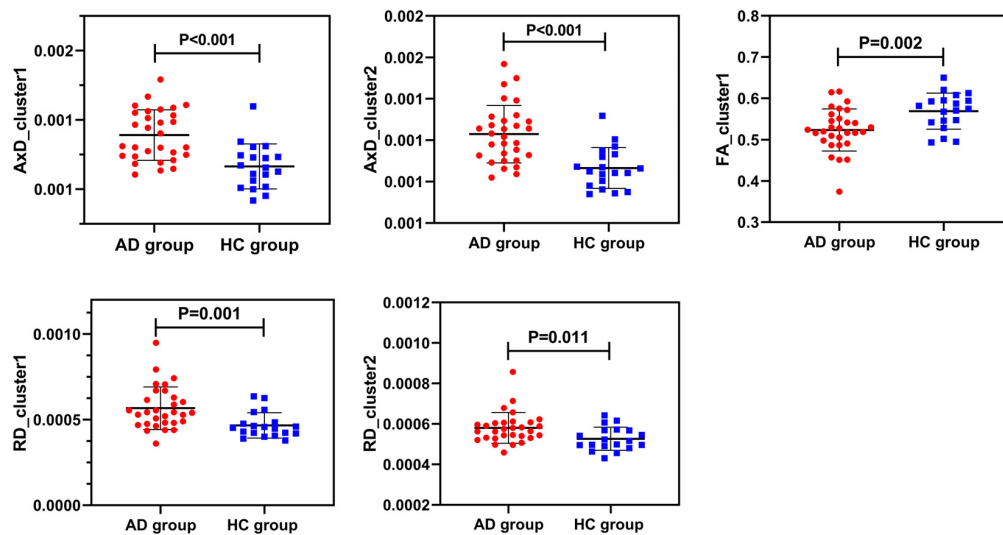


FIGURE 3 | Intergroup comparisons of AxD values, RD values, and FA values between the AD group (red) and the HC group (blue). AxD values, RD values, and FA values of clusters were statistically different between the two groups before FWE correction. AxD, axial diffusivity; RD, radial diffusivity; FA, fractional anisotropy; AD, Alzheimer's disease; HC, healthy controls.

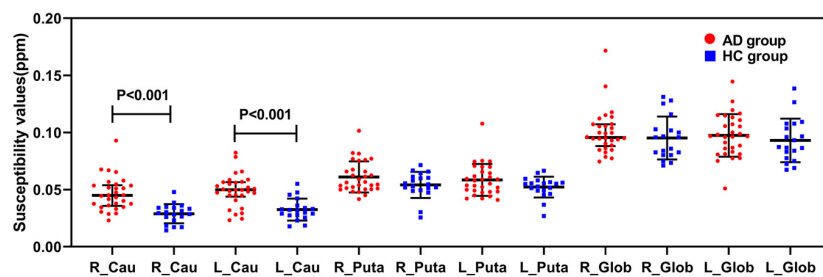


FIGURE 4 | Comparisons of susceptibility values in the basal ganglia between the AD group (red) and the HC group (blue). The susceptibility values of the bilateral caudate nucleus were significantly higher in the AD group than in the HC group ($P < 0.001$). R, right; L, left; Cau, caudate nucleus; Puta, putamen; Glob, globus pallidus.

analysis results. After FDR correction, the susceptibility values of the right caudate nucleus have a significant negative correlation with the MMSE scores in Alzheimer's patients ($r = -0.404$, $P = 0.033$; **Figure 6A**).

Correlations Between Diffusion Parameters and Susceptibility Values of the Right Caudate Nucleus

The mean AxD values of cluster 2 including the right ALIC, right PLIC, right ACR, and right SCR were positively correlated with the susceptibility values of the right caudate in patients with AD after FDR correction ($r = 0.444$, $P = 0.016$; **Figure 6B**).

Multiple Linear Regression Analysis

In multiple linear regression analysis, the FA values and the susceptibility values of the right caudate nucleus were independent predictors, and the MMSE scores were used to assess the cognitive function of patients with AD. We combined the FA values with the susceptibility values of the right caudate nucleus

to find out which contributed more to the cognitive decline in patients with AD. It was shown in **Table 3** that both the FA values and the susceptibility values of the right caudate nucleus contributed to cognition decline, but the latter contributed more.

DISCUSSION

This study mainly found increased AxD values and RD values and decreased FA values of patients with AD compared with HCs. The susceptibility values of the bilateral caudate nucleus were increased in patients with AD. The increased AxD values in patients with AD were discovered in the right ACR, bilateral SCR, PLIC, and ALIC. Higher RD values were discovered in the right ACR, ALIC, and GCC in patients with AD. Similarly, decreased FA values were observed in the right ACR and GCC. In addition, RD values and FA values were significantly correlated with cognitive scores, and the susceptibility values of the right caudate nucleus had a significant negative correlation with MMSE scores.

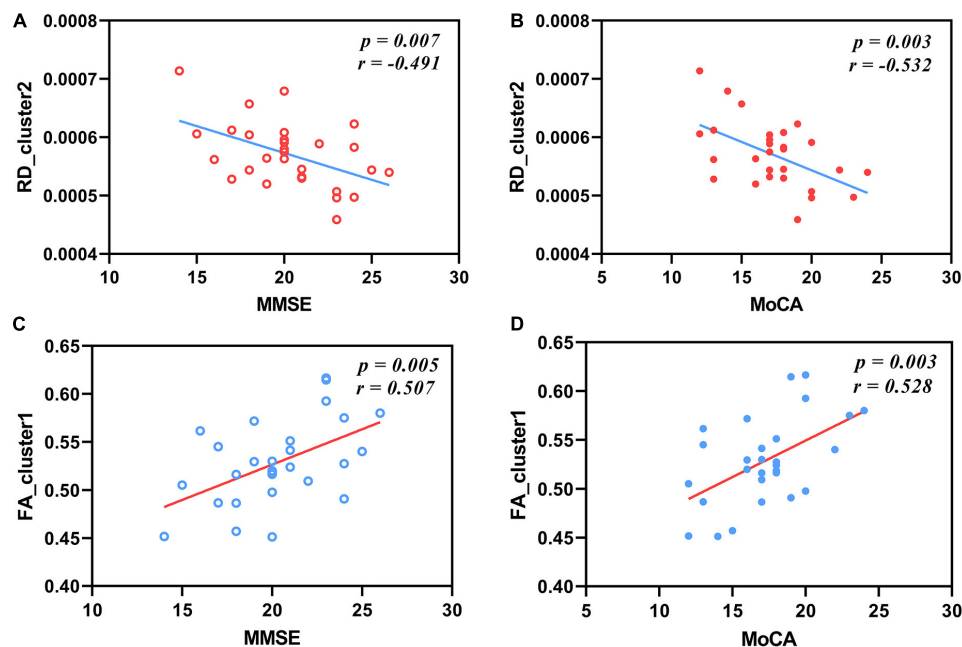


FIGURE 5 | Correlations between RD values, FA values, and cognitive scales in patients with AD. The mean RD values of cluster 2 have negative correlations with MMSE scores (A) and MoCA scores (B) after FDR correction ($r = -0.491$, $P = 0.007$; $r = -0.532$, $P = 0.003$). The mean FA values of cluster 1 have positive correlations with MMSE scores (C) and MoCA scores (D) after FDR correction ($r = 0.507$, $P = 0.005$; $r = 0.528$, $P = 0.003$). RD, radial diffusivity; FA, fractional anisotropy; MMSE, Mini-Mental State Examination; MoCA, Montreal Cognitive Assessment.

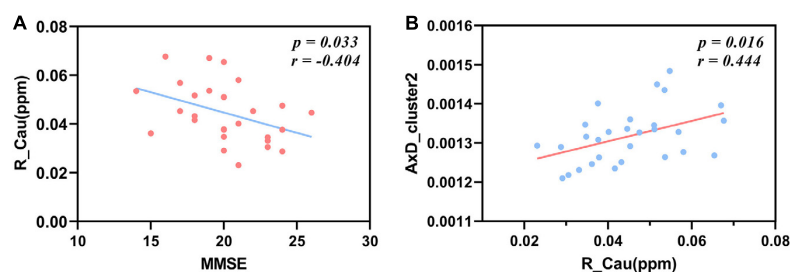


FIGURE 6 | Correlations between the susceptibility values of the right caudate nucleus and MMSE scores, between the susceptibility values of the right caudate nucleus and the AxD values of cluster 2 in patients with AD. The susceptibility values of the right caudate nucleus have a negative correlation with MMSE scores after FDR correction (A) ($r = -0.404$, $P = 0.033$). The mean AxD values of cluster 2 have a positive correlation with the susceptibility values of the right caudate nucleus after FDR correction (B) ($r = 0.444$, $P = 0.016$). MMSE, Mini-Mental State Examination; AxD, axial diffusivity; R_Cau, right caudate nucleus.

TABLE 3 | Multiple linear regression results for different predictors.

Predictors	Coefficients	Standard error	P value	VIF	R ² (%)
Intercept	7.277	5.864	0.002		39
FA_cluster1	31.681	10.269	0.005	1.009	
R_Cau	-87.513	38.070	0.030	1.009	

VIF, variance inflation factor.

It is worth noting that AxD of cluster 2 including the right SCR, ACR, ALIC, and PLIC was positively correlated with the magnetic susceptibility values of the right caudate nucleus.

Our findings found that patients with AD showed higher AxD values in the right ACR, bilateral SCR, ALIC, and PLIC and higher RD values in the right ACR, ALIC, and GCC than HCs.

In addition, RD values had significantly negative correlations with the MMSE scores and the MoCA scores. Several previous articles summarized the white matter fiber bundles related to important physiological function, such as the internal capsule and the corpus callosum (Medina and Gaviria, 2008; Lo Buono et al., 2020). The internal capsule, corpus callosum, and corona radiata

have complex anatomic connectivity that supports cognitive, sensory, and motor systems in the cortex (Gage and Baars, 2018). A good example is the presence of frontal bridge bundles and prethalamic radiation in the ALIC, if the ALIC is damaged, it may cause memory loss, anxiety, inattention, and so on. Our findings were consistent with some previous studies (Pievani et al., 2010; Chitra et al., 2017; Mayo et al., 2017, 2019; Bigham et al., 2020). Increased AxD values are relevant to axonal injury and Wallerian degeneration in patients. Similarly, alterations in AxD may imply axonal damage, and RD is likely to reflect changes in myelination (Alm and Bakker, 2019). Another explanation is that decreased tissue density can increase water diffusivity, but the basic fiber directional structure remains the same in patients with AD (Englund, 1998; Bronge et al., 2002). Besides, AxD is more likely affected by myelination, axonal diameters, and axonal packing (Song et al., 2003).

Similarly, we also observed that decreased FA values existed in the right ACR and GCC of patients with AD. Furthermore, the FA values and the cognitive scores including MMSE and MoCA were positively correlated. Our findings are consistent with the findings of previous studies; both found that the FA values of patients with AD are reduced (Naggara et al., 2006; Ukmar et al., 2008; Liu et al., 2011; Brueggen et al., 2019). Past studies have also shown that cognitive function is associated with diffusion indexes (Vasconcelos et al., 2009; Ling et al., 2011; Mayo et al., 2019), suggesting that white matter damage adversely affects cognitive function. FA reflects the dispersion direction of the white matter, the regular and organized white matter has higher FA values, and if the structure of the white matter becomes disordered, FA values will decrease. Therefore, FA stands for the integrity of the white matter (Stebbins and Murphy, 2009). The decrease of FA in patients with cognitive impairment may be related to the histopathological features (Parente et al., 2008). The water content of the white matter increases with the decrease of the myelin component under various pathological states (Ringman et al., 2007). The pathological basis of AD is β -amyloid deposition and neurofibrillary tangles, which can damage axonal microstructure, myelin integrity, and axonal transport (Englund, 1998; Ukmar et al., 2008). Changes in the microstructure of the white matter can affect the diffusion motion of water molecules in the brain tissues, which can be reflected and measured by using the diffusion parameters of DTI (Hanyu et al., 1997; Horsfield and Jones, 2002).

As a diffusion imaging technique, DTI is highly sensitive to changes in the white matter fiber tracts and is a valuable method for studying neurodegenerative diseases. Unlike AD, PD is a chronic progressive neurodegenerative disease. The main lesions are in the substantia nigra and striatum pathways. Bradykinesia, resting tremor, myotonia, and postural instability are the four basic manifestations of the disease. Meta-analysis studies of DTI showed decreased FA and/or increased MD in the substantia nigra, corpus callosum, frontal lobe, cingulate, and temporal lobe of patients with PD (Cochrane and Ebmeier, 2013; Deng et al., 2018). Amyotrophic lateral sclerosis (ALS) is a progressive neurodegenerative disease involving the upper and lower motor neurons, characterized by progressive weakness of the limbs, respiratory muscles, and medulla. Reviews of DTI indicated decreased FA and/or increased RD, MD, and AxD

in the corticospinal tract, PLIC, corpus callosum, and frontal white matter in patients with ALS (Filippini et al., 2010; Li et al., 2012). Huntington's disease is an autosomal dominant neurodegenerative disease. Huntington protein accumulates in the brain and affects brain structure and function. Dyskinesia, mental disorder, and dementia are the three main characteristics of the disease. Meta-analysis study of DTI showed increased FA in the caudate, putamen, and globus pallidus, increased MD in the putamen and thalamus, decreased FA in the corpus callosum, increased RD and AD in the corpus callosum of patients with Huntington's disease (Liu et al., 2016). There are some overlapping results in DTI studies of different neurodegenerative diseases, which may be related to the similar symptoms of these diseases, and the differences in DTI results may be related to specific structural abnormalities in specific degenerative diseases.

It is known that the susceptibility value can be used to reflect the iron level of the brain tissue. Our findings showed that the susceptibility values of the bilateral caudate nucleus increased in patients with AD and the magnetic susceptibility of the right caudate nucleus was negatively correlated with MMSE scores. The association can be supported by another study that ferritin levels of the cerebrospinal fluid have positive connection with cognitive performance (Ayton et al., 2015). Our previous work has found that the increased susceptibility values of the left caudate have decreased cognitive scores, once again proving that higher susceptibility values in the caudate nucleus, a proxy for tissue iron, can predict the cognitive decline. In multiple linear regression analysis, we discovered that both the FA values and the susceptibility values of the right caudate nucleus contributed to cognition decline, but the latter contributed more, which illustrates that the susceptibility values of the caudate nucleus influence cognitive function to a greater extent than FA values. We speculate that the magnetic susceptibility of the caudate nucleus may be a better MRI-based biomarker reflecting cognitive impairment of patients with AD. Biochemical studies of postmortem brain tissue have proven that the globus pallidus, putamen, red nucleus, and substantia nigra have the highest iron content (Griffiths and Crossman, 1993; Cornett et al., 1998; Hebbrecht et al., 1999). The basal ganglia is a major iron-accumulating brain area, especially with pathological degenerative changes, and iron accumulation in the brain of patients with AD is relevant to senile plaques and neurofibrillary tangles (Lovell et al., 1998; Masaldan et al., 2019). Iron-mediated events, such as iron leading to hyperphosphorylation and accumulation of tau (Chan and Shea, 2006), may aggravate neurodegeneration and functional impairment, which are more complicated than iron-related oxidative injury (Masaldan et al., 2019).

Another major discovery was that the AxD values of the right SCR, right ACR, right ALIC, and right PLIC were positively correlated with the susceptibility values of the right caudate nucleus. The study has shown that disease-associated demyelination can reduce FA but does not affect AxD (Rovaris et al., 2005), indirectly providing the possibility that iron may affect AxD. In addition, some scholars have found that increased magnetic susceptibility value is associated with white matter damage (Morey et al., 2015). The myelin's compact layers of the lamellae are held together with proteins, but they are

vulnerable to destruction from reactive oxidative substances, such as iron-associated oxide and lipid peroxidation due to secondary degeneration (Baumann and Pham-Dinh, 2001), reflecting that iron does affect white matter function to a certain extent. The increased iron content and iron oxide in the caudate nucleus may cause damage to the axons and myelin, which may lead to the diffusion dysfunction of water molecules. Increased susceptibility values in specific brain regions due to excessive iron and demyelination of the white matter may indicate impaired cognitive function (Haacke et al., 2005; Carmeli et al., 2014). The explanation for asymmetry is that the right hemisphere is the important functional hemisphere and the structural and functional abnormalities in the right hemisphere may lead to earlier clinical manifestations. Therefore, at the mild stage, it may be easy to detect patients with AD who have brain structural changes and functional impairment (Ding et al., 2008).

This study found that the susceptibility values of the caudate nucleus contribute more to cognitive decline than the FA values in patients with AD and explored the relationship between diffusion function of the white matter and magnetic susceptibility of the basal ganglia. The findings provide new notions that the changes of susceptibility values due to excessive iron in the basal ganglia have correlations with the alterations of diffusion properties of the white matter in patients with AD. Our results found that the changes of susceptibility values in the right caudate nucleus were correlated with the alterations of Ax/D of the white matter in patients with AD, suggesting that excessive iron accumulation may affect the diffusion function of the white matter.

LIMITATIONS

This study has some limitations. Firstly, we made TBSS analysis based on whole brain instead of the ROI-based approach, which resulted in existing multiple fiber bundles in a cluster, so the latter can better explore and distinguish the specific white matter fiber associated with cognitive function. We employed two widely recognized brain atlases and had access to relevant documents to improve the accuracy of identifying fiber bundles. Secondly, the number of subjects is not enough, which may reduce the statistical effect of group analysis. In the future, our research will enlarge the number of participants to reveal the relationships between diffusion properties, magnetic susceptibility values, and cognitive function. Thirdly, we targeted only iron-rich basal ganglia and adopted simple but inaccurate manual segmentation method. Two observers separately drew ROIs and obtain the mean values to minimize inaccuracy. Other regions, such as red nucleus, substantia nigra, and hippocampus, are not in the scope of this study. They may be worthy of our follow-up research. Finally, we use the most common iron deposition as the main reason to illustrate the increased susceptibility values without considering other factors. In view of the anatomical complexity of the white matter fibers and the complexity of the biochemical and pathophysiological mechanisms in AD, further research is needed in the future.

CONCLUSION

In conclusion, our research found changes in diffusion properties and magnetic susceptibility related to AD. Diffusion properties of the white matter and magnetic susceptibility of the caudate nucleus were correlated with cognitive function, and the latter has a greater impact on cognitive decline. The susceptibility values of the caudate nucleus may be a better MRI-based biomarker of the cognitive impairment of AD. We also concluded that excessive iron accumulation may affect the diffusion function of the white matter.

DATA AVAILABILITY STATEMENT

The original contributions presented in the study are included in the article/**Supplementary Material**, further inquiries can be directed to the corresponding author/s.

ETHICS STATEMENT

The studies involving human participants were reviewed and approved by the ethics committee of China-Japan Friendship Hospital. The patients/participants provided their written informed consent to participate in this study. Written informed consent was obtained from the individual(s) for the publication of any potentially identifiable images or data included in this article.

AUTHOR CONTRIBUTIONS

XL, LD, BZ, and ZZ analyzed and explained the data and drafted and revised the manuscript. LD and GM designed the study. WG, BL, and JL searched and managed the literature. YC, YW, and HY collected data. All authors approved the final manuscript.

FUNDING

This study was supported and funded by the National Key Research and Development Program of China (Nos. 2020YFC2003903, 2019YFC0120903, and 2016YFC1307001) and the National Natural Science Foundation of China (NSFC) (Nos. 81971585, 81571641, 91959123, and 81720108022).

ACKNOWLEDGMENTS

The authors thank all the participants who were involved in the study as well as everyone who offered help. Besides, the authors thank Dr. Lizhi Xie from GE Healthcare for help in solving MR technical problems.

SUPPLEMENTARY MATERIAL

The Supplementary Material for this article can be found online at: <https://www.frontiersin.org/articles/10.3389/fnins.2021.616163/full#supplementary-material>

REFERENCES

- Acosta-Cabrero, J., Williams, G. B., Cardenas-Blanco, A., Arnold, R. J., Lupson, V., and Nestor, P. J. (2013). In vivo quantitative susceptibility mapping (QSM) in Alzheimer's disease. *PLoS One* 8:e81093. doi: 10.1371/journal.pone.0081093
- Alexander, A. L., Lee, J. E., Lazar, M., and Field, A. S. (2007). Diffusion tensor imaging of the brain. *Neurotherapeutics* 4, 316–329. doi: 10.1016/j.nurt.2007.05.011
- Alm, K. H., and Bakker, A. (2019). Relationships between diffusion tensor imaging and cerebrospinal fluid metrics in early stages of the Alzheimer's disease continuum. *J. Alzheimers Dis.* 70, 965–981. doi: 10.3233/Jad-181210
- Alves, G. S., Knochel, V. O., Knochel, C., Carvalho, A. F., Pantel, J., Engelhardt, E., et al. (2015). Integrating retrogenesis theory to Alzheimer's disease pathology: insight from DTI-TBSS investigation of the white matter microstructural integrity. *Biomed. Res. Int.* 2015:291658. doi: 10.1155/2015/291658
- Amlien, I. K., and Fjell, A. M. (2014). Diffusion tensor imaging of white matter degeneration in Alzheimer's Disease and mild cognitive impairment. *Neuroscience* 276, 206–215. doi: 10.1016/j.neuroscience.2014.02.017
- Araque Caballero, M., Suárez-Calvet, M., Duering, M., Franzmeier, N., Benzinger, T., Fagan, A. M., et al. (2018). White matter diffusion alterations precede symptom onset in autosomal dominant Alzheimer's disease. *Brian* 141, 3065–3080. doi: 10.1093/brian/awy229
- Arfanakis, K., Gui, M. Z., Tamhane, A. A., and Carew, J. D. (2007). Investigating the medial temporal lobe in Alzheimer's disease and mild cognitive impairment, with turboprop diffusion tensor imaging, MRI-volumetry, and T-2-relaxometry. *Brain Imaging Behav.* 1, 11–21. doi: 10.1007/s11682-007-9001-4
- Ayton, S., Faux, N. G., Bush, A. I., and Initia, A. D. N. (2015). Ferritin levels in the cerebrospinal fluid predict Alzheimer's disease outcomes and are regulated by APOE. *Nat. Commun.* 6:6760. doi: 10.1038/ncomms7760
- Baumann, N., and Pham-Dinh, D. (2001). Biology of oligodendrocyte and myelin in the mammalian central nervous system. *Physiol. Rev.* 81, 871–927. doi: 10.1152/physrev.2001.81.2.871
- Bigham, B., Zamanpour, S. A., Zemorshidi, F., Boroumand, F., Zare, H., and Alzheimer's Disease Neuroimaging, I. (2020). Identification of superficial white matter abnormalities in Alzheimer's disease and mild cognitive impairment using diffusion tensor imaging. *J. Alzheimers Dis. Rep.* 4, 49–59. doi: 10.3233/JAD-190149
- Bronge, L., Bogdanovic, N., and Wahlund, L. O. (2002). Postmortem MRI and histopathology of white matter changes in Alzheimer brains – a quantitative, comparative study. *Dement. Geriatr. Cogn.* 13, 205–212. doi: 10.1159/000057698
- Bruegger, K., Dyrba, M., Cardenas-Blanco, A., Schneider, A., Fliessbach, K., Buerger, K., et al. (2019). Structural integrity in subjective cognitive decline, mild cognitive impairment and Alzheimer's disease based on multicenter diffusion tensor imaging. *J. Neurol.* 266, 2465–2474. doi: 10.1007/s00415-019-09429-3
- Carmeli, C., Fornari, E., Jalili, M., Meuli, R., and Knyazeva, M. G. (2014). Structural covariance of superficial white matter in mild Alzheimer's disease compared to normal aging. *Brain Behav.* 4, 721–737. doi: 10.1002/brb3.252
- Chan, A., and Shea, T. B. (2006). Dietary and genetically-induced oxidative stress alter tau phosphorylation: Influence of folate and apolipoprotein E deficiency. *J. Alzheimers Dis.* 9, 399–405. doi: 10.3233/jad-2006-9405
- Chen, H. J., Gao, Y. Q., Che, C. H., Lin, H. L., and Ruan, X. L. (2018). Diffusion tensor imaging with tract-based spatial statistics reveals white matter abnormalities in patients with vascular cognitive impairment. *Front. Neuroanat.* 12:53. doi: 10.3389/fnana.2018.00053
- Chen, S. Q., Kang, Z., Hu, X. Q., Hu, B., and Zou, Y. (2007). Diffusion tensor imaging of the brain in patients with Alzheimer's disease and cerebrovascular lesions. *J. Zhejiang Univ. Sci. B* 8, 242–247. doi: 10.1631/jzus.2007.B0242
- Chitra, R., Bairavi, K., Vinisha, V., and Kavitha, A. (2017). “Analysis of Structural connectivity on progression of Alzheimer's disease using diffusion tensor imaging,” in *Proceedings of the 2017 Fourth International Conference on Signal Processing, Communication and Networking (ICSCN)*, New York, NY.
- Cochrane, C. J., and Ebmeier, K. P. (2013). Diffusion tensor imaging in parkinsonian syndromes a systematic review and meta-analysis. *Neurology* 80, 857–864. doi: 10.1212/WNL.0b013e318284070c
- Cornett, C. R., Markesbery, W. R., and Ehmann, W. D. (1998). Imbalances of trace elements related to oxidative damage in Alzheimer's disease brain. *Neurotoxicology* 19, 339–345.
- Deng, X. Y., Wang, L., Yang, T. T., Li, R., and Yu, G. (2018). A meta-analysis of diffusion tensor imaging of substantia nigra in patients with Parkinson's disease. *Sci. Rep.* 8:2914. doi: 10.1038/s41598-018-20076-y
- Ding, B., Chen, K. M., Ling, H. W., Zhang, H., Chai, W. M., Li, X., et al. (2008). Diffusion tensor imaging correlates with proton magnetic resonance spectroscopy in posterior cingulate region of patients with Alzheimer's disease. *Dement. Geriatr. Cogn.* 25, 218–225. doi: 10.1159/000113948
- Du, L., Zhao, Z. F., Cui, A. L., Zhu, Y. J., Zhang, L., Liu, J., et al. (2018). Increased iron deposition on brain quantitative susceptibility mapping correlates with decreased cognitive function in Alzheimer's disease. *Acs Chem. Neurosci.* 9, 1849–1857. doi: 10.1021/acschemneuro.8b00194
- Englund, E. (1998). Neuropathology of white matter changes in Alzheimer's disease and vascular dementia. *Dement. Geriatr. Cogn.* 9, 6–12. doi: 10.1159/000051183
- Filippini, N., Douaud, G., Mackay, C. E., Knight, S., Talbot, K., and Turner, M. R. (2010). Corpus callosum involvement is a consistent feature of amyotrophic lateral sclerosis. *Neurology* 75, 1645–1652. doi: 10.1212/WNL.0b013e3181fb84d1
- Gage, N. M., and Baars, B. J. (2018). “Chapter 2 – the brain,” in *Fundamentals of Cognitive Neuroscience*, 2nd Edn, eds N. M. Gage and B. J. Baars (San Diego, CA: Academic Press), 17–52.
- Gaugler, J., James, B., Johnson, T., Marin, A., Weuve, J., and Assoc, A. S. (2019). 2019 Alzheimer's disease facts and figures. *Alzheimers Dement.* 15, 321–387. doi: 10.1016/j.jalz.2019.01.010
- Goodrich-Hunsaker, N. J., Abildskov, T. J., Black, G., Bigler, E. D., Cohen, D. M., Mihalov, L. K., et al. (2018). Age- and sex-related effects in children with mild traumatic brain injury on diffusion magnetic resonance imaging properties: a comparison of voxelwise and tractography methods. *J. Neurosci. Res.* 96, 626–641. doi: 10.1002/jnr.24142
- Griffiths, P. D., and Crossman, A. R. (1993). Distribution of iron in the basal ganglia and neocortex in postmortem tissue in Parkinson's disease and Alzheimer's disease. *Dementia* 4, 61–65. doi: 10.1159/000107298
- Haacke, E. M., Chengb, N. Y. C., House, M. J., Liu, Q., Neelavalli, J., Ogg, R. J., et al. (2005). Imaging iron stores in the brain using magnetic resonance imaging. *Magn. Reson. Imaging* 23, 1–25. doi: 10.1016/j.mri.2004.10.001
- Hanyu, H., Shindo, H., Kakizaki, D., Abe, K., Iwamoto, T., and Takasaki, M. (1997). Increased water diffusion in cerebral white matter in Alzheimer's disease. *Gerontology* 43, 343–351. doi: 10.1159/000213874
- Hardy, J. (2006). Alzheimer's disease: the amyloid cascade hypothesis: an update and reappraisal. *J. Alzheimers Dis.* 9, 151–153. doi: 10.3233/jad-2006-9s317
- Hebbrecht, G., Maenhaut, W., and De Reuck, J. (1999). Brain trace elements and aging. *Nucl. Instrum. Meth. B* 150, 208–213. doi: 10.1016/S0168-583x(98)00938-0
- Horsfield, M. A., and Jones, D. K. (2002). Applications of diffusion-weighted and diffusion tensor MRI to white matter diseases – a review. *NMR Biomed.* 15, 570–577. doi: 10.1002/nbm.787
- Hua, K., Zhang, J. Y., Wakana, S., Jiang, H. Y., Li, X., Reich, D. S., et al. (2008). Tract probability maps in stereotaxic spaces: analyses of white matter anatomy and tract-specific quantification. *Neuroimage* 39, 336–347. doi: 10.1016/j.neuroimage.2007.07.053
- Hwang, E. J., Kim, H. G., Kim, D., Rhee, H. Y., Ryu, C. W., Liu, T., et al. (2016). Texture analyses of quantitative susceptibility maps to differentiate Alzheimer's disease from cognitive normal and mild cognitive impairment. *Med. Phys.* 43, 4718–4728. doi: 10.1118/1.4958959
- Li, J. P., Pan, P. L., Song, W., Huang, R., Chen, K., and Shang, H. F. (2012). A meta-analysis of diffusion tensor imaging studies in amyotrophic lateral sclerosis. *Neurobiol. Aging* 33, 1833–1838. doi: 10.1016/j.neurobiolaging.2011.04.007
- Li, W., Wu, B., and Liu, C. L. (2011). Quantitative susceptibility mapping of human brain reflects spatial variation in tissue composition. *Neuroimage* 55, 1645–1656. doi: 10.1016/j.neuroimage.2010.11.088

- Lin, Q. X., Bu, X., Wang, M. H., Liang, Y., Chen, H., Wang, W. Q., et al. (2020). Aberrant white matter properties of the callosal tracts implicated in girls with attention-deficit/hyperactivity disorder. *Brain Imaging Behav.* 14, 728–735. doi: 10.1007/s11682-018-0010-2
- Ling, H. W., Ding, B., Wang, T., Zhang, H., and Chen, K. M. (2011). Could iron accumulation be an etiology of the white matter change in Alzheimer's disease: using phase imaging to detect white matter iron deposition based on diffusion tensor imaging. *Dement. Geriatr. Cogn.* 31, 300–308. doi: 10.1159/000327167
- Liu, W. L., Yang, J., Burgunder, J., Cheng, B. C., and Shang, H. F. (2016). Diffusion imaging studies of Huntington's disease: a meta-analysis. *Parkinsonism Relat. Disord.* 32, 94–101. doi: 10.1016/j.parkreldis.2016.09.005
- Liu, Y. W., Spulber, G., Lehtimäki, K. K., Kononen, M., Hallikainen, I., Grohn, H., et al. (2011). Diffusion tensor imaging and tract-based spatial statistics in Alzheimer's disease and mild cognitive impairment. *Neurobiol. Aging* 32, 1558–1571. doi: 10.1016/j.neurobiolaging.2009.10.006
- Lo Buono, V., Palmeri, R., Corallo, F., Allone, C., Pria, D., Bramanti, P., et al. (2020). Diffusion tensor imaging of white matter degeneration in early stage of Alzheimer's disease: a review. *Int. J. Neurosci.* 130, 243–250. doi: 10.1080/00207454.2019.1667798
- Lovell, M. A., Robertson, J. D., Teesdale, W. J., Campbell, J. L., and Markesbery, W. R. (1998). Copper, iron and zinc in Alzheimer's disease senile plaques. *J. Neurol. Sci.* 158, 47–52. doi: 10.1016/S0022-510X(98)00092-6
- Madhavan, A., Schwarz, C. G., Duffy, J. R., Strand, E. A., Machulda, M. M., Drubach, D. A., et al. (2016). Characterizing white matter tract degeneration in syndromic variants of Alzheimer's disease: a diffusion tensor imaging study. *J. Alzheimers Dis.* 49, 633–643. doi: 10.3233/Jad-150502
- Masaldan, S., Bush, A. I., Devos, D., Rolland, A. S., and Moreau, C. (2019). Striking while the iron is hot: iron metabolism and ferroptosis in neurodegeneration. *Free Radic. Biol. Med.* 133, 221–233. doi: 10.1016/j.freeradbiomed.2018.09.033
- Mayo, C. D., Garcia-Barrera, M. A., Mazerolle, E. L., Ritchie, L. J., Fisk, J. D., Gawryluk, J. R., et al. (2019). Relationship between DTI metrics and cognitive function in Alzheimer's disease. *Front. Aging Neurosci.* 10:436. doi: 10.3389/fnagi.2018.00436
- Mayo, C. D., Mazerolle, E. L., Ritchie, L., Fisk, J. D., Gawryluk, J. R., and Initia, A. D. N. (2017). Longitudinal changes in microstructural white matter metrics in Alzheimer's disease. *Neuroimage Clin.* 13, 330–338. doi: 10.1016/j.nicl.2016.12.012
- Medina, D. A., and Gaviria, M. (2008). Diffusion tensor imaging investigations in Alzheimer's disease: the resurgence of white matter compromise in the cortical dysfunction of the aging brain. *Neuropsychiatr. Dis. Treat.* 4, 737–742. doi: 10.2147/ndt.s3381
- Mielke, M. M., Kozauer, N. A., Chan, K. C. G., George, M., Toroney, J., Zerrate, M., et al. (2009). Regionally-specific diffusion tensor imaging in mild cognitive impairment and Alzheimer's disease. *Neuroimage* 46, 47–55. doi: 10.1016/j.neuroimage.2009.01.054
- Mitsumori, F., Watanabe, H., and Takaya, N. (2009). Estimation of brain iron concentration in Vivo using a linear relationship between regional iron and apparent transverse relaxation rate of the tissue water at 4.7T. *Magn. Reson. Med.* 62, 1326–1330. doi: 10.1002/mrm.22097
- Moon, Y., Han, S. H., and Moon, W. J. (2016). Patterns of brain iron accumulation in vascular dementia and Alzheimer's dementia using quantitative susceptibility mapping imaging. *J. Alzheimers Dis.* 51, 737–745. doi: 10.3233/jad-151037
- Morey, R. A., Haswell, C. C., Li, W., Beall, S. K., Fox, C. R., Marx, C. E., et al. (2015). Assessment of myelin compromise in mild traumatic brain injury with quantitative susceptibility mapping. *Biol. Psychiat.* 77, 40S–40S.
- Naggara, O., Oppenheim, C., Rieu, D., Raoux, N., Rodrigo, S., Dalla Barba, G., et al. (2006). Diffusion tensor imaging in early Alzheimer's disease. *Psychiat. Res. Neuroim.* 146, 243–249. doi: 10.1016/j.pscychres.2006.01.005
- Nichols, T. E., and Holmes, A. P. (2002). Nonparametric permutation tests for functional neuroimaging: a primer with examples. *Hum. Brain Mapp.* 15, 1–25. doi: 10.1002/hbm.1058
- Oppo, K., Leen, E., Angerson, W. J., Cooke, T. G., and McArdle, C. S. (1998). Doppler perfusion index: an interobserver and intraobserver reproducibility study. *Radiology* 208, 453–457. doi: 10.1148/radiology.208.2.9680575
- Oshiro, S., Morioka, M. S., and Kikuchi, M. (2011). Dysregulation of iron metabolism in Alzheimer's disease, Parkinson's disease, and amyotrophic lateral sclerosis. *Adv. Pharmacol. Sci.* 2011:378278. doi: 10.1155/2011/378278
- Parente, D. B., Gasparetto, E. L., da Cruz, L. C. H., Domingues, R. C., Baptista, A. C., Carvalho, A. C. P., et al. (2008). Potential role of diffusion tensor MRI in the differential diagnosis of mild cognitive impairment and Alzheimer's disease. *Am. J. Roentgenol.* 190, 1369–1374. doi: 10.2214/Ajr.07.2617
- Pena, F., Gutierrez-Lerma, A. I., Quiroz-Baez, R., and Arias, C. (2006). The role of beta-amyloid protein in synaptic function: implications for Alzheimer's disease therapy. *Curr. Neuropharmacol.* 4, 149–163. doi: 10.2174/157015906776359531
- Pievani, M., Agosta, F., Pagani, E., Canu, E., Sala, S., Absinta, M., et al. (2010). Assessment of white matter tract damage in mild cognitive impairment and Alzheimer's disease. *Hum. Brain Mapp.* 31, 1862–1875. doi: 10.1002/hbm.20978
- Ringman, J. M., O'Neill, J., Geschwind, D., Medina, L., Apostolova, L. G., Rodriguez, Y., et al. (2007). Diffusion tensor imaging in preclinical and presymptomatic carriers of familial Alzheimer's disease mutations. *Brain* 130, 1767–1776. doi: 10.1093/brain/awm102
- Rovaris, M., Gass, A., Bammer, R., Hickman, S. J., Ciccarelli, O., Miller, D. H., et al. (2005). Diffusion MRI in multiple sclerosis. *Neurology* 65, 1526–1532. doi: 10.1212/01.wnl.0000184471.83948.e0
- Sampedro, A., Pena, J., Ibarretxe-Bilbao, N., Cabrera-Zubizarreta, A., Sanchez, P., Gomez-Gastiasoro, A., et al. (2020). Brain white matter correlates of creativity in schizophrenia: a diffusion tensor imaging study. *Front. Neurosci.* 14:572. doi: 10.3389/fnins.2020.00572
- Schweser, F., Deistung, A., Lehr, B. W., and Reichenbach, J. R. (2011). Quantitative imaging of intrinsic magnetic tissue properties using MRI signal phase: an approach to in vivo brain iron metabolism? *Neuroimage* 54, 2789–2807. doi: 10.1016/j.neuroimage.2010.10.070
- Schweser, F., Sommer, K., Deistung, A., and Reichenbach, J. R. (2012). Quantitative susceptibility mapping for investigating subtle susceptibility variations in the human brain. *Neuroimage* 62, 2083–2100. doi: 10.1016/j.neuroimage.2012.05.067
- Smith, S. M., Jenkinson, M., Johansen-Berg, H., Rueckert, D., Nichols, T. E., Mackay, C. E., et al. (2006). Tract-based spatial statistics: voxelwise analysis of multi-subject diffusion data. *Neuroimage* 31, 1487–1505. doi: 10.1016/j.neuroimage.2006.02.024
- Song, S. K., Sun, S. W., Ju, W. K., Lin, S. J., Cross, A. H., and Neufeld, A. H. (2003). Diffusion tensor imaging detects and differentiates axon and myelin degeneration in mouse optic nerve after retinal ischemia. *Neuroimage* 20, 1714–1722. doi: 10.1016/j.neuroimage.2003.07.005
- Stebbins, G. T., and Murphy, C. M. (2009). Diffusion tensor imaging in Alzheimer's disease and mild cognitive impairment. *Behav. Neurol.* 21, 39–49. doi: 10.1155/2009/915041
- Sun, Y., Du, X. K., Zhang, Z. X., and Chen, X. (2004). Relationship between the data from MR-diffusion tensor imaging and the clinical cognitive evaluation in Alzheimer's disease. *Zhongguo Yi Xue Ke Xue Yuan Xue Bao* 26, 134–138.
- Takahashi, H., Ishii, K., Kashiwagi, N., Watanabe, Y., Tanaka, H., Murakami, T., et al. (2017). Clinical application of apparent diffusion coefficient mapping in voxel-based morphometry in the diagnosis of Alzheimer's disease. *Clin. Radiol.* 72, 108–115. doi: 10.1016/j.crad.2016.11.002
- Teipel, S. J., Wegrzyn, M., Meindl, T., Frisoni, G., Bokde, A. L. W., Fellgiebel, A., et al. (2012). Anatomical MRI and DTI in the diagnosis of Alzheimer's disease: a european multicenter study. *J. Alzheimers Dis.* 31, S33–S47. doi: 10.3233/Jad-2012-112118
- Ukmar, M., Makuc, E., Onor, M. L., Garbin, G., Trevisiol, M., and Cova, M. A. (2008). Evaluation of white matter damage in patients with Alzheimer's disease and in patients with mild cognitive impairment by using diffusion tensor imaging. *Radiol. Med.* 113, 915–922. doi: 10.1007/s11547-008-0286-1
- Vasconcelos, L. G., Brucki, S. M. D., Jackowski, A. P., and Bueno, O. F. A. (2009). Diffusion tensor imaging for Alzheimer's disease: a review of concepts and potential clinical applicability. *Dement. Neuropsychol.* 3, 268–274. doi: 10.1590/S1980-57642009DN30400002
- Wakana, S., Jiang, H. Y., Nagae-Poetscher, L. M., van Zijl, P. C. M., and Mori, S. (2004). Fiber tract-based atlas of human white matter anatomy. *Radiology* 230, 77–87. doi: 10.1148/radiol.2301021640

- Wei, H. J., Dibb, R., Zhou, Y., Sun, Y. W., Xu, J. R., Wang, N., et al. (2015). Streaking artifact reduction for quantitative susceptibility mapping of sources with large dynamic range. *NMR Biomed.* 28, 1294–1303. doi: 10.1002/nbm.3383
- Winkler, A. M., Ridgway, G. R., Webster, M. A., Smith, S. M., and Nichols, T. E. (2014). Permutation inference for the general linear model. *Neuroimage* 92, 381–397. doi: 10.1016/j.neuroimage.2014.01.060
- Zhong, J. H., Ni, H. Y., Zhu, T., Ekholm, S., and Kavcic, V. (2004). MR diffusion tensor imaging (DTI) and neuropsychological testing for neuronal connectivity in Alzheimer's disease (AD) patients. *Pro. Biomed. Opt. Imag.* 5, 238–249. doi: 10.1117/12.535752

Conflict of Interest: The authors declare that the research was conducted in the absence of any commercial or financial relationships that could be construed as a potential conflict of interest.

Copyright © 2021 Liu, Du, Zhang, Zhao, Gao, Liu, Liu, Chen, Wang, Yu and Ma. This is an open-access article distributed under the terms of the Creative Commons Attribution License (CC BY). The use, distribution or reproduction in other forums is permitted, provided the original author(s) and the copyright owner(s) are credited and that the original publication in this journal is cited, in accordance with accepted academic practice. No use, distribution or reproduction is permitted which does not comply with these terms.



Systematic Review: Quantitative Susceptibility Mapping (QSM) of Brain Iron Profile in Neurodegenerative Diseases

Parsa Ravanfar^{1*}, Samantha M. Loi^{1,2}, Warda T. Syeda¹, Tamsyn E. Van Rheenen^{1,3}, Ashley I. Bush⁴, Patricia Desmond^{5,6}, Vanessa L. Cropley^{1,3}, Darius J. R. Lane⁴, Carlos M. Opazo⁷, Bradford A. Moffat^{1,5}, Dennis Velakoulis^{1,2†} and Christos Pantelis^{1,7†}

¹ Melbourne Neuropsychiatry Centre, Department of Psychiatry, The University of Melbourne and Melbourne Health, Carlton South, VIC, Australia, ² Neuropsychiatry, The Royal Melbourne Hospital, Parkville, VIC, Australia, ³ Centre for Mental Health, Swinburne University of Technology, Hawthorn, VIC, Australia, ⁴ Melbourne Dementia Research Centre, Florey Institute of Neuroscience & Mental Health, The University of Melbourne, Parkville, VIC, Australia, ⁵ Melbourne Brain Centre Imaging Unit, Department of Medicine and Radiology, The University of Melbourne, Parkville, VIC, Australia, ⁶ Department of Radiology, The Royal Melbourne Hospital, The University of Melbourne, Parkville, VIC, Australia, ⁷ Florey Institute of Neuroscience and Mental Health, The University of Melbourne, Parkville, VIC, Australia

OPEN ACCESS

Edited by:

Yi Wang,
Cornell University, United States

Reviewed by:

Alan Wilman,
University of Alberta, Canada
Mauro Costagli,
University of Genoa, Italy

*Correspondence:

Parsa Ravanfar
sravanfar@student.unimelb.edu.au

[†]These authors share
senior authorship

Specialty section:

This article was submitted to
Neurodegeneration,
a section of the journal
Frontiers in Neuroscience

Received: 19 October 2020

Accepted: 07 January 2021

Published: 18 February 2021

Citation:

Ravanfar P, Loi SM, Syeda WT, Van Rheenen TE, Bush AI, Desmond P, Cropley VL, Lane DJR, Opazo CM, Moffat BA, Velakoulis D and Pantelis C (2021) Systematic Review: Quantitative Susceptibility Mapping (QSM) of Brain Iron Profile in Neurodegenerative Diseases. *Front. Neurosci.* 15:618435. doi: 10.3389/fnins.2021.618435

Iron has been increasingly implicated in the pathology of neurodegenerative diseases. In the past decade, development of the new magnetic resonance imaging technique, quantitative susceptibility mapping (QSM), has enabled for the more comprehensive investigation of iron distribution in the brain. The aim of this systematic review was to provide a synthesis of the findings from existing QSM studies in neurodegenerative diseases. We identified 80 records by searching MEDLINE, Embase, Scopus, and PsycInfo databases. The disorders investigated in these studies included Alzheimer's disease, Parkinson's disease, amyotrophic lateral sclerosis, Wilson's disease, Huntington's disease, Friedreich's ataxia, spinocerebellar ataxia, Fabry disease, myotonic dystrophy, pantothentate-kinase-associated neurodegeneration, and mitochondrial membrane protein-associated neurodegeneration. As a general pattern, QSM revealed increased magnetic susceptibility (suggestive of increased iron content) in the brain regions associated with the pathology of each disorder, such as the amygdala and caudate nucleus in Alzheimer's disease, the substantia nigra in Parkinson's disease, motor cortex in amyotrophic lateral sclerosis, basal ganglia in Huntington's disease, and cerebellar dentate nucleus in Friedreich's ataxia. Furthermore, the increased magnetic susceptibility correlated with disease duration and severity of clinical features in some disorders. Although the number of studies is still limited in most of the neurodegenerative diseases, the existing evidence suggests that QSM can be a promising tool in the investigation of neurodegeneration.

Keywords: quantitative susceptibility mapping, brain, iron, Alzheimer's disease, Parkinson's disease, neurodegenerative diseases

INTRODUCTION

While the presence of iron is vital for normal function and development of the brain, excess iron deposition has been proposed to play an important role in the pathology of neurodegenerative diseases (Morris et al., 2018). Iron is a key element in several metabolic pathways throughout the body including oxidative phosphorylation and DNA synthesis and is responsible for oxygen transport in the blood. In the central nervous system (CNS), in addition to its general metabolic roles, iron plays a critical part in myelin synthesis and neurotransmitter production (Mills et al., 2010). On the other hand, there has been a growing body of evidence in recent decades suggesting a role for iron in the pathology of neurodegenerative diseases, such as Alzheimer's disease (AD), Parkinson's disease (PD), and Huntington's disease (HD) (Masaldan et al., 2019).

The proposed role of iron in neurodegeneration is mediated through two mechanisms. In the first mechanism that can occur in all individuals regardless of illness, iron induces oxidative damage through production of reactive oxygen species and orchestrates "ferroptosis," a recently identified form of iron-mediated cell death (see more about ferroptosis at Dixon et al., 2012) (Ndayisaba et al., 2019). The second mechanism is more disease-specific. Iron has been shown to interact with hallmark features of neurodegenerative illnesses, such as amyloid- β (A β) plaques, α -synuclein aggregates, and tau protein. The interplay between iron and these proteins promotes their production and aggregation, and incorporation of iron in their structure further increases the oxidizing capacity resulting in neuronal cell death (Masaldan et al., 2019; Ndayisaba et al., 2019).

For the reasons mentioned above, *in vivo* evaluation of brain iron has been of great interest in neurodegenerative diseases. Magnetic resonance imaging (MRI) can detect iron due to its high magnetic susceptibility. Magnetic susceptibility is a dimensionless physical property that indicates the

magnetizability of a material when exposed to an applied magnetic field. Elements and compounds are categorized as paramagnetic or diamagnetic based on their magnetic susceptibility. Paramagnetic substances (such as most biologic forms of iron and copper) have a positive magnetic susceptibility, are attracted to an external magnetic field, and increase the mean tissue magnetic susceptibility. On the other hand, diamagnetic substances (such as water, myelin, and calcifications) have a negative magnetic susceptibility, are slightly repelled by an external magnetic field and decrease the mean tissue magnetic susceptibility (Liu et al., 2015; Rumble, 2020).

Mean magnetic susceptibility of organic tissues is determined by their composition and the magnetic susceptibility of their constituents. The brain tissue is generally weakly diamagnetic since water (slightly diamagnetic) constitutes 70–85% of the brain. Magnetic susceptibility varies slightly among brain regions due to the differences in their tissue composition. The major contributors to the measurable changes of magnetic susceptibility across the brain are myelin (weakly diamagnetic) and iron-containing molecules (mostly strongly paramagnetic). The largest proportion of non-heme iron in the brain is bound to ferritin, which makes up the greatest contribution to the tissue magnetic susceptibility among all iron compounds. Other forms of iron, including free and transferrin-bound iron only minimally contribute to the measured mean tissue susceptibility (Liu et al., 2015; Deistung et al., 2017; Duyn and Schenck, 2017). Another iron-containing complex that is abundant in the substantia nigra pars compacta (SNc) and locus coeruleus and constitutes a main source of magnetic susceptibility in these areas is neuromelanin. Neuromelanin is a dark pigment with a structure similar to melanin found in the skin and iris. It is produced from the oxidation of DOPA and dopamine and has high affinity and capacity for chelation of iron and other metals, constituting a major iron storage site in the catecholaminergic ganglia (Haining and Achat-Mendes, 2017).

MRI sequences that are sensitive to tissue magnetic susceptibility are used for investigation of iron. The contrast in susceptibility-based MRI techniques, such as susceptibility weighted imaging (SWI), T_2^* -weighted imaging (quantifying effective transverse relaxation), R_2^* imaging (reciprocal of T_2^*), and quantitative susceptibility mapping (QSM), arises from microscopic magnetic field shifts due to the variations of tissue magnetic susceptibility. Recently developed QSM techniques provide quantitative estimates of local magnetic susceptibility at a voxel-level (Deistung et al., 2017). In each voxel, the local magnetic field that is used to calculate susceptibility is comprised of the background field (magnetic field from sources outside the brain or even outside the scanner), the magnetic field from neighboring voxels, and the local magnetic field produced by the tissue within the voxel. The main strength of QSM compared to traditional susceptibility-sensitive imaging techniques is that it disentangles the local magnetic field from the non-local contributions by solving a complex field-to-source inversion problem (Haacke et al., 2015). Advanced inference techniques enable QSM to localize, quantify, and produce a voxel-wise mapping of mean tissue susceptibility (Haacke et al., 2015; Wang and Liu, 2015).

Abbreviations: A β , Amyloid- β ; AD, Alzheimer's disease; ALS, Amyotrophic lateral sclerosis; ALSFRS, Amyotrophic lateral sclerosis Functional Rating Scale; aMCI, amnesic mild cognitive impairment; AR-PD, akinetic-rigid Parkinson's disease; AUC, area under curve; CN, caudate nucleus; CNS, central nervous system; CSF, cerebrospinal fluid; CST, corticospinal tract; DLB, dementia with Lewy bodies; DM1, myotonic dystrophy 1; DM2, myotonic dystrophy 2; DN, dentate nucleus; DTI, diffusion tensor imaging; FD, Fabry disease; FRDA, Friedreich's ataxia; GP, globus pallidus; GRE, gradient (recalled) echo; GRE, gradient echo; H&Y, Hoehn and Yahr; HD, Huntington's disease; iLSQR, iterative LSQR; LSQR, sparse linear equation and least-squares; MCI, mild cognitive impairment; MEDI, morphology enabled dipole inversion; MMSE, mini-mental status examination; MoCA, Montreal cognitive assessment; MPAN, mitochondrial membrane protein-associated neurodegeneration; MRI, magnetic resonance imaging; MSA, multiple system atrophy; NBIA, neurodegeneration with brain iron accumulation syndromes; nMEDI, non-linear MEDI; PD, Parkinson's disease; PDF, projection onto dipole fields; PET, positron emission tomography; PKAN, pantothenate-kinase-associated neurodegeneration; PLS, progressive primary lateral sclerosis; PSP, progressive supranuclear palsy; QSM, quantitative susceptibility mapping; RE-SHARP, regularization-enabled SHARP; RN, red nucleus; ROC, receiver operating characteristic curve; SCA, spinocerebellar ataxia; SHARP, sophisticated harmonic artifact reduction for phase; SN, substantia nigra; SNc, substantia nigra pars compacta; SNr, substantia nigra pars reticulata; SOD1, superoxide dismutase 1; STN, sub-thalamic nucleus; SWI, susceptibility weighted imaging; TD-PD, tremor-dominant Parkinson's disease; UPDRS, unified Parkinson's disease rating scale; V-SHARP, variable-radius SHARP; WD, Wilson's disease.

In the deep gray matter structures, due to less confounding effect from myelin and negligible contribution from other paramagnetic metals, QSM has been shown to reliably quantify changes of iron content (Langkammer et al., 2012). The accuracy of QSM in identifying iron deposition in these regions has been validated in post-mortem studies showing significant correlations between QSM contrast and histochemical measurement of iron (Langkammer et al., 2012; Sun et al., 2015; Hametner et al., 2018; Lee et al., 2018; Lewis et al., 2018; Wang et al., 2020). In the white matter, on the other hand, alterations in magnetic susceptibility measured by QSM may result from changes in myelin as well as iron. In other words, in the basal ganglia, an increased magnetic susceptibility is most likely arising from an increase in iron content (except in the conditions where other paramagnetic metals are also increased), while such increase in the white matter can be a result of both an increase in iron, a decrease in myelin (demyelination) or both (Hametner et al., 2018).

Over the past decade, QSM has been used by an increasing number of studies in investigations of brain changes in neurodegenerative disorders. In this paper, we systematically reviewed existing human studies that investigated brain changes in neurodegenerative diseases using QSM. It is important to note that QSM does not directly measure iron content, rather it provides an accurate measurement of tissue magnetic susceptibility. To determine whether the alterations in magnetic susceptibility are indicative of changes in iron content, the brain region where such changes are observed (white vs. gray matter), as well as the pathophysiologic processes involved in each neurodegenerative disease should be taken into account. Therefore, in reporting the findings from QSM studies, we present the direct measures made by QSM, which is tissue magnetic susceptibility. In the discussion section, we will provide the implications of the findings in terms of brain iron changes in each neurodegenerative disease separately.

The overarching aim of this review was to determine regional disease-specific patterns of brain iron distribution in these disorders. To this end, we sought to address the following questions:

- Are there any differences in brain tissue magnetic susceptibility in patients with neurodegenerative diseases in comparison to healthy individuals?
- In patients with neurodegenerative diseases, do the regional changes of magnetic susceptibility correlate with the clinical manifestations of the disease and the areas that are most affected in these conditions?
- Is there evidence that the pattern of magnetic susceptibility changes identified by QSM can differentiate neurodegenerative diseases?

METHODS AND MATERIALS

Search Protocol

This review followed the Preferred Reporting Items for Systematic Reviews and Meta-Analyses (PRISMA) guidelines (Moher et al., 2009; Shamseer et al., 2015). Our protocol

was registered at the International Prospective Register of Systematic Reviews (<https://www.crd.york.ac.uk/prospero/>) (CRD42020168598) and was also published as a preprint at the publicly available domain, MedRxiv (Ravanfar et al., 2020).

We searched MEDLINE (PubMed interface), Embase (Ovid interface), Scopus, and PsycInfo (Ovid interface) databases. To ensure the inclusiveness of our search, we examined the reference lists of reviewed studies and relevant literature reviews to identify any further relevant records. Literature search strategies were developed to identify any record containing QSM or “quantitative susceptibility mapping” and any disease name under the Medical Subject Headings (<https://www.ncbi.nlm.nih.gov/mesh/>) subheading for “neurodegenerative diseases” in their title, abstract and keywords. Details of our search strategy can be found in our systematic review protocol, provided in **Supplementary Material 1**. The initial search was performed in January 2020 and amended in April 2020 to include all studies published during the time of preparing the manuscript.

Study Selection

Authors PR and SL independently screened the records for inclusion according to the eligibility criteria specified below. In the first stage, titles and abstracts were screened and studies that met our eligibility criteria were included. Full text records of the studies included in the first stage were obtained and screened in the second stage for final decision on inclusion or exclusion. The two reviewers discussed any disagreements and if a consensus could not be reached, a third reviewer (CP) adjudicated the case. Studies included in this review were human studies published as journal articles in English without any limitation of publication date, according to the following criteria.

Design

We included cross-sectional and longitudinal case control studies, retrospective and prospective. Case reports and case series were not included.

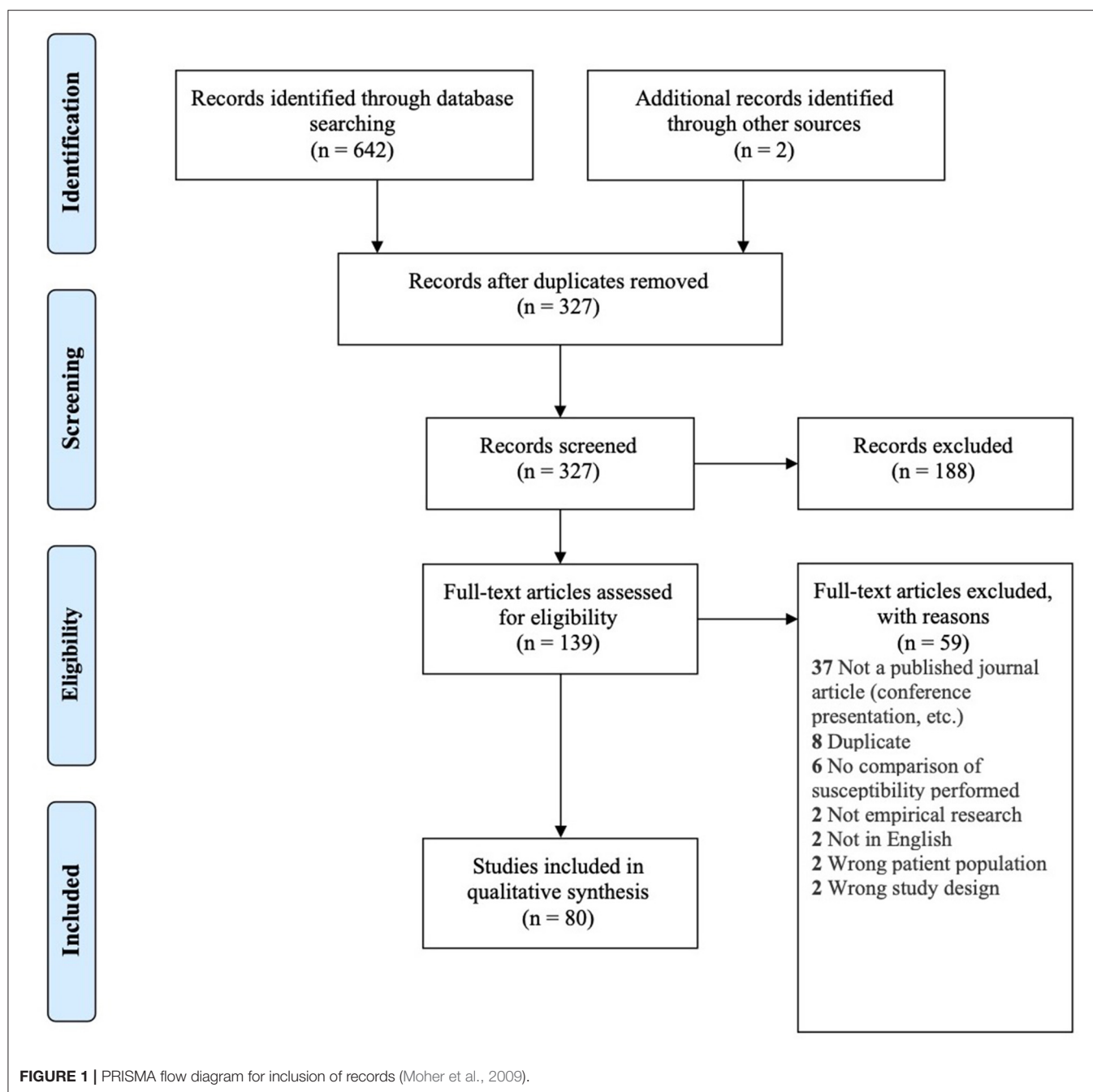
Participants

We included studies investigating patients who were formally diagnosed with any of the disorders recognized as a neurodegenerative disease according to the National Institute of Health, Medical Subject Headings (MeSH), regardless of age. It should be noted that although a large number of QSM studies in multiple sclerosis exist, since the disorder is not classified as a neurodegenerative disease in MeSH, it has not been included in this review [Studies of QSM in individuals with MS have been reviewed elsewhere (Lee et al., 2017)].

Only those studies that presented the results from an independent sample of data were included. If a study population was used in more than one study, only the first published study was included provided that it satisfied other eligibility criteria.

Investigations

Of interest to this review were the studies investigating the brain structure in neurodegenerative diseases using QSM imaging with MRI scanners of any field strength. Studies that used other



susceptibility-based imaging techniques, such as SWI, T_2^* , and R_2^* without QSM were excluded.

Comparators

Included studies were those that:

- compared QSM findings between each neurodegenerative disease and healthy controls and/or,
- compared different subtypes or clinical features of a disease and/or,

- examined the relationship of QSM indices with pathologic markers of the disease.

Studies that focused on the QSM protocols and technical aspects using a population of either healthy participants or patients without any comparison between patients and healthy groups were excluded.

Outcomes

The outcome measure of interest for this review was magnetic susceptibility reported in ppm (parts per million) or ppb (parts

per billion). In some studies, mean susceptibility values of the brain regions of interest (ROIs) were not reported, but the results from inter-group comparisons and correlation analyses were provided. This was not considered as an exclusion factor.

Data Extraction, Synthesis, and Quality Assessment

Relevant information was extracted and recorded in summary tables for each study by PR and SL independently and compared for discrepancies. Quality assessment was performed by evaluating the risk of bias in each study using a modified version of the National Heart, Lung, and Blood Institute quality assessment tool for case-control studies which was customized to improve its application to our target studies (**Supplementary Material 1**). Factors, such as unclear description of study population and eligibility criteria, data processing by researchers who were not blinded to the clinical characteristics of subjects, inconsistent MRI acquisition and/or QSM processing, and failure to account for confounders, such as age in the statistical analysis, were considered to pose a risk of bias and reduce the quality of the study. Based on these factors, the risk of bias was reported as “high,” “medium,” and “low” for each study. The data extraction table and quality assessment tool are available in the systematic review protocol (**Supplementary Material 1**).

Due to the different methods of MRI acquisition, QSM processing, brain segmentation, and QSM reference regions among the reviewed studies, a meta-analysis was not possible. However, in an effort to quantify the magnitude of magnetic susceptibility differences between patient and healthy control groups reported by each study, we calculated the effect size (Hedge's *g*) for each ROI where the mean and standard deviation (or standard error of mean) were reported. Data synthesis was conducted as a narrative report with tables used to summarize and demonstrate the patterns of alteration in magnetic susceptibility across the reviewed studies for each neurodegenerative disease.

RESULTS

Search Summary

A total of 642 records were found in our search across the four different databases. After removal of 315 duplicates, the remaining 327 studies were screened for eligibility, of which 80 were included in our review (see **Figure 1** for PRISMA flow diagram).

The neurodegenerative diseases investigated in these studies included: AD, PD, HD, amyotrophic lateral sclerosis (ALS), Wilson's disease (WD) and rare genetic neurodegenerative diseases including Friedreich's ataxia (FRDA), multiple system atrophy (MSA), myotonic dystrophy (DM), spinocerebellar ataxia (SCA), progressive supranuclear palsy (PSP), Fabry disease, and syndrome of neurodegeneration with brain iron accumulation (NBIA). **Table 1** shows the number of studies found for each neurodegenerative disease.

In the following sections, we will present the findings of the review for each neurodegenerative disease structured into the following subheadings: (1) changes in tissue magnetic susceptibility when compared to healthy controls; (2) correlations between QSM findings and clinical features or other pathologic biomarkers; and (3) accuracy of QSM in differentiation of patients from healthy individuals. Reported changes of susceptibility in the brain regions examined by each study and the calculated effect size for the inter-group differences are summarized in color-coded **Tables 2A–J**. Detailed characteristics, main findings and quality assessment of studies are provided in the **Supplementary Tables 1A–H**. A summary of susceptibility changes across all neurodegenerative diseases reviewed in this paper are presented in **Table 3**.

As shown in **Table 1**, there are very few QSM studies published in most neurodegenerative diseases. To adhere to the reporting standards for systematic reviews, we have included and presented the findings of all existing studies. However, to improve the readability of this paper, for the rare neurodegenerative diseases where fewer than three studies have been published (FRDA, SCA, Fabry disease, DM, PKAN, and MPAN), their relevant subheadings in the results and discussion sections have been presented in **Supplementary Material 3** instead of the main text. Although, in the same way as the other disorders, their findings are presented in the **Supplementary Tables 1F–H**, **2**, and the color coded tables (**Tables 2I, J**, **3**).

Alzheimer's Disease and Mild Cognitive Impairment (MCI)

Magnetic Susceptibility Changes in Alzheimer's Disease and Mild Cognitive Impairment in Comparison With Healthy Individuals

This review included 10 studies that used QSM to evaluate brain iron changes in AD, five studies that included a group of MCI subjects (with or without an AD group), and two studies that investigated the association of QSM and A β or APOE4 gene in a healthy population (see **Supplementary Table 1A**).

TABLE 1 | Number of records included in this review for each neurodegenerative disease.

Neurodegenerative disease	Number of studies included
Alzheimer's disease	13
Parkinsonian diseases	43
Amyotrophic lateral sclerosis	8
Wilson's disease	4
Huntington's disease	3
Friedreich's ataxia	2
Spinocerebellar ataxia	2
Fabry disease	1
Myotonic dystrophy	1
Pantothenate-kinase-associated neurodegeneration	2
Mitochondrial membrane protein-associated neurodegeneration	1

TABLE 2 | Color-coded tables for magnetic susceptibility changes in the regions of interest in each neurodegenerative disease.**(A) Summary of QSM changes in the subcortical structures in AD and MCI.**

References	Sample size (age, years)	BG	PUT	GP	CN	AMY	HP	TH	PUL	NA	SN	DN	RN
Acosta-Cabronero et al. (2013)	Early-stage probable AD: 8 (72 ± 6) HC: 8 (70 ± 5) Young HC: 3 (32 ± 2)		↑		↑	↑							
Van Bergen et al. (2016b)	aMCI: 15 (75.27 ± 7.63) HC: 22 (71.91 ± 5.25)		−0.123	−0.235	−0.176	−0.077	0.072	−0.149		0			
Moon et al. (2016)	Probable AD: 27 (78.63 ± 8.11) HC: 18 (46.89 ± 14.69)		1.315	0.335	0.945				0.244				
Hwang et al. (2016)a	HC: 18 (65.2 ± 6.41) aMCI: 18 (66.9 ± 5.51) AD: 18 (69.9 ± 9.81)												
Ayton et al. (2017)a	HC: 64 (not reported) MCI: 17 (not reported) AD: 19 (not reported)												
Kim et al. (2017)	HC: 19 (65.37 ± 6.29) AD: 19 (69.79 ± 10.27)		2.765	1.283	↑	5.832	5.799	4.761	3.885				
	HC: 19 (65.37 ± 6.29) aMCI: 19 (65.95 ± 6.75)		2.115	0.146		2.271	3.047	3.107	2.515				
Du L. et al. (2018)	HC: 30 (66.2 ± 7.8) Mild-Moderate AD: 30 (68.3 ± 6.6)		↑	~	↑			↓			↓	↓	↓
Tiepol et al. (2018)	HC: 10 (67.1) AD: 10 (74.1)		Left: 9.225 Right: 7.897	Left: 22.349 Right: 19.18									
Meineke et al. (2018)	Mild to moderate AD: 6 (58 ± 6) HC: 10 (59 ± 7)		↑	↑	↑		~	↓					
	MCI: 8 (63 ± 6) HC: 10 (59 ± 7)		↑	↓	↑		~	↓					
Kan et al. (2020)	HC: 19 (71 ± 5) AD: 38 (80 ± 6)				↑	↑	↑						

TABLE 2 | Continued

(B) Summary of QSM changes in the cortical regions in AD and MCI

References	Sample size (age, years)	Whole cortex	Entorhinal cortex	Frontal	Temporal	Parietal	Occipital	Cingulate	Insula	Neocortex	Allocortex
Acosta-Cabronero et al. (2013)	Early-stage probable AD: 8 (72 ± 6) HC: 8 (70 ± 5) Young HC: 3 (32 ± 2)				↑	↑	↑				
Van Bergen et al. (2016b)	aMCI: 15 (75.27 ± 7.63) HC: 22 (71.91 ± 5.25)		0.154	0.058	0.227	−0.04	0.024				
Hwang et al. (2016)	HC: 18 (65.2 ± 6.41) aMCI: 18 (66.9 ± 5.51) AD: 18 (69.9 ± 9.81)										
Ayton et al. (2017)	HC: 64 (not reported) MCI: 17 (not reported) AD: 19 (not reported)										
Kim et al. (2017)	HC: 19 (65.37 ± 6.29) AD: 19 (69.79 ± 10.27)	Allocortex: 6.570 Neocortex: 6.566	5.738	precentral gyrus	↑ parahippocampal gyrus, rt superior and transverse temporal gyrus	postcentral gyrus, Precuneus: 6.059		Anterior: 6.251 Posterior: 5.643	↑	6.566	6.57
	HC: 19 (65.37 ± 6.29) aMCI: 19 (65.95 ± 6.75)	Allocortex: 4.260	2.594			Precuneus: 3.867		Anterior: 3.670 Posterior: 3.76			
Tiepol et al. (2018)	HC: 10 (67.1) AD: 10 (74.1)			Left superior orbitofrontal cortex: −17.302 right mesial orbitofrontal cortex: 0.333	left superior temporal cortex: −13.680 left medial temporal cortex: −6.501 left inferior temporal cortex: −13.776		left lingual gyrus: 1.751	left anterior cingulate cortex: −2.443	Left: −11.225		

TABLE 2 | Continued

(C) Summary of QSM changes in the subcortical structures in PD

References	Sample size (age, years)	BG	PUT	GP	CN	AMY	HP	TH	PUL	NA	SN	SNc	SNr	DN	RN	FN	STN	Nigrosome-1
Lottipour et al. (2012)	PD: 9 (66.6) HC: 11 (59.2)										↑	↑						
Ide et al. (2014)	PD: 19 (72.6 ± 7.65) HC: 41 (69.4 ± 9.10)			Lateral: −0.576 Medial: −0.26														
Barbosa et al. (2015)	PD: 20 (66 ± 8) HC: 30 (64 ± 7)		−0.261	0.304	0.017			0.052			0.981	1.022			−0.240			
He et al. (2015)	PD: 44 (58 ± 8.76) HC: 35 (60.49 ± 6.48)		−0.73	0.34	−0.003						0.971				0.643			
Murakami et al. (2015)	PD: 21 (72.0 ± 7.5) HC: 21 (69.7 ± 8.6)		−0.176	−0.215	0			0.023			1.752				−0.343			
Azuma et al. (2016)	PD: 24 (63.3 ± 11.0) HC: 24 (64.1 ± 10.0)		−0.309	−0.322	−0.004						1.087				0.075			
Peckham et al. (2016)	PD: 18 (69.1 ± 11.2) HC: 16 (64.4 ± 6.1)										↑					↑		
Langkammer et al. (2016)	PD: 66 (64.7 ± 8.8) HC: 58 (65.0 ± 9.3)		0	0.464	0.002			0.497			0.669				0.446			
Du et al. (2016)	PD: 47 (65.8 ± 10.1) HC: 47 (62.2 ± 8.8)											1.02						
He et al. (2017)	TD-PD: 19 (62.7 ± 8.2) HC: 48 (61.7 ± 6.5)													0.656				
Sjöström et al. (2017)	PD: 62 (65.2 ± 10.5) HC: 14 (63.5 ± 5.3)		~	↑							↑				↓			
Ito et al. (2017)	PD: 26 (64) HC: 20 (68.5)																	
Xuan et al. (2017)	EOPD: 35 (50.0 ± 5.3) Younger HC: 24 (51.8 ± 7.5)		−0.071	−0.072	0							0.703	0.616		0.098			
	M-LOPD: 33 (61.9 ± 6.0) Older HC: 22 (63.1 ± 7.3)		0.57	0.114	−0.448							0.891	0.594		0.538			
Guan et al. (2017b)	TD-PD: 27 (55.3 ± 9.0) HC: 40 (56.6 ± 9.9)		↑	↓	↓			↑				↑	↑	↑	↑			
	AR-PD: 27 (55.4 ± 9.9) HC: 40 (56.6 ± 9.9)		↑	↑	↓			↑				↑	↑	~	↑			
Guan et al. (2017a)	ES-PD: 15 (55.8 ± 8.3) HC: 40 (56.6 ± 9.9)		↑	−0.046	↓							↑	↑	↑	↑			
	LS-PD: 45 (61.1 ± 6.7) HC: 40 (56.6 ± 9.9)		↑	0.853	↓							↑	↑	↑	↑			
Zhao et al. (2017)	PD: 29 (67.9 ± 6.7) HC: 25 (64.7 ± 8.3)		0.147	−0.141	−0.316						0.771				−0.078			

(Continued)

TABLE 2 | Continued

(C) Summary of QSM changes in the subcortical structures in PD

References	Sample size (age, years)	BG	PUT	GP	CN	AMY	HP	TH	PUL	NA	SN	SNc	SNr	DN	RN	FN	STN	Nigrosome-1
Acosta-Cabronero et al. (2017)	PD: 25 (63.6 ± 8.6) HC: 50 (63.6 ± 8.5)		↑	↑	↓	↑	↑	↑			↑			↓	↑			
Takahashi et al. (2018b)	PD: 39 (69.24 ± 6.04) HC: 25 (67.14 ± 6.81)											0.703						
Kim et al. (2018)	ES-PD: 38 (68.3 ± 9.2) HC: 25 (65.0 ± 6.3)										1.855							
Du G. et al. (2018)	PD: 72 (66.3 ± 9.5) HC: 62 (66.2 ± 10.2)											0.761	0.681		0.067			
Shin et al. (2018)	High-NMS: 13 (69.8 ± 11.2) HC: 19 (67.6 ± 8.0)		0.281	0.235	0.353							0.277	0.361	0.197	0.466			
	Low-NMS: 16 (71.4 ± 6.8) HC: 19 (67.6 ± 8.0)		0.11	0.106	0.28							0.098	0.275	−0.094	0.313			
Takahashi et al. (2018a)	ES-PD: 18 (71.2 ± 6.94) HC: 18 (67.1 ± 4.75)											0.741						
An et al. (2018)	PD: 44 (67.3 ± 9.8) HC: 31 (66.9 ± 9.0)										0.736							
Li et al. (2018)	PD: 31 (63.1 ± 8.3) HC: 27 (62.0 ± 7.0)		↓	↑	↓	↑	(Rt)↑	(Rt) ↑			↑			↓	↑			
Guan et al. (2019b)	PD: 90 (59.38 ± 8.54) HC: 38 (57.93 ± 8.04)										↑	↑						
Chen et al. (2019)	PD: 33 (64.55 ± 11.2) HC: 26 (62.62 ± 10.62)		0.616	GPI: 0.553	1.143			0.258				1.838	0.507	0.111	0.707	1.357	0.296	
Li et al. (2019)	PD: 28 (68.20 ± 6.1) HC: 28 (64.75 ± 8.0)										0.714							
Azuma et al. (2019)	PD: 18 (69.6 ± 6.2) HC: 18 (69.1 ± 7.0)		−0.428	−0.474	0.046						1.085				0.705			
Shahmaei et al. (2019)	PD: 30 (66.2 ± 8.5) HC: 15 (64.9 ± 9.2)		−0.421	2.449	−0.085			0.995			4.016				1.758			
Sethi et al. (2019)	PD: 20 (67.0 ± 10) HC: 174 (45.1 ± 14.2)										1.446				0.189			
Uchida et al. (2019)	PD: 22 (70.8 ± 5.9) HC: 20 (71.4 ± 5.2)		0.369	0.201	0.203	0.371	0.131	0.107			0.237				0.033			
	PD-MCI: 24 (74.9 ± 5.5) HC: 20 (71.4 ± 5.2)		0.373	0.268	0.417	0.356	0.25	0.158			0.269				0.095			
Sun et al. (2019)	PD: 32 (61.6 ± 6.5) HC: 50 (62.0 ± 7.5)		−0.174	1.022	0.087						1.701				0.874			
Cheng et al. (2019)	PD: 87 (60.9 ± 8.1) HC: 77 (63.4 ± 7.3)																	0.641
Ghassaban et al. (2019)	PD: 25 (61.8 ± 6.4) HC: 24 (63.4 ± 8.0)		1.157	0.036	0.987			0.061	1.073		3.949			1.212	1.018			

(Continued)

TABLE 2 | Continued

(C) Summary of QSM changes in the subcortical structures in PD

References	Sample size (age, years)	BG	PUT	GP	CN	AMY	HP	TH	PUL	NA	SN	SNc	SNr	DN	RN	FN	STN	Nigrosome-1
Wang et al. (2019)	PD: 35 (71.0 ± 7.4) HC: 37 (70.4 ± 7.8)					-0.103	0.273			-0.262								
Bergsland et al. (2019)	PD: 18 (60.1 ± 6.2) HC: 16 (58.1 ± 8.7)										0.761							
Ahmadi et al. (2020)	PD: 23 (68.8 ± 8.7) HC: 27 (65.7 ± 6.5)											↑						
Thomas et al. (2020)	PD: 100 (64.5 ± 7.7) HC: 37 (66.1 ± 9.4)		↑								0.504							

(D) Summary of QSM changes in the subcortical structures in PSP

References	Sample size (age, years)	PUT	CN	GP	SN	RN	STN	HP	NA	AMY
Ito et al. (2017) ^b	PSP: 14 (68.5) PD: 26 (64)	Anterior ↑		↑						
Sjöström et al. (2017)	PSP: 15 (69.1 ± 6.0) HC: 14 (63.5 ± 5.3)	↑		↑	↑	↑				
Mazzucchi et al. (2019) ^b	PSP: 13 (70.3 ± 5.9) PD: 35 (61.0 ± 8.6)	0.919	0.201	0.349	0.908	1.94	1.523			
Wang et al. (2019)	PSP: 17 (72.5 ± 9.7) HC: 37 (70.4 ± 7.8)							0.506	-0.455	-0.043
Azuma et al. (2019)	PSP: 8 (69.5 ± 7.7) HC: 18 (69.1 ± 7.0)	0.898	0.636	1.459	2.474	1.315				

TABLE 2 | Continued

(E) Summary of QSM changes in the subcortical structures in MSA

References	Sample size (age, years)	PUT	CN	GP	SN	RN	DN	STN	HP	NA	AMY
Ito et al. (2017) ^b	MSA-P: 6 (67.5) PD: 26 (64)	Posterior ↑		~							
Sjöström et al. (2017)	MSA: 11 (68.9 ± 13.1) HC: 14 (63.5 ± 5.3)	↑		↑	↑	↑					
Mazzucchi et al. (2019) ^c	MSA: 12 (65.6 ± 8.1) PD: 35 (61.0 ± 8.6)	1.234	0.134	0.344	0.341	0.842		1.071			
Wang et al. (2019)	MSA-P: 16 (66.4 ± 8.2) HC: 37 (70.4 ± 7.8)								-0.029	-0.492	-0.285
Sugiyama et al. (2019)	MSA-C: 28 (63.8 ± 9.5) HC: 23 (62.9 ± 8.1)	~	↓	↑	↑	~	↑				

(F) Summary of QSM changes in the subcortical structures in ALS and PLS

References	Sample size (age, years)	Motor Cortex	PUT	GP	RN	SN	HP	Subcortical white matter	Corticospinal tract
Schweitzer et al. (2015) ^c	Motor neuron disease: 16 (56.3) (ALS: 12, PLS: 4) HC: 23 (56.6)	1.159							
Costagli et al. (2016)	ALS: 17 (62 ± 11) HC: 13 (55 ± 11)	0.85							
Lee et al. (2017)	ALS: 26 (61.08) HC: 26 (60.88)	0.275						-0.355	
Acosta-Cabrero et al. (2018)	ALS: 28 (61) HC: 39 (61)	0.842	↑	0.777	0.849	0.816	↑		-0.674
Weidman et al. (2019) ^c	ALS/PLS: 43 (60.6 ± 14.9) Non-UMN controls: 15 (58.5 ± 8.4)	0.54							
Welton et al. (2019)	ALS: 21 (54 ± 14) HC: 63 (48 ± 18)	1.134							
Contarino et al. (2020)	ALS: 42 (61.4 ± 9.1) HC: 23 (57.4 ± 7.3)	0.399							

TABLE 2 | Continued

(G) Summary of QSM changes in the subcortical structures in WD

References	Sample size (age, years)	PUT	GP	CN	SN	RN	TH	Pons
Fritzsche et al. (2014)	WD: 11 (44) HC: 10 (41)	1.059	1.565	0.678	1.726	1.232		
Doganay et al. (2018)	Neurologic WD: 11 (15 ± 3.3) HC: 14 (13.2 ± 2.4)	0.811	0.822	0.19	↑		Right: 1.371	↑
Saracoglu et al. (2018)	Asymptomatic WD: 12 (13.7 ± 3.3) HC: 14 (13.2 ± 2.4)	↑(left posterior)	↑	left ↑ right ↓	↑		↑	↑
Dezortova et al. (2019)	Neurologic WD: 28 (47.1 ± 9.5) HC: 26 (44.8 ± 11.7)	1.742	2.282	1.831			2.234	

(H) Summary of QSM changes in the subcortical structures in HD

References	Sample size (age, years)	BG	PUT	GP	CN	AMY	HP	TH	SN	RN
Dominguez et al. (2016)	Premanifest HD: 31 (42.0 ± 8.9) HC: 30 (40.4 ± 12.1)		0.834	0.581	0.626			0.152		
	Symptomatic HD: 32 (52.2 ± 9.2) HC: 30 (40.4 ± 12.1)		1.59	1.05	1.418			−0.115		
Van Bergen et al. (2016b)	Premanifest HD: 15 (42.4 ± 8.7) HC: 16 (43.3 ± 11.7)		1.879	1.068	1.995	−0.479	−0.638	0.371	−0.835	−0.346
Chen et al. (2018)	Early and premanifest HD: 24 (42.5 ± 12.9) HC: 16 (44.8 ± 15.8)		0.86	0.886	0.914		0.244		0.061	0.055

TABLE 2 | Continued

(I) Summary of QSM changes in the brain regions in Ataxic disorders

References	Sample size (age, years)	CN	GP	PUT	SN	DN	RN	TH	Pons	Motor cortex	Motor white matter
Harding et al. (2016)	FRDA: 30 (35.7 ± 12.2) HC: 33 (36.9 ± 13.1)	0.269	0.406	0.277	0.168	1.149	0.912	0			
Ward et al. (2019)	FRDA: 20 (34.3 ± 12.5) HC: 18 (39.7 ± 13.3)					1.619					
Xie et al. (2019)	SCA3: 18 (44.22 ± 5.51) HC: 18 (41.33 ± 10.83)	0	0.661	−0.067	0.897	0.586	0.903		0	0.256	−0.397
Sugiyama et al. (2019)	SCA6: 9 (60.7 ± 9.1) HC: 23 (62.9 ± 8.1)	↓	↑	↓	~	↓	↓				

(J) Summary of QSM changes in the subcortical structures in NBIA

References	Sample size (age, years)	PUT	GP	CN	SN	RN	TH	Internal capsule
Dusek et al. (2014)	PKAN: 2 (21 and 32 years) HC: 13 (39.7 ± 13.6)		↑		↑			↑
Zeng et al. (2019)	PKAN: 6 (age range: 6-25 years) HC: 8 (mean: 22.5 years)		↑		left: 1.508	Left: −1.589	Right: −0.385	
Dusek et al. (2019)	MPAN: 4 (21.0 ± 2.9) HC: 19 (41.2 ± 14.9)	↓	↑	↑	↑		↓	
	C19orf12 mutation carriers: 9 (50.4 ± 9.8) HC: 19 (41.2 ± 14.9)	↑	↑	↑	↓		↑	

^aNo significant difference was reported between any of the groups.

^bComparison with PD not healthy controls.

^cResults demonstrated for comparison of both ALS and PLS vs. controls.

AD, Alzheimer's disease; ALS, amyotrophic lateral sclerosis; aMCI, amnesic mild cognitive impairment; AMY, amygdala; AR, akinetic-rigid; asymp-WD, asymptotic Wilson's disease; BG, basal ganglia; CN, caudate nucleus; DN, dentate nucleus; EOPD, early-onset PD; ES, early stage; FN, fascicula nigrale; FRDA, Friedreich's ataxia; GP, globus pallidus; GPi, internal globus pallidus; GPe, external globus pallidus; HC, healthy control; HD, Huntington's disease; HP, hippocampus; LOPD, late-onset PD; LS, late stage; MCI, mild cognitive impairment; MPAN, mitochondrial membrane protein-associated neurodegeneration; MSA, multiple system atrophy; MSA-P, Parkinsonian type MSA; MSA-C, cerebellar type MSA; NA, nucleus accumbens; NBIA, neurodegeneration with brain iron accumulation; neuro-WD, neurologic Wilson's disease; NMS, non-motor symptoms; PD, Parkinson's disease; PKAN, pantothenate kinase-associated neurodegeneration; PLS, primary lateral sclerosis; PSP, progressive supranuclear palsy; PUL, pulvinar nucleus; PUT, putamen; RN, red nucleus; SCA, spinocerebellar ataxia; SN, substantia nigra; SNc, substantia nigra pars compacta; SNr, substantia nigra pars reticulata; STN, subthalamic nucleus; TD, tremor dominant; TH, thalamus; UMN, upper motor neuron disease; UMN, upper motor neuron; WD, Wilson's disease; VaD, vascular dementia.

Green: No significant difference.

Gray: Not studied.

Red: Increased magnetic susceptibility.

Blue: Decreased magnetic susceptibility.

Red: significantly higher susceptibility in the patient group, Blue: significantly lower susceptibility in the patient group, Green: non-significant difference. Gray: ROI not studied. Numbers in each cell represent the calculated effect size (Hedge's g) based on the reported mean and standard deviation. Arrows indicate the direction of changes in the patient group compared with controls and ~ indicates equal means among two groups where calculation of effect size was not possible/data not provided. Empty cells indicate that the data required to determine the direction of inter-group differences was not provided.

The comparison of magnetic susceptibility in the subcortical structures among people with AD and healthy individuals revealed inconsistent findings. The most consistent evidence for increased susceptibility was observed in the amygdala, caudate nucleus (CN), and putamen. All three studies that investigated the amygdala reported increased susceptibility in both mild (Acosta-Cabronero et al., 2013) and moderate (Kim et al., 2017) stages of AD (Kan et al., 2020). In people with amnesic MCI (aMCI), the amygdala did not show any significant difference compared to healthy individuals (Van Bergen et al., 2016b). In the CN, six out of seven studies reported higher susceptibility in AD. This increase was detected in both mild and moderate stages of AD (Acosta-Cabronero et al., 2013; Moon et al., 2016; Kim et al., 2017; Du L. et al., 2018; Meineke et al., 2018; Kan et al., 2020) but not in MCI (Hwang et al., 2016; Van Bergen et al., 2016b; Ayton et al., 2017; Meineke et al., 2018). Only a few studies reported the mean susceptibility values in the investigated ROIs to enable the estimation of the effect size of differences between groups (**Table 2A**).

Among seven studies that investigated the putamen, four reported higher susceptibility in both mild and moderate AD (Acosta-Cabronero et al., 2013; Moon et al., 2016; Du L. et al., 2018; Meineke et al., 2018), while in two studies on mild to moderate and moderate AD stages, no changes were found (Hwang et al., 2016; Kim et al., 2017). One study did not provide a description of disease stage in the study population (Ayton et al., 2017). In studies of patients with MCI, none detected any change in susceptibility in the putamen (Hwang et al., 2016; Van Bergen et al., 2016b; Ayton et al., 2017; Kim et al., 2017; Meineke et al., 2018).

Among other studied regions, limited evidence for increased susceptibility was provided in moderate AD in the hippocampus (two out of six studies) (Kim et al., 2017; Kan et al., 2020), in mild-moderate AD in the globus pallidus (GP) (one out of six studies) (Tiepol et al., 2018) and in moderate AD in the thalamus (one out of four studies) (Kim et al., 2017) (**Table 2A**).

Cortical gray matter was examined in five studies. Patients with early-stage AD showed increased susceptibility in widespread regions over the temporal, parietal and occipital cortices (Acosta-Cabronero et al., 2013). Further, in studies of moderate AD, clusters of increased susceptibility were distributed across the cortex including the frontal, parietal, temporal, limbic, and insular lobes (**Supplementary Table 1A**) (Kim et al., 2017). Other studies, however, did not report any difference of mean susceptibility in the cortex between patients with mild or moderate AD and healthy individuals (Hwang et al., 2016; Ayton et al., 2017; Tiepol et al., 2018). Among four studies that investigated QSM in the cortex in individuals with MCI; one reported increased susceptibility in the precuneus, allocortex, and anterior and posterior cingulate gyrus (Kim et al., 2017), while the others did not detect any difference between the MCI and healthy groups (Hwang et al., 2016; Van Bergen et al., 2016b; Ayton et al., 2017) (**Table 2B**).

Correlation of QSM Findings in AD and MCI With Clinical Features and Other Pathologic Biomarkers

Few studies examined the relationship between QSM changes and severity of cognitive deficits in AD. An association of

magnetic susceptibility with mini-mental state examination (MMSE) and Montreal cognitive assessment (MoCA) in patients with AD was reported in the left CN (Du L. et al., 2018) and GP (Tiepol et al., 2018). However, such correlations were not replicated in the study by Moon et al. (2016). In a longitudinal study combining A β positron emission tomography (PET) and QSM in AD, MCI, and cognitively normal individuals, Ayton et al. (2017) followed the study population by serial neuropsychiatric assessments and neuroimaging scans over 6 years. Interestingly, in both A β -positive and -negative subjects, magnetic susceptibility within certain ROIs was associated with deficits in specific cognitive domains. In the A β -negative group, higher QSM in the frontal lobe and CN was associated with subtle deterioration in language function. In the A β -positive individuals (MCI and AD), magnetic susceptibility of the hippocampus correlated with decline in episodic memory, attention and executive function in serial assessments, while susceptibility values in the temporal and frontal lobes predicted decline in language functions.

In a limited number of studies, the correlation of A β deposition and increased magnetic susceptibility in QSM was investigated in AD. Ayton et al. (2017) reported a significant correlation of A β -PET signal and QSM in the frontal, parietal, and occipital cortices but not in the parietal lobe, hippocampus, CN, or cingulate gyrus. On the other hand, in the study by Tiepol et al. (2018), where authors examined the correlation of magnetic susceptibility and A β -PET only in the GP, no such correlation was detected. In a recent study, ultra-high field (9.4 and 14.1T) QSM at a resolution of 37 μ m isotropic voxels in the frontal cortex of a post-mortem brain from a patient with AD showed that the pattern of increased susceptibility in the cortical layers strongly matched the A β depositions in histochemical staining (Tuzzi et al., 2020). In individuals with MCI, increased susceptibility significantly correlated with A β deposition in the cortical regions where altered functional coupling with the medial prefrontal cortex was shown in fMRI (Van Bergen et al., 2016b), while in healthy individuals, the significant correlation of magnetic susceptibility and A β PET signal was detected in clusters spread across the cortex and subcortical gray matter, with the strongest correlations in the GP, CN, and putamen (Van Bergen et al., 2018).

The association between APOE-e4 gene and QSM was investigated in two studies. Van Bergen et al. (2016b) studied a group of MCI subjects ($n = 15$) in comparison with healthy controls ($n = 22$). Forty percent of the MCI group and thirty-one percent of the control group were APOE-e4 carriers. While no differences of magnetic susceptibility in any of the ROIs existed between the MCI and healthy groups, in the MCI group, APOE-e4 carriers had significantly higher susceptibility in the CN as well as frontal, parietal, occipital, and temporal cortices than APOE-e4 negative subjects. In another study, Kagerer et al. (2020) reported no significant variation of susceptibility between APOE-e4 positive and APOE-e4 negative cognitively healthy adults. However, increased magnetic susceptibility and positive APOE-e4 gene status, were synergistically associated with increased default mode network activity. This relationship was most pronounced in the posterior cingulate cortex, precuneus, and lateral parietal cortex. In this study, the authors did not

report any correlation with the cognitive control network, which would be relevant to the disorders of cognition.

Diagnostic Accuracy of QSM in Differentiation of Patients With AD From Healthy Individuals

A number of studies used the Receiver Operating Characteristic (ROC)-curve analysis to evaluate the diagnostic accuracy of QSM in differentiation of people with AD and MCI from healthy subjects. In AD vs. healthy controls, high sensitivity, and specificity was observed for magnetic susceptibility of the GP (90 and 100%, respectively) (Tiepol et al., 2018), while the CN showed lower accuracy (sensitivity and specificity = 61.67%) (Du L. et al., 2018).

Kim et al. (2017) examined both AD and MCI in comparison with healthy controls. The area under curve (AUC) was 0.850, 0.831, and 0.803 for susceptibility of the precuneus, amygdala, and hippocampus, respectively, showing good accuracy in differentiation of AD from healthy groups. Furthermore, in differentiation of people with MCI from healthy individuals, susceptibility in the hippocampus, thalamus, precuneus, and various cortical areas showed moderate accuracy (AUC: 0.692–0.759). In the comparison between MCI and healthy controls by Hwang et al. (2016), the mean susceptibility of the white matter yielded a sensitivity of 55.56% and specificity of 94.44%.

Parkinsonian Diseases

Forty-three studies using QSM in the investigation of brain iron in PD and other parkinsonian diseases, such as MSA, PSP, and corticobasal degeneration were included in this review.

Magnetic Susceptibility Changes in Parkinsonian Diseases in Comparison With Healthy Individuals

Thirty-seven studies reported the measurement and comparison of magnetic susceptibility in the subcortical gray matter structures among the PD and control groups. Of this, 33 investigated the SN or its subregions [SNc and substantia nigra pars reticulata (SNr)], with 30 (90.9%) reporting significantly increased magnetic susceptibility in PD (Table 2C). Investigated in one study, magnetic susceptibility in the SN was also increased in idiopathic REM sleep behavior disorder which is considered as a prodromal phase for synucleinopathies with high rates of conversion to PD (Sun et al., 2019). The next most investigated region was the red nucleus (RN) (22 studies), where seven studies (31.8%) reported increased susceptibility in PD (Table 2C). Figures 2, 3 demonstrate the effect sizes for susceptibility differences in the SN and RN respectively, in patients with PD compared to healthy individuals.

The alterations in susceptibility were less consistent in the basal ganglia in PD patients. Only four of 22 studies (18.1%) of the putamen showed a significant increase in susceptibility while one study reported significantly decreased susceptibility in the putamen (He et al., 2015). Six of 21 studies (28.6%) investigating the GP reported increased susceptibility and only one of 18 studies (5.5%) reported significantly higher susceptibility in the CN. It is worth mentioning that, while not statistically significant, a trend toward lower susceptibility in the basal ganglia was

reported in a noticeable proportion of the studies (Putamen: 8 out of 22, GP: 8 out of 21, and CN: 9 out of 18) (Table 2C).

In the hippocampus, significantly unilateral (Li et al., 2018) or bilateral (Acosta-Cabronero et al., 2017) higher susceptibility was reported in two out of four studies. In the thalamus, and cerebellar dentate nucleus (DN), most of the studies reported no significant changes in regional magnetic susceptibility. These findings are summarized in Table 2C and Supplementary Table 1B.

In one of the first studies to investigate QSM in cortical gray matter in PD, Acosta-Cabronero et al. (2017) reported increased susceptibility in widespread regions of the cortex including the lateral occipital, posterior parietal, rostral middle prefrontal, and middle temporal cortex. In a further update, the same group reported increased susceptibility in prefrontal and right insular cortices in PD (Thomas et al., 2020). In the study by Uchida et al. (2019), higher susceptibility was observed in the cuneus, precuneus, fusiform gyrus, insula and cerebellum in PD patients. None of these studies found any brain region with lower susceptibility in patients with PD. On the other hand, the mean susceptibility value of the whole cortex did not show any difference between patients with PD and healthy controls in the study by Chen et al. (2019). Surprisingly, Lewy-body dementia, which is characterized by cortical involvement by the same pathology as PD (α -synuclein), has not been examined in QSM studies.

In one study investigating white matter QSM in PD, Guan et al. (2019a) reported alterations in widespread areas in the frontal, temporal, and parietal lobes (details in Supplementary Table 1B). In the inferior longitudinal fasciculus, there were increases in both magnetic susceptibility and radial diffusivity measured by diffusion tensor imaging (DTI).

In six studies, QSM was compared between controls and PD or other parkinsonian syndromes, such as PSP and MSA (Tables 2D,E). Compared to healthy controls, susceptibility was increased in the RN, SN, and GP in PSP (Sjöström et al., 2017; Azuma et al., 2019), in the RN, putamen, and SN, in MSA (Sjöström et al., 2017), and in the DN and SN in cerebellar type of MSA (MSA-C) (Sugiyama et al., 2019). Compared to PD, magnetic susceptibility was higher in the SN, subthalamic nucleus (STN), putamen, and RN in both patients with MSA and PSP, while in PSP, higher susceptibility was further detected in the GP (Ito et al., 2017; Sjöström et al., 2017; Azuma et al., 2019; Mazzucchi et al., 2019). In comparison with PD, patients with parkinsonism dominant MSA (MSA-P) showed higher susceptibility in the posterior putamen (Ito et al., 2017), lateral SN, STN, and RN (Mazzucchi et al., 2019) (Supplementary Table 1B).

Studies comparing PSP and MSA reported higher susceptibility of the GP, RN, and the medial part of the SN in PSP (Sjöström et al., 2017; Mazzucchi et al., 2019). The only study that compared limbic structures among PD, MSA, and PSP using QSM, reported no susceptibility differences in the hippocampus, amygdala, and nucleus accumbens (Wang et al., 2019). Nevertheless, it should be noted that in some of the studies on MSA, PSP, and PD, study groups were not matched based on age and disease characteristics. In the study by Mazzucchi

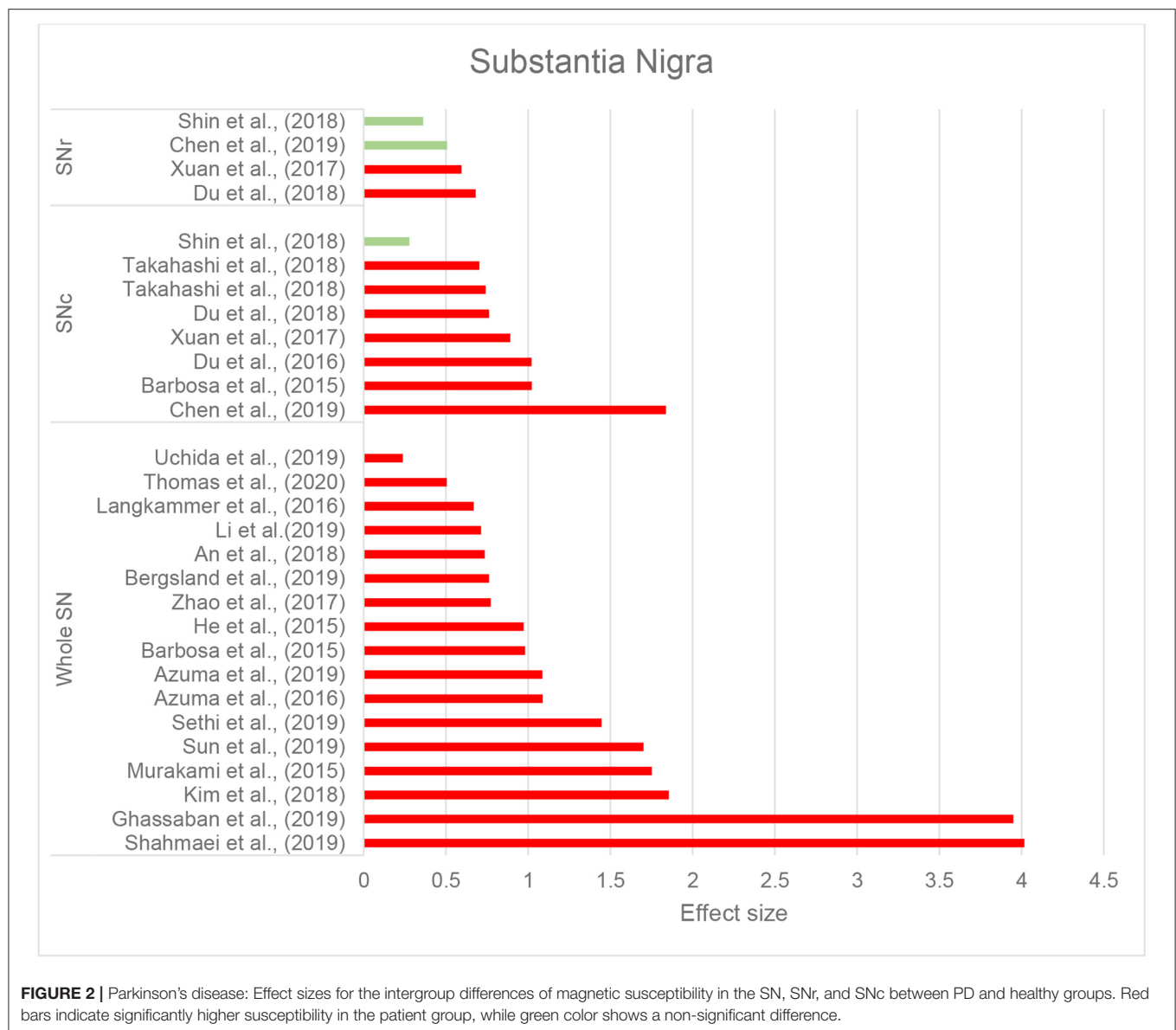


FIGURE 2 | Parkinson's disease: Effect sizes for the intergroup differences of magnetic susceptibility in the SN, SNr, and SNc between PD and healthy groups. Red bars indicate significantly higher susceptibility in the patient group, while green color shows a non-significant difference.

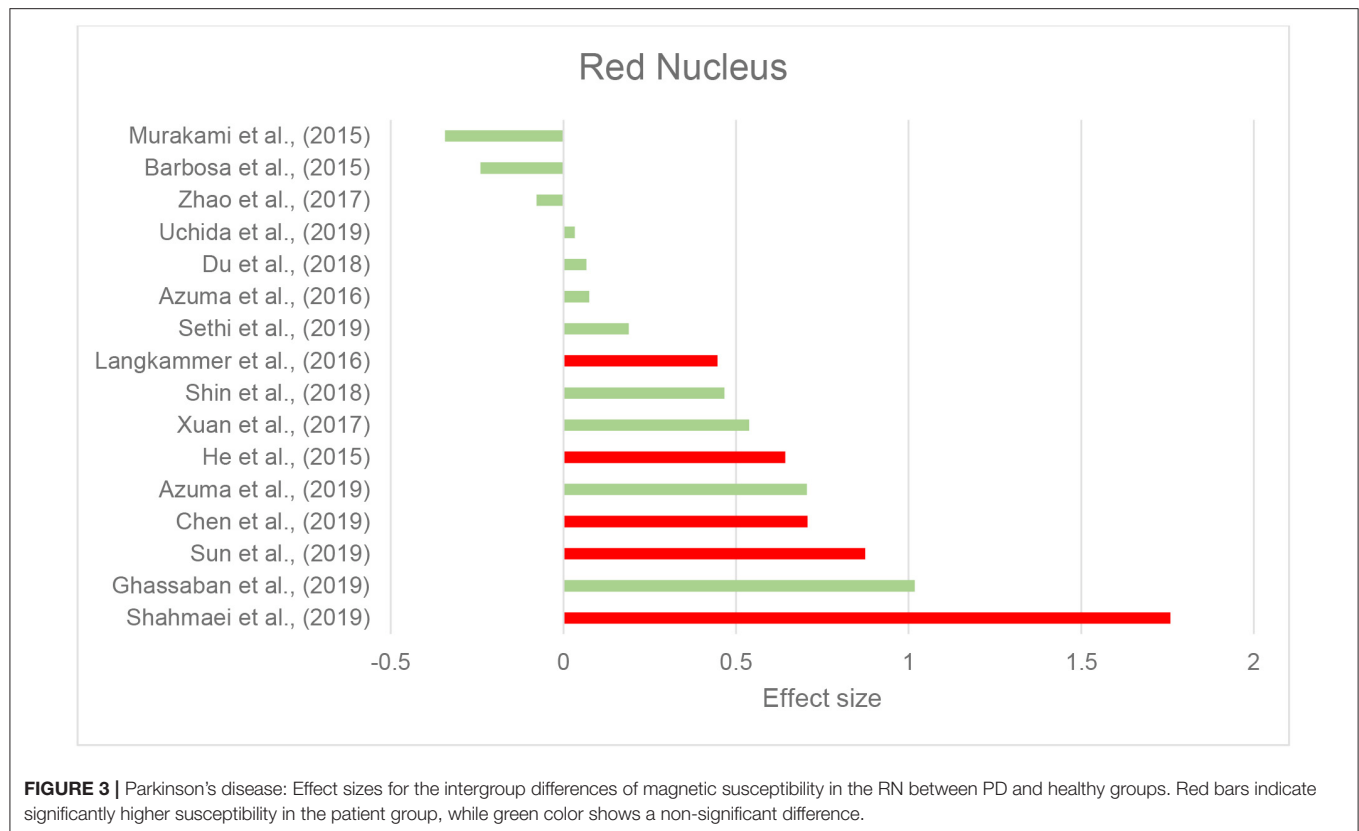
et al. (2019), patients with PSP were older than the MSA and PD groups. In the study by Ito et al. (2017) patients with PD were at lower disease stages compared to the other groups. Also in the studies by Mazzucchi et al. (2019) and Wang et al. (2019), the PD group had lower clinical severity scores compared to the other groups.

Correlation of QSM Findings in PD With Clinical Features and Other Pathologic Biomarkers

In addition to the comparison of QSM in various brain regions among PD and healthy individuals, studies have also evaluated its correlation with duration and severity of symptoms, disease stage, and clinical features of PD. Magnetic susceptibility of the SN (He et al., 2015) and SNc (Du et al., 2016) were shown to positively correlate with disease duration, however, such a correlation has not been agreed upon by all studies

(Ghassaban et al., 2019). Additionally, this correlation was not found in any of the other subcortical structures including the GP, putamen, CN, thalamus, RN, and cerebellar DN (Barbosa et al., 2015; Langkammer et al., 2016; Shin et al., 2018; Sun et al., 2019).

In the PD studies included, disease progression stage was generally assessed by Hoehn and Yahr (H&Y) scale and clinical severity of symptoms were evaluated by Unified Parkinson's Disease Rating Scale (UPDRS). H&Y staging evaluates the overall clinical progression of motor impairments in PD on a scale of 1–5, with a score of 1 indicating limited unilateral involvement and 5 indicating a wheelchair-bound or bedridden state (Goetz et al., 2004). UPDRS is a PD severity assessment scale, comprised of three parts: UPDRS-I evaluates mental status and cognition; UPDRS-II assesses the impairment of daily activities; and UPDRS-III evaluates the severity of motor



dysfunction (Movement Disorder Society Task Force on Rating Scales for Parkinson's Disease, 2003).

The majority of evidence indicates a significant association of susceptibility in the SN and its subfields with H&Y illness stage (Langkammer et al., 2016; Guan et al., 2017a,b; Xuan et al., 2017; An et al., 2018; Chen et al., 2019; Shahmaei et al., 2019). A similar association was found in the RN and GP in some (Guan et al., 2017a; Chen et al., 2019; Shahmaei et al., 2019), but not all studies (Shin et al., 2018; Sun et al., 2019).

The correlation of UPDRS sub-scores have been evaluated by a number of studies, showing inconsistent findings. While some studies suggested a correlation of UPDRS scores with susceptibility in subcortical structures, such as CN, GP, putamen, and SN (He et al., 2015; Du et al., 2016; Langkammer et al., 2016; Guan et al., 2017b; Xuan et al., 2017; An et al., 2018; Du G. et al., 2018; Mazzucchi et al., 2019; Uchida et al., 2019; Thomas et al., 2020), others did not report such findings (Du et al., 2016; Acosta-Cabronero et al., 2017; Zhao et al., 2017; Shin et al., 2018; Bergsland et al., 2019; Ghassaban et al., 2019; Sun et al., 2019) (**Supplementary Table 1B**).

Tremor Dominant vs. Akinetic-Rigid PD

Tremor-dominant and akinetic-rigid clinical presentations of PD were found to have distinct QSM patterns in specific regions of the brain. While in the SN, magnetic susceptibility did not differ among tremor-dominant and akinetic-rigid groups, the cerebellar DN and RN showed higher susceptibility in tremor-dominant PD, which positively correlated with tremor

severity (Guan et al., 2017b; He et al., 2017; Mazzucchi et al., 2019). Additionally, the patients with akinetic-rigid PD showed higher susceptibility in the CN compared to those with tremor-dominant disease (Guan et al., 2017b).

Cognitive Impairment in PD

In patients with PD, cognitive impairment was significantly correlated with higher susceptibility in the hippocampus, rostral CN, thalamus, amygdala, and right putamen (Li et al., 2018; Uchida et al., 2019; Thomas et al., 2020) but not in the SN and its subregions, midbrain, and DN (He et al., 2017; Du G. et al., 2018; Ahmadi et al., 2020). Cortical regions where increased susceptibility correlated with lower MoCA scores include the basal forebrain, caudal regions of ventromedial prefrontal cortex, right insular cortex (Thomas et al., 2020), cuneus, and fusiform gyrus (Uchida et al., 2019).

Further, compared to patients with PD who had normal cognition, those with MCI showed higher susceptibility in the head of CN, entorhinal cortex, parahippocampal gyrus, amygdala, and precuneus (Uchida et al., 2019). In another study, Li et al. (2018) reported higher susceptibility in the left hippocampus in patients with PD with dementia, compared to cognitively normal PD patients.

Olfaction in PD

Hyposmia is a common non-motor symptom in PD which occurs in up to 90% of patients (Pantelis and Brewer, 2006; Xiao et al., 2014). Two studies compared QSM among PD patients with

and without olfactory deficits. Uchida et al. (2019) reported that higher susceptibility in the amygdala, cuneus and fusiform gyrus was associated with olfactory deficits. However, in the study by Hwang et al. (2019), differences were only observed in the thalamus, with significantly higher susceptibility in the left thalamus and lower susceptibility in the right thalamus (showing a more heterogeneous distribution of susceptibility) in patients with hyposmia.

Diagnostic Accuracy of QSM in Parkinsonian Diseases

In nine studies, ROC analysis was used to evaluate the accuracy of QSM in differentiating parkinsonian disease groups. QSM in the SN was able to differentiate patients with PD from healthy individuals with an accuracy of 68–88.7% (Azuma et al., 2016; Zhao et al., 2017; Takahashi et al., 2018a,b; Li et al., 2019), with the highest accuracy in the posterior part of SN (Azuma et al., 2016). Magnetic susceptibility in the DN could differentiate patients with MSA-C from healthy individuals with an accuracy of 83.4% (Sugiyama et al., 2019), while magnetic susceptibility in the posterior putamen (AUC = 0.91) (Ito et al., 2017), RN (AUC = 0.86) (Sjöström et al., 2017), and STN (AUC = 0.808) differentiated MSA from PD (Mazzucchi et al., 2019). The highest accuracy for differentiation of PSP from PD has been reported for susceptibility in the GP (AUC = 0.903) (Azuma et al., 2019) and RN (AUC = 0.97) (Sjöström et al., 2017), while the accuracy of QSM in differentiating between MSA and PSP, was 0.826 in the RN, 0.785 in the medial part of the SN (Mazzucchi et al., 2019), and 0.73 in the GP (Sjöström et al., 2017).

Amyotrophic Lateral Sclerosis (ALS) and Primary Lateral Sclerosis (PLS)

Magnetic Susceptibility Changes in ALS and PLS in Comparison With Healthy Individuals

We identified eight records investigating brain iron in patients with ALS using QSM, in which the motor cortex was the primary

focus. The majority of studies reported higher susceptibility within the motor cortex compared to the control groups (Acosta-Cabronero et al., 2018; Welton et al., 2019) (**Figure 4** and **Table 2F**). Costagli et al. (2016) reported focally increased susceptibility in the deep layers of the hand and foot motor cortices corresponding to the most affected limb, compared to healthy controls. Such increase was primarily observed in ALS patients who had evident T2* hypointensities in the deep cortical layers and was not found in those without the T2* hypointensities. In the study by Contarino et al. (2020), the entire motor cortex including the precentral gyrus and paracentral lobule was examined as one ROI. The results revealed a close-to-significant trend of higher mean susceptibility, and a significantly higher skewness and standard deviation of susceptibility values across the motor cortex in ALS patients, which indicates increased heterogeneity of susceptibility distribution. One study did not observe any susceptibility difference in the motor cortex of patients with ALS compared with controls, but reported a significantly larger susceptibility variation from the motor cortex to the adjacent subcortical white matter in patients with ALS compared to healthy individuals (Lee et al., 2017) (**Supplementary Table 1C**).

Comparison of individuals with ALS and PLS with healthy controls revealed higher maximum (Weidman et al., 2019) and mean (Schweitzer et al., 2015) susceptibility in the motor cortex in the patients with ALS or PLS but no difference existed between patients with ALS and those with PLS (Schweitzer et al., 2015). In the only study to investigate the subcortical structures and whole brain susceptibility changes in ALS, Acosta-Cabronero et al. (2018) reported a markedly increased susceptibility in the motor cortex, pars opercularis of the prefrontal cortex, premotor medial areas, and the primary somatosensory fields, SN, RN, GP, putamen, and hippocampus in patients with ALS. Tissue magnetic susceptibility was significantly lower in the corticospinal tract (CST), which positively correlated with fractional anisotropy and negatively correlated with mean diffusivity and radial diffusivity of the tract measured by DTI.

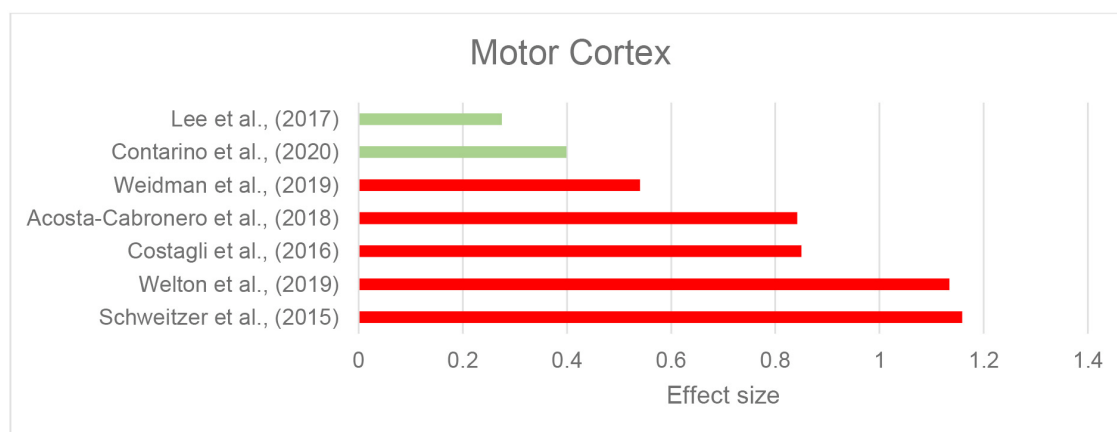


FIGURE 4 | Amyotrophic lateral sclerosis: Effect sizes for the intergroup differences of magnetic susceptibility in the motor cortex between ALS and control groups. Red bars indicate significantly higher susceptibility in the patient group, while green color shows a non-significant difference.

Correlation of QSM Findings in ALS With Clinical Features and Other Biomarkers

The correlation of QSM findings of altered susceptibility with disease severity and duration was investigated in four studies, but the results were inconsistent. Two studies reported that susceptibility was not associated with disease severity (Acosta-Cabronero et al., 2018; Welton et al., 2019) or duration (Welton et al., 2019; Contarino et al., 2020). In contrast, two studies reported that disease severity was associated with the median susceptibility of the motor cortex (Contarino et al., 2020) and mean and maximum susceptibility of the left motor cortex (Lee et al., 2017).

In a recent study, the orofacial region of the primary motor cortex was investigated in relation to bulbar onset of ALS presentation. Magnetic susceptibility was significantly higher in those with marked T2* hypointensity in the deep layer of orofacial region of the motor cortex, which was predominantly observed in patients with bulbar-onset disease (Donatelli et al., 2019).

Diagnostic Accuracy of QSM in Differentiating Patients With ALS From Healthy Individuals

The ROC curve analysis of QSM in the motor cortex showed an AUC of 0.632 for the maximum (Lee et al., 2017) and 0.70 for the mean susceptibility of the motor cortex relative to the adjacent white matter (sensitivity: 74%, specificity: 54.8%) for the differentiation of ALS from controls. In the study by Schweitzer et al. (2015), susceptibility of the motor cortex showed high accuracy for the differentiation of patients with ALS and PLS from healthy controls (AUC: 0.88, sensitivity: 87.5%, specificity: 87%).

Wilson's Disease

There were four articles included in this review that described the use of QSM in WD, two studies in pediatric patients with WD and two studies on adult patients with WD, with comparisons to age-matched healthy individuals (Table 2G and Supplementary Table 1D).

Doganay et al. (2018) found increased susceptibility in the putamen, CN, SN, thalamus, and pons in 11 pediatric patients (mean age = 15 years) with neurological-WD compared to healthy controls, while T1 and T2 images did not show any differences among the groups. The same research group investigated brain QSM changes in 12 asymptomatic children (mean age 13.3 years) with a positive WD mutation. QSM evaluation of the same ROIs as the previous study revealed a similar pattern of higher susceptibility except for GP and SN (Saracoglu et al., 2018).

In the first QSM study in adult WD, Fritzsche et al. (2014) used a 7T MRI scanner to investigate brain changes in 11 adult patients with WD (six with neurologic WD, and five with hepatic WD) with a mean age of 44, and 10 age-matched healthy controls. The results showed a differential pattern of increased susceptibility in the subcortical structures among patients with neurologic and hepatic WD compared to controls. In both groups of patients with WD, the SN and right GP showed higher susceptibility. Susceptibility was further found to be increased in the left GP and putamen in neurologic WD group, and in the RN in patients with hepatic WD (Fritzsche et al., 2014).

Dezortova et al. (2019) used a 3T MRI scanner to study a larger sample of participants with WD (28 with neurologic-WD and 10 with mild hepatic-WD) and comparisons were made with 26 healthy controls. In addition to increased susceptibility in the putamen and GP in neurologic WD, similar to the findings of Fritzsche et al. (2014), the CN and thalamus also showed this increase. Of note, this pattern was only observed in the neurologic WD group, while patients with hepatic WD showed no significant differences in any of these regions compared to healthy controls (Dezortova et al., 2019). **Figure 5** demonstrates the effect sizes for increased magnetic susceptibility in the basal ganglia in patients with WD compared to healthy individuals.

Correlation of clinical assessments with QSM and the accuracy of QSM in the differentiation of patients with WD from healthy individuals have not been examined in these studies.

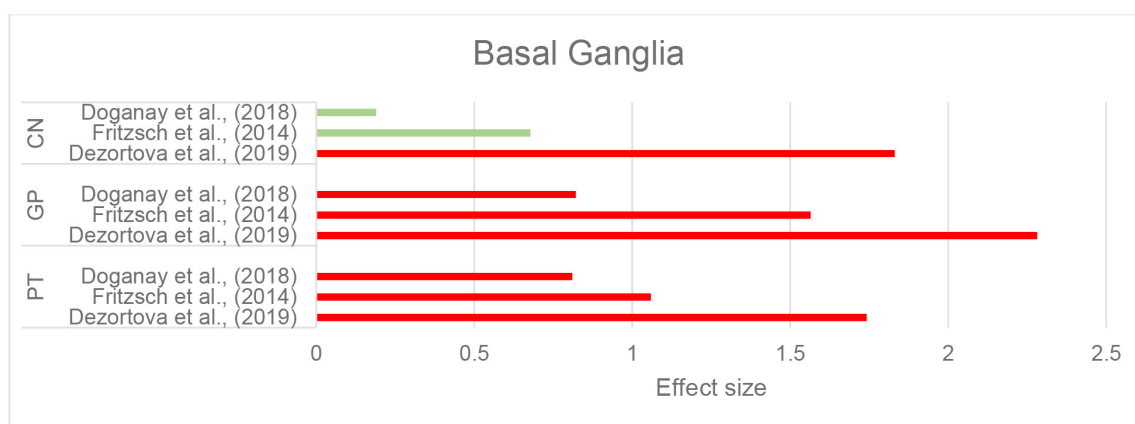


FIGURE 5 | Wilson's disease: Effect sizes for the intergroup differences of magnetic susceptibility in the basal ganglia between WD and healthy groups. Red bars indicate significantly higher susceptibility in the patient group, while green color shows a non-significant difference.

Huntington's Disease

Magnetic Susceptibility Changes in HD in Comparison With Healthy Individuals

Three studies that investigated brain iron distribution in HD using QSM were included in this review. These studies consistently reported higher susceptibility in the CN, GP, and putamen in both asymptomatic carriers of the HD gene mutation and in patients with HD compared to healthy controls (Domínguez et al., 2016; Van Bergen et al., 2016a; Chen et al., 2018) (**Supplementary Table 1E**, **Figure 6**, and **Table 2H**). Increased susceptibility within these regions also significantly correlated with their atrophy (Van Bergen et al., 2016a; Chen et al., 2018).

In the thalamus and RN, QSM did not show any alterations in HD compared to healthy controls (Domínguez et al., 2016; Van Bergen et al., 2016a; Chen et al., 2018). In one study investigating preclinical carriers of HD genotype, lower susceptibility in the SN and hippocampus was reported compared to healthy individuals (Van Bergen et al., 2016a), however, such a finding was not observed in another study (Chen et al., 2018).

Correlation of QSM Findings in HD With Clinical Features and Other Pathologic Biomarkers

Higher susceptibility values in the CN, putamen, and GP significantly correlated with composite scales of age and genetic burden of the disease (CAG-age product scaled score, see **Supplementary Table 1E**) (Domínguez et al., 2016; Van Bergen et al., 2016a; Chen et al., 2018). The CAG-age product scale score is calculated based on age and length of CAG trinucleotide repeats, and estimates the probability of disease onset within 5 years (Zhang et al., 2011). This increase in susceptibility, however, was not correlated with clinical motor symptoms and function, as measured by the Unified Huntington Disease Rating Scale or cognitive assessments by MoCA in any of the studies (Domínguez et al., 2016; Van Bergen et al., 2016a; Chen et al., 2018).

Methodological Diversity of QSM Processing in Reviewed Studies

Among the studies included in this review, we observed a variety of MRI acquisition sequences, post-processing methods and reference regions used to produce QSM images. **Table 3** provides an overview of this methodological diversity. A detailed description of MRI acquisition and QSM processing methods implemented in each study is brought in the **Supplementary Table 2**.

Scanner Field Strength

QSM studies were most frequently conducted using scanners with the magnetic field strength of 3T (66/80 studies) (**Table 3**), while a smaller number of studies were carried out using 1.5T, 7T, or 9.4T scanners (2, 9, and 1 studies, respectively). Sixty-seven studies employed multi-channel receiver coils.

Data Acquisition Parameters

All studies performed QSM on MRI scans from single head orientation, with the majority of studies using a gradient echo sequence with or without flow compensation. Fourteen studies reported single-echo acquisition, and fifty-four studies acquired multi-echo data with inter-echo spacing varying between 2 and 12 ms. The first echo times ranged between 2 and 53 ms (**Supplementary Table 2**).

The spatial resolution is an important factor that affects the accuracy of the magnetic susceptibility estimates. Images with smaller voxels have higher spatial resolution. Sixteen studies had a voxel-size equal to or smaller than $0.5 \times 0.5 \times 2 \text{ mm}^3$, which is the recommended voxel-size to ensure reasonably accurate magnetic susceptibility estimates (Haacke et al., 2015). Sixty-nine studies had voxel-sizes $>0.5 \times 0.5 \times 2 \text{ mm}^3$ (**Table 4**).

Phase Unwrapping Methods

Laplacian-based phase unwrapping algorithms were employed by thirty studies to recover true phase of the MRI signal from the measured phase, which is wrapped between $-\pi$ and π (**Table 3**).

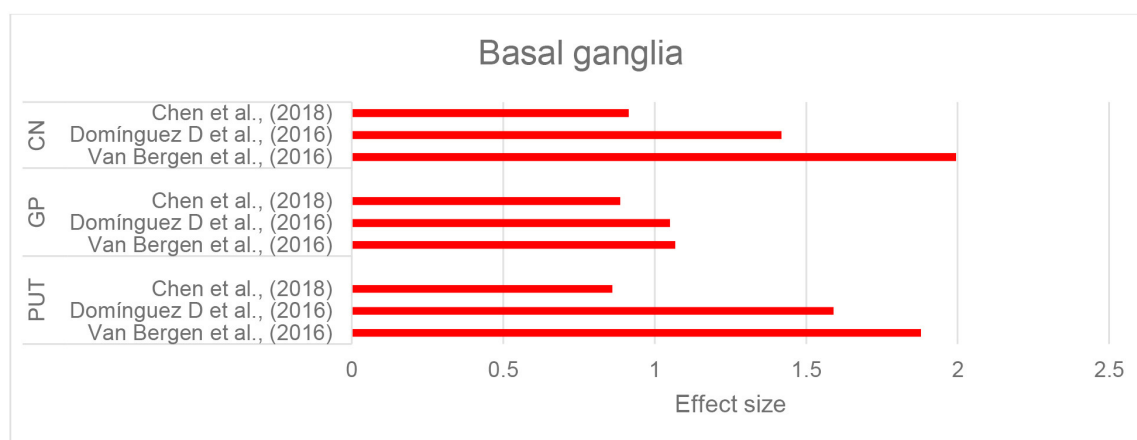


FIGURE 6 | Huntington's disease: Effect sizes for the intergroup differences of magnetic susceptibility in the basal ganglia between HD and control groups. Red bars indicate significantly higher susceptibility in the patient group.

TABLE 3 | Summary of the methods used for QSM processing and referencing in the reviewed studies.

Scanner strength	Field strength	1.5T		1.5T/3T		3T		7T		9.4T						
	Number of studies	2		2		66		9		1						
Phase unwrapping	Method	Laplacian-based		Best path	Magnitude-guided spatial unwrapping		FSL prelude		Quality-guided		One-dimensional temporal unwrapping		Not reported			
	Number of studies	30		1	3		2		3		1		40			
Background field removal	Method	SHARP	RE-SHARP	V-SHARP	TSVD-SHARP	HARPERELLA			PDF			Not reported				
	Number of studies	10	3	26	1	1			9			27				
Dipole inversion	Method	LSQR	iLSQR	SFCR	HEIDI	MEDI	SDI	MUDICK	STAR-QSM	TKD	Other	JEDI	1	MSDI	2	Not reported
	Number of studies	4	19	1	3	13	2	1	4	2	4	24				
Reference regions	Tissue type	CSF		White matter		Whole brain		Calcarine sulcus		Not referenced			Not reported			
	Number of studies	18		19		7		1		2			33			

CSF, cerebrospinal fluid; HARPERELLA, harmonic phase removal with the Laplacian operator; HEIDI, homogeneity enabled incremental dipole inversion; iLSQR, iterative LSQR; JEDI, joint background-field removal and segmentation-enhanced dipole inversion; LSQR, sparse linear equation and least-squares; MEDI, morphology enabled dipole inversion; MSDI, multi-scale dipole inversion; MUDICK, multiple dipole-inversion combination with *k*-space segmentation; PDF, projection onto dipole fields; RE-SHARP, regularization-enabled SHARP; SDI, superfast dipole inversion; SFCR, structural feature-based collaborative reconstruction algorithm; SHARP, Sophisticated Harmonic Artifact Reduction for Phase; STAR-QSM, streaking artifact reduction for QSM; TKD, truncated *k*-space division; TSVD-SHARP, truncated singular value decomposition SHARP; V-SHARP, variable-radius SHARP.

The Laplacian-based phase unwrapping techniques utilize spatial information in the Fourier space to correct for arbitrary 2π jumps present in the measured phase images (Schofield and Zhu, 2003; Deistung et al., 2017). Other phase unwrapping methods used in these studies include best path algorithm, FSL Prelude, magnitude- and quality-guided spatial unwrapping and temporal unwrapping. A detailed description of these methods can be found elsewhere (Schweser et al., 2017; Fortier and Levesque, 2018). Out of eighty studies included in this review, forty studies did not report the phase unwrapping method used to obtain QSM estimates.

Background Field Removal Algorithms

In order to identify local contributions to the magnetic susceptibility, 40 studies used a variant of Sophisticated Harmonic Artifact Reduction for Phase data (SHARP)-based background field removal techniques (Table 3). Such techniques eliminate the harmonic background magnetic field component using its spherical mean value property and reconstruct the non-harmonic local field component using a deconvolution operation on the filtered phase images (Schweser et al., 2011). SHARP-based methods are susceptible to cortical surface artifact, leading to limited accuracy in determining cortical magnetic susceptibility distribution. Advanced SHARP-based techniques use regularization (RE-SHARP) and variable high-pass filter sizes and regularization parameters (V-SHARP) to reduce surface and streaking artifacts in magnetic susceptibility maps (Schweser et al., 2017).

Nine studies used the projection onto dipole field (PDF) method, that uses the orthogonality between magnetic fields produced by dipoles outside and inside an ROI to eliminate background field susceptibility contributions (Liu et al., 2011).

Dipole Inversion

Twenty-eight studies employed a sparse linear equation and least-squares (LSQR)-based method to perform dipole inversion for the purpose of estimating magnetic susceptibility from local field shifts. The iterative LSQR (iLSQR) was the most frequently employed dipole inversion method. Thirteen studies used morphology enabled dipole inversion (MEDI) to suppress artifacts using edge information from the magnitude images (Liu et al., 2011). Twenty-three studies did not report the dipole inversion method used for estimating magnetic susceptibility maps (Table 3).

Normalization of Magnetic Susceptibility Values

Magnetic susceptibility values were normalized using mean susceptibility values from ventricular CSF (18 studies), white matter (19 studies), or whole brain (seven studies), while two studies did not use referencing of the QSM values and thirty-three studies did not report their normalization process.

DISCUSSION

In the results section, we provided a report of the existing evidence supplied by QSM in neurodegenerative disorders. This section is structured in two main parts. In the first part, we will provide a synthesis of the QSM findings and their implications in

TABLE 4 | Summary of magnetic susceptibility changes in the brain regions across neurodegenerative diseases compared to healthy individuals.

	Number of studies	PUT	CN	GP	AMY	HP	TH	PUL	NA	SN	SNc	SNr	DN	RN	FN	STN	Motor cortex	Pons
AD	9	4 3	6 1	1 5	3	2 4	1 3	3		1			1	1				
PD	38	4 17	1 1	6 17	4	2 2	3 8	1	1	21 2	11 2	3 3	2 6	7 1	1 1	1		
MSA	3	1 1	1	2	1	1			1	2			1	1				
PSP	3	1 1	1	2	1	1			1	2				2				
ALS/PLS	6	1		1		1				1				1			4 2	
WD	4	4	1 3	3 1			3			2 1				1				2
HD	2	2	2	2		1	1			1				1				
FRDA	2	1	1	1			1			1			2	1				
SCA3	1	1	1	1						1			1	1			1	1
SCA6	1	1	1	1						1			1	1				
Fabry	1	1	1	1						1			1	1				
DM1	1	1	1	1	1	1	1		1	1			1	1		1		
DM2	1	1	1	1	1	1	1		1	1			1	1		1		
PKAN	2	1	1	2			2			2				1 1				
MPAN	1	1	1	1			1			1								

Numbers inside the cells indicate the number of studies reporting that finding.

AD, Alzheimer's disease; ALS, amyotrophic lateral sclerosis; aMCI, amnesic mild cognitive impairment; AMY, amygdala; asymp-WD, asymptotic Wilson's disease; BG, basal ganglia; CN, caudate nucleus; DN, dentate nucleus; FN, fascicula nigrale; FRDA, Friedreich's ataxia; GP, globus pallidus; HD, Huntington's disease; HP, hippocampus; MCA, mild cognitive impairment; MPAN, mitochondrial membrane protein-associated neurodegeneration; MSA, multiple system atrophy; NA, nucleus accumbens; NBIA, neurodegeneration with brain iron accumulation; neuro-WD, neurologic Wilson's disease; PD, Parkinson's disease; PKAN, pantothenate kinase-associated neurodegeneration; PLS, primary lateral sclerosis; PSP, progressive supranuclear palsy; PUL, pulvinar nucleus; PUT, putamen; RN, red nucleus; SCA, spinocerebellar ataxia; SN, substantia nigra; SNc, substantia nigra pars compacta; SNr, substantia nigra pars reticulata; STN, subthalamic nucleus; TH, thalamus; WD, Wilson's disease.

No change in magnetic susceptibility.
 Not studied.
 Increased magnetic susceptibility.
 Decreased magnetic susceptibility.

each neurodegenerative disease. Similar to the results section, the discussion relating to the less studied neurodegenerative diseases (FRDA, SCA, Fabry disease, DM, PKAN, and MPAN) is moved to the **Supplementary Material 3**. In the second part, we provide a discussion of our overall current understanding, limitations of QSM and suggested future directions for QSM studies.

The Implications of QSM Findings in Neurodegenerative Diseases

Alzheimer's Disease

Abnormal iron homeostasis has been hypothesized to play a role in the pathogenesis of AD, with evidence suggesting a bidirectional pathological interaction between iron and A β (Masaldan et al., 2019). Excess iron upregulates gene expression of amyloid precursor protein, shifts its physiologic non-amyloidogenic processing toward amyloidogenic cleavage that produces A β peptides, and contributes to the misfolding of A β peptides and production of insoluble A β plaques (Rogers et al., 2008). A β plaques in turn, absorb free iron, which enhances

their neurotoxicity through production of reactive oxygen species and oxidative stress (Telling et al., 2017; Cheignon et al., 2018). Further, abnormal iron deposition has been detected in A β plaques in histologic evaluation of post-mortem brains from AD patients (Lovell et al., 1998), and APOE-e4 gene status, which is the most common predisposing genetic risk factor for AD, has been linked to increased iron in certain regions of the brain (Van Bergen et al., 2016b; Kagerer et al., 2020). These findings support the involvement of iron in the pathogenesis of AD.

Our review of studies using QSM in AD shows that there is an increased iron deposition in the CN and amygdala, in both mild and moderate stages of AD (**Table 2B**). The amygdala is one of the main regions involved in the pathologic processes in AD and undergoes significant atrophy in the early stages of AD. Atrophy of the amygdala is comparable to that of the hippocampus and correlates with cognitive deficits (Poulin et al., 2011). Although less investigated, the striatum shows evidence of A β deposition in the early stages of AD at even higher levels than the cortical regions, and volumetric assessments have revealed

significant changes in the CN in AD. While some studies have reported reduced volumes, others found increased size of the CN in early AD (Tentolouris-Piperas et al., 2017; Persson et al., 2018). Although this inconsistency remains unexplained, these significant changes suggest the involvement of the CN in AD.

In the other subcortical and cortical regions, findings of susceptibility changes were inconsistent. The hippocampus, which is one of the key areas undergoing significant atrophy in AD (Blair et al., 2020), showed changes in susceptibility in only two out of six studies. Similarly, key cortical regions involved in AD, such as the medial temporal lobe, precuneus, and cingulate gyrus have been shown by a limited number of studies to have increased susceptibility, while others did not confirm these results. One reason for the inconsistent results in the hippocampus and cortical regions can be the inaccuracies in QSM measurements at the edges of the brain where environments with drastically difference susceptibilities meet. This limitation is further discussed in section Methodological Aspects of QSM. It is also important to note that the susceptibility measurements depend on the precise segmentation of an ROI. Inclusion of the surrounding tissues within a segmented ROI leads to mean susceptibility measurements that are less representative of the actual values. Experience shows that the segmentation of the hippocampus and amygdala are particularly challenging. This reduces the reliability of both positive and negative findings in these regions and warrants further evaluations with more accurate segmentation methods.

MCI is defined as the slight impairment of cognition often in the memory domain, but not sufficiently severe to be characterized as dementia. Individuals with MCI are at higher risk for AD but do not necessarily progress to AD (Kelley and Petersen, 2007). Amnesic MCI, however, is recognized as a precursor to AD (Morris et al., 2001) with conversion rates to AD estimated to be between 7.5 and 16.5% per year (Ward et al., 2013). The QSM findings in aMCI and MCI have been inconsistent. Based on the studies suggesting a colocalization of A β PET signal and increased susceptibility in QSM, it would be expected to detect changes in the brain regions where accumulation of A β plaques occur (Ayton et al., 2017). One possible explanation of the negative findings of QSM changes in MCI may be that the increased iron content in the regions with A β deposition does not reach the level that enables its detection by QSM. We did not find any longitudinal QSM studies in people with MCI to examine susceptibility changes over time and its association with progression to AD.

Parkinson's Disease

PD is the second most common neurodegenerative disease presenting with motor and cognitive impairment. The disease is characterized by degeneration and atrophy of the dopaminergic neurons in the SN along with intracellular α -synuclein deposition (Lewy bodies) (Poewe et al., 2017). In PD, nigral iron accumulation is suggested to result from dysregulation of iron transmembrane transporters, decreased ferritin, and impaired iron export mechanisms (Masaldan et al., 2019). Excess iron contributes to neurodegeneration by inducing the aggregation of

α synuclein (Bharathi and Rao, 2007) and formation of Lewy bodies (Castellani et al., 2000), in addition to the pathways of oxidative toxicity, which are common across neurodegenerative diseases (Wang et al., 2017).

The centerpiece of pathology in PD is within the SN. Physiologically, SN is one of the iron-rich regions of the brain, storing large amounts of iron required for dopamine synthesis, mainly bound to neuromelanin (Sulzer et al., 2018). Abundance of iron in the SN enables highly accurate visualization of this region required for deep brain stimulation surgeries, which has resulted in a large number of published studies examining QSM in PD. These studies have shown consistent evidence of higher susceptibility in the SN in patients with PD compared to healthy individuals, suggestive of increased iron content. In other subcortical structures including the basal ganglia, RN, thalamus, and hippocampus, evidence for increased susceptibility has been inconsistent, with the majority of the studies finding no changes in PD.

Although susceptibility in the SN was increased in most studies, there have been inconsistent findings of its association with disease duration, stage and severity of clinical symptoms. This may relate to important confounders, such as medication. For example, in some studies, clinical assessments have been performed in the “on-state” (with dopaminergic agonist treatment) while in others, assessments were in the “off-state” (no dopaminergic treatment). Further, since more advanced stages of the disease inherently interfere with the ability of patients to participate in studies due to excessive movements throughout the MRI acquisition and other comorbidities, the populations of PD patients in studies are predominantly limited to earlier stages of the disease. It is possible that the selective inclusion of individuals who are at the early (or late) stages of the disease leads to the failure to detect a correlation that may exist in the long-term progression of the disease. This limitation is not unique to PD and occurs in the neuroimaging research involving most neurodegenerative disorders.

In a limited number of studies, increased susceptibility was found in widespread cortical regions and correlated with cognitive impairment. Importantly, such involvement points to a cortical pathology in PD, however, no QSM study has examined dementia with Lewy bodies (DLB), a disorder characterized by a similar α -synuclein-related pathology. Future studies focussing on DLB are needed to examine the pattern of cortical iron alterations in synucleinopathies.

QSM studies have also examined susceptibility changes in other parkinsonian syndromes, such as PSP and MSA. PSP and MSA are progressive neurodegenerative diseases with parkinsonian features (such as tremor, rigidity, and abnormal movement). PSP is considered to be a tauopathy characterized by vertical gaze palsy, postural instability, rigidity, and cognitive impairment (Armstrong, 2018). According to two meta-analyses of morphometric studies in PSP, among the subcortical structures, the putamen, CN, thalamus, midbrain, and anterior cerebellum show significant atrophy in PSP (Shao et al., 2014; Pan et al., 2017). This involvement is reflected in the increased susceptibility shown by QSM in the SN, RN, and putamen. In the globus pallidus, however, although QSM shows

higher susceptibility, such involvement has not been reported in morphometric studies.

MSA is an α -synucleinopathy (similar to DLB and PD) typically involving the striatum and SN, most commonly presents with Parkinsonian features and dysfunction of the autonomic system (Cykowski et al., 2015). Structural MRI studies have reported greatest gray matter reductions in the putamen and claustrum followed by the thalamus and cerebellum (Yu et al., 2015). In a similar fashion, QSM showed higher susceptibility in the SN and putamen, as well as the RN.

Clinical diagnosis and differentiation of the parkinsonian disorders is often challenging. In the limited number of studies reviewed, the pattern revealed by QSM in parkinsonian diseases showed high accuracy in their differentiation. This may suggest a clinical diagnostic utility for QSM in combination with other diagnostic tools. However, this remains to be more explored.

ALS

ALS is a progressive neurodegenerative disease characterized by the degeneration of upper and lower motor neurons in the motor cortex, brainstem and spinal cord. Copper-zinc superoxide dismutase (SOD1) mutation is one of the implicated genetic risk factors in ALS (Morgan and Orrell, 2016; Oskarsson et al., 2018). In animal models, it has been shown that SOD1 mutation results in increased expression of ferritin, transferrin receptor 1, and divalent metal transporter-1, leading to significant increase of iron in neural cells (Jeong et al., 2009). Additionally, even in the absence of SOD1 mutation, increased oxidative stress has been detected in patients with ALS, and suggested to play an important role in ALS pathogenesis (D'Amico et al., 2013). Further, in human studies, dysregulation in iron homeostasis has been reported in patients with ALS, including increased serum ferritin and decreased transferrin (Lovejoy and Guillemin, 2014).

ALS is commonly associated with MRI evidence for atrophy and reduced thickness in the motor cortex (precentral gyrus) (Cosottini et al., 2012; Chiò et al., 2014), and most QSM studies have focused on this region. Increased susceptibility was reported in these studies, which is in line with reports of increased oxidative stress in motor cortex and its correlation with disease severity (Ikawa et al., 2015). Further, T₂, T₂^{*}, and SWI studies also support the finding of increased iron in the motor cortex of patients with ALS (Yu et al., 2014; Sheelakumari et al., 2016). An explanation for this iron accumulation can be the regional migration of iron-containing microglia and macrophages observed in post-mortem analyses (Kwan et al., 2012; Adachi et al., 2015).

The few studies investigating subcortical structures in ALS have reported inconsistent volume reductions in the basal ganglia and hippocampus (Grolez et al., 2016). One QSM study has examined these brain regions in ALS, showing increased susceptibility in the putamen, GP, RN and SN, and reduced susceptibility in the corticospinal tract (CST). Increased susceptibility in the basal ganglia is consistent with pathological findings in the nigrostriatal pathways in ALS (Takahashi et al., 1993), and transactive response (TAR) DNA binding protein 43 (TDP-43) pathology in the RN and striatum (Brettschneider et al., 2013). The CST is another key region involved in ALS (Toosy

et al., 2003; Rajagopalan and Pioro, 2017), with its degeneration characterized by T₂ hyperintensities (Goodin et al., 1988; da Rocha et al., 2004). Decreased susceptibility in the CST correlated with reduced fractional anisotropy and increased mean and radial diffusivity in DTI. These DTI changes usually indicate myelin degeneration and abnormalities. Thus, the QSM finding is surprising given that demyelination usually results in increased, rather than decreased susceptibility. Decrease in susceptibility may be due to other tissue microstructural changes, although this remains speculative (Takahashi et al., 1993; Brettschneider et al., 2013; Grolez et al., 2016; Acosta-Cabronero et al., 2018). Further, it is important to note that QSM measurement of susceptibility is dependent on the orientation of the neural fiber tracts and subject's head in relation to the scanner's magnetic field (Lee et al., 2017), which can pose a large confounding effect on QSM assessment of the white matter (Lancione et al., 2017).

Wilson's Disease

WD is an autosomal recessive condition, resulting from a mutation in the *ATP7B* gene, characterized by excessive deposition of copper within tissues. Most commonly affected organs are the brain and liver leading to neurodegeneration and hepatic damage, respectively. The most-affected brain regions are the basal ganglia, thalamus, cerebellum, and upper brainstem, leading to movement, cognitive and psychiatric impairments (Członkowska et al., 2018). QSM studies showed an increased susceptibility in subcortical structures including the putamen, GP, thalamus, SN and pons, reflecting their recognized pattern of involvement in both adult and pediatric patients with WD with neurologic involvement. Of note, the abnormal changes of susceptibility in the putamen, thalamus, and pons were also detectable in asymptomatic children with the WD genotype. This finding suggests that QSM can be a useful tool in exploring the complex pre-clinical pathophysiological changes in WD.

It is not clear whether the increased susceptibility in the basal ganglia in WD is attributable to copper, iron or both. Although increased, the concentration of copper in the putamen, GP, and DN in patients with neurologic-WD is less than iron (Litwin et al., 2013; Dusek et al., 2017). There is an increased brain iron content in WD which results from dysfunction of the multicopper-dependent ferroxidase activity of ceruloplasmin. Ceruloplasmin is a multicopper containing protein that has a vital role in the export of iron from glial cells. In WD, the deficiency of *ATP7B* gene product leads to failure of incorporation of copper in ceruloplasmin (Członkowska et al., 2018). In the absence of functional ceruloplasmin, iron accumulates inside cells. In a study examining the correlation of iron and copper concentrations with R₂^{*} mapping of susceptibility in post-mortem brain tissue from patients with WD, there was a strong correlation of R₂^{*} measures with iron but not with copper concentrations (Dusek et al., 2017). Further, it is suggested that increased brain copper content in WD is likely in its diamagnetic Cu(I) state (Wender et al., 1974). Therefore, it is likely that increased magnetic susceptibility in WD results predominantly from secondary brain iron accumulation.

Huntington's Disease

HD is a genetic neurodegenerative syndrome, characterized by chorea, movement disorder and cognitive decline, and is caused by expansion of CAG trinucleotide repeats in exon 1 of huntingtin gene on chromosome 4. Evidence shows that abnormal huntingtin protein impairs iron homeostasis in the brain and is suggested to upregulate the expression of iron regulatory protein 1, transferrin, and transferrin receptor, which can result in increased iron accumulation (Niu et al., 2018). In mouse models of HD, increased production of mitochondrial iron uptake transporter (mitoferrin) and reduced frataxin lead to mitochondrial iron accumulation (Agrawal et al., 2018). Frataxin is a mitochondrial protein involved in the synthesis of iron-sulfur proteins necessary for oxidative phosphorylation in the mitochondria.

The brain structural hallmark of HD is degeneration of the CN and putamen and to a lesser extent, the GP, SN, STN, and locus coeruleus (Bhidayasiri and Truong, 2004). Higher iron content was reported in the basal ganglia by all of the studies in both patients with symptomatic HD and pre-symptomatic carriers of HD mutation, which correlated with atrophy in these structures, as well as age and genetic burden of HD. These findings are consistent with the recognized involvement of the basal ganglia in HD. Further, the increased iron content in asymptomatic individuals with the HD genotype is supportive of the findings from molecular studies indicating the association of abnormal huntingtin protein and dysregulation of iron homeostasis. Lower susceptibility was found in one study in the SN and hippocampus in patients with HD. The reason for this finding is not clearly understood but it may be associated with redistribution of iron within the brain (Van Bergen et al., 2016a).

In the cortical gray matter, structural studies have shown atrophy in the prefrontal and insular cortices (Lambrecq et al., 2013). Additionally, widespread deposition of huntingtin aggregates has been detected in the cortical regions including the insula, cingulate, and frontal cortices in clinical and preclinical HD (Gutkunst et al., 1999). These findings suggest a pathologic involvement of the cortex in HD in addition to the basal ganglia. To date, no QSM evaluation has been made in the cortical gray matter in HD. Such research would provide important information on the nature of cortical pathology in HD and verify whether a similar pattern of iron changes occurs in the cortex.

Our Current Understanding, QSM Limitations and Future Directions

Measurements of magnetic susceptibility by QSM provide valuable information about the changes in tissue composition in the target regions. The existing literature suggests that QSM shows promise in the investigation of the pathophysiology of neurodegeneration by revealing changes in the gray matter, where considering the relative concentrations of paramagnetic and diamagnetic substances, increased susceptibility is most likely derived from increased levels of iron. In the white matter, however, due to the abundance of diamagnetic myelin, an increase in magnetic susceptibility may result from both demyelination and/or iron deposition (Langkammer et al., 2012;

Sun et al., 2015; Hametner et al., 2018; Lee et al., 2018; Lewis et al., 2018; Wang et al., 2020). Further, susceptibility estimates in the white matter are often confounded by its geometrical properties, as the axonal orientation distribution with respect to the direction of the applied magnetic field has been shown to influence the inference of the true magnetic susceptibility distribution of the white matter tracts from the MRI phase images. Accounting for orientational dependence of white matter magnetic susceptibility estimates necessitates multiple orientation acquisitions or concurrent diffusion-weighted images, which can lead to longer scan times, subject discomfort and limited clinical feasibility (Liu, 2010; Lancione et al., 2017; Kaden et al., 2020).

Generally, studies using QSM showed increased susceptibility, suggestive of higher iron content, in the brain regions that are associated with the pathophysiology of each neurodegenerative disease, such as the SN in PD, the basal ganglia in HD, the amygdala and CN in AD, motor cortex in ALS and cerebellar DN in FRDA (Table 3). However, this pattern has not been consistently detected throughout all disorders, such as in AD where QSM did not reveal any changes in the hippocampus, which is recognized as one of the regions most involved by the pathologic processes in AD (Serrano-Pozo et al., 2011). One shortcoming of the reviewed papers on rare genetic neurodegenerative disorders is that most studies have restricted their scope of QSM evaluations to the iron rich basal ganglia and midbrain structures where susceptibility changes appear to be a common finding across some of these disorders (Table 3). A whole brain approach or investigation of a larger number of ROIs within all regions of the brain will provide a more exhaustive picture. It should also be noted that a number of relatively common neurodegenerative diseases, such as frontotemporal dementia, DLB, and prion diseases have not been investigated by QSM.

Methodological Aspects of QSM

QSM is an advanced post-processing technique for voxel-wise quantitative estimation of susceptibility, however, there are inherent limitations to the technique that restrict the robustness and reproducibility of susceptibility measurements by QSM. First, QSM estimates are sensitive to scanner field strength, acquisition parameters (such as echo time and voxel size), receiver noise, subject orientation and choice of QSM processing methods (Haacke et al., 2015). A description and critical comparison of these methods can be found in Deistung et al. (2017).

These dependencies lead to variations across studies in terms of the accuracy of measured susceptibilities. Another limitation of QSM is the surface artifacts (arising from strong susceptibility gradient at tissue interfaces, such as at the brain surfaces or around the blood vessels) and streaking artifacts (due to noise and mathematical limitations in solving the point-dipole problem) (Deistung et al., 2017; Taege et al., 2019; Jung et al., 2020). The third factor that contributes to the heterogeneity of susceptibility measurements across sites and studies is the inconsistent reference regions considered for relative measurement of magnetic susceptibility. In this review,

we observed a diversity of reference regions used in studies including various white matter areas (frontal, occipital, etc.), CSF, or mean susceptibility value of the whole brain. Reporting the absolute susceptibility value without referencing has also been preferred in some studies. These discrepancies among referencing methods have made it difficult or impossible to directly compare the susceptibility values across different studies and disorders. Therefore, it is not currently feasible to perform a meta-analysis. QSM processing methods are under constant improvements, enhancing their robustness and reproducibility. Future studies using more robust and standardized QSM methods may enable more homogeneous and comparable measurements. Additionally, using a consensual referencing region in each neurodegenerative disease in future studies can be a step towards the comparison of QSM findings across studies. Finally, the possible effect of atrophy in measurements of mean susceptibility should not be overlooked. It has been suggested that atrophy of a ROI may result in higher iron concentration and therefore mean susceptibility in the absence of a change in absolute iron content (Taeye et al., 2019). To account for and further explore this possibility, studies should consider the effect of atrophy as a confounder in magnetic susceptibility comparisons in their statistical analyses.

Future Directions

Although the small number of studies and the limitations of QSM make it difficult to draw definitive conclusions, the existing evidence suggests that QSM can greatly contribute to a better understanding of the underlying pathological changes in neurodegeneration. In most neurodegenerative diseases reviewed in this article, future studies with larger datasets, more consistent QSM referencing, and longitudinal designs are required. Multimodal studies using QSM and other neuroimaging techniques, such as PET can provide valuable information on the correlation of iron and pathologic protein aggregates. In the white matter, investigation of QSM together with diffusion weighted imaging allows more accurate examination of the alterations in myelin and iron. Finally, the high accuracy of QSM in differentiating certain neurodegenerative diseases, such as parkinsonian disorders, warrants further investigations aiming to evaluate its utility in clinical diagnosis of neurodegenerative diseases as an add-on imaging tool to the existing methods.

CONCLUSION

Our review indicates that QSM provides evidence of altered iron distribution in the brain in neurodegenerative diseases. Currently, the number of QSM studies in most neurodegenerative diseases is limited, especially in the rare disorders. In PD that has been more widely studied by QSM, higher iron content in the SN as the most involved brain region has been revealed. The small number of studies in AD, ALS, and HD makes a confident conclusion out of reach. Nevertheless, this limited evidence is suggestive of disease-specific patterns of microenvironmental changes that

are worthy of further investigation. This *in-vivo* evidence is in line with the reports from cellular and molecular studies (suggesting a pathologic role for iron in neurodegeneration) and post-mortem studies (indicating increased iron content in the brain in these disorders) (Zecca et al., 2004). Further, the increased burden of iron correlates with cognitive deficits in AD, disease stage in PD, and genetic burden and age in HD. Such associations may point out ongoing relationships between iron accumulation and neurodegeneration, either causal, intermediate, or independent.

Based on the findings of this review, QSM provides a unique opportunity for investigation of neurodegenerative diseases that can improve our understanding of the pathologic processes involved.

DATA AVAILABILITY STATEMENT

The original contributions presented in the study are included in the article/**Supplementary Material**, further inquiries can be directed to the corresponding author/s.

AUTHOR CONTRIBUTIONS

PR developed the search strategies, ran the database search. PR and SML, have each independently performed the screening of studies for inclusion, data extraction, and quality assessment. CP adjudicated the conflicts between two reviewers, PR and SML, in screening, data extraction, and quality assessment. Development of the protocol was done by PR, and all authors have collaborated to improve, and approved the final protocol. Data synthesis was performed by PR and SML. CP, DV, AIB, and BAM provided the intellectual input to data synthesis and interpretation. VLC, WTS, PD, AIB, BAM, DV, CP, TEVR, CMO, DJRL, and SML provided the intellectual input into the manuscript draft prepared by PR. All authors have read, provided feedback, and approved the final manuscript.

ACKNOWLEDGMENTS

The authors would like to thank Prof. Martha E. Shenton and Dr. Amanda E. Lyall (Psychiatry Neuroimaging Laboratory, Brigham and Women's Hospital, Harvard Medical School, Boston, MA, USA) for their valuable contributions and feedback on the drafts of this manuscript. CP was supported by a National Health and Medical Research Council (NHMRC) Senior Principal Research Fellowship (1105825), an NHMRC L3 Investigator Grant (1196508). AIB was supported by a NHMRC L3 Investigator Grant (1194028). VLC was supported by an Australian National Health and Medical Research Council EL2 Investigator Grant (1177370) and a University of Melbourne Dame Kate Campbell Fellowship. BAM holds a fellowship from the National Imaging Facility, funded by the Australian Government NCRIS program.

SUPPLEMENTARY MATERIAL

The Supplementary Material for this article can be found online at: <https://www.frontiersin.org/articles/10.3389/fnins.2021.618435/full#supplementary-material>

Supplementary Material 1 | Protocol for systematic review.

Supplementary Material 2 | Tables S1A–H. Summary of the characteristics, findings and risk of bias assessment of QSM studies in neurodegenerative diseases.

Supplementary Material 3 | Results and discussion sections on less studied neurodegenerative disorders.

Supplementary Material 4 | Table S2. Details of MRI acquisition and QSM processing methods used by reviewed studies.

REFERENCES

- Acosta-Cabrero, J., Cardenas-Blanco, A., Betts, M. J., Butryn, M., Valdes-Herrera, J. P., Galazky, I., et al. (2017). The whole-brain pattern of magnetic susceptibility perturbations in Parkinson's disease. *Brain* 140, 118–131. doi: 10.1093/brain/aww278
- Acosta-Cabrero, J., Machts, J., Schreiber, S., Abdulla, S., Kollewé, K., Petri, S., et al. (2018). Quantitative susceptibility MRI to detect brain iron in amyotrophic lateral sclerosis. *Radiology* 289, 195–203. doi: 10.1148/radiol.2018180112
- Acosta-Cabrero, J., Williams, G. B., Cardenas-Blanco, A., Arnold, R. J., Lupson, V., and Nestor, P. J. (2013). *In vivo* quantitative susceptibility mapping (QSM) in Alzheimer's disease. *PLoS ONE* 8:e81093. doi: 10.1371/journal.pone.0081093
- Adachi, Y., Sato, N., Saito, Y., Kimura, Y., Nakata, Y., Ito, K., et al. (2015). Usefulness of SWI for the detection of iron in the motor cortex in amyotrophic lateral sclerosis. *J. Neuroimaging* 25, 443–451. doi: 10.1111/jon.12127
- Agrawal, S., Fox, J., Thyagarajan, B., and Fox, J. H. (2018). Brain mitochondrial iron accumulates in Huntington's disease, mediates mitochondrial dysfunction, and can be removed pharmacologically. *Free Radic. Biol. Med.* 120, 317–329. doi: 10.1016/j.freeradbiomed.2018.04.002
- Ahmadi, S. A., Bötzel, K., Levin, J., Maiostre, J., Klein, T., Wein, W., et al. (2020). Analyzing the co-localization of substantia nigra hyper-echogenicities and iron accumulation in Parkinson's disease: a multi-modal atlas study with transcranial ultrasound and MRI. *Neuroimage Clin.* 26:102185. doi: 10.1016/j.nicl.2020.102185
- An, H., Zeng, X., Niu, T., Li, G., Yang, J., Zheng, L., et al. (2018). Quantifying iron deposition within the substantia nigra of Parkinson's disease by quantitative susceptibility mapping. *J. Neurol. Sci.* 386, 46–52. doi: 10.1016/j.jns.2018.01.008
- Armstrong, M. J. (2018). Progressive supranuclear palsy: an update. *Curr. Neurol. Neurosci. Rep.* 18:12. doi: 10.1007/s11910-018-0819-5
- Ayton, S., Fazlollahi, A., Bourgeat, P., Raniga, P., Ng, A., Lim, Y. Y., et al. (2017). Cerebral quantitative susceptibility mapping predicts amyloid-beta-related cognitive decline. *Brain* 140, 2112–2119. doi: 10.1093/brain/awx137
- Azuma, M., Hirai, T., Nakaura, T., Kitajima, M., Yamashita, S., Hashimoto, M., et al. (2019). Combining quantitative susceptibility mapping to the morphometric index in differentiating between progressive supranuclear palsy and Parkinson's disease. *J. Neurol. Sci.* 406:116443. doi: 10.1016/j.jns.2019.116443
- Azuma, M., Hirai, T., Yamada, K., Yamashita, S., Ando, Y., Tateishi, M., et al. (2016). Lateral asymmetry and spatial difference of iron deposition in the substantia nigra of patients with Parkinson disease measured with quantitative susceptibility mapping. *Am. J. Neuroradiol.* 37, 782–788. doi: 10.3174/ajnr.A4645
- Barbosa, J. H. O., Santos, A. C., Tumas, V., Liu, M., Zheng, W., Haacke, E. M., et al. (2015). Quantifying brain iron deposition in patients with Parkinson's disease using quantitative susceptibility mapping, R2 and R2*. *Magn. Reson. Imaging* 33, 559–565. doi: 10.1016/j.mri.2015.02.021
- Bergsland, N., Zivadinov, R., Schweser, F., Hagemeier, J., Lichter, D., and Guttuso, T. (2019). Ventral posterior substantia nigra iron increases over 3 years in Parkinson's disease. *Mov. Disord.* 34, 1006–1013. doi: 10.1002/mds.27730
- Bharathi, and Rao, K. S. J. (2007). Thermodynamics imprinting reveals differential binding of metals to α -synuclein: Relevance to parkinson's disease. *Biochem. Biophys. Res. Commun.* 359, 115–120. doi: 10.1016/j.bbrc.2007.05.060
- Bhidayasiri, R., and Truong, D. D. (2004). Chorea and related disorders. *Postgrad. Med. J.* 80, 527–534. doi: 10.1136/pgmj.2004.019356
- Blair, J. C., Lasiecka, Z. M., Patrie, J., Barrett, M. J., and Druzgal, T. J. (2020). Cytoarchitectonic mapping of MRI detects rapid changes in Alzheimer's disease. *Front. Neurol.* 11:241. doi: 10.3389/fneur.2020.00241
- Brettschneider, J., Del Tredici, K., Toledo, J. B., Robinson, J. L., Irwin, D. J., Grossman, M., et al. (2013). Stages of pTDP-43 pathology in amyotrophic lateral sclerosis. *Ann. Neurol.* 74, 20–38. doi: 10.1002/ana.23937
- Castellani, R. J., Siedlak, S. L., Perry, G., and Smith, M. A. (2000). Sequestration of iron by Lewy bodies in Parkinson's disease. *Acta Neuropathol.* 100, 111–114. doi: 10.1007/s004010050001
- Cheignon, C., Tomas, M., Bonnefont-Rousselot, D., Faller, P., Hureau, C., and Collin, F. (2018). Oxidative stress and the amyloid beta peptide in Alzheimer's disease. *Redox Biol.* 14:450–464. doi: 10.1016/j.redox.2017.10.014
- Chen, L., Hua, J., Ross, C. A., Cai, S., van Zijl, P. C. M., and Li, X. (2018). Altered brain iron content and deposition rate in Huntington's disease as indicated by quantitative susceptibility MRI. *J. Neurosci. Res.* 97, 467–479. doi: 10.1002/jnr.24358
- Chen, Q., Chen, Y., Zhang, Y., Wang, F., Yu, H., Zhang, C., et al. (2019). Iron deposition in Parkinson's disease by quantitative susceptibility mapping. *BMC Neurosci.* 20:23. doi: 10.1186/s12868-019-0505-9
- Cheng, Z., Zhang, J., He, N., Li, Y., Wen, Y., Xu, H., et al. (2019). Radiomic features of the nigrosome-1 region of the substantia nigra: using quantitative susceptibility mapping to assist the diagnosis of idiopathic Parkinson's disease. *Front. Aging Neurosci.* 11:167. doi: 10.3389/fnagi.2019.00167
- Chiò, A., Pagani, M., Agosta, F., Calvo, A., Cistaro, A., and Filippi, M. (2014). Neuroimaging in amyotrophic lateral sclerosis: Insights into structural and functional changes. *Lancet Neurol.* 13, 1228–1240. doi: 10.1016/S1474-4422(14)70167-X
- Contarino, V. E., Conte, G., Morelli, C., Trogu, F., Scola, E., Calloni, S. F., et al. (2020). Toward a marker of upper motor neuron impairment in amyotrophic lateral sclerosis: a fully automatic investigation of the magnetic susceptibility in the precentral cortex. *Eur. J. Radiol.* 124:108815. doi: 10.1016/j.ejrad.2020.108815
- Cosottini, M., Pesaresi, I., Piazza, S., Diciotti, S., Cecchi, P., Fabbri, S., et al. (2012). Structural and functional evaluation of cortical motor areas in amyotrophic lateral sclerosis. *Exp. Neurol.* 234, 169–180. doi: 10.1016/j.expneurol.2011.12.024
- Costagli, M., Donatelli, G., Biagi, L., Caldarazzo Ienco, E., Siciliano, G., Tosetti, M., et al. (2016). Magnetic susceptibility in the deep layers of the primary motor cortex in amyotrophic lateral sclerosis. *Neuroimage Clin.* 12, 965–969. doi: 10.1016/j.nicl.2016.04.011
- Cykowski, M. D., Coon, E. A., Powell, S. Z., Jenkins, S. M., Benarroch, E. E., Low, P. A., et al. (2015). Expanding the spectrum of neuronal pathology in multiple system atrophy. *Brain* 138, 2293–2309. doi: 10.1093/brain/awv114
- Członkowska, A., Litwin, T., Dusek, P., Ferenci, P., Lutsenko, S., Medici, V., et al. (2018). Wilson disease. *Nat. Rev. Dis. Prim.* 4:21. doi: 10.1038/s41572-018-0018-3
- da Rocha, A. J., Oliveira, A. S. B., Fonseca, R. B., Maia, A. C. M. J., Buainain, R. P., and Lederman, H. M. (2004). Detection of corticospinal tract compromise in amyotrophic lateral sclerosis with brain MR imaging: relevance of the T1-weighted spin-echo magnetization transfer contrast sequence. *AJNR. Am. J. Neuroradiol.* 25, 1509–1515.
- D'Amico, E., Factor-Litvak, P., Santella, R. M., and Mitsumoto, H. (2013). Clinical perspective on oxidative stress in sporadic amyotrophic lateral sclerosis. *Free Radic. Biol. Med.* 65, 509–527. doi: 10.1016/j.freeradbiomed.2013.06.029
- Deistung, A., Schweser, F., and Reichenbach, J. R. (2017). Overview of quantitative susceptibility mapping. *NMR Biomed.* 30, e3569. doi: 10.1002/nbm.3569

- Dezortova, M., Lescinskij, A., Dusek, P., Herynek, V., Acosta-Cabronero, J., Bruha, R., et al. (2019). Multiparametric quantitative brain MRI in neurological and hepatic forms of Wilson's disease. *J. Magn. Reson. Imaging* 51, 1829–1835. doi: 10.1002/jmri.26984
- Dixon, S. J., Lemberg, K. M., Lamprecht, M. R., Skouta, R., Zaitsev, E. M., Gleason, C. E., et al. (2012). Ferroptosis: an iron-dependent form of nonapoptotic cell death. *Cell* 149, 1060–1072. doi: 10.1016/j.cell.2012.03.042
- Doganay, S., Gumus, K., Koc, G., Bayram, A. K., Dogan, M. S., Arslan, D., et al. (2018). Magnetic susceptibility changes in the basal ganglia and brain stem of patients with Wilson's disease: evaluation with quantitative susceptibility mapping. *Magn. Reson. Med. Sci.* 17, 73–79. doi: 10.2463/mrms.mp.2016-0145
- Domínguez, D. J. F., Ng, A. C. L., Poudel, G., Stout, J. C., Churchyard, A., Chua, P., et al. (2016). Iron accumulation in the basal ganglia in Huntington's disease: cross-sectional data from the IMAGE-HD study. *J. Neurol. Neurosurg. Psychiatry* 87, 545–549. doi: 10.1136/jnnp-2014-310183
- Donatelli, G., Caldarazzo Ienco, E., Costagli, M., Migaleddu, G., Cecchi, P., Siciliano, G., et al. (2019). MRI cortical feature of bulbar impairment in patients with amyotrophic lateral sclerosis. *Neuroimage Clin.* 24:101934. doi: 10.1016/j.nicl.2019.101934
- Du, G., Lewis, M. M., Sica, C., He, L., Connor, J. R., Kong, L., et al. (2018). Distinct progression pattern of susceptibility MRI in the substantia nigra of Parkinson's patients. *Mov. Disord.* 33, 1423–1431. doi: 10.1002/mds.27318
- Du, G., Liu, T., Lewis, M. M., Kong, L., Wang, Y., Connor, J., et al. (2016). Quantitative susceptibility mapping of the midbrain in Parkinson's disease. *Mov. Disord.* 31, 317–324. doi: 10.1002/mds.26417
- Du, L., Zhao, Z., Cui, A., Zhu, Y., Zhang, L., Liu, J., et al. (2018). Increased iron deposition on brain quantitative susceptibility mapping correlates with decreased cognitive function in Alzheimer's Disease. *ACS Chem. Neurosci.* 9, 1849–1857. doi: 10.1021/acscchemneuro.8b00194
- Dusek, P., Bahn, E., Litwin, T., Jablonka-Salach, K., Łuciuk, A., Huelnhagen, T., et al. (2017). Brain iron accumulation in Wilson disease: a post mortem 7 Tesla MRI–histopathological study. *Neuropathol. Appl. Neurobiol.* 43, 514–532. doi: 10.1111/nan.12341
- Dusek, P., Mekle, R., Skowronska, M., Acosta-Cabronero, J., Huelnhagen, T., Robinson, S. D., et al. (2019). Brain iron and metabolic abnormalities in C19orf12 mutation carriers: a 7.0 tesla MRI study in mitochondrial membrane protein-associated neurodegeneration. *Mov. Disord.* 35, 142–150. doi: 10.1002/mds.27827
- Dusek, P., Tovar Martinez, E. M., Madai, V. I., Jech, R., Sobesky, J., Paul, F., et al. (2014). 7-Tesla magnetic resonance imaging for brain iron quantification in homozygous and heterozygous PANK2 mutation carriers. *Mov. Disord. Clin. Pract.* 1, 329–335. doi: 10.1002/mdc3.12080
- Duyn, J. H., and Schenck, J. (2017). Contributions to magnetic susceptibility of brain tissue. *NMR Biomed.* 30:e3546. doi: 10.1002/nbm.3546
- Fortier, V., and Levesque, I. R. (2018). Phase processing for quantitative susceptibility mapping of regions with large susceptibility and lack of signal. *Magn. Reson. Med.* 79, 3103–3113. doi: 10.1002/mrm.26989
- Fritzsche, D., Reiss-Zimmermann, M., Trampel, R., Turner, R., Hoffmann, K. T., and Schäfer, A. (2014). Seven-tesla magnetic resonance imaging in Wilson disease using quantitative susceptibility mapping for measurement of copper accumulation. *Invest. Radiol.* 49, 299–306. doi: 10.1097/RLI.0000000000000010
- Ghassaban, K., He, N., Sethi, S. K., Huang, P., Chen, S., Yan, F., et al. (2019). Regional high iron in the substantia nigra differentiates Parkinson's disease patients from healthy controls. *Front. Aging Neurosci.* 11:106. doi: 10.3389/fnagi.2019.00106
- Goetz, C. G., Poewe, W., Rascol, O., Sampaio, C., Stebbins, G. T., Counsell, C., et al. (2004). Movement Disorder Society Task Force report on the Hoehn and Yahr staging scale: status and recommendations. *Mov. Disord.* 19, 1020–1028. doi: 10.1002/mds.20213
- Goodin, D. S., Rowley, H. A., and Olney, R. K. (1988). Magnetic resonance imaging in amyotrophic lateral sclerosis. *Ann. Neurol.* 23, 418–420. doi: 10.1002/ana.410230424
- Grolez, G., Moreau, C., Danel-Brunaud, V., Delmaire, C., Lopes, R., Pradat, P. F., et al. (2016). The value of magnetic resonance imaging as a biomarker for amyotrophic lateral sclerosis: a systematic review. *BMC Neurol.* 16:155. doi: 10.1186/s12883-016-0672-6
- Guan, X., Huang, P., Zeng, Q., Liu, C., Wei, H., Xuan, M., et al. (2019a). Quantitative susceptibility mapping as a biomarker for evaluating white matter alterations in Parkinson's disease. *Brain Imaging Behav.* 13, 220–231. doi: 10.1007/s11682-018-9842-z
- Guan, X., Xuan, M., Gu, Q., Huang, P., Liu, C., Wang, N., et al. (2017a). Regionally progressive accumulation of iron in Parkinson's disease as measured by quantitative susceptibility mapping. *NMR Biomed.* 30:e3489. doi: 10.1002/nbm.3489
- Guan, X., Xuan, M., Gu, Q., Xu, X., Huang, P., Wang, N., et al. (2017b). Influence of regional iron on the motor impairments of Parkinson's disease: a quantitative susceptibility mapping study. *J. Magn. Reson. Imaging* 45, 1335–1342. doi: 10.1002/jmri.25434
- Guan, X., Zhang, Y., Wei, H., Guo, T., Zeng, Q., Zhou, C., et al. (2019b). Iron-related nigral degeneration influences functional topology mediated by striatal dysfunction in Parkinson's disease. *Neurobiol. Aging* 75, 83–97. doi: 10.1016/j.neurobiolaging.2018.11.013
- Gutkunst, C. A., Li, S. H., Yi, H., Mulroy, J. S., Kummerle, S., Jones, R., et al. (1999). Nuclear and neuropil aggregates in Huntington's disease: relationship to neuropathology. *J. Neurosci.* 19, 2522–2534. doi: 10.1523/jneurosci.19-07-02522.1999
- Haacke, E. M., Liu, S., Buch, S., Zheng, W., Wu, D., and Ye, Y. (2015). Quantitative susceptibility mapping: current status and future directions. *Magn. Reson. Imaging* 33, 1–25. doi: 10.1016/j.mri.2014.09.004
- Haining, R. L., and Achat-Mendes, C. (2017). Neuromelanin, one of the most overlooked molecules in modern medicine, is not a spectator. *Neural Regen. Res.* 12, 372–375. doi: 10.4103/1673-5374.202928
- Hametner, S., Endmayr, V., Deistung, A., Palmrich, P., Prihoda, M., Haimburger, E., et al. (2018). The influence of brain iron and myelin on magnetic susceptibility and effective transverse relaxation—a biochemical and histological validation study. *Neuroimage* 179, 117–133. doi: 10.1016/j.neuroimage.2018.06.007
- Harding, I. H., Raniga, P., Delatycki, M. B., Stagnitti, M. R., Corben, L. A., Storey, E., et al. (2016). Tissue atrophy and elevated iron concentration in the extrapyramidal motor system in Friedreich ataxia: the IMAGE-FRDA study. *J. Neurol. Neurosurg. Psychiatry* 87, 1261–1263. doi: 10.1136/jnnp-2015-312665
- He, N., Huang, P., Ling, H., Langley, J., Liu, C., Ding, B., et al. (2017). Dentate nucleus iron deposition is a potential biomarker for tremor-dominant Parkinson's disease. *NMR Biomed.* 30:e3554. doi: 10.1002/nbm.3554
- He, N., Ling, H., Ding, B., Huang, J., Zhang, Y., Zhang, Z., et al. (2015). Region-specific disturbed iron distribution in early idiopathic Parkinson's disease measured by quantitative susceptibility mapping. *Hum. Brain Mapp.* 36, 4407–4420. doi: 10.1002/hbm.22928
- Hwang, E. J., Kim, H. G., Kim, D., Rhee, H. Y., Ryu, C. W., Liu, T., et al. (2016). Texture analyses of quantitative susceptibility maps to differentiate Alzheimer's disease from cognitive normal and mild cognitive impairment. *Med. Phys.* 43, 4718–4728. doi: 10.1118/1.4958959
- Hwang, E. J., Ryu, D. W., Lee, J. E., Park, S. H., Choi, H. S., and Kim, J. S. (2019). Magnetic resonance imaging assessment of the substrate for hyposmia in patients with Parkinson's disease. *Clin. Radiol.* 74, 489.e9–489.e15. doi: 10.1016/j.crad.2019.02.003
- Ide, S., Kakeda, S., Ueda, I., Watanabe, K., Murakami, Y., Moriya, J., et al. (2014). Internal structures of the globus pallidus in patients with Parkinson's disease: evaluation with quantitative susceptibility mapping (QSM). *Eur. Radiol.* 25, 710–718. doi: 10.1007/s00330-014-3472-7
- Ikawa, M., Okazawa, H., Tsujikawa, T., Matsunaga, A., Yamamura, O., Mori, T., et al. (2015). Increased oxidative stress is related to disease severity in the ALS motor cortex. *Neurology* 84, 2033–2039. doi: 10.1212/WNL.0000000000001588
- Ito, K., Ohtsuka, C., Yoshioka, K., Kameda, H., Yokosawa, S., Sato, R., et al. (2017). Differential diagnosis of parkinsonism by a combined use of diffusion kurtosis imaging and quantitative susceptibility mapping. *Neuroradiology* 59, 759–769. doi: 10.1007/s00234-017-1870-7
- Jeong, S. Y., Rathore, K. I., Schulz, K., Ponka, P., Arosio, P., and David, S. (2009). Dysregulation of iron homeostasis in the CNS contributes to disease progression in a mouse model of amyotrophic lateral sclerosis. *J. Neurosci.* 29, 610–619. doi: 10.1523/JNEUROSCI.5443-08.2009
- Jung, W., Bollmann, S., and Lee, J. (2020). Overview of quantitative susceptibility mapping using deep learning: current status, challenges and opportunities. *NMR Biomed.* e4292, 1–14. doi: 10.1002/nbm.4292

- Kaden, E., Gyor, N. G., Rudrapatna, S. U., Barskaya, I. Y., Dragonu, I., Does, M. D., et al. (2020). Microscopic susceptibility anisotropy imaging. *Magn. Reson. Med.* 84, 2739–2753. doi: 10.1002/mrm.28303
- Kagerer, S. M., van Bergen, J. M. G., Li, X., Quevenno, F. C., Gietl, A. F., Studer, S., et al. (2020). APOE4 moderates effects of cortical iron on synchronized default mode network activity in cognitively healthy old-aged adults. *Alzheimer's Dement. Diagn. Assess. Dis. Monit.* 12:e12002. doi: 10.1002/dad2.12002
- Kan, H., Uchida, Y., Arai, N., Ueki, Y., Aoki, T., Kasai, H., et al. (2020). Simultaneous voxel-based magnetic susceptibility and morphometry analysis using magnetization-prepared spoiled turbo multiple gradient echo. *NMR Biomed.* 33:e4272. doi: 10.1002/nbm.4272
- Kelley, B. J., and Petersen, R. C. (2007). Alzheimer's disease and mild cognitive impairment. *Neurol. Clin.* 25, 577–609, v. doi: 10.1016/j.ncl.2007.03.008
- Kim, E. Y., Sung, Y. H., Shin, H. G. G., Noh, Y., Nam, Y., and Lee, J. (2018). Diagnosis of early-stage idiopathic parkinson's disease using high-resolution quantitative susceptibility mapping combined with histogram analysis in the substantia nigra at 3 T. *J. Clin. Neurol.* 14, 90–97. doi: 10.3988/jcn.2018.14.1.90
- Kim, H.-G. G., Park, S., Rhee, H. Y., Lee, K. M., Ryu, C.-W. W., Rhee, S. J., et al. (2017). Quantitative susceptibility mapping to evaluate the early stage of Alzheimer's disease. *Neuroimage Clin.* 16, 429–438. doi: 10.1016/j.nicl.2017.08.019
- Kwan, J. Y., Jeong, S. Y., Van Gelderen, P., Deng, H.-X., Quezado, M. M., Danielian, L. E., et al. (2012). Iron accumulation in deep cortical layers accounts for MRI signal abnormalities in ALS: correlating 7 Tesla MRI and pathology. *PLoS ONE* 7:e35241. doi: 10.1371/journal.pone.0035241
- Lambrecq, V., Langbour, N., Guehl, D., Bioulac, B., Burbaud, P., and Rotge, J. Y. (2013). Evolution of brain gray matter loss in Huntington's disease: a meta-analysis. *Eur. J. Neurol.* 20, 315–321. doi: 10.1111/j.1468-1331.2012.03854.x
- Lancione, M., Tosetti, M., Donatelli, G., Cosottini, M., and Costagli, M. (2017). The impact of white matter fiber orientation in single-acquisition quantitative susceptibility mapping. *NMR Biomed.* 30:e3798. doi: 10.1002/nbm.3798
- Langkammer, C., Pirpamer, L., Seiler, S., Deistung, A., Schweser, F., Franthal, S., et al. (2016). Quantitative susceptibility mapping in Parkinson's disease. *PLoS ONE* 11:e0162460. doi: 10.1371/journal.pone.0162460
- Langkammer, C., Schweser, F., Krebs, N., Deistung, A., Goessler, W., Scheurer, E., et al. (2012). Quantitative susceptibility mapping (QSM) as a means to measure brain iron? A post mortem validation study. *Neuroimage* 62, 1593–1599. doi: 10.1016/j.neuroimage.2012.05.049
- Lee, H., Baek, S. Y., Chun, S. Y., Lee, J. H., and Cho, H. J. (2018). Specific visualization of neuromelanin-iron complex and ferric iron in the human post-mortem substantia nigra using MR relaxometry at 7T. *Neuroimage* 172, 874–885. doi: 10.1016/j.neuroimage.2017.11.035
- Lee, J. Y., Lee, Y. J., Park, D. W., Nam, Y., Kim, S. H., Park, J., et al. (2017). Quantitative susceptibility mapping of the motor cortex: a comparison of susceptibility among patients with amyotrophic lateral sclerosis, cerebrovascular disease, and healthy controls. *Neuroradiology* 59, 1213–1222. doi: 10.1007/s00234-017-1933-9
- Lewis, M. M., Du, G., Baccon, J., Snyder, A. M., Murie, B., Cooper, F., et al. (2018). Susceptibility MRI captures nigral pathology in patients with parkinsonian syndromes. *Mov. Disord.* 33, 1432–1439. doi: 10.1002/mds.27381
- Li, D. T. H. H., Hui, E. S., Chan, Q., Yao, N., Chua, S. E. E., McAlonan, G. M., et al. (2018). Quantitative susceptibility mapping as an indicator of subcortical and limbic iron abnormality in Parkinson's disease with dementia. *Neuroimage Clin.* 20, 365–373. doi: 10.1016/j.nicl.2018.07.028
- Li, G., Zhai, G., Zhao, X., An, H., Spincemille, P., Gillen, K. M., et al. (2019). 3D texture analyses within the substantia nigra of Parkinson's disease patients on quantitative susceptibility maps and R2* maps. *Neuroimage* 188, 465–472. doi: 10.1016/j.neuroimage.2018.12.041
- Litwin, T., Gromadzka, G., Szpak, G. M., Jablonka-Salach, K., Bulska, E., and Czlonkowska, A. (2013). Brain metal accumulation in Wilson's disease. *J. Neurol. Sci.* 329, 55–58. doi: 10.1016/j.jns.2013.03.021
- Liu, C. (2010). Susceptibility tensor imaging. *Magn. Reson. Med.* 63, 1471–1477. doi: 10.1002/mrm.22482
- Liu, C., Li, W., Tong, K. A., Yeom, K. W., and Kuzminski, S. (2015). Susceptibility-weighted imaging and quantitative susceptibility mapping in the brain. *J. Magn. Reson. Imaging* 42, 23–41. doi: 10.1002/jmri.24768
- Liu, T., Khalidov, I., de Rochefort, L., Spincemille, P., Liu, J., Tsiouris, A. J., et al. (2011). A novel background field removal method for MRI using projection onto dipole fields (PDF). *NMR Biomed.* 24, 1129–1136. doi: 10.1002/nbm.1670
- Lotfipour, A. K., Wharton, S., Schwarz, S. T., Gontu, V., Schäfer, A., Peters, A. M., et al. (2012). High resolution magnetic susceptibility mapping of the substantia nigra in Parkinson's disease. *J. Magn. Reson. Imaging* 35, 48–55. doi: 10.1002/jmri.22752
- Lovejoy, D. B., and Guillemain, G. J. (2014). The potential for transition metal-mediated neurodegeneration in amyotrophic lateral sclerosis. *Front. Aging Neurosci.* 6:173. doi: 10.3389/fnagi.2014.00173
- Lovell, M. A., Robertson, J. D., Teesdale, W. J., Campbell, J. L., and Markesbery, W. R. (1998). Copper, iron and zinc in Alzheimer's disease senile plaques. *J. Neurol. Sci.* 158, 47–52. doi: 10.1016/S0022-510X(98)00092-6
- Masaldan, S., Bush, A. I., Devos, D., Rolland, A. S., and Moreau, C. (2019). Striking while the iron is hot: Iron metabolism and ferroptosis in neurodegeneration. *Free Radic. Biol. Med.* 133, 221–233. doi: 10.1016/j.freeradbiomed.2018.09.033
- Mazzucchi, S., Frosini, D., Costagli, M., Del Prete, E., Donatelli, G., Cecchi, P., et al. (2019). Quantitative susceptibility mapping in atypical Parkinsonisms. *Neuroimage Clin.* 24:101999. doi: 10.1016/j.nicl.2019.101999
- Meineke, J., Wenzel, F., De Marco, M., Venneri, A., Blackburn, D. J., Teh, K., et al. (2018). Motion artifacts in standard clinical setting obscure disease-specific differences in quantitative susceptibility mapping. *Phys. Med. Biol.* 63:14NT01. doi: 10.1088/1361-6560/aacc52
- Mills, E., Dong, X. P., Wang, F., and Xu, H. (2010). Mechanisms of brain iron transport: insight into neurodegeneration and CNS disorders. *Future Med. Chem.* 2:51. doi: 10.4155/fmc.09.140
- Moher, D., Liberati, A., Tetzlaff, J., Altman, D. G., Altman, D., Antes, G., et al. (2009). Preferred reporting items for systematic reviews and meta-analyses: the PRISMA statement. *PLoS Med.* 6:e1000097. doi: 10.1371/journal.pmed.1000097
- Moon, Y., Han, S. H. H., and Moon, W. J. J. (2016). Patterns of brain iron accumulation in vascular dementia and Alzheimer's dementia using quantitative susceptibility mapping imaging. *J. Alzheimers Dis.* 51, 737–745. doi: 10.3233/JAD-151037
- Morgan, S., and Orrell, R. W. (2016). Pathogenesis of amyotrophic lateral sclerosis. *Br. Med. Bull.* 119, 87–97. doi: 10.1093/bmb/ldw026
- Morris, G., Berk, M., Carvalho, A. F., Maes, M., Walker, A. J., and Puri, B. K. (2018). Why should neuroscientists worry about iron? The emerging role of ferroptosis in the pathophysiology of neurodegenerative diseases. *Behav. Brain Res.* 341, 154–175. doi: 10.1016/j.bbr.2017.12.036
- Morris, J. C., Storandt, M., Miller, J. P., McKeel, D. W., Price, J. L., Rubin, E. H., et al. (2001). Mild cognitive impairment represents early-stage Alzheimer disease. *Arch. Neurol.* 58, 397–405. doi: 10.1001/archneur.58.3.397
- Movement Disorder Society Task Force on Rating Scales for Parkinson's Disease (2003). The Unified Parkinson's Disease Rating Scale (UPDRS): status and recommendations. *Mov. Disord.* 18, 738–750. doi: 10.1002/mds.10473
- Murakami, Y., Kakeda, S., Watanabe, K., Ueda, I., Ogasawara, A., Moriya, J., et al. (2015). Usefulness of quantitative susceptibility mapping for the diagnosis of Parkinson disease. *Am. J. Neuroradiol.* 36, 1102–1108. doi: 10.3174/ajnr.A4260
- Ndayisaba, A., Kaindlstorfer, C., and Wenning, G. K. (2019). Iron in neurodegeneration—cause or consequence? *Front. Neurosci.* 13:180. doi: 10.3389/fnins.2019.00180
- Niu, L., Ye, C., Sun, Y., Peng, T., Yang, S., Wang, W., et al. (2018). Mutant huntingtin induces iron overload via up-regulating IRP1 in Huntington's disease. *Cell Biosci.* 8:41. doi: 10.1186/s13578-018-0239-x
- Oskarsson, B., Gendron, T. F., and Staff, N. P. (2018). Amyotrophic lateral sclerosis: an update for 2018. *Mayo Clin. Proc.* 93, 1617–1628. doi: 10.1016/j.mayocp.2018.04.007
- Pan, P. L., Liu, Y., Zhang, Y., Zhao, H., Ye, X., and Xu, Y. (2017). Brain gray matter abnormalities in progressive supranuclear palsy revisited. *Oncotarget* 8, 80941–80955. doi: 10.18632/oncotarget.20895
- Pantelis, C., and Brewer, W. J. (2006). "Olfactory impairment in neuropsychiatric disorders," in *Olfaction and the Brain*, eds C. Pantelis, D. Castle, and W. J. Brewer (Cambridge: Cambridge University Press), 259–278. doi: 10.1017/CBO9780511543623.016
- Peckham, M. E., Dashtipour, K., Holshouser, B. A., Kani, C., Boscanin, A., Kani, K., et al. (2016). Novel pattern of iron deposition in the fascicula nigrale in

- patients with Parkinson's disease: a pilot study. *Radiol. Res. Pract.* 2016, 1–7. doi: 10.1155/2016/9305018
- Persson, K., Bohbot, V. D., Bogdanovic, N., Selbæk, G., Brækhus, A., and Engedal, K. (2018). Finding of increased caudate nucleus in patients with Alzheimer's disease. *Acta Neurol. Scand.* 137, 224–232. doi: 10.1111/ane.12800
- Poewe, W., Seppi, K., Tanner, C. M., Halliday, G. M., Brundin, P., Volkman, J., et al. (2017). Parkinson disease. *Nat. Rev. Dis. Prim.* 3:17013. doi: 10.1038/nrdp.2017.13
- Poulin, S. P., Dautoff, R., Morris, J. C., Barrett, L. F., and Dickerson, B. C. (2011). Amygdala atrophy is prominent in early Alzheimer's disease and relates to symptom severity. *Psychiatry Res. Neuroimaging* 194, 7–13. doi: 10.1016/j.pscychres.2011.06.014
- Rajagopalan, V., and Pioro, E. P. (2017). Differential involvement of corticospinal tract (CST) fibers in UMN-predominant ALS patients with or without CST hyperintensity: a diffusion tensor tractography study. *Neuroimage Clin.* 14, 574–579. doi: 10.1016/j.nicl.2017.02.017
- Ravanfar, P., Loi, S., Van Rheen, T., Bush, A., Desmond, P., Cropley, V., et al. (2020). Systematic review protocol: Quantitative susceptibility mapping of brain iron accumulation in neurodegenerative diseases. *medRxiv* 2020.02.18.20022608. doi: 10.1101/2020.02.18.20022608
- Rogers, J. T., Bush, A. I., Cho, H. H., Smith, D. H., Thomson, A. M., Friedrich, A. L., et al. (2008). Iron and the translation of the amyloid precursor protein (APP) and ferritin mRNAs: riboregulation against neural oxidative damage in Alzheimer's disease. *Biochem. Soc. Trans.* 36, 1282–1287. doi: 10.1042/BST0361282
- Rumble, J. R. (Ed.). (2020). "Section: 4[Magnetic susceptibility of the elements and inorganic compounds]," in *CRC Handbook of Chemistry and Physics, 101st Edn. (Internet Version 2020)* (Boca Raton, FL: CRC Press; Taylor & Francis) 1–3.
- Saracoglu, S., Gumus, K., Doganay, S., Koc, G., Kacar Bayram, A., Arslan, D., et al. (2018). Brain susceptibility changes in neurologically asymptomatic pediatric patients with Wilson's disease: evaluation with quantitative susceptibility mapping. *Acta Radiol.* 59, 1380–1385. doi: 10.1177/0284185118759821
- Schofield, M. A., and Zhu, Y. (2003). Fast phase unwrapping algorithm for interferometric applications. *Opt. Lett.* 28:1194. doi: 10.1364/ol.28.001194
- Schweitzer, A. D., Liu, T., Gupta, A., Zheng, K., Seedial, S., Shtilbans, A., et al. (2015). Quantitative susceptibility mapping of the motor cortex in amyotrophic lateral sclerosis and primary lateral sclerosis. *Am. J. Roentgenol.* 204, 1086–1092. doi: 10.2214/AJR.14.13459
- Schweser, F., Deistung, A., Lehr, B. W., and Reichenbach, J. R. (2011). Quantitative imaging of intrinsic magnetic tissue properties using MRI signal phase: an approach to *in vivo* brain iron metabolism? *Neuroimage* 54, 2789–2807. doi: 10.1016/j.neuroimage.2010.10.070
- Schweser, F., Robinson, S. D., de Rochefort, L., Li, W., and Bredies, K. (2017). An illustrated comparison of processing methods for phase MRI and QSM: removal of background field contributions from sources outside the region of interest. *NMR Biomed.* 30. doi: 10.1002/nbm.3604
- Serrano-Pozo, A., Frosch, M. P., Masliah, E., and Hyman, B. T. (2011). Neuropathological alterations in Alzheimer disease. *Cold Spring Harb. Perspect. Med.* 1:a006189. doi: 10.1101/cshperspect.a006189
- Sethi, S. K., Kisch, S. J., Ghassaban, K., Rajput, Ali, Rajput, Alex, Babyn, P. S., Liu, S., Szkup, P., et al. (2019). Iron quantification in Parkinson's disease using an age-based threshold on susceptibility maps: the advantage of local versus entire structure iron content measurements. *Magn. Reson. Imaging* 55, 145–152. doi: 10.1016/j.mri.2018.10.001
- Shahmaei, V., Faeghi, F., Mohammadbeigi, A., Hashemi, H., and Ashrafi, F. (2019). Evaluation of iron deposition in brain basal ganglia of patients with Parkinson's disease using quantitative susceptibility mapping. *Eur. J. Radiol. Open* 6, 169–174. doi: 10.1016/j.ejro.2019.04.005
- Shamseer, L., Moher, D., Clarke, M., Ghersi, D., Liberati, A., Petticrew, M., et al. (2015). Preferred reporting items for systematic review and meta-analysis protocols (PRISMA-P) 2015: elaboration and explanation. *BMJ* 349, 1–25. doi: 10.1136/bmj.g7647
- Shao, N., Yang, J., Li, J., and Shang, H. F. (2014). Voxelwise meta-analysis of gray matter anomalies in progressive supranuclear palsy and Parkinson's disease using anatomic likelihood estimation. *Front. Hum. Neurosci.* 8:63. doi: 10.3389/fnhum.2014.00063
- Sheelakumari, R., Madhusoodanan, M., Radhakrishnan, A., Ranjith, G., and Thomas, B. (2016). A potential biomarker in amyotrophic lateral sclerosis: can assessment of brain iron deposition with SWI and corticospinal tract degeneration with DTI help? *Am. J. Neuroradiol.* 37, 252–258. doi: 10.3174/ajnr.A4524
- Shin, C., Lee, S., Lee, J. Y. Y., Rhim, J. H., and Park, S.-W. W. (2018). Non-motor symptom burdens are not associated with iron accumulation in early parkinson's disease: a quantitative susceptibility mapping study. *J. Korean Med. Sci.* 33:e96. doi: 10.3346/jkms.2018.33.e96
- Sjöström, H., Granberg, T., Westman, E., and Svenningsson, P. (2017). Quantitative susceptibility mapping differentiates between parkinsonian disorders. *Park. Relat. Disord.* 44, 51–57. doi: 10.1016/j.parkreldis.2017.08.029
- Sugiyama, A., Sato, N., Kimura, Y., Fujii, H., Maikusa, N., Shigemoto, Y., et al. (2019). Quantifying iron deposition in the cerebellar subtype of multiple system atrophy and spinocerebellar ataxia type 6 by quantitative susceptibility mapping. *J. Neurol. Sci.* 407:116525. doi: 10.1016/j.jns.2019.116525
- Sulzer, D., Cassidy, C., Horga, G., Kang, U. J., Fahn, S., Casella, L., et al. (2018). Neuromelanin detection by magnetic resonance imaging (MRI) and its promise as a biomarker for Parkinson's disease. *NPJ Park. Dis.* 4:11. doi: 10.1038/s41531-018-0047-3
- Sun, H., Walsh, A. J., Lebel, R. M., Blevins, G., Catz, I., Lu, J. Q., et al. (2015). Validation of quantitative susceptibility mapping with Perls' iron staining for subcortical gray matter. *Neuroimage* 105, 486–492. doi: 10.1016/j.neuroimage.2014.11.010
- Sun, J., Lai, Z., Ma, J., Gao, L., Chen, M., Chen, J., et al. (2019). Quantitative evaluation of iron content in idiopathic rapid eye movement sleep behavior disorder. *Mov. Disord.* 35, 478–485. doi: 10.1002/mds.27929
- Taege, Y., Hagemeyer, J., Bergsland, N., Dwyer, M. G., Weinstock-Guttman, B., Zivadinov, R., et al. (2019). Assessment of mesoscopic properties of magnetic susceptibility and R2*-a pilot study in patients with multiple sclerosis and normal controls. *Neuroimage* 186, 308–320. doi: 10.1016/j.neuroimage.2018.11.011
- Takahashi, H., Snow, B., Bhatt, M. H., Peppard, R., Eisen, A., and Calne, D. B. (1993). Evidence for a dopaminergic deficit in sporadic amyotrophic lateral sclerosis on positron emission scanning. *Lancet* 342, 1016–1018. doi: 10.1016/0140-6736(93)92878-W
- Takahashi, H., Watanabe, Y., Tanaka, H., Mihara, M., Mochizuki, H., Liu, T., et al. (2018a). Quantifying changes in nigrosomes using quantitative susceptibility mapping and neuromelanin imaging for the diagnosis of early-stage Parkinson's disease. *Br. J. Radiol.* 91:20180037. doi: 10.1259/bjr.20180037
- Takahashi, H., Watanabe, Y., Tanaka, H., Mihara, M., Mochizuki, H., Takahashi, K., et al. (2018b). Comprehensive MRI quantification of the substantia nigra pars compacta in Parkinson's disease. *Eur. J. Radiol.* 109, 48–56. doi: 10.1016/j.ejrad.2018.06.024
- Telling, N. D., Everett, J., Collingwood, J. F., Dobson, J., van der Laan, G., Gallagher, J. J., et al. (2017). Iron biochemistry is correlated with amyloid plaque morphology in an established mouse model of Alzheimer's disease. *Cell Chem. Biol.* 24, 1205–1215.e3. doi: 10.1016/j.chembiol.2017.07.014
- Tentolouris-Piperas, V., Ryan, N. S., Thomas, D. L., and Kinnunen, K. M. (2017). Brain imaging evidence of early involvement of subcortical regions in familial and sporadic Alzheimer's disease. *Brain Res.* 1655, 23–32. doi: 10.1016/j.brainres.2016.11.011
- Thomas, G. E. C., Leyland, L. A., Schrag, A. E., Lees, A. J., Acosta-Cabrero, J., and Weil, R. S. (2020). Brain iron deposition is linked with cognitive severity in Parkinson's disease. *J. Neurol. Neurosurg. Psychiatry* 91, 418–425. doi: 10.1136/jnnp-2019-322042
- Tiepol, S., Schäfer, A., Rullmann, M., Roggenhofer, E., Gertz, H. J., Schroeter, M. L., et al. (2018). Quantitative susceptibility mapping of amyloid- β aggregates in Alzheimer's disease with 7T MR. *J. Alzheimer Dis.* 64, 393–404. doi: 10.3233/JAD-180118
- Toosy, A. T., Werring, D. J., Orrell, R. W., Howard, R. S., King, M. D., Barker, G. J., et al. (2003). Diffusion tensor imaging detects corticospinal tract involvement at multiple levels in amyotrophic lateral sclerosis. *J. Neurol. Neurosurg. Psychiatry* 74, 1250–7. doi: 10.1136/jnnp.74.9.1250
- Tuzzi, E., Balla, D. Z., Loureiro, J. R. A., Neumann, M., Laske, C., Pohmann, R., et al. (2020). Ultra-high field MRI in Alzheimer's disease: effective transverse relaxation rate and quantitative susceptibility mapping of human brain *in vivo* and *ex vivo* compared to histology. *J. Alzheimers Dis.* 73:1481–1499. doi: 10.3233/JAD-190424

- Uchida, Y., Kan, H., Sakurai, K., Arai, N., Kato, D., Kawashima, S., et al. (2019). Voxel-based quantitative susceptibility mapping in Parkinson's disease with mild cognitive impairment. *Mov. Disord.* 34, 1164–1173. doi: 10.1002/mds.27717
- Van Bergen, J. M. G., Hua, J., Unschuld, P. G., Lim, I. A. L., Jones, C. K., Margolis, R. L., et al. (2016a). Quantitative susceptibility mapping suggests altered brain iron in premanifest Huntington disease. *Am. J. Neuroradiol.* 37, 789–796. doi: 10.3174/ajnr.A4617
- Van Bergen, J. M. G., Li, X., Hua, J., Schreiner, S. J., Steininger, S. C., Quevenco, F. C., et al. (2016b). Colocalization of cerebral iron with amyloid beta in mild cognitive impairment. *Sci. Rep.* 6:35514. doi: 10.1038/srep35514
- Van Bergen, J. M. G., Li, X., Quevenco, F. C., Gietl, A. F., Treyer, V., Meyer, R., et al. (2018). Simultaneous quantitative susceptibility mapping and flutemetamol-PET suggests local correlation of iron and β -amyloid as an indicator of cognitive performance at high age. *Neuroimage* 174, 308–316. doi: 10.1016/j.neuroimage.2018.03.021
- Wang, C., Foxley, S., Ansoorge, O., Bangert-Christensen, S., Chiew, M., Leonte, A., et al. (2020). Methods for quantitative susceptibility and R2* mapping in whole post-mortem brains at 7T applied to amyotrophic lateral sclerosis. *Neuroimage* 222:117216. doi: 10.1016/j.neuroimage.2020.117216
- Wang, E. W., Du, G., Lewis, M. M., Lee, E. Y., De Jesus, S., Kanekar, S., et al. (2019). Multimodal MRI evaluation of parkinsonian limbic pathologies. *Neurobiol. Aging* 76, 194–200. doi: 10.1016/j.neurobiolaging.2019.01.004
- Wang, Y., and Liu, T. (2015). Quantitative susceptibility mapping (QSM): decoding MRI data for a tissue magnetic biomarker. *Magn. Reson. Med.* 73, 82–101. doi: 10.1002/mrm.25358
- Wang, Y., Spincemaille, P., Liu, Z., Dimov, A., Deh, K., Li, J., et al. (2017). Clinical quantitative susceptibility mapping (QSM): biometal imaging and its emerging roles in patient care. *J. Magn. Reson. Imaging* 46, 951–971. doi: 10.1002/jmri.25693
- Ward, A., Tardiff, S., Dye, C., and Arrighi, H. M. (2013). Rate of conversion from prodromal Alzheimer's disease to Alzheimer's dementia: a systematic review of the literature. *Dement. Geriatr. Cogn. Dis. Extra* 3, 320–332. doi: 10.1159/000354370
- Ward, P. G. D., Harding, I. H., Close, T. G., Corben, L. A., Delatycki, M. B., Storey, E., et al. (2019). Longitudinal evaluation of iron concentration and atrophy in the dentate nuclei in friedreich ataxia. *Mov. Disord.* 34, 335–343. doi: 10.1002/mds.27606
- Weidman, E. K., Schweitzer, A. D., Niogi, S. N., Brady, E. J., Starikov, A., Askin, G., et al. (2019). Diffusion tensor imaging and quantitative susceptibility mapping as diagnostic tools for motor neuron disorders. *Clin. Imaging* 53, 6–11. doi: 10.1016/j.clinimag.2018.09.015
- Welton, T., Maller, J. J., Lebel, R. M., Tan, E. T., Rowe, D. B., and Grieve, S. M. (2019). Diffusion kurtosis and quantitative susceptibility mapping MRI are sensitive to structural abnormalities in amyotrophic lateral sclerosis. *Neuroimage Clin.* 24:101953. doi: 10.1016/j.nicl.2019.101953
- Wender, M., Adamczewska, Z., Gruszczyńska, U., and Dezor, A. (1974). The cerebral copper-protein complexes in hepato-lenticular degeneration studied by means of electron-spin-resonance technique. *Acta Neurol. Scand.* 50, 812–815. doi: 10.1111/j.1600-0404.1974.tb02821.x
- Xiao, Q., Chen, S., and Le, W. (2014). Hyposmia: a possible biomarker of Parkinson's disease. *Neurosci. Bull.* 30, 134–140. doi: 10.1007/s12264-013-1390-3
- Xie, F., Weihua, L., Lirong, O., Wang, X., and Xing, W. (2019). Quantitative susceptibility mapping in spinocerebellar ataxia type 3/Machado-Joseph disease (SCA3/MJD). *Acta Radiol.* 61, 520–527. doi: 10.1177/0284185119868906
- Xuan, M., Guan, X., Gu, Q., Shen, Z., Yu, X., Qiu, T., et al. (2017). Different iron deposition patterns in early- and middle-late-onset Parkinson's disease. *Park. Relat. Disord.* 44, 23–27. doi: 10.1016/j.parkreldis.2017.08.013
- Yu, F., Barron, D. S., Tantiwongkosi, B., and Fox, P. (2015). Patterns of gray matter atrophy in atypical parkinsonism syndromes: a VBM meta-analysis. *Brain Behav.* 5, 1–10. doi: 10.1002/brb3.329
- Yu, J., Qi, F., Wang, N., Gao, P., Dai, S., Lu, Y., et al. (2014). Increased iron level in motor cortex of amyotrophic lateral sclerosis patients: an *in vivo* MR study. *Amyotroph. Lateral Scler. Frontotemporal Degener.* 15, 357–61. doi: 10.3109/21678421.2014.906618
- Zecca, L., Youdim, M. B. H., Riederer, P., Connor, J. R., and Crichton, R. R. (2004). Iron, brain ageing and neurodegenerative disorders. *Nat. Rev. Neurosci.* 5, 863–873. doi: 10.1038/nrn1537
- Zeng, J., Xing, W., Liao, W., and Wang, X. (2019). Magnetic resonance imaging, susceptibility weighted imaging and quantitative susceptibility mapping findings of pantothenate kinase-associated neurodegeneration. *J. Clin. Neurosci.* 59, 20–28. doi: 10.1016/j.jocn.2018.10.090
- Zhang, Y., Long, J. D., Mills, J. A., Warner, J. H., Lu, W., and Paulsen, J. S. (2011). Indexing disease progression at study entry with individuals at-risk for Huntington disease. *Am. J. Med. Genet. Part B Neuropsychiatr. Genet.* 156, 751–763. doi: 10.1002/ajmg.b.31232
- Zhao, X., An, H., Liu, T., Shen, N., Bo, B., Zhang, Z., et al. (2017). Quantitative susceptibility mapping of the substantia nigra in Parkinson's disease. *Appl. Magn. Reson.* 48, 533–544. doi: 10.1007/s00723-017-0877-x

Conflict of Interest: The authors declare that the research was conducted in the absence of any commercial or financial relationships that could be construed as a potential conflict of interest.

Copyright © 2021 Ravanfar, Loi, Syeda, Van Rheenen, Bush, Desmond, Cropley, Lane, Opazo, Moffat, Velakoulis and Pantelis. This is an open-access article distributed under the terms of the Creative Commons Attribution License (CC BY). The use, distribution or reproduction in other forums is permitted, provided the original author(s) and the copyright owner(s) are credited and that the original publication in this journal is cited, in accordance with accepted academic practice. No use, distribution or reproduction is permitted which does not comply with these terms.



Nigral Iron Deposition Is Associated With Levodopa-Induced Dyskinesia in Parkinson's Disease

Tianbin Song^{1,2†}, Jiping Li^{3†}, Shanshan Mei⁴, Xiaofei Jia³, Hongwei Yang^{1,2}, Yongquan Ye⁵, Jianmin Yuan⁶, Yuqing Zhang^{3*} and Jie Lu^{1,2*}

¹ Department of Radiology and Nuclear Medicine, Xuanwu Hospital, Capital Medical University, Beijing, China, ² Beijing Key Laboratory of Magnetic Resonance Imaging and Brain Informatics, Beijing, China, ³ Beijing Institute of Functional Neurosurgery, Xuanwu Hospital, Capital Medical University, Beijing, China, ⁴ Department of Neurology, Xuanwu Hospital, Capital Medical University, Beijing, China, ⁵ UIH America, Inc., Houston, TX, United States, ⁶ Central Research Institute, UIH Group, Shanghai, China

OPEN ACCESS

Edited by:

Yi Wang,
Cornell University, United States

Reviewed by:

Jianqi Li,
East China Normal University, China
Jinyoung Youn,
Sungkyunkwan University School
of Medicine, South Korea
Alexander Shtilbans,
Hospital for Special Surgery,
United States

*Correspondence:

Yuqing Zhang
yuzqzhang@vip.163.com
Jie Lu
imaginglu@hotmail.com

[†] These authors have contributed
equally to this work and share first
authorship

Specialty section:

This article was submitted to
Brain Imaging Methods,
a section of the journal
Frontiers in Neuroscience

Received: 29 December 2020

Accepted: 16 February 2021

Published: 22 March 2021

Citation:

Song T, Li J, Mei S, Jia X, Yang H,
Ye Y, Yuan J, Zhang Y and Lu J (2021)
Nigral Iron Deposition Is Associated
With Levodopa-Induced Dyskinesia
in Parkinson's Disease.
Front. Neurosci. 15:647168.
doi: 10.3389/fnins.2021.647168

Objective: To investigate iron deposition in the substantia nigra (SN) of Parkinson's disease (PD) patients associated with levodopa-induced dyskinesia (LID).

Methods: Seventeen PD patients with LID, 17 PD patients without LID, and 16 healthy controls were recruited for this study. The mean QSM values of the whole, left, and right SN were compared among the three groups. A multivariate logistic regression model was constructed to determine the factors associated with increased risk of LID. The receiver operating characteristic curve of the QSM value of SN in discriminating PD with and without LID was evaluated.

Results: The mean QSM values of the whole and right SN in the PD with LID were higher than those in the PD without LID (**P* = 0.03, **P* = 0.03). Multivariate logistic regression analysis revealed that the QSM value of whole, left, or right SN was a predictor of the development of LID (**P* = 0.03, **P* = 0.04, and **P* = 0.04). The predictive accuracy of LID in adding the QSM value of the whole, left, and right SN to LID-related clinical risk factors was 70.6, 64.7, and 67.6%, respectively. The QSM cutoff values between PD with and without LID of the whole, left, and right SN were 148.3, 165.4, and 152.7 ppb, respectively.

Conclusion: This study provides the evidence of higher iron deposition in the SN of PD patients with LID than those without LID, suggesting that the QSM value of the SN may be a potential early diagnostic neuroimaging biomarker for LID.

Keywords: Parkinson's disease, dyskinesia, levodopa, quantitative susceptibility mapping, substantia nigra

INTRODUCTION

Parkinson's disease (PD) is a progressive movement disorder caused primarily by the loss of nigrostriatal neurons and depletion of dopamine (Thomas and Beal, 2007). Dopamine replacement therapeutics, such as levodopa, relieve the symptoms of PD but can lead to a motor complication known as levodopa-induced dyskinesia (LID), which is a major cause of disability in PD patients

(Pahwa et al., 2019). LID is observed in approximately 90% of PD patients after 10 years of levodopa treatment (Manson et al., 2012).

Iron is essential for normal brain functions, but iron overload has been highly implicated in the pathology and pathogenesis of PD. Biochemical and neuroimaging studies have shown increased iron deposition in the nigrostriatal pathway in PD patients, specifically in the substantia nigra (SN) (Rouault, 2013; Ward et al., 2014; Du et al., 2016; Acosta-Cabronero et al., 2017). Iron deposition in the SN in PD patients, determined *via* quantitative susceptibility mapping (QSM) of iron-sensitive magnetic resonance imaging (MRI) (Homayoon et al., 2019; Sun et al., 2020), was significantly higher than that in healthy people and in patients with idiopathic rapid eye movement sleep behavior disorder, dystonia, and essential tremor. Iron deposition also contributes to the clinical motor symptoms of PD (Martin et al., 2008; He et al., 2015). An existing study also showed that the $R2^*$ value of SN in PD patients with LID was higher than those without LID (Lewis et al., 2013). However, the association between the iron content of SN measured by QSM and the LID is still unclear.

Therefore, this study aimed at using QSM to investigate the iron deposition difference in SN between PD patients with and without LID and to determine whether iron deposition in the SN is a potential neuroimaging biomarker of LID event.

MATERIALS AND METHODS

Subjects

Thirty-four PD patients (17 with LID and 17 without LID) who were prepared to undergo deep brain stimulation surgery were recruited from the functional neurosurgery department of the Xuanwu Hospital of Capital Medical University. All PD patients were evaluated using the Movement Disorder Society's revision of the Unified Parkinson's Disease Rating Scale (MDS-UPDRS) Part III for motor symptoms in the medication-off state (Postuma et al., 2015), after at least a 12-h overnight withdrawal from dopaminergic medication, the Unified Dyskinesia Rating Scale (UDysRS) for dyskinesia in on and off state, and UPDRS Part IV for severity of motor fluctuation. All PD patients belong to akinetic rigid subtype. All assessments were performed by a single trained neurologist (10 years). The inclusion criteria for PD patients were as follows: (1) meeting the MDS clinical diagnostic criteria of PD (Postuma et al., 2015), (2) had undergone levodopa treatment for at least 6 months and stable medication dose for at least 4 weeks, and (3) with no history of cerebrovascular disease, seizures, brain surgery, and psychiatric disorders. PD patients with evident cerebral lesions on MRI structural images and evident motion artifacts in QSM images were excluded. PD patients with a score of MDS-UPDRS Part IV item 33 ≥ 1 were included in the LID group, and the rest with a score of zero were included in the PD without LID group. Sixteen age- and sex-matched healthy controls (HCs) were recruited from the local community. All of the HCs had normal movement function and no neurological or psychiatric diseases (Table 1). All experiments

in this study were approved by the Institutional Review Board of Xuanwu Hospital. All participants signed informed consent forms prior to the experiment.

MRI Data Acquisition

Magnetic resonance imaging data acquisition was performed using a hybrid 3.0-T PET/MR scanner (uPMR790, UIH, Shanghai, China) with a 24-channel head/neck coil. A three-dimensional (3D) multi-echo gradient-echo (GRE) sequence was used for QSM data acquisition with the following parameters: FA = 15° , voxel size = $1\text{ mm} \times 1\text{ mm} \times 2\text{ mm}$ (interpreted as 1 mm^3), repetition time = 29 ms, six echo times = 3.1/6.4/9.7/13.0/16.3/19.6 ms, and bandwidth = 500 Hz/px, acquisition matrix: 256×256 , number of slices: 68, slice orientation: F-H, parallel imaging, acceleration factor: 2, and monopolar readout gradients were used with a total scan time of 5 min and 41 s. T2-weighted imaging (T2WI), diffusion-weighted imaging, and 3D T1-weighted imaging (T1WI) data were also collected from all participants. During data acquisition, the participant's head was stabilized with foam pads on both sides to reduce motion. All PD patients were scanned during their off-state condition (12 h after last medication).

QSM Image Processing

The multi-echo GRE data were used for the QSM calculation. The B0 field map was extracted using the multidimensional integration method, unwrapped of aliased phases using seed prioritized unwrapping (SPUN) (Ye et al., 2019), and the background field was removed using vSHARP. QSM was obtained by solving the L1 regularization problem using the precondition conjugate gradient method (Bilgic et al., 2014), with an extra term for streaking artifact suppression (Li et al., 2015) and dynamic Bayesian regularization (De Rochefort et al., 2010). We used CSF as the reference tissue, as suggested in the review article (Haacke et al., 2015). To draw the CSF reference region of interest (ROI), first the short TE magnitude images of the multi-echo GRE was selected, which showed a clear boundary of the CSF. Then, we manually drew the ROI on this short TE magnitude image, placed it centrally in the cerebrospinal fluid of the lateral ventricles and avoided other non-CSF contents. Then, this ROI was directly copied to the QSM image of the same slice, which was calculated from the same data and thus was strictly aligned with each other. For each case, three or more CSF ROIs were determined, and the mean QSM value from these ROIs was used as the final reference.

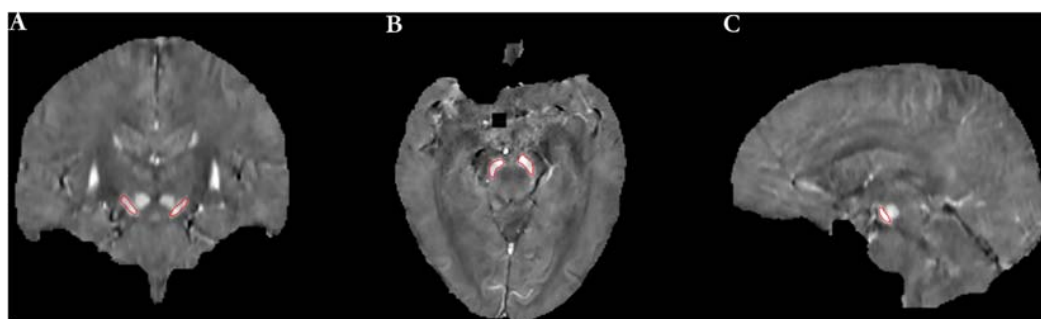
Regions of Interest

Reference region of interests were manually drawn on left and right SN as shown in Figure 1 and were used to extract QSM values. When drawing ROIs on bilateral SNs, the first and last slices of SN were discarded, and those remaining consecutive slices showing portions of the SN with clear and visible boundaries were used. As a result, generally four to five slices were measured for each case. To assess the inter-rater reliability of the ROIs, two radiologists were instructed to draw the ROIs independently. Mean QSM values of the left and right

TABLE 1 | Demographic and clinical characteristics of the study participants and mean QSM values in whole, left, and right SN.

	PD with LID	PD without LID	HCS	ANOVA	P value (post hoc)		
	(n = 17)	(n = 17)	(n = 16)	P value	LID vs without LID	LID vs HCs	Without LID vs HCs
Age (years old)	63.88 ± 4.64	65.2 ± 7.18	61.06 ± 4.42	0.11	—	—	—
Age of onset	55 ± 5.21	54.88 ± 10.85	—	0.94	—	—	—
Gender (female)	17 (12)	17 (12)	16 (10)	0.85	—	—	—
BMI (kg/m ²)	23.98 ± 0.90	23.53 ± 1.21	23.75 ± 2.43	0.94	—	—	—
Onset of motor symptom	10L/7R	7L/10R	—	0.49	—	—	—
Disease duration (years)	9 ± 2.52	8.53 ± 3.41	—	0.65	—	—	—
H-Y stage	2.85 ± 0.63	2.79 ± 0.64	—	0.79	—	—	—
Duration of levodopa therapy (years)	7.53 ± 2.15	7.06 ± 3.61	—	0.65	—	—	—
MDS-UPDRS III score	50.29 ± 10.43	63.24 ± 10.78	—	0.04*	—	—	—
UPDRS IV score	9.9 ± 2.1	5.5 ± 3.6	—	<0.01**	—	—	—
LEDD (mg/day)	1,099 ± 581	814 ± 359	—	0.09	—	—	—
LEDD of levodopa (mg/day)	540 ± 164	509 ± 137	—	0.56	—	—	—
UDysRS total score	23.59 ± 9.86	—	—	—	—	—	—
UDysRS score on off state	6.3 ± 4.2 (10/17)	—	—	—	—	—	—
LID duration (months)	25.52 ± 14.40	—	—	—	—	—	—
Whole SN (ppb)	162.36 ± 26.85	140.25 ± 26.85	113.23 ± 21.5	<0.01**	0.03*	<0.01**	<0.01**
Left SN (ppb)	159.17 ± 29.68	139.47 ± 29.68	108.07 ± 24.43	<0.01**	0.09	<0.01**	<0.01**
Right SN (ppb)	165.55 ± 28.51	141.03 ± 28.518	118.40 ± 21.23	<0.01**	0.03*	<0.01**	0.02*

The values presented are the number of patients or mean ± standard deviation. LID, levodopa-induced dyskinesia; MMSE, Mini-Mental State Exam; PD, Parkinson's disease; H-Y stage, Hoehn-Yahr stage; MDS-UPDRS III, Part III of Movement Disorder Society's Revision of the Unified Parkinson's Disease Rating Scale (MDS-UPDRS); LEDD, levodopa equivalent daily dose; UDysRS, Unified Dyskinesia Rating Scale; HCs, healthy controls. ppb, parts per billion; L, left; R, right; BMI, body mass index. *P < 0.05 and **P < 0.01 were considered statistically significant.

**FIGURE 1** | The definition of regions of interest (ROIs) included the left and right SN [(A) coronal image, (B) axial image, and (C) sagittal image].

SN were measured, and the average of the two was used as the mean QSM value of the whole SN.

Statistical Analysis

The intraclass correlation coefficient (ICC) was used to evaluate the inter-rater reliability of the measured QSM value of left and right SN. An ICC value of over 0.81 was considered to indicate excellent agreement, 0.61–0.80 good agreement, 0.41–0.60 moderate agreement, 0.21–0.40 fair agreement, and less than 0.20 poor agreement. ICC values were calculated by using the International Business Machines Statistical Package for the Social Sciences (SPSS) version 17.0 software.

The demographic characteristics were compared among the three groups, and the chi-squared test was applied for sex, onset side of motor symptom, and analysis of variance (ANOVA)

analysis for age and age of onset. Two-tailed *t* tests were performed to compare disease duration, duration of levodopa therapy, H-Y stage, MDS-UPDRS III score, MDS-UPDRS IV score, levodopa equivalent daily dose (LEDD), and LEDD of levodopa between PD patients with and without LID. The mean QSM values of the whole SN, left SN, and right SN were compared by using ANOVA among the three groups, respectively. Statistical analysis was performed using GraphPad Prism 7.0.

Multiple variables were included in a multivariate logistic regression model analysis to determine the independent risk factors associated with LID, including iron content of the whole SN, sex, body mass index (BMI), disease duration, duration of levodopa therapy, age of onset, and LEDD/LEDD of levodopa, as well as left and right SN, respectively. First, multivariate logistic regression model analysis was used to calculate the diagnostic

accuracy rate of all clinical risk factors. Second, we added the iron content of SN into all these clinical risk factors to perform a multivariate logistic regression model analysis. The effect of the iron content of SN on the predictive accuracy rate of LID was evaluated. Statistical analysis was performed using the SPSS for Windows (version 17.0, SPSS Inc., Chicago, IL, United States).

The discriminative power of the QSM value on LID was evaluated in the whole, left, and right SN, respectively, by the receiver operating characteristic curve. Pearson's correlation analysis was used to study the association between the QSM values of whole, left, and right SN and clinical assessments (UDysRS total score and LID duration) in the PD with LID group, respectively. Statistical analysis was performed using GraphPad Prism 7.0. $P < 0.05$ was considered a statistically significant difference.

RESULTS

Participants' Characteristics

Demographic details are summarized in **Table 1**. There were no significant differences in almost all clinical and demographic data between the groups of PD patients with and without LID, or the HCs ($P > 0.05$), except for UPDRS III and IV scores between PD patients with and without LID ($*P = 0.04 < 0.05$, and $**P < 0.01$). Also, no significant associations were observed between the QSM values of SN and UPDRS III scores in both PD groups ($P > 0.05$, $P > 0.05$). UPDRS III score of PD without LID was slightly higher than PD with LID in this study. UPDRS IV score of PD with LID was slightly higher than PD without LID in this study.

Test-Retest Reliability Analysis

The test-retest reliability of the ROI drawn manually by two radiologists was evaluated by ICC analysis. The ICC value of consistency in the left and right SN between them was 0.95 and 0.97, respectively, indicating excellent intra-rater agreement.

Comparison of the Mean QSM Value of SN Among Three Groups

The mean QSM values of the left and right SN in each group are shown in **Table 1** and **Figure 2**. PD with LID had significantly higher QSM values in the right and whole SN than PD without LID ($*P = 0.03 < 0.05$, and $*P = 0.03 < 0.05$) and HCs ($**P < 0.01$ and $**P < 0.01$). PD without LID had a significantly higher QSM value in the left, right, and whole SN than that of HCs ($**P < 0.01$, $**P < 0.01$, and $*P = 0.02 < 0.05$), but no significant difference was found in the left SN between PD with and without LID ($P > 0.05$). UPDRS IV score was added as a covariate to compare the difference between PD patients with LID and without LID group, significant difference in the QSM value of left SN was found between PD patients with LID and without LID groups ($t = 6.131$, $*P = 0.02 < 0.05$), there was no significant difference in the QSM value of whole SN but the P value is close to 0.05 between two groups ($t = 3.902$, $P = 0.057 \approx 0.05$), and no significant difference in the QSM value of right SN was found between two groups ($t = 2.690$, $P = 0.11 > 0.05$).

Multivariate Logistic Regression Analysis for LID Related Risk Factors

The predictive accuracy of LID to LID-related clinical risk factors, with added factors of the QSM value of whole and left and right SN, was 70.6, 64.7, and 67.6% respectively. Also, iron deposition of the whole, left, and right SN can be considered as an independent predictor of LID ($*P < 0.05$, $*P < 0.05$, and $*P < 0.05$) (**Tables 2, 3**).

Receiver Operating Characteristic Curve Analysis for QSM Value in Discriminative Efficacy Among Three Groups

The discriminative power of the QSM value in the whole, left, and right SN among three groups is shown in **Figure 3**. The cutoff value of the whole SN QSM for discrimination between PD patients with LID and HCs was 127.3 ppb (accuracy, 0.9301; sensitivity, 0.8824; specificity, 0.8124) ($**P < 0.01$). This QSM cutoff value was 117.7 ppb (accuracy, 0.9044; sensitivity, 0.9412; specificity, 0.75) ($**P < 0.01$) and 146.9 ppb (accuracy, 0.9228; sensitivity, 0.7647; specificity, 0.9375) ($**P < 0.01$) for left and right SN, respectively. Between PD without LID and HC groups, the QSM cutoff values were 137.2 ppb (accuracy, 0.7904; sensitivity, 0.5882; specificity, 0.875) ($**P < 0.01$), 106.6 ppb (accuracy, 0.8125; sensitivity, 0.9412; specificity, 0.5625) ($**P < 0.01$), and 115.3 ppb (accuracy, 0.7592; sensitivity, 0.7647; and specificity, 0.625) ($*P = 0.01 < 0.05$) in the whole, left, and right SN, respectively. Between PD groups with and without LID, the QSM cutoff values were 148.3 ppb (accuracy, 0.7163; sensitivity, 0.7647; specificity, 0.5882) ($*P = 0.03 < 0.05$), 165.4 ppb (accuracy, 0.7059; sensitivity, 0.5294; specificity, 0.8235) ($*P = 0.04 < 0.05$), and 152.7 ppb (accuracy, 0.7024; sensitivity, 0.7059; specificity, 0.6471) ($*P = 0.04 < 0.05$) in the whole, left, and right SN, respectively.

Associations Between the QSM Value of the SN and UDysRS or LID Duration

No significant correlation was observed between the QSM values of the SN and UDysRS total scores (whole SN, $R = -0.26$ and $P = 0.31 > 0.05$; left SN, $R = -0.21$ and $P = 0.42 > 0.05$; right SN, $R = -0.33$ and $P = 0.20 > 0.05$, respectively) or between the QSM values of the SN and LID duration (whole SN, $R = -0.21$ and $P = 0.43 > 0.05$; left SN, $R = 0.18$ and $P = 0.50 > 0.05$; right SN, $R = -0.20$ and $P = 0.43 > 0.05$, respectively).

DISCUSSION

Iron deposition in the whole and right SN was significantly higher in PD patients with LID compared to PD patients without LID and HCs, but it was not associated with the severity of LID or LID duration. Our results also revealed that iron deposition of the whole, left, and right SN was an independent risk factor of LID among LID-related clinical risk factors of iron content of SN, sex, disease duration, duration of levodopa therapy, age at onset, LEDD, and LEDD of levodopa.

We should study the structure of SN, which highly expresses D1 and D2 receptors, though most studies focused on the striatum. Studies on dyskinetic rats revealed a relationship between the expression of abnormal involuntary movements and elevated level of extracellular GABA in SN (Mela et al., 2007), which suggests that GABA released from nigrostriatal neurons generates LID. Elevated released levels of GABA in SNr were induced by L-DOPA, reflecting hyperactivity of nigrostriatal pathway, which suggests that hyperactivity plays

an important role in LID event (Cenci, 2007). D1 and D2 receptor blocked in SNr reduced LID event that happened, which suggests that SN generates dyskinesia. L-DOPA can be converted to DA in SNr (Sarre et al., 1998), and L-DOPA administration leads to elevated level of extracellular DA in SNr and striatum of rats with dyskinesia (Lindgren et al., 2010; Mela et al., 2012).

Iron is an essential element involved in numerous neurobiological processes in the human brain (Jenner, 2008;

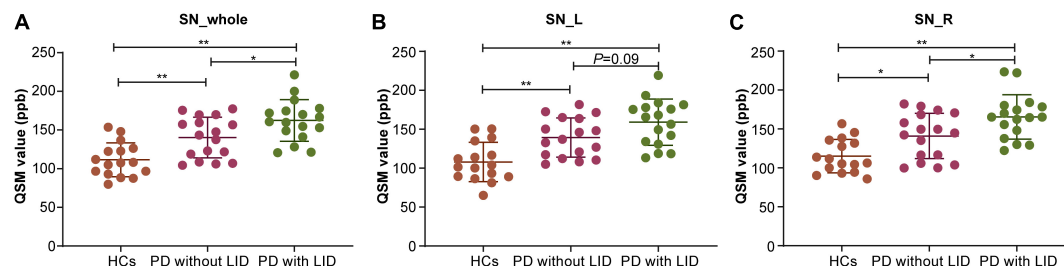


FIGURE 2 | Compare mean quantitative susceptibility mapping (QSM) value of the whole, left, and right SN among the three groups. **(A)** Analysis of variance (ANOVA) analysis of QSM value in the whole SN (SN_{whole}): Parkinson's disease (PD) with levodopa-induced dyskinesia (LID) > PD without LID > healthy controls (HCs) (* $P_{LIDvswithoutLID} < 0.05$, ** $P_{LID} vs HCs < 0.01$, ** $P_{withoutLID} vs HCs < 0.01$). **(B)** ANOVA analysis of QSM value in the left SN (SN_L): PD with LID > HCs (** $P_{LIDvsHCs} < 0.01$) and PD without LID > HCs (** $P_{withoutLIDvsHCs} < 0.01$). **(C)** ANOVA analysis of QSM value in the right SN (SN_R): PD with LID > PD without LID > HCs (* $P_{LID} vs withoutLID < 0.05$, ** $P_{LIDvsHCs} < 0.01$, * $P_{withoutLIDvsHCs} < 0.05$).

TABLE 2 | Multivariate logistic regression analysis of risk factors correlated to LID event among 34 PD patients.

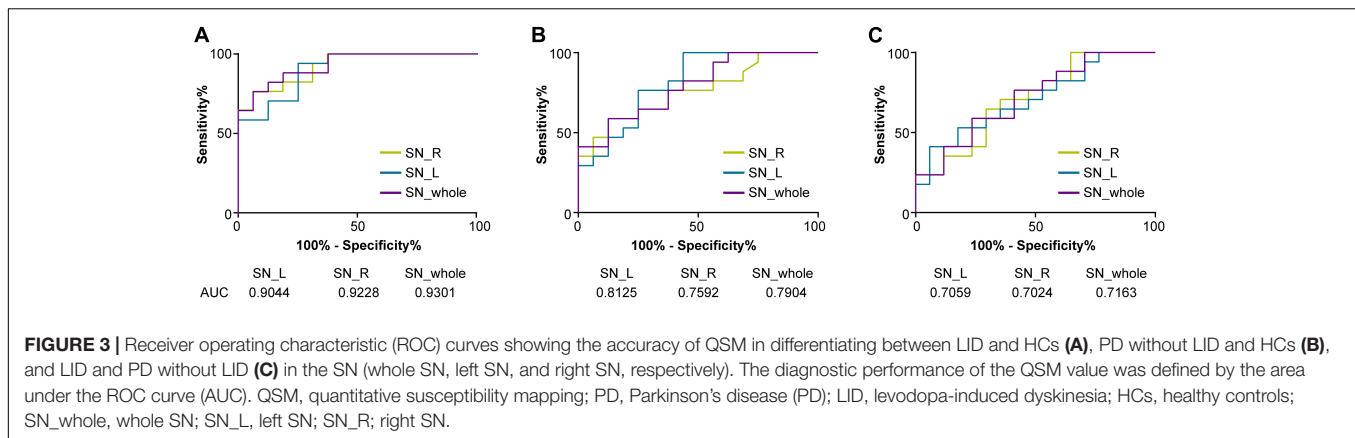
	Whole SN		Left SN		Right SN	
	OR (95% CI)	P value	OR (95% CI)	P value	OR (95% CI)	P value
QSM value	1.038 (1.003–1.074)	0.03*	1.033 (1.002–1.065)	0.04*	1.035 (1.002–1.070)	0.04*
Age of onset	0.993 (0.890–1.107)	0.90	0.993 (0.889–1.111)	0.91	0.988 (0.887–1.100)	0.83
Sex	1.828 (0.255–13.098)	0.55	1.741 (0.257–11.808)	0.57	2.009 (0.280–14.402)	0.49
BMI	1.028 (0.844–1.252)	0.78	1.013 (0.832–1.233)	0.90	1.046 (0.862–1.270)	0.65
Disease duration	1.032 (0.549–1.942)	0.92	1.105 (0.628–1.945)	0.73	1.004 (0.516–1.953)	0.99
Duration of levodopa therapy	0.916 (0.494–1.701)	0.78	0.888 (0.498–1.583)	0.69	0.924 (0.489–1.745)	0.81
LEDD	1.002 (1.000–1.004)	0.09	1.002 (1.000–1.004)	0.07	1.002 (1.000–1.004)	0.11

Data were analyzed using multivariate logistic regression analysis [adapted factors: quantitative susceptibility mapping value, age of onset, sex, disease duration (years), duration of levodopa therapy (years), and levodopa equivalent daily dose (mg/day), LEDD]. BMI, body mass index; OR, odds ratio; CI, confidence interval. * $P < 0.05$ was considered statistically significant.

TABLE 3 | Multivariate logistic regression analysis of risk factors correlated to LID event among 34 PD patients.

	Whole SN		Left SN		Right SN	
	OR (95% CI)	P value	OR (95% CI)	P value	OR (95% CI)	P value
QSM value	1.038 (1.003–1.074)	0.03*	1.032 (1.002–1.064)	0.04*	1.036 (1.004–1.069)	0.03*
Age of onset	1.020 (0.921–1.130)	0.70	1.023 (0.922–1.134)	0.67	1.015 (0.917–1.123)	0.78
Sex	0.777 (0.134–4.491)	0.78	0.769 (0.139–4.249)	0.76	0.869 (0.153–4.945)	0.87
BMI	0.998 (0.814–1.224)	0.98	0.977 (0.799–1.194)	0.82	1.022 (0.835–1.251)	0.83
Disease duration	1.020 (0.921–1.130)	0.70	0.957 (0.586–1.563)	0.86	0.87 (0.488–1.551)	0.64
Duration of levodopa therapy	1.123 (0.659–1.912)	0.67	1.098 (0.665–1.813)	0.71	1.127 (0.649–1.956)	0.67
LEDD of levodopa	1.003 (0.997–1.008)	0.35	1.003 (0.998–1.008)	0.29	1.002 (0.997–1.007)	0.46

Data were analyzed using multivariate logistic regression analysis [adapted factors: quantitative susceptibility mapping value, age of onset, sex, disease duration (years), duration of levodopa therapy (years), and levodopa equivalent daily dose (mg/day), LEDD]. BMI, body mass index; OR, odds ratio; CI, confidence interval. * $P < 0.05$ was considered statistically significant.



Prashanth et al., 2011). However, iron can also be detrimental by causing oxidative stress *via* redox reactions, which can even lead to neuronal apoptosis in iron-overloaded cells (Cozzi et al., 2019). The accumulation of iron was confirmed to be related to the pathophysiology of PD, such as the loss of dopaminergic neurons in the SN and the presence of α -synuclein-rich Lewy bodies (Dexter et al., 1991; Bisaglia et al., 2014; Murakami et al., 2015). Previous studies have revealed that the iron content of the SN is increased in PD patients (Kordower et al., 2013; Guan et al., 2017). Excessive iron deposition contributes to the dysfunction of the nigrostriatal pathway, which is related to motor dysfunction in PD patients (Martin et al., 2008; He et al., 2015; Hare and Double, 2016), but previous studies have not reported the relationship between SN cell loss and LID event. Nigral cell degeneration leads to the function alterations of basal ganglia, which is a cause of dyskinesia, and the degeneration extent of SN may regulate the duration of drug exposure, which induces dyskinesia (Jenner, 2008).

The previous study showed that the $R2^*$ value of SN in PD with LID was higher than PD without LID (Lewis et al., 2013). However, it has been shown that QSM is more sensitive than $R2^*$ mapping in the detection of the increased iron levels of SN in PD patients (Deistung et al., 2013; Barbosa et al., 2015; Du et al., 2016). In the present study, we directly compared the QSM value of SN between PD with LID and without LID, and found that the QSM values of the whole and right SN of PD with LID was significantly higher than that of PD without LID. It demonstrates that excess iron deposition in the SN actually happens in PD patients with LID, which is an important factor that contributes to the LID event. We also found that iron depositions in the whole, left, and right SN of PD with the LID and without LID groups are both significantly higher than that of HCs, which demonstrated that iron deposition of SN in patients with PD is higher than that in HCs, which is consistent with a previous study (Du et al., 2016). However, we did not find that iron deposition in the left SN in PD with LID being higher than that of PD without LID, which was not reported by previous studies. No relationships between the $R2^*$ value of SN and levodopa dosage, UPDRS-III score, LEDD, and disease duration were reported in either PD with LID or without LID in a previous study (Du et al., 2016), nor did those clinical scores associated with

QSM values of the whole, left, and right SN in either PD with LID or without LID.

Levodopa-induced dyskinesia is a common and potentially disabling complication of levodopa treatment in patients with PD. Evidence indicates that LID occurs in response to pulsatile dopaminergic stimulation together with the short half-life of levodopa (Espay et al., 2018). The younger age of onset, longer disease duration, higher levodopa dose, and longer duration of levodopa therapy are considered major clinical risk factors for LID (Zappia and Quattrone, 2008; Warren et al., 2013; Cilia et al., 2014; Perez-Lloret et al., 2017; Matarazzo et al., 2018; Picconi et al., 2018). Young PD patients had a higher risk of LID than PD patients with old age of onset (Kumar et al., 2005; Dhall and Kreitzman, 2016). We analyzed the effect of iron content of SN on all the above clinical risk factors and found that the QSM value of the whole SN showed high accuracy in discriminating PD with LID and HCs (whole SN, 0.9273; left SN, 0.9066; right SN, 0.91) and PD with LID and without LID (whole SN, 0.7163; left SN, 0.7059; right SN, 0.7024). The QSM cutoff value of the SN may help predict LID event in PD progression. We found that the QSM cutoff value of the whole SN, which was 127.3 ppb, can discriminate between PD with LID and HCs (sensitivity, 88.24%; specificity, 81.24%), and for the left and right SN, the cutoff values were 117.7 ppb (sensitivity, 94.12%; specificity, 75%) and 146.9 ppb (sensitivity, 76.47%; specificity, 93.75%), respectively. The QSM cutoff value of the whole SN, left SN, and right SN was 148.3 ppb (sensitivity, 76.47%; specificity, 58.82%), 165.4 ppb (sensitivity, 52.94%; specificity, 82.35%), and 152.7 ppb (sensitivity, 70.59%; specificity, 64.71%) in discrimination between PD with and without LID, respectively. These findings suggest that the QSM value of SN can well discriminate between PD patients with LID and without LID; this may suggest that PD patients with a low QSM value in the SN were less prone to develop LID.

We also investigated the correlations between the iron content of SN with UDysRS score and LID duration. No significant associations between them were found, suggesting that iron deposition in the SN is not associated with the severity and duration of LID.

Despite these strengths, the main limitation of our study was the small sample size. Larger cohorts will be further recruited to validate the results, and longitudinal prospective evaluation of changes of the iron deposition over time in LID patients is needed to be studied in the future. The correlation between the QSM value of the sub-regions of the SN, such as pars compacta and pars reticulata, and LID also needs to be further studied in the future. The correlation between the loss of DA neurons and iron deposition of SN in PD with LID should be studied in the future. The difference in the QSM value of SN among off period dystonia, peak dose dyskinesia, and diphasic dyskinesia of LID groups also needs to be further studied in the future.

CONCLUSION

In conclusion, our study revealed that iron deposition in the SN was significantly higher in PD patients with LID than in those without LID by using the QSM method, but it was not associated with the severity of LID. Iron deposition in the SN measured by QSM sequence is a potential neuroimaging biomarker of LID event.

DATA AVAILABILITY STATEMENT

The raw data supporting the conclusions of this article will be made available by the authors, without undue reservation.

REFERENCES

- Acosta-Cabrero, J., Cardenas-Blanco, A., Betts, M. J., Butryn, M., Valdes-Herrera, J. P., Galazky, I., et al. (2017). The whole-brain pattern of magnetic susceptibility perturbations in Parkinson's disease. *Brain* 140, 118–131. doi: 10.1093/brain/aww278
- Barbosa, J. H., Santos, A. C., Tumas, V., Liu, M., and Zheng, W. (2015). Quantifying brain iron deposition in patients with Parkinson's disease using quantitative susceptibility mapping, R2 and R2*. *Magn. Reson. Imaging* 33, 559–565. doi: 10.1016/j.mri.2015.02.021
- Bilgic, B., Fan, A. P., Polimeni, J. R., Cauley, S. F., Bianciardi, M., Adalsteinsson, E., et al. (2014). Fast quantitative susceptibility mapping with L1-regularization and automatic parameter selection. *Magn. Reson. Med.* 72, 1444–1459. doi: 10.1002/mrm.25029
- Bisaglia, M., Filograna, R., Beltrami, M., and Bubacco, L. (2014). Are dopamine derivatives implicated in the pathogenesis of Parkinson's disease? *Ageing Res. Rev.* 13, 107–114. doi: 10.1016/j.arr.2013.12.009
- Cenci, M. A. (2007). L-DOPA-induced dyskinesia: cellular mechanisms and approaches to treatment. *Park. Relat. Disord.* 13(Suppl. 3), S263–S267. doi: 10.1016/S1353-8020(08)70014-2
- Cilia, R., Akpalu, A., Sarfo, F. S., Cham, M., Amboni, M., Cereda, E., et al. (2014). The modern pre-levodopa era of Parkinson's disease: insights into motor complications from sub-Saharan Africa. *Brain* 137, 2731–2742. doi: 10.1093/brain/awu195
- Cozzi, A., Orellana, D. I., Santambrogio, P., Rubio, A., Cancellieri, C., Giannelli, S., et al. (2019). Stem cell modeling of neuroferritinopathy reveals iron as a determinant of senescence and ferroptosis during neuronal aging. *Stem Cell Rep.* 13, 832–846. doi: 10.1016/j.stemcr.2019.09.002
- De Rochefort, L., Liu, T., Kressler, B., Liu, J., Spincemaille, P., Lebon, V., et al. (2010). Quantitative susceptibility map reconstruction from MR phase data using bayesian regularization: validation and application to brain imaging. *Magn. Reson. Med.* 63, 194–206. doi: 10.1002/mrm.22187

ETHICS STATEMENT

The studies involving human participants were reviewed and approved by all experiments in this study were approved by the Institutional Review Board of Xuanwu Hospital. The patients/participants provided their written informed consent to participate in this study.

AUTHOR CONTRIBUTIONS

TS and JL: execution of the project, statistical analysis, interpretation of data, and first draft of the manuscript. SM: review and critique of statistical analysis. XJ and YY: statistical analysis. HY: performed MR scan and statistical analysis. JY: review and critique of statistical analysis. YZ: conception of the project and review and critique of the manuscript. JL: conception and organization of the project, review and critique of the manuscript. All authors contributed to the article and approved the submitted version.

FUNDING

This study was supported by Beijing Municipal Administration of Hospitals' Ascent Plan (Grant No. DFL20180802) and Wu Jieping Medical Foundation (320.6750.19089-78).

- Deistung, A., Schäfer, A., Schweser, F., Biedermann, U., and Turner, R. (2013). Toward in vivo histology: a comparison of quantitative susceptibility mapping (QSM) with magnitude-, phase-, and R2*-imaging at ultra-high magnetic field strength. *Neuroimage* 65, 299–314. doi: 10.1016/j.neuroimage.2012.09.055
- Dexter, D. T., Carayon, A., Javoy-Agid, F., Agid, Y., and Wells, F. R. (1991). Alterations in the levels of iron, ferritin and other trace metals in Parkinson's disease and other neurodegenerative diseases affecting the basal ganglia. *Brain* 114(Pt 4), 1953–1975. doi: 10.1093/brain/114.4.1953
- Dhall, R., and Kreitzman, D. L. (2016). Advances in levodopa therapy for Parkinson disease: review of RYTARY (carbidopa and levodopa) clinical efficacy and safety. *Neurology* 86, S13–S24. doi: 10.1212/WNL.0000000000002510
- Du, G., Liu, T., Lewis, M. M., Kong, L., and Wang, Y. (2016). Quantitative susceptibility mapping of the midbrain in Parkinson's disease. *Mov. Disord.* 31, 317–324. doi: 10.1002/mds.26417
- Espay, A. J., Morgante, F., Merola, A., Fasano, A., and Marsili, L. (2018). Levodopa-induced dyskinesia in Parkinson's disease: current and evolving concepts. *Ann. Neurol.* 84, 797–811. doi: 10.1002/ana.25364
- Guan, X., Xuan, M., Gu, Q., Huang, P., Liu, C., Wang, N., et al. (2017). Regionally progressive accumulation of iron in Parkinson's disease as measured by quantitative susceptibility mapping. *NMR Biomed.* 30:10.1002/nbm.3489. doi: 10.1002/nbm.3489
- Haacke, E. M., Liu, S., Buch, S., Zheng, W., Wu, D., and Ye, Y. (2015). Quantitative susceptibility mapping: current status and future directions. *Magn. Reson. Imaging* 33, 1–25. doi: 10.1016/j.mri.2014.09.004
- Hare, D. J., and Double, K. L. (2016). Iron and dopamine: a toxic couple. *Brain* 139, 1026–1035. doi: 10.1093/brain/aww022
- He, N., Ling, H., Ding, B., Huang, J., and Zhang, Y. (2015). Region-specific disturbed iron distribution in early idiopathic Parkinson's disease measured by quantitative susceptibility mapping. *Hum. Brain Mapp.* 36, 4407–4420. doi: 10.1002/hbm.22928
- Homayoon, N., Pirpamer, L., Frantal, S., Katschnig-Winter, P., Kögl, M., Seiler, D., et al. (2019). Nigral iron deposition in common

- tremor disorders. *Mov. Disord.* 34, 129–132. doi: 10.1002/mds.27549
- Jenner, P. (2008). Molecular mechanisms of L-DOPA-induced dyskinesia. *Nat. Rev. Neurosci.* 9, 665–677. doi: 10.1038/nrn2471
- Kordower, J. H., Olanow, C. W., Dodiya, H. B., Chu, Y., and Beach, T. G. (2013). Disease duration and the integrity of the nigrostriatal system in Parkinson's disease. *Brain* 136, 2419–2431. doi: 10.1093/brain/awt192
- Kumar, N., Van Gerpen, J. A., Bower, J. H., and Ahlskog, J. E. (2005). Levodopa-dyskinesia incidence by age of Parkinson's disease onset. *Mov. Disord.* 20, 342–344. doi: 10.1002/mds.20360
- Lewis, M. M., Du, G., Kidacki, M., Patel, N., Shaffer, M. L., Mailman, R. B., et al. (2013). Higher iron in the red nucleus marks Parkinson's dyskinesia. *Neurobiol. Aging* 34, 1497–1503. doi: 10.1016/j.neurobiolaging.2012.10.025
- Li, W., Wang, N., Yu, F., Han, H., Cao, W., Romero, R., et al. (2015). A method for estimating and removing streaking artifacts in quantitative susceptibility mapping. *Neuroimage* 108, 111–122. doi: 10.1016/j.neuroimage.2014.12.043
- Lindgren, H. S., Andersson, D. R., Lagerkvist, S., Nissbrandt, H., and Cenci, M. A. (2010). L-DOPA-induced dopamine efflux in the striatum and the substantia nigra in a rat model of Parkinson's disease: temporal and quantitative relationship to the expression of dyskinesia. *J. Neurochem.* 112, 1465–1476. doi: 10.1111/j.1471-4159.2009.06556.x
- Manson, A., Stirpe, P., and Schrag, A. (2012). Levodopa-induced-dyskinesias clinical features, incidence, risk factors, management and impact on quality of life. *J. Parkinsons Dis.* 2, 189–198. doi: 10.3233/JPD-2012-120103
- Martin, W. R., Wieler, M., and Gee, M. (2008). Midbrain iron content in early Parkinson disease: a potential biomarker of disease status. *Neurology* 70, 1411–1417. doi: 10.1212/01.wnl.0000286384.31050.b5
- Matarazzo, M., Perez-Soriano, A., and Stoessl, A. J. (2018). Dyskinesias and levodopa therapy: why wait? *J. Neural. Transm. (Vienna)* 125, 1119–1130. doi: 10.1007/s00702-018-1856-6
- Mela, F., Marti, M., Bido, S., Cenci, M. A., and Morari, M. (2012). In vivo evidence for a differential contribution of striatal and nigral D1 and D2 receptors to L-DOPA induced dyskinesia and the accompanying surge of nigral amino acid levels. *Neurobiol. Dis.* 45, 573–582. doi: 10.1016/j.nbd.2011.09.015
- Mela, F., Marti, M., Dekundy, A., Danysz, W., Morari, M., and Cenci, M. A. (2007). Antagonism of metabotropic glutamate receptor type 5 attenuates L-DOPA-induced dyskinesia and its molecular and neurochemical correlates in a rat model of Parkinson's disease. *J. Neurochem.* 101, 483–497. doi: 10.1111/j.1471-4159.2007.04456.x
- Murakami, Y., Kakeda, S., Watanabe, K., Ueda, I., and Ogasawara, A. (2015). Usefulness of quantitative susceptibility mapping for the diagnosis of Parkinson disease. *AJNR Am. J. Neuroradiol.* 36, 1102–1108. doi: 10.3174/ajnr.A4260
- Pahwa, R., Isaacson, S., Jimenez-Shaheed, J., Malaty, I. A., and Deik, A. (2019). Impact of dyskinesia on activities of daily living in Parkinson's disease: results from pooled phase 3 ADS-5102 clinical trials. *Parkinsonism Relat. Disord.* 60, 118–125. doi: 10.1016/j.parkreldis.2018.09.005
- Perez-Lloret, S., Negre-Pages, L., Damier, P., Delval, A., and Derkinderen, P. (2017). L-DOPA-induced dyskinesias, motor fluctuations and health-related quality of life: the COPARK survey. *Eur. J. Neurol.* 24, 1532–1538. doi: 10.1111/ene.13466
- Picconi, B., Hernández, L. F., Obeso, J. A., and Calabresi, P. (2018). Motor complications in Parkinson's disease: striatal molecular and electrophysiological mechanisms of dyskinesias. *Mov. Disord.* 33, 867–876. doi: 10.1002/mds.27261
- Postuma, R. B., Berg, D., Stern, M., Poewe, W., Olanow, C. W., Oertel, W., et al. (2015). MDS clinical diagnostic criteria for Parkinson's disease. *Mov. Disord.* 30, 1591–1601. doi: 10.1002/mds.26424
- Prashanth, L. K., Fox, S., and Meissner, W. G. (2011). L-Dopa-induced dyskinesia-clinical presentation, genetics, and treatment. *Int. Rev. Neurobiol.* 98, 31–54. doi: 10.1016/B978-0-12-381328-2.00002-X
- Rouault, T. A. (2013). Iron metabolism in the CNS: implications for neurodegenerative diseases. *Nat. Rev. Neurosci.* 14, 551–564. doi: 10.1038/nrn3453
- Sarre, S., Vandeneede, D., Ebinger, G., and Michotte, Y. (1998). Biotransformation of L-DOPA to dopamine in the substantia nigra of freely moving rats: effect of dopamine receptor agonists and antagonists. *J. Neurochem.* 70, 1730–1739. doi: 10.1046/j.1471-4159.1998.70041730.x
- Sun, J., Lai, Z., Ma, J., Gao, L., Chen, M., Chen, J., et al. (2020). Quantitative evaluation of iron content in idiopathic rapid eye movement sleep behavior disorder. *Mov. Disord.* 35, 478–485. doi: 10.1002/mds.27929
- Thomas, B., and Beal, M. F. (2007). Parkinson's disease. *Hum. Mol. Genet.* 16, R183–R194. doi: 10.1093/hmg/ddm159
- Ward, R. J., Zucca, F. A., Duyn, J. H., Crichton, R. R., and Zecca, L. (2014). The role of iron in brain ageing and neurodegenerative disorders. *Lancet Neurol.* 13, 1045–1060. doi: 10.1016/S1474-4422(14)70117-6
- Warren, O. C., Kieburtz, K., Rascol, O., Poewe, W., Schapira, A. H., Emre, M., et al. (2013). Factors predictive of the development of Levodopa-induced dyskinesia and wearing-off in Parkinson's disease. *Mov. Disord.* 28, 1064–1071. doi: 10.1002/mds.25364
- Ye, Y., Zhou, F., Zong, J., Lyu, J., Chen, Y., Zhang, S., et al. (2019). Seed prioritized unwrapping (SPUN) for MR phase imaging. *J. Magn. Reson. Imaging* 50, 62–70. doi: 10.1002/jmri.26606
- Zappia, M., and Quattrone, A. (2008). Continuous dopaminergic stimulation: is it the answer to the motor complications of levodopa? *Mov. Disord.* 23, 1062–1063. doi: 10.1002/mds.21819

Conflict of Interest: YY was employed by the company UIH America.

The remaining authors declare that the research was conducted in the absence of any commercial or financial relationships that could be construed as a potential conflict of interest.

Copyright © 2021 Song, Li, Mei, Jia, Yang, Ye, Yuan, Zhang and Lu. This is an open-access article distributed under the terms of the Creative Commons Attribution License (CC BY). The use, distribution or reproduction in other forums is permitted, provided the original author(s) and the copyright owner(s) are credited and that the original publication in this journal is cited, in accordance with accepted academic practice. No use, distribution or reproduction is permitted which does not comply with these terms.

Advantages of publishing in Frontiers



OPEN ACCESS

Articles are free to read
for greatest visibility
and readership



FAST PUBLICATION

Around 90 days
from submission
to decision



HIGH QUALITY PEER-REVIEW

Rigorous, collaborative,
and constructive
peer-review



TRANSPARENT PEER-REVIEW

Editors and reviewers
acknowledged by name
on published articles

Frontiers

Avenue du Tribunal-Fédéral 34
1005 Lausanne | Switzerland

Visit us: www.frontiersin.org

Contact us: frontiersin.org/about/contact



REPRODUCIBILITY OF RESEARCH

Support open data
and methods to enhance
research reproducibility



DIGITAL PUBLISHING

Articles designed
for optimal readership
across devices



FOLLOW US

@frontiersin



IMPACT METRICS

Advanced article metrics
track visibility across
digital media



EXTENSIVE PROMOTION

Marketing
and promotion
of impactful research



LOOP RESEARCH NETWORK

Our network
increases your
article's readership